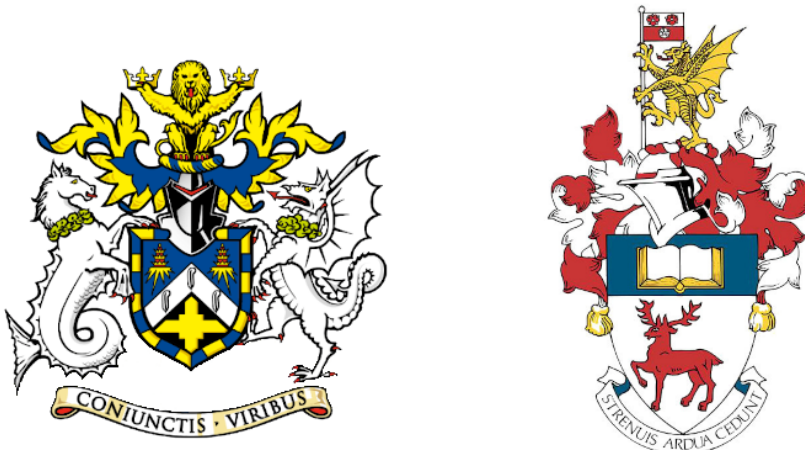


<sup>1</sup> ADVANCING NEUTRINO  
<sup>2</sup> DETECTION AND TRIGGERING IN  
<sup>3</sup> DUNE



<sup>5</sup> Francisco Martínez López

<sup>6</sup> Submitted in partial fulfillment of the requirements  
<sup>7</sup> of the Degree of Doctor of Philosophy

<sup>8</sup> School of Physical and Chemical Sciences  
<sup>9</sup> Queen Mary University of London

<sup>10</sup> School of Physics and Astronomy  
<sup>11</sup> University of Southampton

<sup>12</sup> December 2024



13

## Statement of originality

14 I, Francisco Martínez López, confirm that the research included within this thesis is my  
15 own work or that where it has been carried out in collaboration with, or supported by  
16 others, that this is duly acknowledged below and my contribution indicated. Previously  
17 published material is also acknowledged below.

18 I attest that I have exercised reasonable care to ensure that the work is original, and  
19 does not to the best of my knowledge break any UK law, infringe any third party's  
20 copyright or other Intellectual Property Right, or contain any confidential material.

21 I accept that the University has the right to use plagiarism detection software to check  
22 the electronic version of the thesis.

23 I confirm that this thesis has not been previously submitted for the award of a degree  
24 by this or any other university.

25 The copyright of this thesis rests with the author and no quotation from it or information  
26 derived from it may be published without the prior written consent of the author.

27 Signature: [can be digital signature]

28 Date:

29 Details of collaboration and publications:

30 [insert details here if applicable]



# Abstract

31

32 Work in progress ...



*¡Oh memoria, enemiga mortal de mi descanso!*

---

*El ingenioso hidalgo don Quijote de la Mancha*

MIGUEL DE CERVANTES SAAVEDRA



## Acknowledgements

34 Work in progress ...



# Contents

35

36	Statement of originality . . . . .	3
37	Abstract . . . . .	5
38	Acknowledgements . . . . .	9
39	<b>List of Figures</b>	<b>15</b>
40	<b>List of Tables</b>	<b>31</b>
41	<b>List of Abbreviations</b>	<b>33</b>
42	<b>1 Introduction</b>	<b>35</b>
43	<b>2 Neutrino physics</b>	<b>37</b>
44	2.1 Neutrinos in the SM . . . . .	37
45	2.2 Trouble in the neutrino sector . . . . .	41
46	2.2.1 The solar neutrino problem . . . . .	41
47	2.2.2 The atmospheric neutrino problem . . . . .	43
48	2.3 Massive neutrinos . . . . .	45
49	2.4 Neutrino oscillation formalism . . . . .	47
50	2.4.1 Oscillations in vacuum . . . . .	49
51	2.4.2 Oscillations in matter . . . . .	52
52	2.4.3 Current status of neutrino oscillations . . . . .	54
53	2.5 Open questions in the neutrino sector . . . . .	55
54	2.6 Neutrino interactions . . . . .	56

## CONTENTS

55	<b>3 The Deep Underground Neutrino Experiment</b>	<b>61</b>
56	3.1 Overview . . . . .	61
57	3.2 Physics goals of DUNE . . . . .	63
58	3.3 LBNF beamline . . . . .	65
59	3.4 Near Detector . . . . .	66
60	3.4.1 ND-LAr . . . . .	69
61	3.4.2 TMS/ND-GAr . . . . .	70
62	3.4.3 PRISM . . . . .	71
63	3.4.4 SAND . . . . .	72
64	3.5 A More Capable Near Detector . . . . .	72
65	3.5.1 Requirements . . . . .	73
66	3.5.2 Reference design . . . . .	73
67	3.5.3 R&D efforts . . . . .	76
68	3.6 Far Detector . . . . .	79
69	3.6.1 Horizontal Drift . . . . .	80
70	3.6.2 Vertical Drift . . . . .	82
71	3.6.3 FD Data Acquisition System . . . . .	84
72	<b>4 Matched Filter approach to Trigger Primitives</b>	<b>87</b>
73	4.1 Motivation . . . . .	87
74	4.2 Signal-to-noise ratio definition . . . . .	89
75	4.3 Low-pass FIR filter design . . . . .	91
76	4.4 Matched filters . . . . .	94
77	4.5 Using simulated samples . . . . .	100
78	4.5.1 Angular dependence . . . . .	106
79	4.5.2 Distortion and peak asymmetry . . . . .	108
80	4.5.3 Hit sensitivity . . . . .	111
81	<b>5 DM searches with neutrinos from the Sun</b>	<b>121</b>
82	5.1 Motivation . . . . .	121

## CONTENTS

83	5.2 Gravitational capture of DM by the Sun . . . . .	121
84	5.3 Neutrino flux from DM annihilations . . . . .	128
85	5.4 Computing limits from solar neutrino fluxes . . . . .	129
86	5.5 Example: Kaluza-Klein Dark Matter . . . . .	133
87	5.6 High energy DM neutrino signals . . . . .	136
88	5.6.1 DIS events . . . . .	139
89	5.6.2 Single proton QEL events . . . . .	143
90	5.6.3 Results . . . . .	147
91	5.7 Example: Leptophilic Dark Matter . . . . .	149
92	<b>6 Particle ID in ND-GAr</b>	<b>155</b>
93	6.1 GArSoft . . . . .	156
94	6.1.1 Event generation . . . . .	156
95	6.1.2 Detector simulation . . . . .	157
96	6.1.3 Reconstruction . . . . .	158
97	6.2 $dE/dx$ measurement in the TPC . . . . .	161
98	6.2.1 Energy calibration . . . . .	163
99	6.2.2 Truncated $dE/dx$ mean . . . . .	173
100	6.2.3 Mean $dE/dx$ parametrisation . . . . .	176
101	6.2.4 Particle identification . . . . .	180
102	6.3 Muon and pion separation in the ECal and MuID . . . . .	180
103	6.3.1 Track-ECal matching . . . . .	183
104	6.3.2 Classification strategy . . . . .	187
105	6.3.3 Feature selection and importance . . . . .	191
106	6.3.4 Hyperparameter optimisation . . . . .	202
107	6.3.5 Probability calibration . . . . .	206
108	6.3.6 Performance . . . . .	208
109	6.4 ECal time-of-flight . . . . .	208
110	6.4.1 Arrival time estimations . . . . .	210

## CONTENTS

111	6.4.2 Proton and pion separation . . . . .	212
112	6.5 Charged pion decay in flight . . . . .	212
113	6.5.1 Track breakpoints . . . . .	215
114	6.6 Neutral particle identification . . . . .	222
115	6.6.1 ECal clustering . . . . .	222
116	6.6.2 $\pi^0$ reconstruction . . . . .	225
117	<b>7 Event selection in ND-GAr</b>	<b>229</b>
118	7.1 Data sample . . . . .	229
119	7.2 $\nu_\mu$ CC selection . . . . .	229
120	7.2.1 Selection optimisation . . . . .	232
121	7.2.2 Primary muon kinematics . . . . .	233
122	7.3 Charged pion identification . . . . .	233
123	7.3.1 $\nu_\mu$ CC $1\pi^\pm$ selection . . . . .	233
124	<b>8 Conclusions</b>	<b>235</b>
125	<b>A An appendix</b>	<b>237</b>
126	<b>B Bibliography</b>	<b>239</b>

# List of Figures

127

128	2.1 Solar neutrino fluxes for the solar model BS05(OP). . . . .	42
129	2.2 Zenith angle distributions for the selected $\nu_e$ and $\nu_\mu$ events in the SK	
130	detector. . . . .	44
131	2.3 $K^0 \rightleftharpoons \bar{K}^0$ mixing through $W^\pm$ exchange. . . . .	48
132	2.4 Feynman diagrams of the four most relevant CC interactions to long	
133	baseline neutrino oscillation experiments. . . . .	57
134	2.5 Total muon neutrino CC cross section per nucleon as a function of the	
135	neutrino energy. . . . .	58
136	2.6 Schematic representation of a $\nu_\mu$ CCQE interaction with a neutron inside	
137	a nucleus. . . . .	59
138	3.1 Schematic diagram of the DUNE experiment and the LBNF beamline. .	62
139	3.2 Schematic longitudinal section of the LBNF beamline at Fermilab. . .	65
140	3.3 Predicted neutrino fluxes at the FD in FHC mode and RHC mode. . .	66
141	3.4 Representation of the ND hall in Phase II, showing the different subcomponents.	67
142	3.5 Schematic representation of the external components of ND-LAr, including	
143	the cryostat and the PRISM movable system and detailed drawing of one	
144	ArgonCube module. . . . .	68
145	3.6 Schematic view of the TMS detector, highlighting its main parts. . . .	69
146	3.7 Cross section of the ND-GAr geometry, showing the HPgTPC, ECal and	
147	magnet. . . . .	70
148	3.8 Predicted beam muon neutrino flux at the ND location for different off-axis	
149	positions. . . . .	71

## LIST OF FIGURES

150	3.9	Diagram of the ALICE TPC, showing the two drift chambers, inner and outer field cages and readout chambers. . . . .	74
151			
152	3.10	Diagram of the ALICE TPC, showing the two drift chambers, inner and outer field cages and readout chambers. . . . .	75
153			
154	3.11	Photographs of the TOAD pressure vessel at RHUL. . . . .	77
155			
156	3.12	Electron microscope image and schematic diagram of a GEM electrode. . . . .	78
157			
158	3.13	Schematic diagram showing the operating principle of a LArTPC with wire readout. . . . .	79
159			
160	3.14	Proposed design for the FD-1 and FD-2 modules following the HD principle. . . . .	80
161			
162	3.15	Schematic representation of an APA frames showing the U, V, X and G wires. . . . .	81
163			
164	3.16	A PDS module containing 24 X-ARAPUCAs and the location of the modules on the APAs. . . . .	82
165			
166	3.17	Proposed design for the FD-3 module following the VD principle. . . . .	83
167			
168	3.18	Schematic representation of the electrode strip configuration for a top and bottom CRU. . . . .	84
169			
170	3.19	Detailed diagram of the DUNE FD DAQ system. . . . .	85
171			
172	4.1	<i>Schematic representation of an APA. The black lines represent the APA steel frame. The green and magenta lines correspond to the direction of the U and V induction wires respectively. The blue lines indicate the direction of the X collection wires and the wire shielding G.</i> . . . . .	88
173			
174	4.2	<i>Left panel: Zoomed unfiltered waveform corresponding to channel 7840 from the ProtoDUNE-SP raw data capture <code>felix-2020-07-17-21:31:44</code> (blue line). The green dashed lines mark the region <math>\pm 3\sigma_{raw}</math>. The resulting noise waveform is also shown (red line). Top right panel: ADC distribution for channel 7840, where the green shaded region represents <math>\pm \sigma_{raw}</math>. Bottom right panel: noise ADC distribution for channel 7840, where the green shaded region represents <math>\pm \sigma_{noise}</math>.</i> . . . . .	89
175			
176			
177			

## LIST OF FIGURES

178	4.3 <i>Left panel:</i> Zoomed filtered waveform corresponding to channel 7840 from the ProtoDUNE-SP raw data capture <i>felix-2020-07-17-21:31:44</i> (blue line). The filter used was the current implementation of the low-pass FIR filter in <i>dtp-firmware</i> . The green dashed lines mark the region $\pm 3\sigma_{\text{raw}}$ . The resulting noise waveform is also shown (red line). <i>Top right panel:</i> ADC distribution for channel 7840 after filtering, where the green shaded region represents $\pm \sigma_{\text{raw}}$ . <i>Bottom right panel:</i> noise ADC distribution for channel 7840 after filtering, where the green shaded region represents $\pm \sigma_{\text{noise}}$	91
186	4.4 Power spectrum in decibels for the current implementation of the low-pass FIR filter in <i>dtp-firmware</i> (blue line), compared to the response of an optimal filter obtained using the Parks-McClellan algorithm for the same pass-band (red line). Also for comparison I include the spectrum of the optimal filter when taking only the integer part of the coefficients (red dashed line).	92
192	4.5 Relative change in the S/N for the ProtoDUNE-SP raw data capture <i>felix-2020-07-17-21:31:44</i> , using different values of the cutoff frequency $f_c$ and the transition width $\delta f$ . The optimal Chebyshev filters were applied using just the integer part of the coefficients given by the Parks-McClellan algorithm.	93
197	4.6 Distribution of the relative change of the S/N on the different wire planes from the ProtoDUNE-SP raw data capture <i>felix-2020-07-17-21:31:44</i> after the optimal Chebyshev filter was applied. The filter was computed with the Parks-McClellan algorithm using a cutoff of $f_c = 0.068 \text{ ticks}^{-1}$ and a transition width $\delta f = 0.010 \text{ ticks}^{-1}$ .	94

## LIST OF FIGURES

202	4.7	<i>Left panel:</i> Zoomed match filtered waveform corresponding to channel 7840 from the ProtoDUNE-SP raw data capture <i>felix-2020-07-17-21:31:44</i> (blue line). The filter used was directly extracted from the data, being the 32 values around the first peak in the original waveform. The green dashed lines mark the region $\pm 3\sigma_{\text{raw}}$ . The resulting noise waveform is also shown (red line). <i>Top right panel:</i> ADC distribution for channel 7840 after match filtering, where the green shaded region represents $\pm \sigma_{\text{raw}}$ . <i>Bottom right panel:</i> noise ADC distribution for channel 7840 after match filtering, where the green shaded region represents $\pm \sigma_{\text{noise}}$ . . . . .	95
211	4.8	<i>Relative improvement in the S/N for the raw data capture <i>felix-2020-07-17-21:31:44</i>, using the matched filter following the parametrisation in Eq. (4.17). The black crosses in both panels denote the location of the maximum ratio value.</i>	98
214	4.9	<i>Left panel:</i> Optimal matched filter coefficients for the U (blue line) and V (red line) planes. The filters were computed with our parametrisation in Eq. (4.17) for the parameter values $\delta = 0.035$ , $\sigma = 0.191$ and $\delta = 0.018$ , $\sigma = 0.191$ respectively. <i>Right panel:</i> Distribution of the relative change of the S/N on the two induction wire planes from the ProtoDUNE-SP raw data capture <i>felix-2020-07-17-21:31:44</i> after their respective optimal matched filters were applied. . . . .	101
221	4.10	<i>Left panel:</i> distributions of the particles track length in the liquid argon for the generated $E_k = 100$ MeV monoenergetic samples, electrons (blue), muons (red), protons (green) and neutral pions (purple). <i>Right panel:</i> distribution of the length of the longest photon in the neutral pion sample after the decay process $\pi^0 \rightarrow \gamma\gamma$ . . . . .	102

## LIST OF FIGURES

## LIST OF FIGURES

251	4.15 Selected consecutive waveforms corresponding to two monoenergetic $E_k =$	
252	100 MeV muon events, one is parallel to the APA and to the wires in	
253	the U plane (left panel) and the other is normal to the APA plane and	
254	perpendicular to the U plane wires (right panel). The solid lines represent	
255	the raw waveforms whereas the dashed lines correspond to the waveforms	
256	after the matched filter was applied. The waveforms on the left panel have	
257	been scaled by a factor of 0.15 to have similar amplitude to the ones on	
258	the right panel. . . . .	109
259	4.16 Left panel: peak asymmetry distribution for the case of the monoenergetic	
260	$E_k = 100$ MeV muon sample. Each value corresponds to a single bipolar	
261	signal peak from a channel in any event. The blue distribution represents	
262	the peaks on U plane channels, whereas the red corresponds to signal peaks	
263	in V wires. Right panel: relation between the mean peak asymmetry per	
264	event with the S/N for U channel waveforms from the $E_k = 100$ MeV	
265	muon sample. The top subplot shows the decimal logarithm of the mean	
266	S/N for the raw (red) and the matched filtered (blue) waveforms. The	
267	bottom subplot contains the mean S/N improvement ratio after the matched	
268	filter was applied. . . . .	110
269	4.17 Raw data display in the plane time (in firmware ticks) vs. offline channel	
270	number for an $E_k = 100$ MeV electron event. The produced true hits are	
271	superimposed (black boxes) as well as the hits comming from the standard	
272	hit finder chain (blue circles) and the hit finder using the matched filter	
273	(green triangles). . . . .	112

## LIST OF FIGURES

- 274    4.18 *Dependence of the precision (blue), sensitivity (red) and  $F_1$  (green) scores*  
275    *on the threshold values used in the hit finder, for the FIR (left panel)*  
276    *and matched filter (right panel) cases. The results were obtained after*  
277    *matching the hits to the true hits in the case of the isotropic muon sample*  
278    *with kinetic energy in the range 5 to 100 MeV, taking only into account*  
279    *the induction plane channels. The points represent the mean value while*  
280    *the error bars indicate one standard deviation around that mean value.* . . 114
- 281    4.19 *Dependence of the averaged hit sensitivity on the kinetic energy of the*  
282    *events for the matched filter (blue) and standard (red) hits, for the case of*  
283    *the muon (left panel) and electron (right panel) samples, separated between*  
284     *$U$  (top plots) and  $V$  (bottom plots) induction wire planes. The top subplots*  
285    *contain the hit sensitivities for the two hit finder alternatives, while the*  
286    *bottom subplots show the ratio between the two. The horizontal lines sit at*  
287    *the mean value and represent the size of the energy bins, while the vertical*  
288    *error bars indicate one standard deviation around that mean value.* . . . 116
- 289    4.20 *Distributions of the hit sensitivity in the  $U$  (top panels) and  $V$  (bottom*  
290    *panels) planes versus the hit sensitivity in the  $X$  plane, both for the*  
291    *standard hits (left panels) and the matched filter hits (right panels), in the*  
292    *case of the electron sample and a threshold of 30 ADC.* . . . . . 117
- 293    4.21 *Top panels: standard residual plots of the hit sensitivities between the  $X$*   
294    *and  $U$  planes. Bottom panels: quantile-quantile plots of the hit sensitivity*  
295    *standard residuals between the  $X$  and  $U$  planes. In all cases, the left*  
296    *panel corresponds to the standard hits while the right panel represents the*  
297    *matched filter case, all from the electron sample with a 30 ADC threshold.* 118

## LIST OF FIGURES

298	5.1	<i>Input solar parameters used in our capture rate computation as functions of the Sun's radius, from left to right: temperature (with respect to the temperature at the core), mass (in solar masses) and electron number density (with respect to the electron density at the core). All quantities shown correspond to the standard solar model BS2005-OP [1]. . . . .</i>	124
303	5.2	<i>Capture rates as a function of the DM mass for the DM-electron interactions (red lines), SD DM-nucleons interactions (green lines) and SI DM-nucleons interactions (blue lines). Solid lines represent the values computed in this work while the dashed lines are the one given in Ref. [2]. All the rates are shown for a choice of scattering cross section of <math>\sigma_i = 10^{-40} \text{ cm}^2</math>. . .</i>	126
308	5.3	<i>NuWro computed <math>\nu_\mu - {}^{40}\text{Ar}</math> charged-current scattering cross section as a function of the neutrino energy <math>E_\mu</math>. The black line shows to the total cross section, whereas the others correspond to the different contributions (in red quasi-elastic scattering, in green resonant pion exchange, in blue deep inelastic scattering and in purple meson exchange current). . . . .</i>	130
313	5.4	<i>Expected atmospheric neutrino flux as a function of the neutrino energy <math>E_\nu</math> at Homestake at solar minimum, taken from Ref. [3]. The blue solid (dashed) line correspond to muon neutrinos (antineutrinos) and the red solid (dashed) line correspond to electron neutrinos (antineutrinos). . . .</i>	132
317	5.5	<i>Feynman diagrams for <math>B^1B^1</math> annihilation into SM fermions. . . . .</i>	133
318	5.6	<i>Feynman diagrams for <math>B^1B^1</math> annihilation into a Higgs boson pair. . . .</i>	134
319	5.7	<i>Computed spectra of muon neutrinos at the DUNE FD site from <math>B^1</math> annihilations in the Sun for three different values of <math>M_{\text{LKP}}</math>, plotted in relative energy units for legibility. . . . .</i>	135

## LIST OF FIGURES

<p>322    5.8    <i>Projected 90% confidence level upper limit for DUNE (400 kT yr) on the</i>      323    <i>spin-dependent <math>B^1</math>-proton scattering cross section as a function of <math>M_{\text{LKP}}</math></i>      324    <i>(green dots). I also show the previous limits from IceCube [4] (blue line)</i>      325    <i>and Antares [5] (red line) on the LKP cross section. The shaded area</i>      326    <i>represents the disfavoured region (at 95% confidence level) on the mass of</i>      327    <i>the LKP from LHC data [6]. . . . .</i></p>	136
<p>328    5.9    <i>Computed spectra of muon neutrinos at the DUNE FD site from <math>\tau^+\tau^-</math></i>      329    <i>(left panel) and <math>b\bar{b}</math> (right panel) annihilations in the Sun for the DM</i>      330    <i>masses <math>m_{\text{DM}} = 10</math> GeV (red line), 50 GeV (green line) and 100 GeV</i>      331    <i>(blue line), plotted in relative energy units. . . . .</i></p>	137
<p>332    5.10    <i>Distribution of the muon neutrino energies from the <math>\tau^+\tau^-</math> (left panel)</i>      333    <i>and <math>b\bar{b}</math> (right panel) annihilation channels, for <math>m_{\text{DM}} = 10</math> GeV, separated</i>      334    <i>by CC interaction type: QEL (blue), MEC (orange), RES (green) and</i>      335    <i>DIS (red). . . . .</i></p>	138
<p>336    5.11    <i>Distributions of <math>\theta_\mu</math> (left panel), <math>\theta_j</math> (central panel) and <math>\theta_{\text{plane}}</math> (right panel)</i>      337    <i>for the <math>b\bar{b}</math> sample with <math>m_{\text{DM}} = 10</math> GeV (blue) and the atmospheric</i>      338    <i>background (red). . . . .</i></p>	139
<p>339    5.12    <i>Left panel: signal efficiencies (blue lines) and background rejections (red</i>      340    <i>lines) for events passing the cuts <math>\theta &lt; \theta_{\text{cut}}</math> for the jet (solid lines) and</i>      341    <i>muon (dashed lines) angles. Right panel: signal efficiency (blue line) and</i>      342    <i>background rejection (red line) for events passing the cut <math>\theta_{\text{plane}} &lt; \theta_{\text{cut}}</math> for</i>      343    <i>the momentum conservation plane deviation. . . . .</i></p>	141
<p>344    5.13    <i>Signal efficiencies for the <math>\tau^+\tau^-</math> (blue line) and <math>b\bar{b}</math> (red line) DIS samples</i>      345    <i>as functions of the DM mass, <math>m_{\text{DM}}</math>, obtained by applying the optimal</i>      346    <i>angular cuts <math>\theta_\mu &lt; 27^\circ</math>, <math>4^\circ &lt; \theta_j &lt; 26^\circ</math> and <math>\theta_{\text{plane}} &lt; 3.5^\circ</math>. . . . .</i></p>	142
<p>347    5.14    <i>Distributions of <math>\cos \theta_\mu</math> (left panel), <math>\cos \theta_p</math> (central panel) and <math>\cos \theta_N</math></i>      348    <i>(right panel) for the <math>\tau^+\tau^-</math> QEL sample with <math>m_{\text{DM}} = 5</math> GeV (blue) and</i>      349    <i>the atmospheric background (red). . . . .</i></p>	143

## LIST OF FIGURES

350	5.15 Left panel: value of the loss function for the training sample (blue line) and accuracy for the validation sample (red line) versus the number of iterations for the MLP classifier training. Right panel: distributions of the predicted probabilities assigned by the MLP classifier to the test sample for the $\tau^+\tau^-$ QEL signal with $m_{\text{DM}} = 5$ GeV (blue) and the atmospheric background (red). . . . .	144
356	5.16 Signal efficiencies for the $\tau^+\tau^-$ (blue line) and $b\bar{b}$ (red line) single proton QEL samples as functions of the DM mass, $m_{\text{DM}}$ , obtained by requiring a minimum predicted probability from the MLP classifier of 0.97 in order to achieve a background rejection greater than 99.8%. . . . .	146
360	5.17 Projected 90% confidence level upper limit for DUNE (400 kT yr) on the spin-dependent DM-nucleon scattering cross section as a function of $m_{\text{DM}}$ , for the annihilation channels $\tau^+\tau^-$ (blue) and $b\bar{b}$ (red) separated by interaction type (up triangles denote DIS interactions whereas down triangles represent QEL interactions). I also show the previous limits from IceCube [7] (solid lines) and the projected sensitivities for Pingu [8] (dashed lines) and Hyper-Kamiokande [9] (dash-dotted lines), as well as the direct detection limits from PICASSO [10] (solid green line) and PICO-60 C <sub>3</sub> F <sub>8</sub> [11] (dashed green line). . . . .	147
369	5.18 Left panel: Projected 90% confidence level sensitivity of DUNE (400 kT yr) to the scale $\Lambda$ of an EFT containing only leptophilic DM axial-axial interactions (blue line). Right panel: . In both cases the corresponding limits from DarkSide-50 [12] (dotted green line) and XENON1T [13] (dashed red line) are also shown, together with the configurations for which the correct relic density is achieved (black line), all for the coupling values $c_A^e = 10^3$ and $c_A^\nu = 10^{-2}$ . . . . .	152
376	6.1 Schematic diagram showing the different modules involved in the ND-GAr production. . . . .	160

## LIST OF FIGURES

<p>378      6.2 Distribution of the fraction of energy deposits with residual range less 379      than 20% of the total track length, and distribution of the ionisation per 380      unit length after removing the tracks with less than 30% of their energy 381      deposits in the last 20% of the track. . . . .</p> <p>382      6.3 Distribution of the reconstructed ionisation charge per unit length for 383      different reclustering values, and distribution of the median change in 384      <math>dQ/dx</math> per track for the <math>N_{group} = 4</math> reclustering. . . . .</p> <p>385      6.4 Distribution of the Geant4-simulated energy losses per unit length versus 386      residual range for the stopping proton sample. . . . .</p> <p>387      6.5 Fitted most probable <math>dQ/dx</math> values for each <math>dE/dx</math> bin, together with 388      best fit to the logarithmic calibration function. . . . .</p> <p>389      6.6 Fitted most probable <math>dQ/dx</math> values for each <math>dE/dx</math> bin for three different 390      ADC bit limits. . . . .</p> <p>391      6.7 Area normalised <math>dE/dx</math> distributions for the true and the reconstructed 392      energy deposits in the stopping proton sample, both after applying the 393      calibration and the calibration and the normalisation correction. . . . .</p> <p>394      6.8 Fractional residuals between the true and the corrected <math>dE/dx</math> means 395      and the 60% truncated means, and fractional residuals between the true 396      and the uncorrected, corrected and uncalibrated <math>dE/dx</math> 60% truncated 397      means. . . . .</p> <p>398      6.9 Estimated values of the mean <math>dE/dx</math> bias and resolution for the stopping 399      proton sample at different values of the truncation factor. . . . .</p> <p>400      6.10 Examples of the truncated mean <math>dE/dx</math> LanGauss fits for various <math>\beta\gamma</math> 401      bins, from a simulated FHC neutrino sample. . . . .</p> <p>402      6.11 Resulting one and two dimensional projections of the posterior probability 403      distributions of the ALEPH <math>\langle dE/dx \rangle</math> parameters obtained by fitting the 404      60% truncated mean <math>dE/dx</math> values from a FHC neutrino sample. . . . .</p>	<p>164</p> <p>165</p> <p>167</p> <p>168</p> <p>170</p> <p>171</p> <p>173</p> <p>174</p> <p>176</p> <p>177</p>
--	---

## LIST OF FIGURES

405	6.12 Truncated mean $dE/dx$ obtained for the FHC neutrino sample as a function of the $\beta\gamma$ product, together with the fitted most probable values for each $\beta\gamma$ bin and the best fit obtained using the ALEPH parametrisation.	178
408	6.13 Distribution of the 60% truncated mean $dE/dx$ versus reconstructed momentum for the FHC neutrino sample. . . . .	179
410	6.14 Estimated values of the mean $dE/dx$ bias and resolution obtained for the true protons in a FHC neutrino sample. . . . .	180
412	6.15 True momentum distribution for the primary muon in $\nu_\mu$ CC $N\pi^\pm$ interactions inside the fiducial volume of ND-GAr, compared to the post FSI charged pion spectrum. . . . .	181
415	6.16 Distributions of energy deposits in the ECal for a muon and a charged pion with similar momenta. . . . .	182
417	6.17 Left panel: comparison between the precision (blue), sensitivity (yellow) and $F_1$ score (red) obtained for the default (horizontal lines) and new algorithms, both with the $\chi^2$ -based direction estimator (squares) and cheating the directions (circles), for different values of the $\chi^2$ cut. Right panel: comparison of the performance of the new algorithm when applying the cluster $t_0$ correction (squares) and when (circles). . . . .	184
423	6.18 Schematics of a possible option to deal with track-ECal associations in non-zero $t_0$ neutrino interaction events, trying to correct for the drift direction uncertainty in a cluster-by-cluster basis using the cluster time, $t_{cluster}$ . . . . .	186
427	6.19 Momentum distribution for the reconstructed muons (top panel) and charged pions (bottom panel) in a FHC neutrino sample, together with the fraction of them reaching the ECal (red) and MuID (blue). Each entry corresponds to a reconstructed track, backtracked to a true muon or pion which has not produced any other reconstructed track. . . . .	188

## LIST OF FIGURES

<p>432    6.20 Predicted truncated mean <math>dE/dx</math> versus momentum, for electrons, muons, 433    charged pions and protons, obtained using the ALEPH parametrisation. 434    The vertical dashed lines represent the boundaries of the six regions used 435    for the muon and pion classification training. . . . .</p> <p>436    6.21 Example ECal feature distributions for muons and charged pions in the 437    five different momentum ranges considered. . . . .</p> <p>438    6.22 Example MuID feature distributions for muons and charged pions in the 439    three different momentum ranges considered. . . . .</p> <p>440    6.23 Left panel: cumulative explained variance for the first three principal 441    components (top panel) and contribution of the different features to the 442    principal axes in feature space (bottom panel). Right panel: Shapley 443    (blue) and Gini (red) feature importances for the different input features. 444    Both figures correspond to the samples in the momentum range <math>0.3 \leq</math> 445    <math>p &lt; 0.8 \text{ GeV}/c</math>. . . . .</p> <p>446    6.24 Left panel: cumulative explained variance for the first three principal 447    components (top panel) and contribution of the different features to the 448    principal axes in feature space (bottom panel). Right panel: Shapley 449    (blue) and Gini (red) feature importances for the different input features. 450    Both figures correspond to the samples in the momentum range <math>0.8 \leq</math> 451    <math>p &lt; 1.5 \text{ GeV}/c</math>. . . . .</p> <p>452    6.25 Evolution of the SHAP importance for the top six most important features 453    across all five momentum ranges. . . . .</p> <p>454    6.26 Permutation importances for the ten most important features in the 455    different momentum ranges (from left to right, top to bottom, in increasing 456    momentum order). The bars indicate the effect that permutations of 457    each feature have on the purity (blue) and the sensitivity (yellow), the 458    translucent regions representing one standard deviation around the central 459    value. . . . .</p>	<p style="margin-right: 20px;">189</p> <p style="margin-right: 20px;">193</p> <p style="margin-right: 20px;">194</p> <p style="margin-right: 20px;">196</p> <p style="margin-right: 20px;">197</p> <p style="margin-right: 20px;">199</p> <p style="margin-right: 20px;">201</p>
---	--

## LIST OF FIGURES

460	6.27 Values of the precision and sensitivity obtained for 10000 BDT hyperparameter configurations, for the momentum regions I, III and V. . . . .	204
462	6.28 Reliability diagrams for the BDT classifier used in the momentum range	
463	$0.3 \leq p < 0.8 \text{ GeV}/c$ , both for the original (blue circles) and calibrated	
464	(yellow squares) responses. For reference, the response of a perfectly	
465	calibrated classifier is also shown (black dashed line). . . . .	206
466	6.29 Uncalibrated (left panel) and calibrated (right panel) predicted probabilities assigned by the BDT classifiers for true muons (blue) and charged pions	
467	(red) in the momentum range $0.3 \leq p < 0.8 \text{ GeV}/c$ . . . . .	207
469	6.30 Schematic of the hit selection used for the ToF measurement. The grid	
470	represents the layers of the inner ECal, with coloured squares indicating	
471	the tiles with hits. Green squares indicate the selected hits. . . . .	209
472	6.31 Particle velocity versus momentum measured with different ECal arrival	
473	time estimations. From left to right: earliest hit time, average hit time,	
474	and fitted hit time. In all cases the time resolution is $\Delta\tau = 0.1 \text{ ns}$ . . . . .	211
475	6.32 Mass spectra for $p$ (blue) and $\pi^\pm$ (yellow) particles, using different ECal	
476	time resolution values (from top to bottom, in ascending order), and	
477	arrival time estimates. From left to right: earliest hit time, average hit	
478	time, and fitted hit time. The dashed lines indicate the true masses of	
479	the particles. . . . .	213
480	6.33 Efficiency (top panel) and purity (bottom panel) for the proton selection	
481	as a function of the momentum, for $\Delta\tau = 0.10 \text{ ns}$ . . . . .	214
482	6.34 Distributions of the velocities measured by ToF with the inner ECal, for	
483	different momentum bins, in a FHC neutrino interaction sample. The	
484	Gaussian fits are performed around the maxima for each particle species.	215

## LIST OF FIGURES

485	6.35 Left panel: number of non-decaying, decaying and decaying in the fiducial volume pions for a MC sample of 100000, $p = 500$ MeV/ $c$ isotropic positively charged pions inside the TPC. Right panel: event display for a positive pion decaying inside the fiducial volume, with a single reconstructed track for the pion and muon system. . . . .	216
490	6.36 Values of $\chi_k^2(FB)$ (top left panel), $F_k$ (top right panel), $D_k^{1/R}$ (bottom left panel) and $D_k^\phi$ (bottom right panel) versus position along the drift direction for a reconstructed track in a positive pion decay event. The vertical red dashed line indicates the true location of the decay point. . .	217
494	6.37 Fractional residual distributions of the true and reconstructed decay position along the drift coordinate, using the position of the maximum of $\chi_k^2(FB)$ (left panel) and $F_k$ (right panel) as estimates of the decay position. Also shown are double Gaussian fits to these points (red lines). .	218
498	6.38 Distributions of the extreme values of $\chi_k^2(FB)$ (top left panel), $F_k$ (top right panel), $D_k^{1/R}$ (bottom left panel) and $D_k^\phi$ (bottom right panel) for non-decaying reconstructed pion tracks (blue) and tracks which include the decay inside the fiducial volume (red). . . . .	220
502	6.39 Left panel: distributions of the predicted probabilities assigned by the BDT classifier to a test sample of decaying pion+muon tracks (blue) and non-decaying pion tracks (red). Left: signal efficiency versus background acceptance (ROC curve) obtained from the BDT for the test sample. . .	221
506	6.40 Left panel: dependence of the decay position finding resolution on the true value of the decay angle for the $\chi_k^2(FB)$ (red) and $F_k$ (blue) methods. Right panel: signal efficiency (blue line) and background rejection (red line) from the BDT classifier versus true decay angle. . . . .	221

## LIST OF FIGURES

510	6.41 Mean values of the $F_1$ -score marginal distributions for the different	
511	free parameters of the new clustering algorithm, with the error bars	
512	representing one standard deviation around the mean. The $F_1$ -score	
513	values were computed for the 6561 possible parameter configurations	
514	using 1000 $\nu_\mu$ CC interaction events. . . . .	224
515	6.42 Left panel: distributions of the number of ECal clusters per photon from	
516	$\pi^0$ decays for the standard (red) and new (blue) clustering algorithms.	
517	Right panel: reconstructed invariant mass distributions for photon pairs	
518	from single $\pi^0$ events using the standard (red) and new (blue) ECal	
519	clustering algorithms. . . . .	226
520	7.1 Schematic diagram of the HPgTPC including the fiducial volume. . . . .	231
521	7.2 Distributions of the true $\nu_\mu$ CC vertex positions for the full HPgTPC and	
522	the FV. . . . .	232
523	7.3 Cumulative efficiency and purity of the $\nu_\mu$ CC selection. . . . .	234

## List of Tables

524

525	2.1	Values of $T_3$ and $Y/2$ assigned to the first generation of fermions. . . . .	39
526	2.2	Neutral current couplings. . . . .	40
527	2.3	Summary of neutrino oscillation parameters determined in the Neutrino	
528		Global Fit of 2020 [14]. . . . .	55
529	3.1	Summary of the two-phased plan for DUNE. . . . .	63
530	3.2	Exposure and time required to achieve the different physics milestones of	
531		the two phases. . . . .	63
532	4.1	<i>Characteristic parameters of the two monoenergetic muon events selected, relative to the U plane: projected angles in the <math>xz'</math> and <math>y'z'</math> planes, S/N values for the raw and filtered waveforms, mean improvement of the S/N and peak asymmetry.</i> . . . . .	109
536	6.1	Calibration parameters obtained from the fit of the ND-GAr simulated	
537		stopping proton sample to the calibration function, for different ADC limits. . . . .	169
538	6.2	Momentum ranges and description of the PID approach assumed for the	
539		muon and pion classification task. . . . .	190
540	6.3	Optimal values of the hyperparameters used by the BDT, for each	
541		momentum range. . . . .	205
542	6.4	Performance metrics of the BDTs with optimal hyperparameters, for the	
543		different momentum ranges. . . . .	205
544	6.5	Summary of parameters and sampled values used in the optimisation of	
545		the clustering algorithm. . . . .	224

## LIST OF TABLES

546	7.1 Event rates in ND-GAr. . . . .	230
547	7.2 Step-by-step $\nu_\mu$ CC selection cuts and cumulative passing rates. . . . .	233
548		

## List of Abbreviations

<b>ADC</b>	Analog to Digital Converter.
<b>ALEPH</b>	Apparatus for LEP PHysics.
<b>ALICE</b>	A Large Ion Collider Experiment.
<b>BDT</b>	Boosted Decision Tree.
<b>CC</b>	Charged Current.
<b>DM</b>	Dark Matter.
<b>DUNE</b>	Deep Underground Neutrino Experiment.
<b>ECal</b>	Electromagnetic Calorimeter.
<b>FD</b>	Far Detector.
<b>FHC</b>	Forward Horn Current.
<b>HPgTPC</b>	High Pressure gaseous Time Projection Chamber.
<b>LBL</b>	Long BaseLine.
<b>MuID</b>	Muon IDentification system.
<b>NC</b>	Neutral Current.
<b>ND</b>	Near Detector.
<b>ND-GAr</b>	Near Detector Gaseous Argon.
<b>ND-LAr</b>	Near Detector Liquid Argon.
<b>PDG</b>	Particle Data Group.
<b>RHC</b>	Reverse Horn Current.



1

550

## Introduction

551



# Neutrino physics

554        *Little particles of inspiration sleet through the universe all the time traveling  
555        through the densest matter in the same way that a neutrino passes through a  
556        candyfloss haystack, and most of them miss.*

557

– Terry Pratchett, *Sourcery*

558        Ever since they were postulated in 1930 by Wolfgang Pauli to explain the continuous  
559         $\beta$  decay spectrum [15] and later found by F. Reines and C. Cowan at the Savannah  
560        River reactor in 1953 [16], neutrinos have had a special place among all other elementary  
561        particles. They provide a unique way to probe a wide range of quite different physics,  
562        from nuclear physics to cosmology, from astrophysics to colliders. Moreover, there is  
563        compelling evidence to believe that the study of neutrinos may be key to unveil different  
564        aspects of physics beyond the SM, difficult to test elsewhere.

565        In this Chapter, I will review the basics of neutrino physics, from its role within the  
566        SM to the main open questions related to the neutrino sector, paying special attention  
567        to the phenomenology of neutrino oscillations.

## 568        2.1 Neutrinos in the SM

569        The SM of fundamental interactions was initially proposed in 1967 by S. Glashow, S.  
570        Weinberg and A. Salam[17–19]. This theoretical framework describes the dynamics  
571        of leptons and quarks, by introducing a collection of mediating gauge vector bosons  
572        and one scalar particle, known as the Higgs boson. It assumes that the local  $SU(3) \times$

## CHAPTER 2. NEUTRINO PHYSICS

573  $SU(2)_L \times U(1)_Y$  gauge symmetry is an internal symmetry of the system, with  $SU(3)$   
574 describing quantum chromodynamics, and  $SU(2)_L \times U(1)_Y$  being the gauge groups of  
575 the electroweak sector. For a detailed overview of the SM of electroweak interactions,  
576 see Ref. [20].

577 In the SM, neutrinos appear in three flavours, namely  $\nu_e$ ,  $\nu_\mu$ , and  $\nu_\tau$ . These are  
578 associated with the corresponding charged leptons,  $e$ ,  $\mu$ , and  $\tau$ . Neutrinos exist only  
579 as left-handed particles, grouped in doublets with the charged leptons, while the later  
580 come in both chirality states:

$$\begin{pmatrix} \nu_e \\ e_L^- \end{pmatrix}, \quad \begin{pmatrix} \nu_\mu \\ \mu_L^- \end{pmatrix}, \quad \begin{pmatrix} \nu_\tau \\ \tau_L^- \end{pmatrix}, \quad e_R^-, \quad \mu_R^-, \quad \tau_R^-. \quad (2.1)$$

581 Similarly, quarks also exist in both chirality states, and are grouped as:

$$\begin{pmatrix} u_L \\ d_L \end{pmatrix}, \quad \begin{pmatrix} s_L \\ c_L \end{pmatrix}, \quad \begin{pmatrix} t_L \\ b_L \end{pmatrix}, \quad u_R, \quad d_R, \quad s_R, \quad c_R, \quad t_R, \quad b_R. \quad (2.2)$$

582 The fact that there are no right-handed neutrino fields implies that neutrinos are  
583 strictly massless within the SM. This restriction follows from the experimental observation  
584 that all neutrinos produced via weak interactions are pure left-handed helicity states  
585 (and similarly antineutrinos are pure right-handed states). The hypothetical existence  
586 of right-handed neutrinos could be indirectly inferred from the observation of non-zero  
587 neutrino masses, nevertheless the existence of neutrino masses is not a sufficient condition  
588 for the existence of such fields.

589 Left and right-handed fermions transform differently under  $SU(2)_L \times U(1)_Y$  rotations,  
590 as the right-handed particles are singlets under  $SU(2)_L$ . Applying a local transformation,  
591 they change as:

$$\begin{aligned} \psi_L &\longrightarrow e^{-iY\beta(x)/2} e^{-iT_a\alpha_a(x)} \psi_L, \\ \psi_R &\longrightarrow e^{-iY\beta(x)/2} \psi_R, \end{aligned} \quad (2.3)$$

592 where  $Y/2$  and  $T_a$  are the generators of  $SU(2)_L$  and  $U(1)_Y$ , respectively, and  $\beta(x)$  and

## 2.1. NEUTRINOS IN THE SM

**Table 2.1:** Values of  $T_3$  and  $Y/2$  assigned to the first generation of fermions.

	$e_L$	$\nu_e$	$e_R$	$u_L$	$d_L$	$u_R$	$d_R$
$T_3$	-1/2	1/2	0	1/2	-1/2	0	0
$Y/2$	-1/2	-1/2	-1	1/6	1/6	2/3	-1/3

593  $\alpha_a(x)$  are the parameters of the rotation.

594 The values of the quantum numbers  $Y/2$  and  $T_3$ , the third component of the weak  
 595 isospin, have to be assigned to the different particles. The values of  $T_3$  follow from the  
 596 commutation relations of the generators of  $SU(2)$ . After the spontaneous symmetry  
 597 breaking  $SU(2)_L \times U(1)_Y \rightarrow U(1)_{EM}$ , one finds the relation which determines the electric  
 598 charge:

$$Q = T_3 + \frac{Y}{2}, \quad (2.4)$$

599 Setting the electric charge to  $-1$  for electrons, we can find the values of the hypercharge  
 600 for the rest of the fermions. The resulting values for the first generation of leptons and  
 601 quarks are shown in Tab. 2.1.

602 It is clear that the free Lagrangian of the theory is not be invariant under the gauge  
 603 transformations, as the kinetic terms contain derivatives. Therefore, to make it invariant,  
 604 one needs to introduce a set of gauge bosons. They appear in the so-called covariant  
 605 derivative, which replaces the common derivative and transforms in the same way as the  
 606 fermion fields under local rotations. This constrain fixes completely the transformations  
 607 of the spin-1 fields. For left and right-handed particles, the covariant derivatives are  
 608 given by:

$$\begin{aligned} D_\mu \psi_L &= \left( \partial_\mu + ig' \frac{Y}{2} B_\mu + ig T_a W_\mu^a \right) \psi_L, \\ D_\mu \psi_R &= \left( \partial_\mu + ig' \frac{Y}{2} B_\mu \right) \psi_R, \end{aligned} \quad (2.5)$$

609 where  $W_\mu^i$ ,  $i = 1, 2, 3$  and  $B_\mu$  are the gauge bosons for the  $SU(2)_L$  and  $U(1)_Y$  factors,  
 610 respectively, and  $g$  and  $g'$  are the corresponding gauge couplings. It can be shown that  
 611 these fields transform in the adjoint representation of the gauge group.

## CHAPTER 2. NEUTRINO PHYSICS

**Table 2.2:** Neutral current couplings.

	$u$	$d$	$\nu_e$	$e$
$2v_f$	$1 - \frac{8}{3}\sin^2\theta_W$	$-1 + \frac{4}{3}\sin^2\theta_W$	1	$-1 + 4\sin^2\theta_W$
$2a_f$	1	-1	1	-1

612 So far, the theory only contains massless particles, as adding bare mass terms to  
 613 the Lagrangian would spoil the gauge symmetry. Therefore, the mass terms need to  
 614 be induced by a spontaneous violation of the symmetries. In the SM, the responsible  
 615 for this is the Higgs mechanism. The Higgs doublet is coupled to the gauge bosons  
 616 through the covariant derivative, and to the fermions through the Yukawa couplings.  
 617 Upon spontaneous symmetry breaking, the vacuum expectation value of the Higgs field  
 618 generate the mass terms of the particles.

619 In order to obtain the physical intermediate vector boson states, we need to perform  
 620 the following redefinitions:

$$\begin{aligned} A_\mu &= \sin \theta_W W_\mu^3 + \cos \theta_W B_\mu, \\ Z_\mu &= \cos \theta_W W_\mu^3 - \sin \theta_W B_\mu, \\ W_\mu^\pm &= \frac{1}{\sqrt{2}} (W_\mu^1 \mp i W_\mu^2), \end{aligned} \tag{2.6}$$

621 where  $A_\mu$  is the photon field, and  $Z_\mu$  and  $W_\mu^\pm$  are the neutral and the charged weak  
 622 boson fields, respectively. The Weinberg angle,  $\theta_W$ , relates the weak coupling constants  
 623 and the electric charge:

$$e = g' \cos \theta_W = g \sin \theta_W. \tag{2.7}$$

624 At this point, the interacting part of the electroweak Lagrangian can be re-written  
 625 as the sum of three contributions: the electromagnetic (EM), charged-current (CC) and  
 626 neutral-current (NC) components:

$$\begin{aligned} \mathcal{L}_{\text{EW}}^{\text{int}} &= \mathcal{L}_{\text{EM}} + \mathcal{L}_{\text{CC}} + \mathcal{L}_{\text{NC}} \\ &= -e A_\mu J_{\text{EM}}^\mu - \frac{g}{2\sqrt{2}} (W_\mu^+ J_{\text{CC}}^\mu + \text{h.c.}) - \frac{g}{2\cos\theta_W} Z_\mu J_{\text{NC}}^\mu, \end{aligned} \tag{2.8}$$

## 2.2. TROUBLE IN THE NEUTRINO SECTOR

627 with the currents defined as:

$$\begin{aligned}
 J_{\text{EM}}^\mu &= \sum_f Q_f \bar{f} \gamma^\mu f, \\
 J_{\text{CC}}^\mu &= \sum_\ell \bar{\nu}_\ell \gamma^\mu (1 - \gamma_5) \ell + \sum_f \bar{u}_f \gamma^\mu (1 - \gamma_5) d_f, \\
 J_{\text{NC}}^\mu &= \sum_f \bar{f} \gamma^\mu (v_f - a_f \gamma_5) f,
 \end{aligned} \tag{2.9}$$

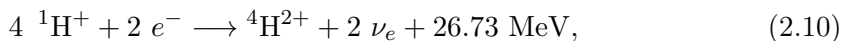
628 where  $f$  denotes any SM fermion,  $\ell$  and  $\nu_\ell$  a charged lepton and a neutrino of any flavour,  
 629 and  $u_f$  and  $d_f$  an up-like and a down-like quarks of any flavour. For the NC case, the  
 630 values of the  $v_f$  and  $a_f$  couplings are given in Tab. 2.2.

631 As seen in Eq. (5.8), in the electroweak theory neutrinos are coupled to the  $Z$  boson  
 632 in a universal way. Therefore, by measuring the so-called invisible decay width of the  $Z$   
 633 boson we have an estimate of the number of light (i.e. lighter than the  $Z$  boson) neutrino  
 634 flavours. This number was measured by LEP in a combined analysis of  $e^+ e^- \rightarrow \mu^+ \mu^-$   
 635 and  $e^+ e^- \rightarrow$  hadrons to be  $N_\nu = 2.9840 \pm 0.0082$  [21].

## 636 2.2 Trouble in the neutrino sector

### 637 2.2.1 The solar neutrino problem

638 Neutrinos are produced everywhere in vast amounts. One of the most prominent sources  
 639 of neutrinos in our vicinity is our Sun. The Sun is powered mainly by two nuclear fusion  
 640 reactions, the p – p chain and the CNO cycle. In both cases, the overall reaction is:



641 where part of the released energy is lost to the neutrinos. The electron neutrinos  
 642 produced are often labelled after the processes that generate them. Figure 2.1 shows the  
 643 solar neutrino flux as a function of the neutrino energy, broken down by the production  
 644 process.

## CHAPTER 2. NEUTRINO PHYSICS

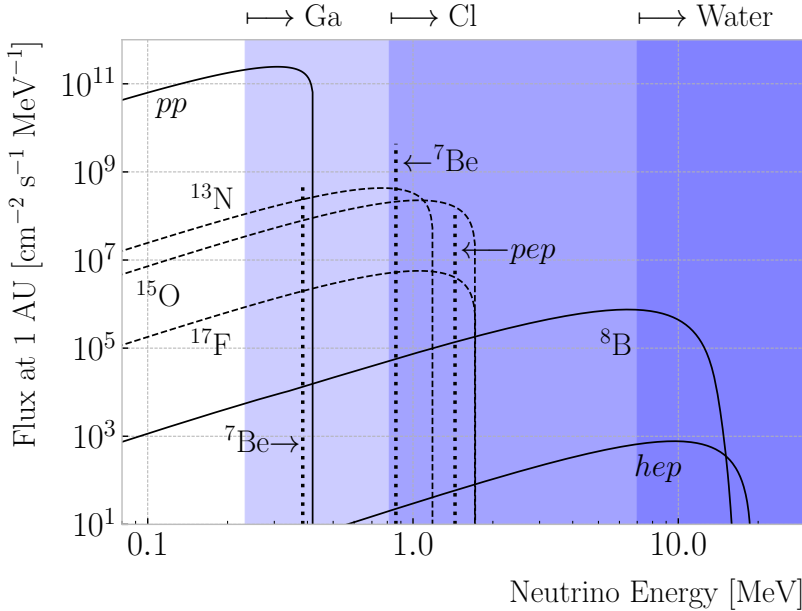


**Figure 2.1:** Solar neutrino fluxes for the solar model BS05(OP). The detection thresholds for Gallium, Chlorine and water-based experiments are also shown. Figure adapted from Ref. [1].

In the late 1960s, the Brookhaven Solar Neutrino Experiment, led by R. Davis, started

data taking with the goal of measuring the solar neutrino flux [22]. The experiment

used a tank containing  $380 \text{ m}^3$  of tetrachloroethene ( $\text{C}_2\text{Cl}_4$ ), a liquid commonly used

in dry-cleaning, located 1.5 km underground in the Homestake mine, in Lead, South

Dakota. The incoming neutrinos would get captured following the reaction:



therefore allowing to measure the neutrino flux by counting the  ${}^{37}\text{Ar}$  isotopes. The

threshold for this reaction is 0.814 MeV, just below the 0.862 MeV line from the  ${}^7\text{Be}$

ground state transition.

The results of the experiment were compared to the theoretical predictions made by

J. Bahcall [23]. During its operation from 1968 to 2002, the experiment observed a solar

$\nu_e$  flux that was approximately a third of the total prediction [24].

In the early 1990s, the SAGE [25] and GALLEX [26] experiments started operations.

## 2.2. TROUBLE IN THE NEUTRINO SECTOR

657 The detection principle used for both experiments was similar to that of the Homestake  
 658 experiment, but using  $^{71}\text{Ga}$  instead of  $\text{C}_2\text{Cl}_4$ . With a detection threshold of 0.233 MeV,  
 659 the Gallium-based experiments were able to observe the  $pp$  neutrino flux. Both  
 660 experiments measured a solar electron neutrino flux that was a factor of two lower  
 661 than the predictions, demonstrating that this deficit was energy-dependent.

662 In the early 2000s, the SNO experiment put an end to the solar neutrino puzzle  
 663 [27, 28]. Thanks to its directionality capabilities, being a Cherenkov light detector, as  
 664 well as to its heavy water target, SNO measured the total solar neutrino flux through  
 665 the NC process:

$$\nu_\alpha + d \longrightarrow n + p + \nu_\alpha, \quad (2.12)$$

666 where  $\alpha = e, \mu, \tau$ . This measurement agreed with the solar model predictions. Then,  
 667 measuring the CC reaction:

$$\nu_e + d \longrightarrow p + p + e^-, \quad (2.13)$$

668 they were able to establish that the  $\nu_\mu$  and  $\nu_\tau$  solar fluxes are in fact non-zero, revealing  
 669 that electron neutrinos were transitioning into different flavours.

### 670 2.2.2 The atmospheric neutrino problem

671 When cosmic-rays interact with the atoms in the upper atmosphere, a plethora of  
 672 hadrons, mainly  $\pi$  and  $K$  mesons, are produced. In particular, for the charged pions,  
 673 we have the following decay chain dominates:

$$\begin{aligned} \pi^+ &\longrightarrow \mu^+ + \nu_\mu, \\ \mu^+ &\longrightarrow e^+ + \bar{\nu}_\mu + \nu_e, \end{aligned} \quad (2.14)$$

674 and similar for the antiparticles. For neutrino energies  $< 1$  GeV, the ratio:

$$\frac{N(\nu_\mu + \bar{\nu}_\mu)}{N(\nu_e + \bar{\nu}_e)}, \quad (2.15)$$

675 of produced neutrinos and antineutrinos is, in good approximation, equal to two [29].

## CHAPTER 2. NEUTRINO PHYSICS

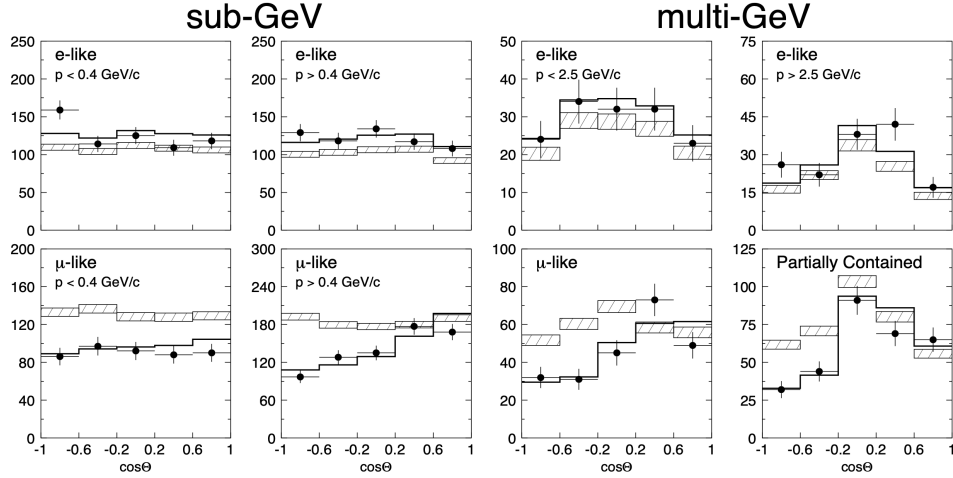


**Figure 2.2:** Zenith angle distributions for the selected  $\nu_e$  (top row) and  $\nu_\mu$  (bottom row) events in the SK detector. The hatched region corresponds to the expectation in the case of no oscillations, whereas the solid line indicates the best-fit in the case of  $\nu_\mu \rightarrow \nu_\tau$  oscillations. Figure taken from Ref. [34].

676 During the 1980s, several proton decay experiments, like Kamiokande [30], IMB [31],

677 MACRO [32], and Soudan-2 [33], measured the flux of atmospheric neutrinos. This was  
678 an important part of their research programme, as the atmospheric neutrinos constitute  
679 their main background. All these experiments reported an atmospheric neutrino ratio  
680 lower than the predictions.

681 A few years before the SNO discovery, in 1998, Super-Kamiokande (SK) collaboration

682 measured the atmospheric  $\nu_e$  and  $\nu_\mu$  spectra as a function of the zenith angle [34].  
683 Upward-going particles have negative zenith angle,  $\cos \Theta < 0$ , indicating that they  
684 entered from the bottom of the detector. These upward-going neutrinos had to travel  
685 through the Earth in order to reach the detector, allowing SK to probe a broad range  
686 of baselines. Figure 2.2 shows the reported distributions (black dots), compared to the  
687 no oscillations prediction (hatched region). This measurement confirmed that muon  
688 neutrinos transition to other flavours, and that this phenomenon depends both on the  
689 energy and the path length of the neutrino.

690 The SK and SNO findings provided definitive evidence for the existence of neutrino

691 oscillations, and therefore non-zero neutrino masses. This constitutes one of the  
692 groundbreaking discoveries of modern physics and has acted as driving force for beyond

## 2.3. MASSIVE NEUTRINOS

the Standard Model (BSM) physics. The minimal extension of the SM we can do to address these phenomena is introducing different masses for at least two of the neutrinos. This way, we are left with three neutrino mass eigenstates  $\nu_1$ ,  $\nu_2$ , and  $\nu_3$ , with masses  $m_1$ ,  $m_2$ , and  $m_3$  respectively, which in general will not coincide with the flavour eigenstates,  $\nu_e$ ,  $\nu_\mu$ , and  $\nu_\tau$ .

### 2.3 Massive neutrinos

The existence of neutrino oscillations imply that neutrinos are massive particles. However, as we have seen before, within the SM neutrinos are massless, as they do not have a mass term in the Lagrangian. If one wants to give neutrinos a mass, the particle content of the SM needs to be expanded.

A way of generating massive neutrinos while maintaining gauge invariance is by introducing an arbitrary number of sterile neutrinos  $N_i$ ,  $i = 1, \dots, m$ . These allow for two different types of neutrino mass terms:

$$-\mathcal{L}_{M_\nu} = \sum_{i=1}^m \sum_{j=1}^3 M_D^{ij} \bar{N}_i \nu_{Lj} + \frac{1}{2} \sum_{i=1}^m \sum_{j=1}^m M_N^{ij} \bar{N}_i N_j^c + \text{h.c.}, \quad (2.16)$$

where  $M_D$  is a complex  $m \times 3$  matrix and  $M_N$  a complex and symmetric  $m \times m$  matrix. The first term, often referred to as the Dirac mass term, arises from the corresponding Yukawa interaction after the spontaneous electroweak symmetry breaking, similar to the other fermions. The second term, called the Majorana mass term, is allowed in the Lagrangian, as it is a singlet of the gauge group. However, it violates lepton number conservation by two units.

If one imposes lepton number symmetry conservation, the Majorana term must banish,  $M_N = 0$ . In this case, if  $m = 3$  we can identify the sterile neutrinos as the right-handed component of the neutrino field. The Dirac mass matrix can be diagonalised using two unitary matrices,  $V_R^\nu$  and  $V_L^\nu$ , as:

$$M_D = V_R^\nu \text{ diag}(m_1, m_2, m_3) V_L^{\nu\dagger}, \quad (2.17)$$

## CHAPTER 2. NEUTRINO PHYSICS

716 where  $m_i$ ,  $i = 1, 2, 3$  are the masses of the three neutrino mass eigenstates.

717 The neutrino mass term can be written in term of the resulting eigenstates as:

$$-\mathcal{L}_{M_\nu} = \sum_{i=1}^3 m_i \bar{\nu}_{Di} \nu_{Di}, \quad (2.18)$$

718 with:

$$\nu_{Di} = \left( V_L^{\nu\dagger} \nu_L \right)_i + \left( V_R^{\nu\dagger} N \right)_i. \quad (2.19)$$

719 In this scenario, both the low energy particle budget and the symmetries of the SM  
 720 have to be modified. Moreover, the masses of the neutrinos are generated exclusively  
 721 through the Higgs mechanism, which does not explain why they are much smaller than  
 722 those of the charged leptons.

723 Going back to the general case, we can re-write Eq. (2.16) in matrix form as:

$$-\mathcal{L}_{M_\nu} = \frac{1}{2} \begin{pmatrix} \bar{\nu}_L^c & \bar{N} \end{pmatrix} \begin{pmatrix} 0 & M_D^T \\ M_D & M_N \end{pmatrix} \begin{pmatrix} \nu_L \\ N^c \end{pmatrix} + \text{h.c.} = \bar{\nu}^c M_\nu \nu + \text{h.c.}, \quad (2.20)$$

724 with  $\nu = (\nu_L, N^c)^T$  being a  $(3+m)$ -dimensional vector grouping the active and the  
 725 sterile neutrinos. The matrix  $M_\nu$ , which is a complex  $(3+m) \times (3+m)$  symmetric  
 726 matrix, can be diagonalised by means of a unitary matrix  $V^\nu$ , yielding:

$$M_\nu = V^\nu \text{ diag}(m_1, m_2, \dots, m_{3+m}) V^{\nu T}. \quad (2.21)$$

727 Using this eigendecomposition, the neutrino mass term can be expressed as:

$$-\mathcal{L}_{M_\nu} = \frac{1}{2} \sum_{i=1}^{3+m} m_i \bar{\nu}_{Mi} \nu_{Mi}, \quad (2.22)$$

728 where the states  $\nu_{Mi}$ , commonly referred to as Majorana neutrinos, are defined as:

$$\nu_{Mi} = \left( V^{\nu\dagger} \nu \right)_i + \left( V^{\nu\dagger} \nu \right)_i^c, \quad (2.23)$$

729 in such a way that the Majorana condition,  $\nu_M^c = \nu_M$ , holds true.

## 2.4. NEUTRINO OSCILLATION FORMALISM

730 As a consequence of the Majorana condition, the neutrino and the antineutrino states  
 731 can be described in terms of a single field. As opposed to the charged leptons, which  
 732 need to be represented by a four-component or Dirac spinor, the Majorana neutrino is  
 733 described by a two-component or Weyl spinor.

734 If the eigenvalues of the Majorana mass matrix,  $M_N$ , are much larger than the  
 735 electroweak symmetry breaking scale, the diagonalisation of  $M_\nu$  leads to 3 light and  $m$   
 736 heavy neutrino states:

$$-\mathcal{L}_{M_\nu} = \frac{1}{2}\bar{\nu}_l M_l \nu_l + \frac{1}{2}\bar{\nu}_h M_h \nu_h, \quad (2.24)$$

737 where the two mass matrices are given by:

$$\begin{aligned} M_l &\simeq -V_l^T M_D^T M_N^{-1} M_D V_l, \\ M_h &\simeq V_h^T M_N V_h, \end{aligned} \quad (2.25)$$

738 with  $V_l$  and  $V_h$  two unitary matrices.

739 This scenario represents the so-called see-saw mechanism [35–39]. The name comes  
 740 from the fact that the masses of the heavy states are proportional to  $M_N$ , whereas for  
 741 the light states they are proportional to  $M_N^{-1}$ . While both the heavy and the light  
 742 neutrinos are Majorana particles, it can be shown that the heavy states are mainly  
 743 right-handed, whereas the light ones are mostly left-handed.

## 744 2.4 Neutrino oscillation formalism

745 Neutrino oscillations were first proposed in 1958 by B. Pontecorvo [40], inspired by the  
 746 neutral kaon oscillation phenomenon [41]. Neutral kaons,  $K^0$  and  $\bar{K}^0$ , have opposite  
 747 strangeness ( $\pm 1$ ) and are produced in strong processes. It was observed that, when  
 748 having a beam initially pure of neutral kaons of one type, these would transition into  
 749 their antiparticles while propagating. Because the weak interaction does not conserve  
 750 strangeness, neutral kaons can change their identity via the processes shown in Fig. 2.3.

751 The mixing considered initially by Pontecorvo was between the neutrino and the

## CHAPTER 2. NEUTRINO PHYSICS

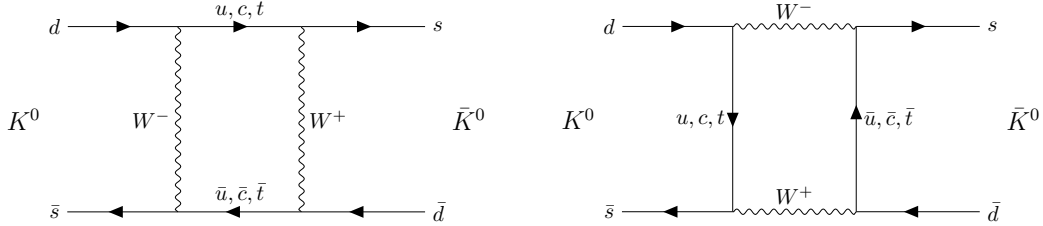


**Figure 2.3:**  $K^0 \rightleftharpoons \bar{K}^0$  mixing through  $W^\pm$  exchange.

752 antineutrino states, as only one neutrino flavour was known at the time. After the  
 753 discovery of the muon neutrino, the mixing between flavours was also explored [42].

754 In the general case, we have 3 active and  $m$  sterile neutrinos, resulting in  $3 + m$   
 755 neutrino mass eigenstates. Working in the mass basis, the leptonic charged-current  
 756 Lagrangian can be written as:

$$-\mathcal{L}_{CC}^{lep} = \frac{g}{\sqrt{2}} (\bar{e}_L, \bar{\mu}_L, \bar{\tau}_L) \gamma^\mu U \begin{pmatrix} \nu_1 \\ \nu_2 \\ \vdots \\ \nu_{3+m} \end{pmatrix} W_\mu^+ + \text{h.c.}, \quad (2.26)$$

757 where  $U$  is a  $3 \times (3 + m)$  matrix which obeys  $UU^\dagger = I_{3 \times 3}$ , but in general will not be  
 758 unitary,  $U^\dagger U \neq I_{(3+m) \times (3+m)}$ .

759 The leptonic mixing matrix,  $U$ , establishes how the neutrino mass states couple to  
 760 the charged leptons. In general, a complex  $n \times n$  matrix can be fully specified by  $2n^2$  real  
 761 parameters. If the matrix is unitary, then the number of independent parameters reduces  
 762 to  $n^2$ , as one has to impose  $n$  normalisation and  $n(n - 1)$  orthogonality constraints.  
 763 In our case, we can further reduce the number of parameters by performing a phase  
 764 redefinition of the charged lepton fields, without affecting the physics. This is not true  
 765 for the neutrinos. As they may be their own antiparticles, one is not allowed to remove  
 766 any physically relevant phases. If we consider  $n$  generations of leptons, the total number  
 767 of parameters in the mixing matrix is  $n^2 - n$ . Out of these, half of them are mixing  
 768 angles, while the other half are complex phase factors.

769 Considering the extended SM without any additional sterile neutrino states, the  
 770 resulting  $3 \times 3$  mixing matrix is unitary. This matrix, often called the Pontecorvo-Maki-

## 2.4. NEUTRINO OSCILLATION FORMALISM

771 Nakagawa-Sakata (PMNS) matrix [43, 44], relates the set of active neutrinos and the  
772 three mass eigenstates as:

$$|\nu_\alpha\rangle = \sum_{i=1}^3 U_{\alpha i}^* |\nu_i\rangle, \quad (2.27)$$

773 where the Greek index  $\alpha$  denotes the flavour  $\{e, \mu, \tau\}$  and the Latin index  $i$  the mass state  
774  $\{1, 2, 3\}$ . This leptonic mixing matrix may be parametrized in terms of 6 parameters, 3  
775 of which are mixing angles  $\theta_{12}$ ,  $\theta_{13}$  and  $\theta_{23}$ , one CP-violating phase  $\delta_{CP}$  and 2 Majorana  
776 phases  $\alpha$  and  $\beta$ :

$$U = \begin{pmatrix} 1 & 0 & 0 \\ 0 & c_{23} & s_{23} \\ 0 & -s_{23} & c_{23} \end{pmatrix} \begin{pmatrix} c_{13} & 0 & s_{13} e^{-i\delta_{CP}} \\ 0 & 1 & 0 \\ -s_{13} e^{i\delta_{CP}} & 0 & c_{13} \end{pmatrix} \begin{pmatrix} c_{12} & s_{12} & 0 \\ -s_{12} & c_{12} & 0 \\ 0 & 0 & 1 \end{pmatrix} \begin{pmatrix} 1 & 0 & 0 \\ 0 & e^{i\alpha} & 0 \\ 0 & 0 & e^{i\beta} \end{pmatrix}, \quad (2.28)$$

777 where  $c_{ij} \equiv \cos \theta_{ij}$  and  $s_{ij} \equiv \sin \theta_{ij}$ . This matrix is analogous to the Cabibbo-Kobayashi-  
778 Maskawa (CKM) matrix in the quark sector. If neutrinos are Dirac fermions, we can  
779 drop the Majorana phases in the PMNS matrix, as in this case we can perform the  
780 phase redefinitions. However, these phases play no role on the neutrino oscillation  
781 phenomenology.

782 In the case that additional sterile neutrinos states are present, the full leptonic mixing  
783 matrix would not be unitary in general. For instance, in the see-saw scenario, the  $3 \times 3$   
784 submatrix for the three light Majorana neutrinos is not unitary. However, the deviations  
785 from unitarity are of the order  $\mathcal{O}(M_D/M_N)$ , and therefore expected to be negligible.

### 786 2.4.1 Oscillations in vacuum

787 Consider the case where a neutrino of flavour  $\alpha$  is produced at  $t = 0$ , and then it  
788 propagates through vacuum. Such a state will evolve in time according to the relation:

$$|\nu_\alpha(\vec{x}, t)\rangle = \sum_{i=1}^3 U_{\alpha i}^* e^{-i(E_i t - \vec{p}_i \cdot \vec{x})} |\nu_i(\vec{x} = \vec{0}, t = 0)\rangle, \quad (2.29)$$

789 in the plane wave approximation, as the mass eigenstates are also eigenstates of the free  
790 Hamiltonian.

## CHAPTER 2. NEUTRINO PHYSICS

This way, the probability for the neutrino to transition from flavour  $\alpha$  to flavour  $\beta$

will be given by:

$$P(\nu_\alpha \rightarrow \nu_\beta) = |\langle \nu_\beta | \nu_\alpha(\vec{x}, t) \rangle|^2 = \left| \sum_{i=1}^3 \sum_{j=1}^3 U_{\alpha i}^* U_{\beta j} e^{-i(E_i t - \vec{p}_i \cdot \vec{x})} \langle \nu_j | \nu_i \rangle \right|^2 \\ = \left| \sum_{i=1}^3 U_{\alpha i}^* U_{\beta i} e^{-i(E_i t - \vec{p}_i \cdot \vec{x})} \right|^2, \quad (2.30)$$

where we have used the orthogonality relation  $\langle \nu_i | \nu_j \rangle = \delta_{ij}$ . A usual approximation to

take at this point is to consider ultra-relativistic neutrinos, i.e.  $p_i \simeq E$ , so we can write

the dispersion relations as:

$$E_i = \sqrt{p_i^2 + m_i^2} \approx E + \frac{m_i^2}{2E}. \quad (2.31)$$

In the end, assuming  $t \approx L$  where  $L$  is the distance between the production and the

detection points, the probability for the  $\nu_\alpha \rightarrow \nu_\beta$  transition becomes:

$$P(\nu_\alpha \rightarrow \nu_\beta) = \sum_{i,j} U_{\alpha i}^* U_{\beta i} U_{\alpha j} U_{\beta j} e^{-i \frac{\Delta m_{ij}^2}{2E} L} \\ = \delta_{\alpha\beta} - 4 \sum_{i < j} \Re e [U_{\alpha i}^* U_{\beta i} U_{\alpha j} U_{\beta j}^*] \sin^2 \left( \frac{\Delta m_{ij}^2}{4E} L \right) \\ + 2 \sum_{i < j} \Im m [U_{\alpha i}^* U_{\beta i} U_{\alpha j} U_{\beta j}^*] \sin \left( \frac{\Delta m_{ij}^2}{2E} L \right), \quad (2.32)$$

where  $\Delta m_{ij}^2$  is the difference of the squared masses of the  $j$ th and  $i$ th neutrino mass

eigenvalues. At this point, it is usual to write the phase responsible for the oscillations

as:

$$\Delta_{ij} \equiv \frac{\Delta m_{ij}^2}{4E} L \simeq 1.27 \frac{\Delta m_{ij}^2}{(\text{eV}^2)} \frac{L}{(\text{km})} \frac{(\text{GeV})}{E}. \quad (2.33)$$

Notice that, in the case of antineutrinos, the only difference would be the sign of the

last term in the oscillation probability. As the process  $\bar{\nu}_\alpha \rightarrow \bar{\nu}_\beta$  is the CP-mirror image

of  $\nu_\alpha \rightarrow \nu_\beta$ , the differences between their oscillation probabilities would be a measure of

## 2.4. NEUTRINO OSCILLATION FORMALISM

804 CP symmetry violation:

$$\begin{aligned} A_{CP}^{\alpha\beta} &= P(\nu_\alpha \rightarrow \nu_\beta) - P(\bar{\nu}_\alpha \rightarrow \bar{\nu}_\beta) \\ &= 4 \sum_{i<j} \Im \left[ U_{\alpha i}^* U_{\beta i} U_{\alpha j} U_{\beta j}^* \right] \sin 2\Delta_{ij}. \end{aligned} \quad (2.34)$$

805 Assuming that CPT invariance holds, then the following relation must be true:

$$P(\nu_\alpha \rightarrow \nu_\beta) = P(\bar{\nu}_\beta \rightarrow \bar{\nu}_\alpha), \quad (2.35)$$

806 as these two process are related by the CPT symmetry. From the definition of probability,  
 807 we also must have:

$$\sum_\beta P(\nu_\alpha \rightarrow \nu_\beta) = \sum_\beta P(\bar{\nu}_\alpha \rightarrow \bar{\nu}_\beta) = 1, \quad (2.36)$$

808 where the sum includes all flavours, including  $\alpha$ . From these two constraints, one can  
 809 probe that:

$$A_{CP}^{\alpha\beta} = -A_{CP}^{\beta\alpha}, \quad (2.37)$$

810 and in particular:

$$A_{CP}^{\alpha\alpha} = 0. \quad (2.38)$$

811 A direct consequence of this last relation is that there are no observable CP-violating  
 812 effects in the so-called disappearance experiments. One needs to perform appearance  
 813 experiments, where the flavour detected is different from the original flavour, in order  
 814 to measure the CP asymmetry. Neutrino experiments often report the amount of CP-  
 815 violation through the Jarlskog invariant. In terms of the parametrisation typically used  
 816 to write the PMNS matrix, it is given by:

$$J = \frac{1}{8} \cos \theta_{13} \sin 2\theta_{12} \sin 2\theta_{13} \sin 2\theta_{23} \sin \delta_{CP}. \quad (2.39)$$

817 The Jarlskog invariant can be used to compare the amount of CP-violation in the lepton  
 818 and the quark sectors, where  $J = 3.12^{+0.13}_{-0.12} \times 10^{-5}$  in the latter [45].

## CHAPTER 2. NEUTRINO PHYSICS

### 2.4.2 Oscillations in matter

When neutrinos propagate through matter, their oscillation can be affected in mainly two ways. First, neutrinos can inelastically scatter with nuclei, thus destroying the coherent propagation of their quantum state. Nevertheless, in most cases this effect is negligible (even in very dense mediums like the core of the Sun). Second, neutrinos can also experience coherent or forward scatterings, that can affect their oscillation but not lose the coherent propagation of the state.

The first proposed model to account for neutrino oscillations in matter was proposed by Mikhaev, Smirnov and Wolfenstein (MSW) [46]. It relies on the fact that, as the only charged lepton present in ordinary matter is the electron, electron neutrinos can undergo both charged and neutral-current interactions with matter whereas for muon and tau neutrinos just neutral currents are possible.

An illustrative way to introduce the MSW mechanism is by considering the two flavours case. It can be shown that the evolution of the two flavour eigenstates in vacuum is given by the following time-dependent Schrödinger equation:

$$i \frac{d}{dt} \begin{pmatrix} \nu_e \\ \nu_\mu \end{pmatrix} = H_V \begin{pmatrix} \nu_e \\ \nu_\mu \end{pmatrix}, \quad (2.40)$$

with a vacuum Hamiltonian given by:

$$H_V = \frac{\Delta m^2}{4E} \begin{pmatrix} -\cos 2\theta & \sin 2\theta \\ \sin 2\theta & \cos 2\theta \end{pmatrix}, \quad (2.41)$$

where  $\Delta m^2$  is the mass splitting between the two neutrino states and  $\theta$  the only mixing angle. For simplicity, I omit the terms of the Hamiltonian that are proportional to the identity, as they do not affect the oscillation phenomenology.

The NC contribution to the matter potential is identical for all the flavours, and has the form:

$$V_{NC} = -\frac{G_F}{\sqrt{2}} N_n(x), \quad (2.42)$$

## 2.4. NEUTRINO OSCILLATION FORMALISM

840 where  $G_F$  is the Fermi constant and  $N_n(x)$  the local neutron density. Because it is  
 841 common to all flavours, I do not take it into account in the effective Hamiltonian, as it  
 842 would appear as a term proportional to the identity. The CC component only affects  
 843 the electron neutrino (and antineutrino). It can be written as:

$$V_{\text{CC}} = \pm \sqrt{2} G_F N_e(x), \quad (2.43)$$

844 with  $N_e(x)$  being the local electron density in the material. In the end, the effective  
 845 Hamiltonian which describes the propagation of the flavour eigenstates in matter only  
 846 contains an extra  $\nu_e - \nu_e$  element:

$$H_M = H_V + \begin{pmatrix} V_{\text{CC}} & 0 \\ 0 & 0 \end{pmatrix}. \quad (2.44)$$

847 The solution to the Schrödinger equation greatly simplifies if one considers the case  
 848 of a constant matter density. In that case, the effective Hamiltonian can be diagonalised,  
 849 obtaining the effective neutrino mass eigenstates in matter. It can be re-written in the  
 850 same form as the vacuum Hamiltonian:

$$H_M = \frac{\Delta m_m^2}{4E} \begin{pmatrix} -\cos 2\theta_m & \sin 2\theta_m \\ \sin 2\theta_m & \cos 2\theta_m \end{pmatrix}, \quad (2.45)$$

851 where the effective mass splitting and the effective mixing angle are given by:

$$\begin{aligned} \Delta m_m^2 &= \lambda \Delta m_m^2, \\ \sin 2\theta_m &= \frac{\sin 2\theta_m}{\lambda} \end{aligned} \quad (2.46)$$

852 with:

$$\begin{aligned} \lambda &= \sqrt{(\cos 2\theta - A)^2 + \sin^2 2\theta}, \\ A &= \pm \frac{2\sqrt{2} G_F N_e E}{\Delta m^2}. \end{aligned} \quad (2.47)$$

853 In terms of the effective matter oscillation parameters, the transition probability

## CHAPTER 2. NEUTRINO PHYSICS

854  $\nu_e \rightarrow \nu_\mu$  (in the two flavour approximation) reads:

$$P(\nu_e \rightarrow \nu_\mu) = \sin^2 2\theta_m \sin^2 \left( \frac{\Delta m_m^2}{2E} L \right) \quad (2.48)$$

855 From this last equation one can see that, when  $\cos 2\theta = A > 0$  the oscillations are  
856 greatly enhanced. This effect is known as the MSW resonance. For the neutrinos, this  
857 resonant condition is only satisfied if  $\Delta m^2 > 0$  (the opposite is true for antineutrinos).  
858 This is can be exploited by long baseline experiments, which can gain sensitivity to the  
859 neutrino mass hierarchy through matter effects.

### 860 2.4.3 Current status of neutrino oscillations

861 A wide range of neutrino experiments provide experimental input to the neutrino  
862 oscillation framework, both using natural or synthetic neutrino sources. The results  
863 from one of the neutrino global fit analyses, shown in Tab. 2.3<sup>1</sup>, summarise well our  
864 current understanding of the different oscillation parameters.

865 **Solar neutrino experiments** detect neutrinos produced in thermonuclear reactions  
866 inside the Sun, mainly from the so-called *pp* chain and the CNO cycle. These neutrinos  
867 have a typical energy in the range from 0.1 to 20 MeV. These experiments (Homestake  
868 [47], GALLEX [26], SAGE [25], Borexino [48], Super-Kamiokande [49] and SNO [50])  
869 provide the best sensitivities to  $\theta_{12}$  and  $\Delta m_{21}^2$ .

870 **Atmospheric neutrino experiments** detect the neutrino flux produced when  
871 cosmic rays scatter with particles in Earth's atmosphere. These collisions generate particle  
872 showers that eventually produce electron and muon neutrinos (and antineutrinos). Their  
873 energies range from few MeV to about  $10^9$  GeV. Experiments, like Super-Kamiokande  
874 [51] and IceCube [52] use atmospheric neutrinos to measure oscillations and are specially  
875 sensitive to  $\theta_{23}$  and  $\Delta m_{32}^2$ .

876 **Reactor neutrino experiments** look for the  $\bar{\nu}_e$  spectrum produced by nuclear  
877 reactors, with energies in the MeV scale. Depending on the distance to the source,

<sup>1</sup>These are the results reported during M. Tórtola's talk at Neutrino 2024 (see this link). I need to keep an eye and see if they publish these or other updated results in the near future.

## 2.5. OPEN QUESTIONS IN THE NEUTRINO SECTOR

**Table 2.3:** Summary of neutrino oscillation parameters determined in the Neutrino Global Fit of 2020 [14].

Parameter	Best fit $\pm 1\sigma$	$3\sigma$ range
$\Delta m_{21}^2$ [eV $^2 \times 10^{-5}$ ]	$7.55^{+0.22}_{-0.20}$	6.98 – 8.19
$ \Delta m_{31}^2 $ [eV $^2 \times 10^{-3}$ ] (NO)	$2.51^{+0.02}_{-0.03}$	2.43 – 2.58
$ \Delta m_{31}^2 $ [eV $^2 \times 10^{-3}$ ] (IO)	$2.41^{+0.03}_{-0.02}$	2.34 – 2.49
$\sin^2 \theta_{12}/10^{-1}$	$3.04 \pm 0.16$	2.57 – 3.55
$\sin^2 \theta_{23}/10^{-1}$ (NO)	$5.64^{+0.15}_{-0.21}$	4.23 – 6.04
$\sin^2 \theta_{23}/10^{-1}$ (IO)	$5.64^{+0.15}_{-0.18}$	4.27 – 6.03
$\sin^2 \theta_{13}/10^{-2}$ (NO)	$2.20^{+0.05}_{-0.06}$	2.03 – 2.38
$\sin^2 \theta_{13}/10^{-2}$ (IO)	$2.20^{+0.07}_{-0.04}$	2.04 – 2.38
$\delta_{CP}/\pi$ (NO)	$1.12^{+0.16}_{-0.12}$	0.76 – 2.00
$\delta_{CP}/\pi$ (IO)	$1.50^{+0.13}_{-0.14}$	1.11 – 1.87

long-baseline experiments like KamLAND [53] are sensitive to the solar mass splitting  $\Delta m_{21}^2$  whereas much shorter baseline experiment such as RENO [54] or DayaBay [55] measure  $\theta_{13}$  and  $\Delta m_{31}^2$ .

**Accelerator experiments** measure neutrino fluxes generated in particle accelerators. Usually mesons are produced in the accelerator to be focused into a beam, then some decay to muon neutrinos and the rest are absorbed by a target. Depending on the configuration one can obtain a beam made of mostly neutrinos or antineutrinos. The typical energies of these neutrinos are in the GeV range. Experiments such as NOvA [56], T2K [57], MINOS [58], OPERA [59] and K2K [60] (and in the future DUNE [61]) are primarily sensitive to  $\theta_{13}$ ,  $\theta_{23}$  and  $\Delta m_{32}^2$ . Also, in the coming years DUNE [61] and Hyper-Kamiokande [62] will be sensitive to  $\delta_{CP}$ .

## 2.5 Open questions in the neutrino sector

A crucial question that remains open these days, and is of vital importance for oscillation phenomena, is whether the mass eigenvalue  $\nu_3$  is the heaviest (what we call normal ordering) or the lightest (referred to as inverted ordering) of the mass eigenstates. In

## CHAPTER 2. NEUTRINO PHYSICS

other words, this means that we do not know the sign of  $\Delta m_{32}^2$ , so we can either have  $m_1 < m_2 < m_3$  (NO) or  $m_3 < m_1 < m_2$  (IO).

Another big puzzle is related to the value of  $\delta_{CP}$ . Nowadays it is poorly constrained, with all values between  $\pi$  and  $2\pi$  being consistent with data. A prospective measurement different from  $\delta_{CP} = 0, \pi$  will predict CP-violation in the leptonic sector, and thus contribute along with the one measured in the quark sector to the total amount of CP-violation. Although it is true that these two contributions by themselves are not enough to explain the matter anti-matter asymmetry in our universe, the amount of CP-violation in the leptonic sector can be key to explain such imbalance.

Both of these questions, because of their nature, could be understood thanks to future oscillation experiments.

Notwithstanding, there are other mysteries that can not be unveiled just by conducting oscillation experiments, as certain quantities do not influence these phenomena. Among these there is the question of the absolute values of the neutrino masses. Depending on the value of the lightest of the neutrino masses we can have different mass spectra, from hierarchical  $m_1 \ll m_2 < m_3$  (NO) or  $m_3 \ll m_1 < m_2$  (IO) to quasi-degenerate  $m_1 \simeq m_2 \simeq m_3$ .

Other open question concerns the nature itself of the neutrinos. If neutrinos are Dirac particles then their mass term can be generated through the usual Higgs mechanism by adding right-handed neutrino fields. However, if they are Majorana particles and therefore their own antiparticles, there is no need to add extra fields to have the mass term in the Lagrangian. Experiments like SuperNEMO [63], SNO+ [64] and NEXT [65], which search for neutrino-less double beta decay, will be able to determine whether neutrinos are Dirac or Majorana.

## 2.6 Neutrino interactions

The study of neutrino-nucleus interactions is of great importance for long baseline neutrino oscillation experiments. The interaction model provides a mapping between

## 2.6. NEUTRINO INTERACTIONS

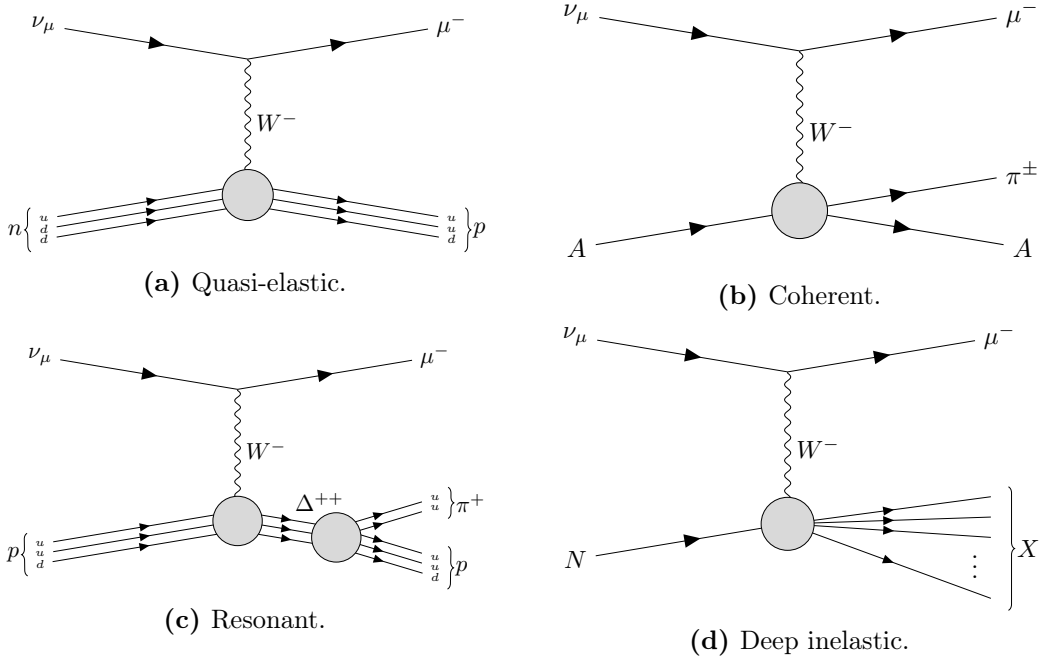


**Figure 2.4:** Feynman diagrams of the four most relevant CC interactions to long baseline neutrino oscillation experiments.

the energy of the incoming neutrino and the final state particles after the interaction.  
Because in this kind of experiments neutrinos are obtained as secondary decay products of mesons, typically charged pions and kaons, their energies are not known a priori. Not only that, but the kinematics of the interacting nucleon are also unknown. Therefore, we rely on the neutrino interaction models to provide this relation between the observables in the detector and the true kinematics of the neutrino. Interaction modelling is expected to be the one of the leading sources of systematic uncertainties in the next generation of long baseline experiments [66–68].

In the case of neutrino interactions with nuclei, at the energies relevant for long baseline oscillation experiments, around the GeV-scale, the process is dominated by the interaction between the neutrino and a single nucleon within the nuclear medium. Figure 2.4 shows examples of the four most common neutrino CC interactions. In this diagrams  $A$  indicated that the interaction happened with the nucleas as a whole, whereas  $N$  denotes a single nucleon.

At low energies, below 1 GeV, quasi-elastic (QE) interactions dominate. In a CCQE

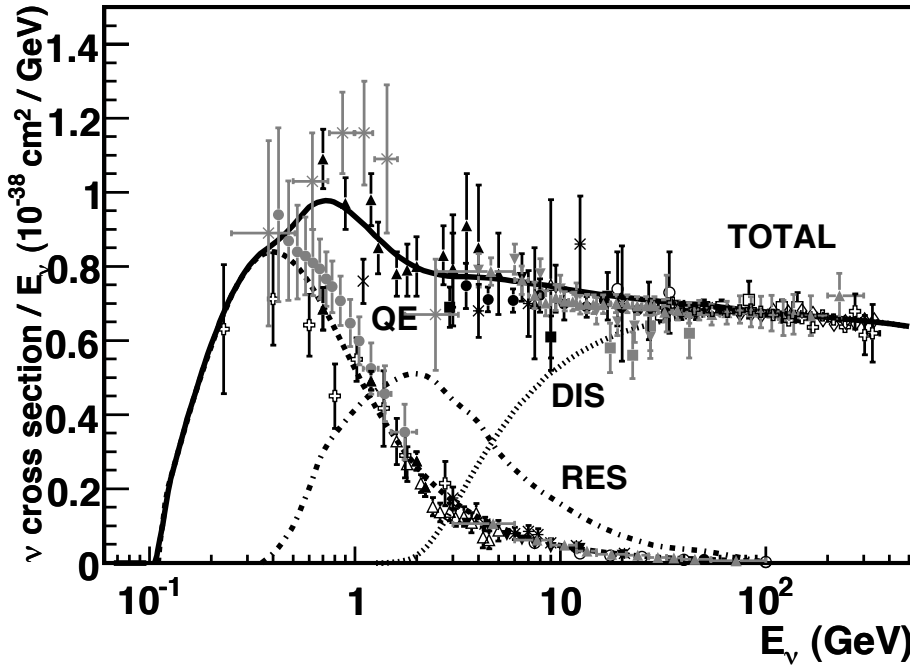


**Figure 2.5:** Total  $\nu_\mu$  CC cross section per nucleon as a function of the neutrino energy. The contributions from the different channels are shown. Figure taken from Ref. [69].

935 interaction a neutrino (antineutrino) interacts with a neutron (proton), converting it into  
 936 a proton (neutron) which is then ejected from the nucleus together with the resulting  
 937 charged lepton. At energies above 1 GeV the neutrino is able to excite the nucleon  
 938 into a baryonic resonance, which promptly decays into a nucleon and a pion. These are  
 939 the so-called resonant (RES) interactions. Neutrinos also interact with entire nucleus  
 940 coherently, in the process known as coherent (COH) interaction. This kind of reactions  
 941 also produce a single pion in the final state. At high neutrino energies, above 5 GeV,  
 942 deep inelastic scattering (DIS) takes place. In these processes, the neutrino interacts  
 943 with a single quark within the nucleon, breaking the nucleon and producing a hadronic  
 944 shower.

945 Figure 2.5 shows a compilation of measurements of the total  $\nu_\mu$  CC cross section  
 946 (see Ref. [69] for the details of the different experimental results). Also shown are the  
 947 contributions from the different interaction modes. The contribution of the CCCOH  
 948 interaction is omitted, as it is negligible compared to the others. This shows how the

## 2.6. NEUTRINO INTERACTIONS

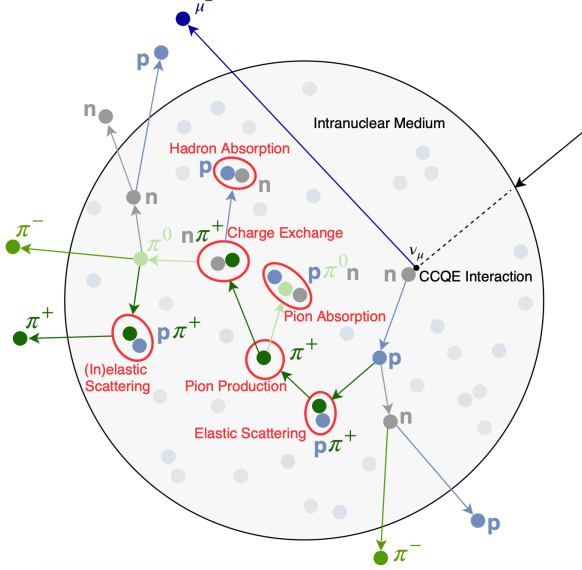


**Figure 2.6:** Schematic representation of a  $\nu_\mu$  CCQE interaction with a neutron inside a nucleus. The reaction produces a muon and a proton, which travel through the nuclear medium. The outgoing proton undergoes various kinds of hadronic FSIs on its way out. Figure taken from Ref. [70].

interaction model needs to accurately predict the neutrino-nucleon cross section for the different interaction modes across a broad energy range, to obtain the correct relative contributions.

Nuclear effects alter the neutrino cross section, as well as the multiplicities of the final state particles. Therefore, the interaction models need to account for the effects introduced by the nuclei. There are several models available to describe the initial state of the nucleus, like the relativistic Fermi gas model [71], spectral functions [72] or the random phase approximation [73]. The other main effect that interaction models have to deal with are the so-called final state interactions (FSI). These are the interactions of the particles produced in the neutrino-nucleon scattering as they travel through the nuclear medium. Typically, the lepton exits the nucleus without interacting. However, hadrons tend to get scattered, absorbed or re-emitted. These effects are usually described by means of intra-nuclear cascade models [74]. Figure 2.6 illustrates the effects of FSI on the observable particle content in the detector after a  $\nu_\mu$  CCQE interaction.

There exists a rich experimental programme dedicated to the measurement of neutrino

## CHAPTER 2. NEUTRINO PHYSICS

964 cross sections. The list of such experiments in the recent years include MiniBooNE  
965 [75], MINERvA [76], MicroBooNE [77] and SBND [78]. Additionally, thanks to their  
966 near detectors, long baseline experiments can perform cross section measurements.  
967 Some recent examples are NOvA [79] or T2K [80]. Future oscillation experiments  
968 will greatly benefit from these measurements, as the measurement of the oscillation  
969 parameters depends on the cross section modelling. However, there are alternative  
970 data-driven approaches to extract the oscillation probabilities without relying on a  
971 neutrino interaction model, which are planned to be explored in the next generation of  
972 experiments [81, 82].

# The Deep Underground Neutrino Experiment

976 The Deep Underground Neutrino Experiment (DUNE) is a next generation long-baseline  
977 neutrino experiment [83]. It will aim to address several questions in neutrino physics,  
978 study neutrinos from astrophysical sources and search for beyond the standard model  
979 physics.

980 This chapter reviews the main goals of the DUNE experiment, the design of the far  
981 detector modules and their data acquisition (DAQ) system, and the role that the near  
982 detector plays in the physics program of DUNE.

## 983 3.1 Overview

984 The main physics goals of DUNE are:

- 985 • measure the neutrino mass hierarchy, the amount of CP violation in the leptonic  
986 sector and the  $\theta_{23}$  octant,
- 987 • detect rare low energy neutrino events, like neutrinos from supernova bursts, and
- 988 • search for proton decay and other beyond the standard model phenomena.

989 The design of DUNE has been tailored with these goals in mind. It will consist  
990 of two neutrino detectors. A near detector (ND) complex will be placed at Fermilab,  
991 574 m downstream of the neutrino production point, whereas a larger far detector

## CHAPTER 3. THE DEEP UNDERGROUND NEUTRINO EXPERIMENT

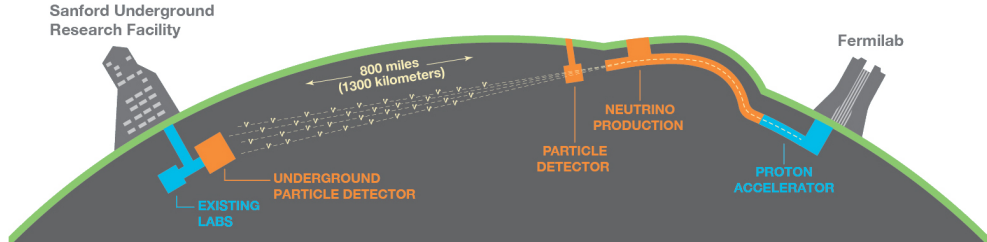


**Figure 3.1:** Schematic diagram of the DUNE experiment and the LBNF beamline [83].

992 (FD) will be built in the Sandford Underground Research Facility (SURF), South  
 993 Dakota, approximately 1300 km away. Figure 3.1 shows a simplified view of the various  
 994 components of DUNE (not to scale).

995 The beam neutrinos will be provided by the Long-Baseline Neutrino Facility (LBNF)  
 996 beamline, the multi-megawatt wide-band neutrino beam planned for Fermilab. It will  
 997 produce neutrinos travelling in the direction of SURF, with the capability to switch  
 998 between neutrino and antineutrino mode.

999 Before arriving to the FD, the neutrino beam meets the ND complex, which serves  
 1000 as the experiment's control. The design of the DUNE ND is mainly driven by the  
 1001 needs of the oscillation physics program, as its main role is to measure the unoscillated  
 1002 neutrino energy spectra. From these we can predict the unoscillated spectra at the FD,  
 1003 which can be compared to the spectra measured at the FD to extract the oscillation  
 1004 parameters. Additionally, the ND has a physics programme of its own, including cross  
 1005 section measurements and BSM physics searches.

1006 The technology chosen for the FD modules of DUNE is the liquid Argon time  
 1007 projection chamber (LArTPC). Its four modules will record neutrino interactions from  
 1008 the accelerator-produced beam arriving at predictable times. As it also aims at recording  
 1009 rare and low energy events, like supernovae and solar neutrinos, the FD requires trigger  
 1010 schemes which can deal with both kinds of physics, and also maximum uptime.

1011 DUNE is planned to be built using a staged approach consisting on two phases,  
 1012 which are summarised in Tab. 3.1. Phase I consists of a FD with 50% of the total

### 3.2. PHYSICS GOALS OF DUNE

**Table 3.1:** Summary of the two-phased plan for DUNE. Adapted from Ref. [84].

Parameter	Phase I	Phase II	Benefit
FD mass	20 kt fiducial	40 kt fiducial	FD statistics
Beam power	up to 1.2 MW	2.4 MW	FD statistics
ND config.	ND-LAr, TMS, SAND	ND-LAr, ND-GAr, SAND	Systematic constraints

**Table 3.2:** Exposure and time required to achieve the different physics milestones of the two phases. The predictions assume a Phase II staging scenario where FD modules 3 and 4 are deployed in years 4 and 6 and both the beam and ND are upgraded after 6 years. Adapted from Ref. [84].

Stage	Physics milestone	Exposure (kt-MW-years)	Years (staged)
Phase I	$5\sigma$ MO ( $\delta_{CP} = -\pi/2$ )	16	1-2
	$5\sigma$ MO (100% of the $\delta_{CP}$ values)	66	3-5
	$3\sigma$ CPV ( $\delta_{CP} = -\pi/2$ )	100	4-6
Phase II	$5\sigma$ CPV ( $\delta_{CP} = -\pi/2$ )	334	7-8
	$\delta_{CP}$ resolution of 10 degrees ( $\delta_{CP} = 0$ )	400	8-9
	$5\sigma$ CPV (50% of the $\delta_{CP}$ values)	646	11
	$3\sigma$ CPV (75% of the $\delta_{CP}$ values)	936	14
	$\sin^2(2\theta_{13})$ resolution of 0.004	1079	16

1013 fiducial mass, a reduced version of the ND complex and a 1.2 MW proton beam. It will  
 1014 be sufficient to achieve some early physics goals, like the determination of the neutrino  
 1015 mass ordering. For its Phase II, DUNE will feature the full four FD modules, a more  
 1016 capable ND and a 2.4 MW proton beam. The physics milestones for the two phases are  
 1017 given in Tab. 3.2, in a staging scenario which assumes that Phase II is completed after  
 1018 6 years of operation.

1019 A summary of the DUNE science program can be found in the DUNE FD Technical  
 1020 Design Report (TDR) Volume I [83]. For a detailed discussion on the two-phased  
 1021 approach the reader is referred to the DUNE Snowmass 2021 report [84].

## 1022 3.2 Physics goals of DUNE

1023 As noted in the literature (see for instance Ref. [14] for a review), the parameter space of  
 1024 the neutrino oscillation phenomena within the three-flavour picture is quite constrained

### CHAPTER 3. THE DEEP UNDERGROUND NEUTRINO EXPERIMENT

1025 by current experimental data. However, there are still crucial open questions, like the  
1026 mass ordering, the value of  $\delta_{CP}$  or the  $\theta_{23}$  octant. One of the main goals of DUNE is to  
1027 determine precisely the values of these parameters [85].

1028 To address these questions DUNE can look to the subdominant oscillation channel  
1029  $\nu_\mu \rightarrow \nu_e$  ( $\bar{\nu}_\mu \rightarrow \bar{\nu}_e$ ) and study the energy dependence of the  $\nu_e$  ( $\bar{\nu}_e$ ) appearance probability.  
1030 When we focus on the antineutrino channel  $\bar{\nu}_\mu \rightarrow \bar{\nu}_e$  there is a change in the sign of  $\delta_{CP}$ ,  
1031 thus introducing CP-violation. Moreover, due to the fact that there are no positrons in  
1032 the composition of Earth, there is a sign difference for the matter effect contribution  
1033 when looking to the antineutrino channel. This asymmetry is proportional to the baseline  
1034 length  $L$  and is sensitive to the sign of  $\Delta m_{31}^2$ , and thus to the neutrino mass ordering.

1035 Another of the main physics goals of DUNE is the search for baryon-number violating  
1036 processes. Specifically, it will try to answer the question of whether protons are stable  
1037 or not. There is no symmetry argument that forbids protons from decaying, but its  
1038 apparent stability seems to suggest that baryon number is conserved [86]. However,  
1039 proton decay is a usual feature of grand-unified theories, where electromagnetic, weak  
1040 and strong interactions are unified above a certain energy scale [87].

1041 As the energy deposition scale for this kind of searches is nearly the same as the one  
1042 for long-baseline neutrino oscillations, DUNE will be able to look for them. It has several  
1043 advantages over other experiments, such as excellent imaging and particle identification,  
1044 which can be translated to lower backgrounds.

1045 The last of the main objectives of DUNE is the detection of neutrinos originated in  
1046 supernovae explosions, what is called a supernova neutrino burst (SNB). These neutrinos  
1047 carry with them information about the core-collapse process, from the progenitor to the  
1048 explosion and the remnant; but also may have information about new exotic physics. So  
1049 far, the only neutrino events ever recorded from such a process were a few dozens of  $\bar{\nu}_e$   
1050 events from the 1987A supernova located in the Magellanic Cloud, 50 kpc away from  
1051 Earth [88, 89].

1052 DUNE aims to collect SNB events. Although these are quite rare, as the expected  
1053 supernovae explosion events are about one every few decades for our galaxy and

### 3.3. LBNF BEAMLINE

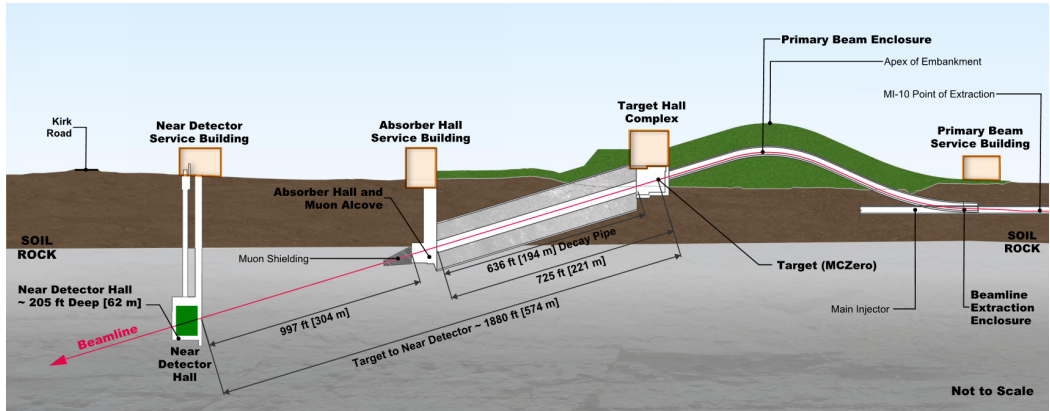


**Figure 3.2:** Schematic longitudinal section of the LBNF beamline at Fermilab (not to scale). Figure taken from Ref. [90].

1054 Andromeda, the long lifetime of the experiment (around a few decades as well) makes it  
 1055 reasonable to expect some. Nowadays the main sensitivity to SNB of most experiments  
 1056 is to the  $\bar{\nu}_e$  through inverse beta decay. One of the advantages of DUNE is its expected  
 1057 sensitivity to  $\nu_e$ , since the dominant channel will be  $\nu_e$  CC scattering.

1058 Moreover, due to the stringent requirements that the main physics goals set for  
 1059 DUNE, it will allow also to perform searches for all kind of BSM physics. Among  
 1060 others, DUNE will be able to look for: active-sterile neutrino mixing, non-unitarity of  
 1061 the PMNS matrix, non-standard interactions, Lorentz and CPT violations, neutrino  
 1062 trident production, light-mass DM, boosted DM and heavy neutral leptons. The reader  
 1063 is referred to the DUNE FD TDR Volume II [85] for a full discussion of the physics  
 1064 scope of DUNE.

### 1065 3.3 LBNF beamline

1066 The LBNF project is responsible for producing the neutrino beam for the DUNE detectors.  
 1067 A detailed discussion of the LBNF program can be found in the DUNE/LBNF CDR  
 1068 Volume III [90].

1069 A schematic diagram of the longitudinal section of the LBNF beamline is shown in  
 1070 Fig. 3.2. First, a beam of 60 – 120 GeV protons is extracted from the Fermilab Main  
 1071 Injector. This beam is aimed towards the target area, where it collides with a cylindrical

### CHAPTER 3. THE DEEP UNDERGROUND NEUTRINO EXPERIMENT

graphite target to produce pions and kaons.

The diffuse, secondary beam of particles is focused by a pair of magnetic horns. These select the positively charged particles when operated in Forward Horn Current (FHC) mode, or the negatively charged ones when the current is reversed, also known as Reverse Horn Current (RHC) mode. The focused secondary beam then enters a 194 m decay pipe where the pions and kaons will predominantly produce  $\mu^+\nu_\mu$  pairs when in FHC mode (or  $\mu^-\bar{\nu}_\mu$  in RHC mode).

At the end of the decay pipe a hadron absorber removes the undecayed hadrons and muons from the beam, which reduces the  $\nu_e$  ( $\bar{\nu}_e$ ) and  $\nu_\mu$  ( $\bar{\nu}_\mu$ ) contamination coming from the  $\mu^+$  ( $\mu^-$ ) decays. The resulting neutrino flux at the FD is shown in Fig. 3.3, both for FHC (left) and RHC (right) modes. These predictions show the intrinsic  $\nu_e$  contamination and wrong sign component from wrong sign and neutral meson decays, as well as muons decaying before reaching the absorber.

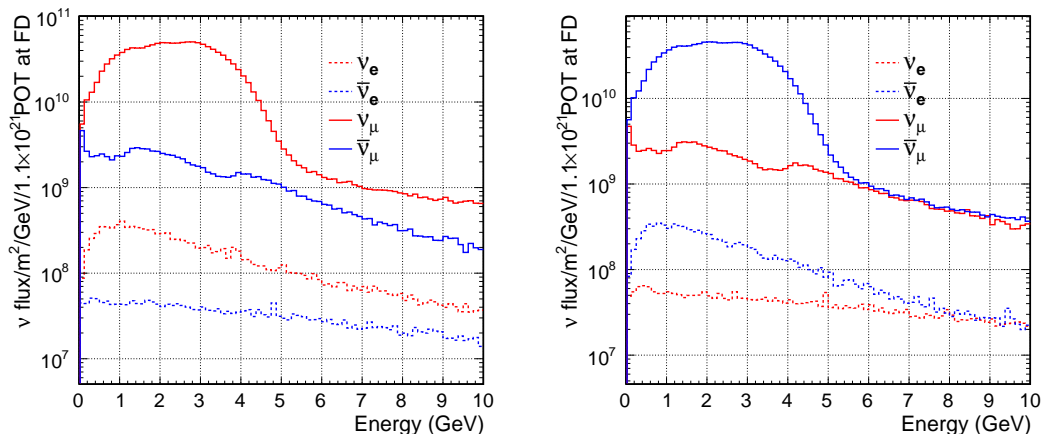


**Figure 3.3:** Predicted neutrino fluxes at the FD in FHC mode (left panel) and RHC mode (right panel). Figures taken from Ref. [85].

### 3.4 Near Detector

To estimate the oscillation parameters we measure the neutrino energy spectra at the FD. This reconstructed energy arises from a convolution of the neutrino flux, cross section, detector response and the oscillation probability. Using theoretical and empirical models

### 3.4. NEAR DETECTOR

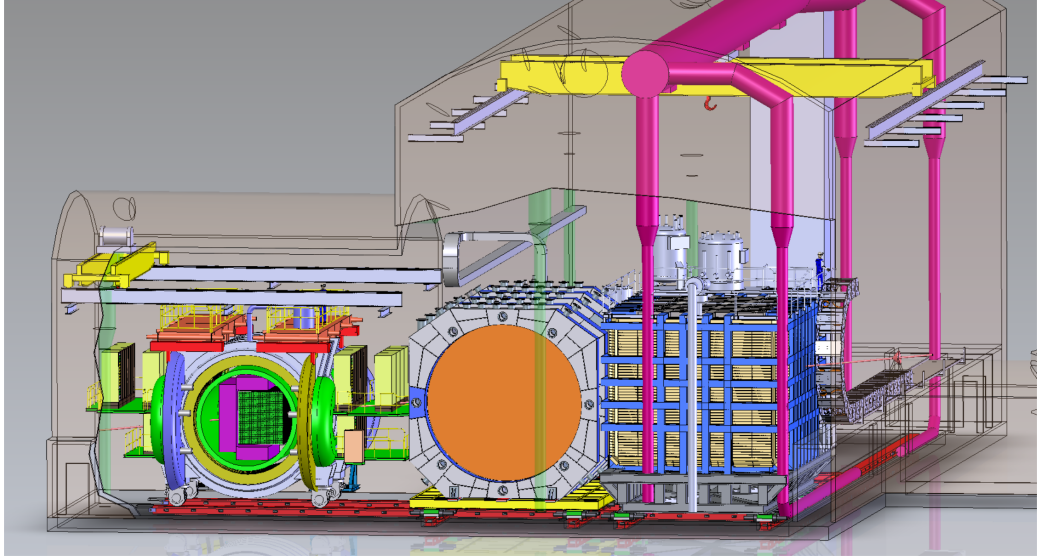


**Figure 3.4:** Representation of the ND hall in Phase II, showing the different subcomponents. From right to left, in the direction of the beam, we have ND-LAr, ND-GAr and SAND. Figure taken from Ref. [91].

1089 to account for the other effects, one can extract the oscillation probability using the  
 1090 measurement. However, these models have associated a number of uncertainties that  
 1091 are then propagated to the oscillation parameters.

1092 One of the main roles of the ND is to measure the neutrino interaction rates before  
 1093 the oscillation effects become relevant, i.e. close to the production point. By measuring  
 1094 the  $\nu_\mu$  and  $\nu_e$  energy spectra, and that of their corresponding antineutrinos, at the ND  
 1095 we can constrain the model uncertainties. A complete cancellation of the uncertainties  
 1096 when taking the ratio between the FD and ND measurements is not possible, as that  
 1097 would require both detectors to have identical designs and the neutrino fluxes to be  
 1098 the same. Because of the distance, the flux probed by the FD will have a different  
 1099 energy and flavour composition than that at the ND, as neutrinos oscillate and the beam  
 1100 spreads. The differences in the flux also determine the design of the detectors, therefore  
 1101 the ND is limited in its capability to match the FD design.

1102 Nevertheless, having a highly capable ND, DUNE can minimise the systematic  
 1103 uncertainties affecting the observed neutrino energy. The ND data can be used to  
 1104 tune the model parameters by comparison with the prediction. Then, one uses the

## CHAPTER 3. THE DEEP UNDERGROUND NEUTRINO EXPERIMENT

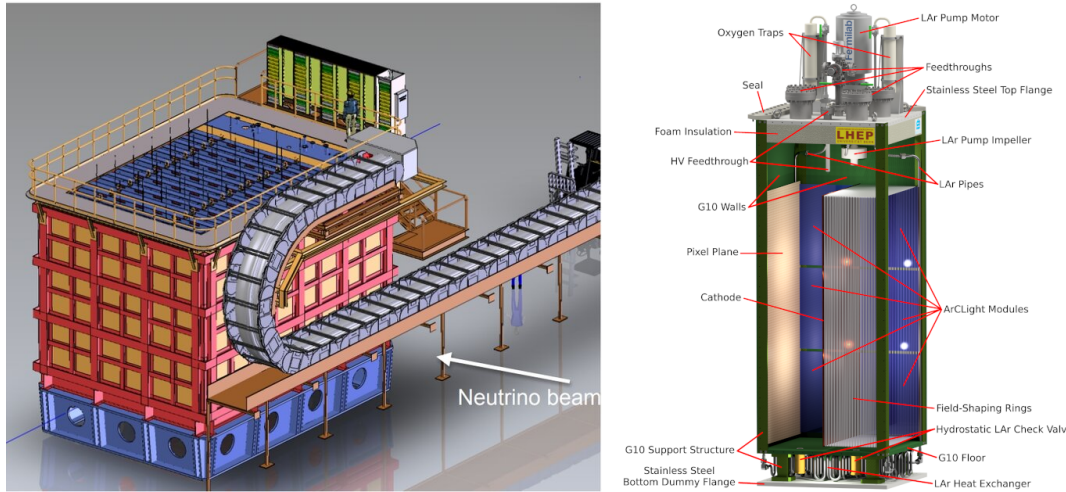


**Figure 3.5:** Schematic representation of the external components of ND-LAr, including the cryostat and the PRISM movable system (left) and detailed drawing of one ArgonCube module (right). Figure adapted from Ref. [83].

1105 tuned model to predict the unoscillated FD spectra. Comparing the prediction with the  
 1106 measured spectra it is possible to extract the oscillation parameters.

1107 Additionally, the ND will have a physics program of its own. In particular, it will  
 1108 measure neutrino cross sections that will then be used to constrain the model used in  
 1109 the long-baseline oscillation analysis. It will also be used to search for BSM phenomena  
 1110 such as heavy neutral leptons, dark photons, millicharged particles, etc.

1111 The DUNE ND can be divided in three main components, a LArTPC known as ND-  
 1112 LAr, a magnetised muon spectrometer, which will be the Temporary Muon Spectrometer  
 1113 (TMS) in Phase I and ND-GAr in Phase II, and the System for on-Axis Neutrino  
 1114 Detection (SAND). The layout of the Phase II DUNE ND can be seen in Fig. 3.4. The  
 1115 first two components of the ND will be able to move off-axis, in what is called the  
 1116 Precision Reaction-Independent Spectrum Measurement (PRISM) concept. More details  
 1117 on the purpose and design of the ND can be found in the DUNE ND Conceptual Design  
 1118 Report (CDR) [91].

### 3.4. NEAR DETECTOR

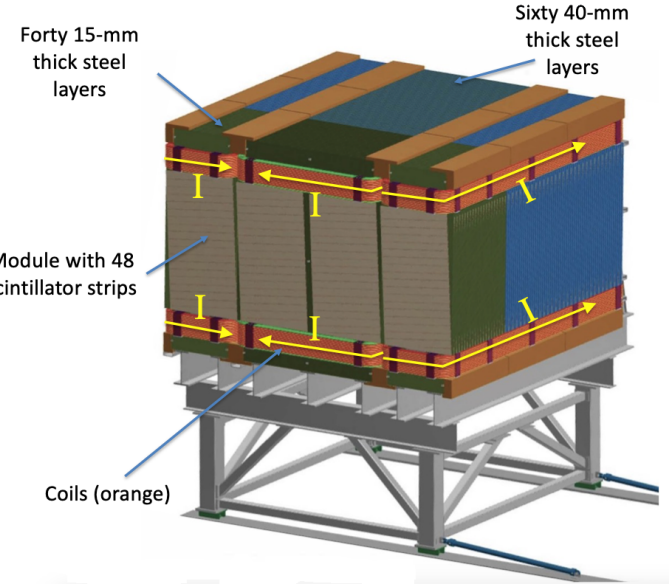


**Figure 3.6:** Schematic view of the TMS detector, highlighting its main parts. Figure adapted from Ref. [83].

#### 3.4.1 ND-LAr

ND-LAr is a LArTPC, as the ND needs a LAr component to reduce cross section and detector systematic uncertainties in the oscillation analysis. However, its design differs significantly from those proposed for the FD modules. Because of the high event rates at the ND, approximately 55 neutrino interaction events per  $10 \mu\text{s}$  spill, ND-LAr will be built in a modular way. Each of the modules, based on the ArgonCube technology, is a fully instrumented, optically isolated TPC with a pixelated readout. The pixelisation allows for a fully 3D reconstruction and the optical isolation reduces the problems due to overlapping interactions. Figure 3.5 shows a representation of the external parts of ND-LAr (left) and a detailed diagram of an ArgonCube module (right).

With a fiducial mass of 67 t and dimensions  $7 \text{ m} (\text{w}) \times 3 \text{ m} (\text{h}) \times 5 \text{ m} (\text{l})$ , ND-LAr will be able to provide high statistics and contain the hadronic systems from the beam neutrino interactions, but muons with a momentum higher than 0.7 GeV will exit the detector.

## CHAPTER 3. THE DEEP UNDERGROUND NEUTRINO EXPERIMENT

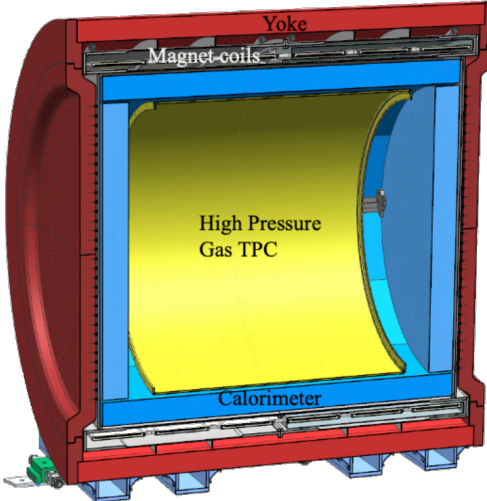


**Figure 3.7:** Cross section of the ND-GAr geometry, showing the HPgTPC, ECal and magnet. Figure adapted from Ref. [92].

### 1133 3.4.2 TMS/ND-GAr

1134 To accurately estimate the neutrino energy, the momentum of the outgoing muons needs  
 1135 to be determined. That is the reason why a muon spectrometer is needed downstream  
 1136 of ND-LAr.

1137 In Phase I that role will be fulfilled by TMS. It is a magnetised sampling calorimeter,  
 1138 with alternating steel and plastic scintillator layers. Figure 3.6 shows a schematic view  
 1139 of the TMS detector. The magnetic field allows a precise measurement of the sign of the  
 1140 muon, so one can distinguish between neutrino and antineutrino interactions.

1141 After the Phase II upgrade, TMS will be replaced with a more capable near detector.  
 1142 The current technology considered is ND-GAr. This detector is a magnetised, high-  
 1143 pressure GAr TPC (often denoted as HPgTPC) surrounded by an electromagnetic  
 1144 calorimeter (ECal) and a muon tagger. A cross section of its geometry can be seen  
 1145 in Fig. 3.7. ND-GAr will be able to measure the momenta of the outgoing muons  
 1146 while also detect neutrino interactions inside the GAr volume. This allows ND-GAr  
 1147 to constrain the systematic uncertainties even further, as it will be able to accurately  
 1148 measure neutrino interactions at low energies thanks to the lower tracking thresholds of  
 1149 GAr.

### 3.4. NEAR DETECTOR

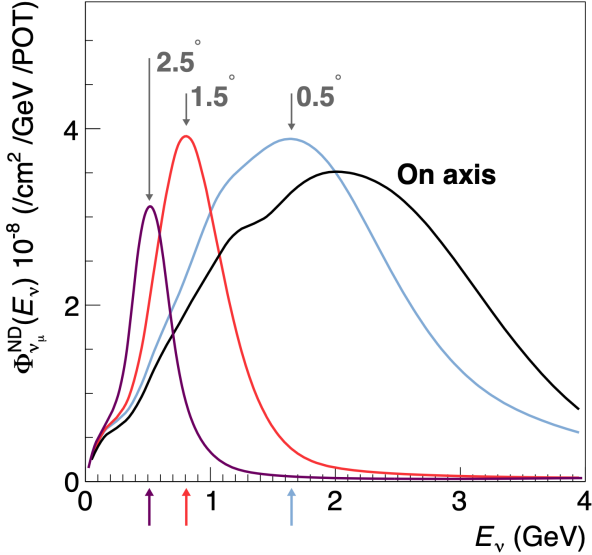


**Figure 3.8:** Predicted beam muon neutrino flux at the ND location for different off-axis positions. Figure taken from Ref. [91].

#### 1150 3.4.3 PRISM

1151 In general, the observed peak neutrino energy of a neutrino beam decreases as the  
 1152 observation angle with respect to the beam direction increases. This feature has been  
 1153 used in other long-baseline neutrino experiments, like T2K ( $2.5^\circ$  off-axis) and NOvA  
 1154 ( $0.8^\circ$  off-axis), to achieve narrower energy distributions. The DUNE PRISM concept  
 1155 exploits this effect using a movable ND. Within PRISM both ND-LAr and the muon  
 1156 spectrometer (TMS in Phase I and ND-GAr in Phase II) can be moved up to  $3.2^\circ$   
 1157 off-axis, equivalent to move the detectors 30.5 m laterally through the ND hall.

1158 This allows to record additional data samples with different energy compositions.  
 1159 Figure 3.8 compares the on-axis muon neutrino flux at the ND with the fluxes at different  
 1160 off-axis positions. As the off-axis position increases the neutrino flux becomes closer to  
 1161 a monoenergetic beam with a lower peak energy. These samples can be used to perform  
 1162 a data-driven determination of the relation between true and reconstructed neutrino  
 1163 energy, to reduce the dependence on the interaction model. The off-axis samples are  
 1164 linearly combined to produce a narrow Gaussian energy distribution centered on a target  
 1165 true energy. From the combination coefficients one can build a sample of reconstructed

## CHAPTER 3. THE DEEP UNDERGROUND NEUTRINO EXPERIMENT

1166 neutrino events that will determine the energy mapping.

1167 The PRISM samples will be used to form a flux at the ND location similar in shape  
1168 to the oscillated flux measured by the FD. This method can be used to extract the  
1169 oscillation parameters with minimal input from the neutrino interaction model.

### 1170 3.4.4 SAND

1171 The role of SAND is to monitor the beam stability by measuring the on-axis neutrino  
1172 energy spectra. As the PRISM program requires that ND-LAr and its downstream  
1173 muon spectrometer spend about half of the time in off-axis positions, it is not possible  
1174 to monitor the stability with the movable detectors. Moreover, for the success of PRISM  
1175 it is essential to have a stable beam configuration, or, at least, a quick assessment and  
1176 modeling of the distortions.

1177 The SAND detector is magnetised, and features an inner low density tracker, a LAr  
1178 target with optical readout and surrounding sampling calorimeter.

## 1179 3.5 A More Capable Near Detector

1180 In DUNE Phase II, a more capable near detector is needed to achieve the ultimate physics  
1181 goals of the experiments. The current leading proposal for this detector is ND-GAr.  
1182 As mentioned previously, it will fulfill the role of TMS, measuring the momentum and  
1183 sign of the charged particles exiting ND-LAr. Additionally, it will be able to measure  
1184 neutrino interactions inside the HPgTPC, achieving lower energy thresholds than those  
1185 of the ND and FD LArTPCs. By doing so ND-GAr will allow to constrain the relevant  
1186 systematic uncertainties for the LBL analysis even further. A detailed discussion on the  
1187 requirements, design, performance and physics of ND-GAr can be found in the DUNE  
1188 ND CDR [91] and the ND-GAr white paper [93].

### 3.5. A MORE CAPABLE NEAR DETECTOR

#### 1189 3.5.1 Requirements

1190 The primary requirement for ND-GAr is to measure the momentum and charge of  
1191 muons from  $\nu_\mu$  and  $\bar{\nu}_\mu$  CC interactions in ND-LAr, in order to measure their energy  
1192 spectrum. To achieve the sensitivity to the neutrino oscillation parameters described  
1193 in the DUNE FD TDR Volume II [85], ND-GAr should be able to constrain the muon  
1194 energy within a 1% uncertainty or better. The main constraint will come from the  
1195 calibration of the magnetic field, which will be performed using neutral kaon decays in  
1196 the HPgTPC.

1197 Another requirement for ND-GAr is the precise measurement of neutrino interactions  
1198 on argon for the energies relevant to the neutrino oscillation program. The goal is to  
1199 constrain the cross section systematic uncertainties in the regions of phase space that  
1200 are not accessible to ND-LAr. This requires the kinematic acceptance for muons in  
1201 ND-GAr to exceed that of ND-LAr, being comparable to the one observed in the FD.

1202 ND-GAr should also be able to help establishing the relationship between true and  
1203 reconstructed energy from neutrino interactions on argon with low thresholds, being  
1204 sensitive to particles that are not observed or may be misidentified in ND-LAr. In  
1205 particular, ND-GAr needs to have low tracking thresholds in order to measure the  
1206 spectrum of pions and protons produced in final-state interactions (FSI). It also must  
1207 be able to accurately measure the pion multiplicity in 1, 2 and 3 pions final states, to  
1208 inform the pion mass correction in the LArTPCs.

#### 1209 3.5.2 Reference design

1210 The final design of ND-GAr is still under preparation. However, a preliminary baseline  
1211 design was in place at the time of the ND CDR. This section summarises the main  
1212 features of that design, as it is also the one used for the default geometry in our simulation.  
1213 A DUNE Phase II white paper, discussing the different options under consideration for  
1214 the ND-GAr design, is in progress.

## CHAPTER 3. THE DEEP UNDERGROUND NEUTRINO EXPERIMENT

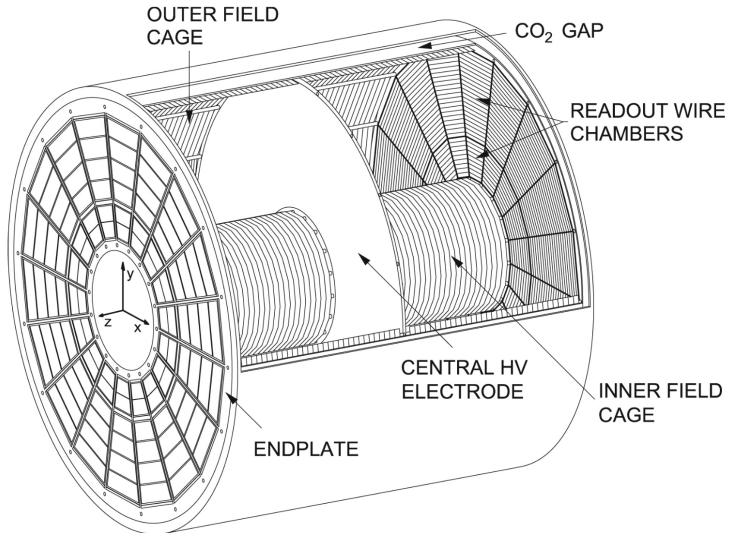


**Figure 3.9:** Diagram of the ALICE TPC, showing the two drift chambers, inner and outer field cages and readout chambers. Figure taken from Ref. [91].

### 1215 HPgTPC

1216 The reference design for the ND-GAr HPgTPC follow closely that of the ALICE TPC.  
 1217 It is a cylinder with a central high-voltage cathode, generating the electric field for  
 1218 the two drift volumes, with a maximum drift distance of 2.5 m each. The anodes will  
 1219 be instrumented with charge readout chambers. The original design repurposed the  
 1220 multi-wire proportional readout chambers (MWPCs) of ALICE, however some of the  
 1221 current R&D efforts focus on a gas electron multiplier (GEM) [94] option instead. Figure  
 1222 3.9 shows a schematic diagram of the ALICE TPC design. The basic ND-GAr geometry  
 1223 will resemble this, except for the inner field cage.

1224 It will use a 90:10 molar fraction Ar:CH<sub>4</sub> mixture at 10 bar. With this baseline gas  
 1225 mixture light collection is not possible, as the quenching gas absorbs most of the VUV  
 1226 photons. Additional R&D efforts are underway, to understand if different mixtures allow  
 1227 for the light signal to be used to provide a  $t_0$  while maintaining stable charge gain.

### 3.5. A MORE CAPABLE NEAR DETECTOR

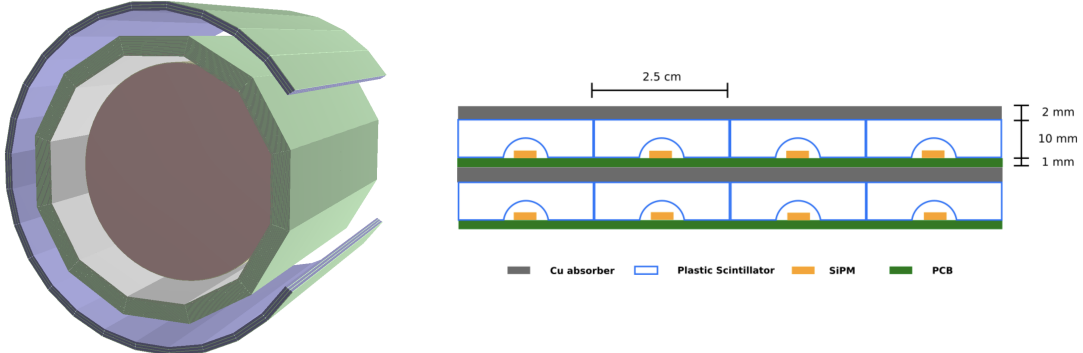


**Figure 3.10:** View of the 12-sided ECal barrel and outer muon tagger geometries (left) and layout of the ECal tile layers for the 2 mm Cu, 10 mm scintillator option (right). Figure adapted from Ref. [91].

#### 1228    ECal

1229    The main role of the ND-GAr ECal is the calorimetric measurement of the electron  
 1230    energies and the reconstruction of photons, in particular those from neutral pion decays.  
 1231    Also, the ECal is able to provide a  $t_0$  timestamp for neutrino interactions, by associating  
 1232    its activity to the tracks in the HPgTPC. The ECal will also be able to perform  
 1233    neutron reconstruction using time of flight and reject external backgrounds, thanks to  
 1234    its sub-nanosecond time resolution.

1235       The ECal design features three independent subdetectors, two end caps at each side  
 1236    and a barrel surrounding the HPgTPC. Each of the detectors is divided in modules,  
 1237    which combine alternating layers of plastic scintillator and absorber material readout  
 1238    by SiPMs. The inner scintillator layers consist of  $2.5 \times 2.5 \text{ cm}^2$  high-granularity tiles,  
 1239    whereas the outer ones are made out of 4 cm wide cross-strips spanning the whole  
 1240    module length. The current barrel geometry consists of 8 tile layers and 34 strip layers,  
 1241    while the end caps feature 6 and 36 respectively. The thickness of the scintillator layers  
 1242    is 7 mm and 5 mm for the Pb absorber layers. The 12-sided geometry of the ECal barrel  
 1243    (left) and the layout of the tile layers (left)<sup>1</sup> can be seen in Fig. 3.10.

---

<sup>1</sup>The figure shows the layout of the tile layers for a previous design with 2 mm Cu absorber and 10 mm plastic scintillator, as mentioned in the text the current choice is 5 mm Pb absorber and 7 mm scintillator.

## CHAPTER 3. THE DEEP UNDERGROUND NEUTRINO EXPERIMENT

### 1244 Magnet

1245 The ND-GAr magnet design, know as the Solenoid with Partial Yoke (SPY), consists of  
1246 two coupled solenoids with an iron return yoke. The idea behind the design is to have a  
1247 solenoid as thin as possible, as well as a return yoke mass distribution that minimises  
1248 the material budget between ND-LAr and ND-GAr. The magnet needs to provide a  
1249 0.5 T field in the direction perpendicular to the beam, parallel to the drift electric field.  
1250 It needs to host the pressure vessel and the surrounding ECal, which points to a inner  
1251 diameter of  $\sim 6.4$  m.

1252 The solenoid is a single layer coil, based on niobium titanium superconducting  
1253 Rutherford cable. The total length of the coil is 7.5 m. The bobbin will be split in four  
1254 segments grouped in pairs with two identical cryostats, connected in series. The iron  
1255 yoke features an aperture in the upstream side to allow the muons coming from ND-LAr.  
1256 Still, its material will be enough to reduce the magnetic field reaching SAND, and also  
1257 stop the charged pions produced inside the HPgTPC.

### 1258 Muon system

1259 The design of the ND-GAr muon system is still in a preliminary stage. Its role is to  
1260 distinguish between muons and pions punching through the ECal. This is especially  
1261 important for wrong-sign determination, to separate these from neutral current events.

1262 In its current form, the muon system consists of three layers of longitudinal sampling  
1263 structures. It alternates 10 cm Fe absorber slabs with 2 cm plastic scintillator strips.  
1264 The transverse granularity required is still under study.

### 1265 3.5.3 R&D efforts

1266 There are several ND-GAr-related prototypes, mostly focused on the TPC charge  
1267 readout and electronics. The priority is to test the full readout chain, in a high-pressure  
1268 environment, using a gas mixture with high argon fraction. A detailed summary of these  
1269 can be found in the DUNE Phase II white paper [92].

### 3.5. A MORE CAPABLE NEAR DETECTOR

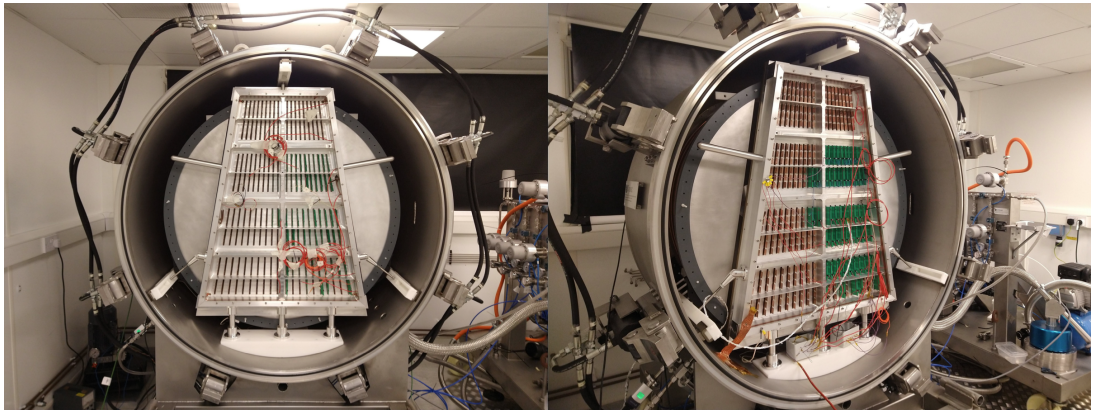


**Figure 3.11:** Photographs of the TOAD pressure vessel at RHUL. The TPC is mounted inside the vessel, and the OROC is supported by an aluminium frame. Figure taken from Ref. [95].

#### **1270 Multi-Wire Proportional Chambers**

1271 As mentioned before, the original ND-GAr design repurposes the MWPCs of the ALICE  
1272 TPC, which became available after the recent upgrade [96]. These were operated using  
1273 a 90:10:5 Ne:CO<sub>2</sub>:N<sub>2</sub> gas mixture at 1 atm. Therefore, their performance needed to be  
1274 studied in an argon gas environment at high pressure.

1275 The Gas-argon Operation of ALICE TPC (GOAT) test stand tested the ALICE  
1276 readout chambers at high pressure. In particular, it used one of the previously operated  
1277 ALICE inner MWPCs, also known as IROCs, in a pressure vessel rated to 10 atm. It  
1278 measured the gas gain at various pressure points, voltages and gas mixtures.

1279 The Test stand of an Overpressure Argon Detector (TOAD) tested an ALICE outer  
1280 MWPC, also known as OROC, up to 5 atm. During its time at RHUL, it was used to  
1281 study the achievable gas gain of the OROC [95]. At the moment, it is being commissioned  
1282 at Fermilab for a full detector test of the readout electronics and the DAQ.

1283 Figure 3.11 shows the interior of the TOAD pressure vessel. The TPC is mounted  
1284 inside the vessel on three rails. The back of the OROC, supported by an aluminium  
1285 frame, can be seen at the front.

### CHAPTER 3. THE DEEP UNDERGROUND NEUTRINO EXPERIMENT

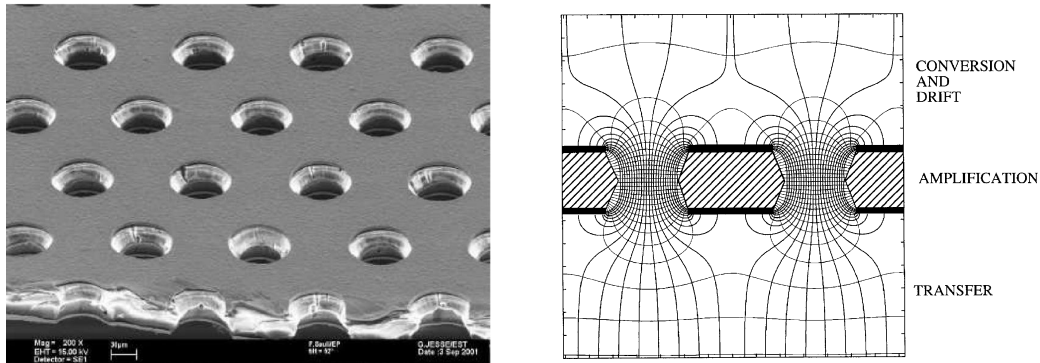


**Figure 3.12:** Left panel: electron microscope image of a 50  $\mu\text{m}$  thick GEM electrode, with hole pitch and diameter of 140 and 70  $\mu\text{m}$ , respectively. Right panel: Schematics of a GEM electrode cross section, showing the electric field lines around the holes. Figures taken from Ref. [97].

#### 1286 Gas Electron Multiplier

1287 An alternative to the MWPC option is the use of GEMs. These are a type of micro-patter  
 1288 detector, where the ionisation electrons passing through the holes in the GEM layers  
 1289 are accelerated by a high intensity electric field. The acceleration causes the electrons  
 1290 to ionise the medium, resulting in an avalanche which increase the signal exponentially  
 1291 [94]. GEMs are used in numerous experiments that need a high spatial resolution, like  
 1292 ALICE [98] and CMS [99] after their upgrades.

1293 Figure 3.12 (left panel) shows an electron microscope picture of a 50  $\mu\text{m}$  thick GEM  
 1294 electrode, with a pitch between neighbouring holes of 140  $\mu\text{m}$  and a hole diameter of  
 1295 70  $\mu\text{m}$ . A schematic representation of the cross section of a GEM layer is shown in Fig.  
 1296 3.12 (left panel).

1297 The Gaseous Argon T0 (GAT0<sup>2</sup>) prototype studies the use of thick GEMs made out  
 1298 of glass to achieve optical imaging of the primary ionisation. Using a 10 atm pressure  
 1299 vessel, the goal is to study different argon-based mixtures that allow for a precise  $t_0$   
 1300 determination.

1301 The GEM Over-pressurized with Reference Gases (GORG<sup>3</sup>) test stand is currently  
 1302 testing a GEM-based charge readout, using a triple-GEM stack.

<sup>2</sup>Spanish for cat.

<sup>3</sup>Persian for wolf.

### 3.6. FAR DETECTOR

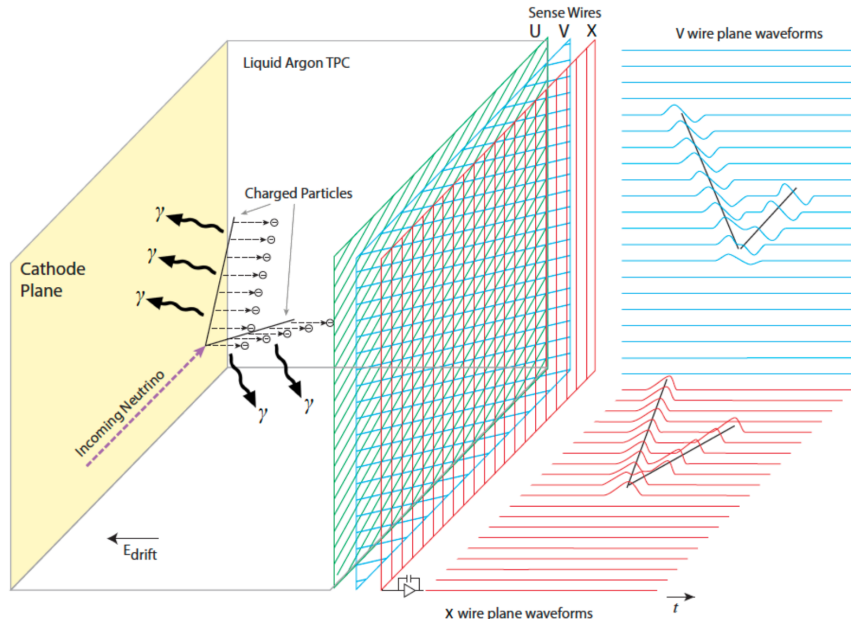


**Figure 3.13:** Schematic diagram showing the operating principle of a LArTPC with wire readout. Figure taken from Ref. [83].

## 1303 3.6 Far Detector

1304 The DUNE FD complex will sit 1300 km away from the beam target and 1.5 km  
 1305 underground at SURF, South Dakota. Two caverns will host the four FD modules, two  
 1306 of them per cavern, each embedded in cryostats of dimensions 18.9 m (w)  $\times$  17.8 m (h)  $\times$   
 1307 65.8 m (l). A central, smaller cavern will host the cryogenic system.

1308 Three out of the four modules will be liquid argon (LAr) time projection chamber  
 1309 detectors, often refer to as LArTPCs, with a LAr fiducial mass of at least 10 kt each.  
 1310 The first and second FD modules, FD-1 and FD-2, will use a Horizontal Drift (HD)  
 1311 technology, whereas the third module, FD-3, will have a Vertical Drift (VD) direction.  
 1312 The technology for the fourth module is still to be decided,

1313 For each event, with energies ranging from a few MeV to several GeV, these detectors  
 1314 collect both the scintillation light and the ionisation electrons created when the charged  
 1315 particles produced in neutrino-nucleus interactions ionise the argon nuclei. In both HD  
 1316 and VD designs the characteristic 128 nm scintillation light of argon is collected by a  
 1317 photon detection system (PDS). This light will indicate the time at which electrons

## CHAPTER 3. THE DEEP UNDERGROUND NEUTRINO EXPERIMENT

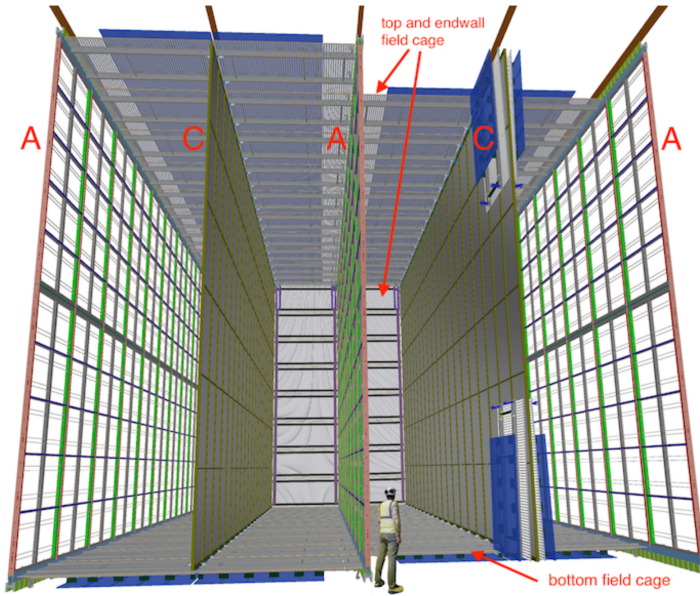


**Figure 3.14:** Proposed design for the FD-1 and FD-2 modules following the HD principle. Figure taken from Ref. [83].

1318 start to drift, thus enabling reconstruction over the drift coordinate when compared  
 1319 to the time when the first ionisation electron arrives to the anode. Reconstruction of  
 1320 the topology in the transverse direction is achieved using the charge readout. Fig. 3.13  
 1321 illustrates the detection principle described, for the case of a HD detector with a wire  
 1322 readout.

### 1323 3.6.1 Horizontal Drift

1324 The HD design the ionisation electrons produced as charged particles traverse the LAr  
 1325 drift horizontally towards the anode planes, due to the effect of an electric field. These  
 1326 anode planes are made out of three layers of wire readout. This design, previously  
 1327 known as single-phase (SP), was tested by the ProtoDUNE-SP detector at CERN. The  
 1328 prototype collected data from a hadron beam and cosmic rays, providing high-quality  
 1329 data sets for calibration and performance studies.

1330 Each FD HD detector module is divided in four drift regions, with a maximum drift  
 1331 length of 3.5 m, by alternating anode and cathode walls. The surrounding field cage  
 1332 ensures the uniformity of the 500 V/cm horizontal electric field across the drift volumes.

### 3.6. FAR DETECTOR

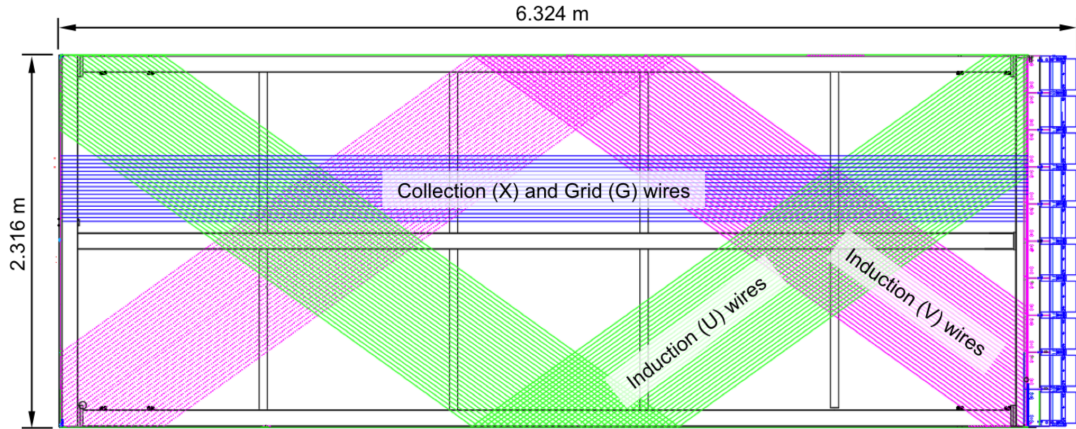


**Figure 3.15:** Schematic representation of an APA. The black lines represent the APA steel frame. The green and magenta lines correspond to the direction of the U and V induction wires respectively. The blue lines indicate the direction of the X collection wires and the wire shielding G. Figure taken from Ref. [83].

1333 The three anode walls, which constitute the charge readout of the detector, are built by  
 1334 stacking anode plane assemblies (APAs), 2 high times 25 wide. The design of the HD  
 1335 modules is shown in Fig. 3.14.

1336 Each APA is made of 2560 active wires arranged in three layers, plus an extra grid  
 1337 layer, wrapped around a metal frame. The two induction wire planes, U and V, sit at  
 1338  $\pm 35.7^\circ$  to the vertical on each side of the APA. The collection and shielding plane wires,  
 1339 X and G, run parallel to the vertical direction. The ionisation electrons drift past the  
 1340 induction planes, generating bipolar signals on those wires, and are collected by the  
 1341 collection plane, producing a monopolar positive signal. The spacing between the wires  
 1342 is  $\sim 5$  mm, and it defines the spatial resolution of the APA.

1343 The front-end readout electronics, or cold electronics as they are immerse in the LAr,  
 1344 are attached to the top of the up APAs and the bottom of the down APAs. Mounted on  
 1345 the front-end mother boards we have a series of ASICs that digitize the signals from the  
 1346 collection and induction planes. Each wire signal goes to a charge-sensitive amplifier,  
 1347 then there is a pulse-shaping circuit and this is followed by the analogue-to-digital  
 1348 converter. This part of the process happens inside the LAr to minimise the number of  
 1349 cables penetrating the cryostat. The digitised signals come out finally via a series of

## CHAPTER 3. THE DEEP UNDERGROUND NEUTRINO EXPERIMENT

1350 high-speed serial links to the warm interface boards (WIBs), from where the data is sent  
1351 to the back-end DAQ through optical fibers.

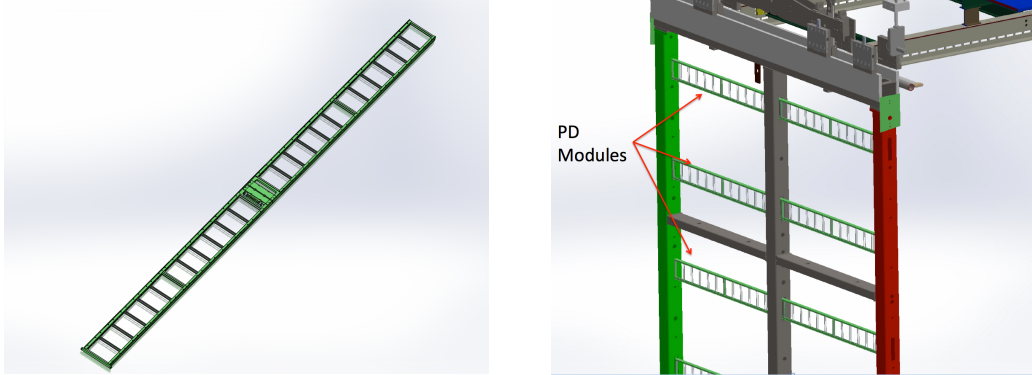


**Figure 3.16:** A PDS module containing 24 X-ARAPUCAs (left) and the location of the modules on the APAs (right). Figure taken from Ref. [83].

1352 The PDS uses modules of X-ARAPUCA devices, mounted on the APA frames  
1353 between the wire planes. Each X-ARAPUCA consists of layers of dichroic filter and  
1354 wavelength-shifter. They shift the VUV scintillation light into the visible spectrum,  
1355 sending then the visible photons to silicon photomultiplier (SiPM) devices. The PDS  
1356 modules are 209 cm × 12 cm × 2 cm bars, containing 24 X-ARAPUCAs. There are 10  
1357 of these PDS modules per APA. Fig. 3.16 shows a PDS module (left) and the placement  
1358 of the modules on the APAs (right).

### 1359 3.6.2 Vertical Drift

1360 In the VD case the ionisation electrons will drift vertically until they meet a printed  
1361 circuit board-based (PCB) readout plane. It is based on the original dual-phase (DP)  
1362 design deployed at CERN, known as ProtoDUNE-DP, used a vertical drift design with  
1363 an additional amplification of the ionization electrons using a gaseous argon (GAr) layer  
1364 above the liquid phase. The VD module incorporates the positive features of the DP  
1365 design without the complications of having the LAr-GAr interface.

1366 The current design of the FD VD module counts with two drift chambers with a  
1367 maximum drift distance of 6.5 cm. A cathode plane splits the detector volume along the  
1368 drift direction while the two anode planes are connected to the bottom and top walls

### 3.6. FAR DETECTOR

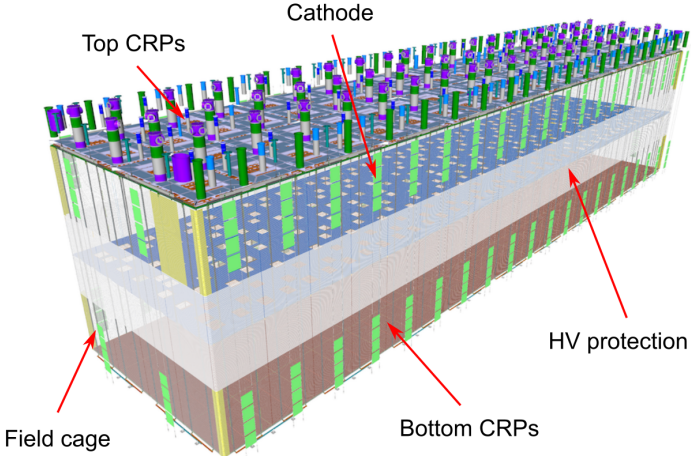


**Figure 3.17:** Proposed design for the FD-3 module following the VD principle. Figure adapted from Ref. [100].

1369 of the detector. The layout of the VD module is shown in Fig. 3.17. Compared with  
 1370 the HD design, the VD option offers a slightly larger instrumented volume and a more  
 1371 cost-effective solution for the charge readout.

1372 As in the HD design, each drift volume features a 500 V/cm electric field and a  
 1373 field cage that ensures its uniformity. The anode planes are arrays of 3.4 m × 3 m  
 1374 charge-readout planes (CRPs). These are formed by a pair of charge-readout units  
 1375 (CRUs), which are built from two double-sided perforated PCBs, with their perforations  
 1376 aligned. The perforations allow the drift electrons to pass between the layers.

1377 The PCB face opposite to the cathode has a copper guard plane which acts as  
 1378 shielding, while its reverse face is etched with electrode strips forming the first induction  
 1379 plane. The outer PCB has electrode strips on both faces, the ones facing the inner PCB  
 1380 form the second induction plane while the outermost ones form the collection plane. Fig.  
 1381 3.18 shows the layout of the electrode strips for the top (left) and bottom (right) CRUs.  
 1382 The magenta and blue lines represent the first and second induction planes respectively,  
 1383 and the green lines correspond to the collection plane.

1384 The PDS in the VD module will use the same X-ARAPUCA technology developed  
 1385 for the HD design. The plan is to place the PDS modules on the cryostat walls and on

## CHAPTER 3. THE DEEP UNDERGROUND NEUTRINO EXPERIMENT

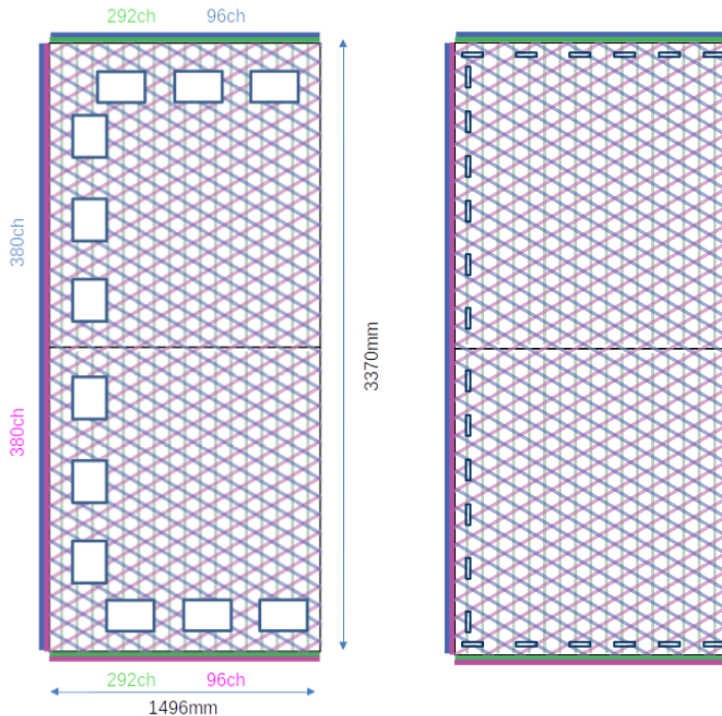


**Figure 3.18:** Schematic representation of the electrode strip configuration for a top (left) and bottom (right) CRU. Figure taken from Ref. [100].

1386 the cathode, in order to maximise the photon yield.

1387 **3.6.3 FD Data Acquisition System**

1388 The data acquisition (DAQ) system receives, processes and stores data from the detector  
1389 modules. In the case of DUNE the DAQ architecture is designed to work for all FD  
1390 modules interchangeably, except some aspects of the upstream part which may depend  
1391 on the specific module technology.

1392 The enormous sample rate and the number of channels in TPC and PD readouts  
1393 will produce a very large volume of data. These pose really strong requirements and  
1394 challenges to the DUNE FD DAQ architecture. It will be required to read out data of  
1395 the order of ten thousand or more channels at rates of a few MHz. To cope with the  
1396 huge data volume, segmented readouts and compression algorithms are used to reduce  
1397 the data rate to manageable levels.

1398 The DAQ system of the DUNE FD is composed of five different subsystems. The

### 3.6. FAR DETECTOR

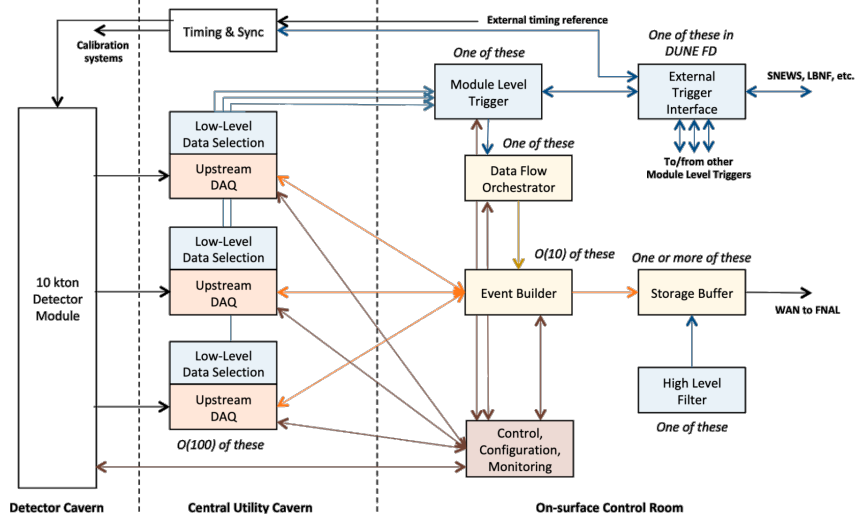


**Figure 3.19:** Detailed diagram of the DUNE FD DAQ system. Figure taken from Ref. [101].

1399 first one is the upstream DAQ, which receives the raw data from the detector, buffers it  
 1400 and perform some low-level pre-processing. The minimally processed data is then fed  
 1401 into a hierarchical data selection system, which then performs a module level trigger  
 1402 decision. In case of a positive decision a trigger command is produced and executed by  
 1403 the data flow orchestrator, located in the back-end (BE) DAQ subsystem. Subsequently  
 1404 the DAQ BE retrieves the relevant data from the buffers located in the upstream DAQ,  
 1405 adds all the data into a cohesive record and saves it to permanent storage. Watching  
 1406 over all the other subsystems we also have the control, configuration and monitoring  
 1407 subsystem and the time and synchronization subsystem. Figure 3.19 shows a schematic  
 1408 diagram of the DAQ system, showing the different subsystems and their relations.

1409 A notorious challenge for the DUNE DAQ system comes from its broad physics  
 1410 goals. We must be prepared to process events spanning a wide range of time windows  
 1411 (from 5 ms in the case of beam and cosmic neutrinos and nucleon decay to 100 s in the  
 1412 case of SNBs) and therefore this requires a continuous readout of the detector modules.  
 1413 Moreover, because of the off-beam measurements we need to ensure the capabilities  
 1414 of online data processing and self-triggering. Having this into account, together with  
 1415 the technical constraints, the DUNE FD DAQ faces a series of challenges: it needs to

### CHAPTER 3. THE DEEP UNDERGROUND NEUTRINO EXPERIMENT

- 1416 be fault tolerant and redundant to reduce downtime, accommodate new components
- 1417 while it keeps serving the operational modules, have large upstream buffers to handle
- 1418 SNB physics, be able to support a wide range of readout windows and last reduce the
- 1419 throughput of data to permanent storage to be at most 30 PB/year.

1420

1421

1422

1423

# Matched Filter approach to Trigger

## Primitives

### 4.1 Motivation

The filter implemented in the firmware of the upstream DUNE FD DAQ is a 32nd-order low-pass finite impulse-response (FIR) filter. The output of such filter for a discrete system can be written as:

$$y[i] = \sum_{j=0}^N h[j]x[i-j], \quad (4.1)$$

where  $N$  is the order of the filter,  $y$  is the output sequence,  $x$  is the input sequence and  $h$  is the set of coefficients of the filter. The current implementation within `dtp-firmware` [102] uses a set of 16 non-zero integer coefficients.

Filtering is a vital step in the hit finder chain. It helps to suppress the noise and enhance the signal peaks with respect to the noiseless baseline. A good filtering strategy allows us to use lower thresholds when forming the trigger primitives (TPs) and thus increasing the sensitivity of our detector to low energy physics events. In such events, the hits produced by the ionisation electrons tend to have lower amplitudes than those of interest to the baseline physics programme of the DUNE experiment.

This is particularly important for the induction planes. In general, signal peaks in the induction wires have smaller amplitude than the ones in the induction plane. This, together with the fact that the pulse shapes are bipolar, reduces our capacity to detect

## CHAPTER 4. MATCHED FILTER APPROACH TO TRIGGER PRIMITIVES

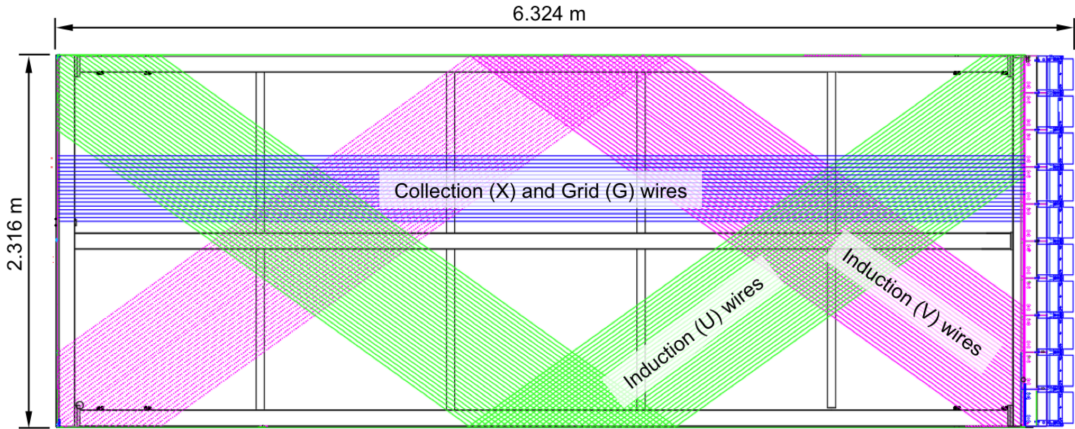


**Figure 4.1:** Schematic representation of an APA. The black lines represent the APA steel frame. The green and magenta lines correspond to the direction of the U and V induction wires respectively. The blue lines indicate the direction of the X collection wires and the wire shielding G.

1439 the hits on these channels. The inefficiency of detecting TPs in the induction planes  
 1440 (denoted as U and V planes) lead trigger algorithms to focus mainly on the TPs from  
 1441 the collection plane (so-called X plane). As a result, the possibility of making trigger  
 1442 decisions based on the coincidence of TPs across the three wire planes remains nowadays  
 1443 unexploited in DUNE. Fig. 4.1 shows a schematic view of an anode plane assembly  
 1444 (APA), with the different wire plane orientations highlighted.

1445 A possible improvement of the current hit finder chain could require optimising  
 1446 the existing or choosing a new filter implementation. A filter strategy which improves  
 1447 the induction signals may be able to enhance the detection efficiency of TPs from the  
 1448 induction planes and ideally make it comparable to that of the collection plane.

1449 The goal is to implement a better finite-impulse response filter design and to evaluate  
 1450 its performance relative to the current filter. To do so, we need to take into account the  
 1451 limitations of the firmware: the FIR filter shall have maximum 32 coefficients (so-called  
 1452 taps) whose values are 12-bit unsigned integers. Although it is technically possible to  
 1453 include non-integer coefficients, it would be a technical challenge as we have 40 FIR  
 1454 instances per APA, as there are 4 FIR per optical link and 10 optical links per APA.  
 1455 With these restrictions, the task is to provide a set of 32 coefficients which yield an

## 4.2. SIGNAL-TO-NOISE RATIO DEFINITION

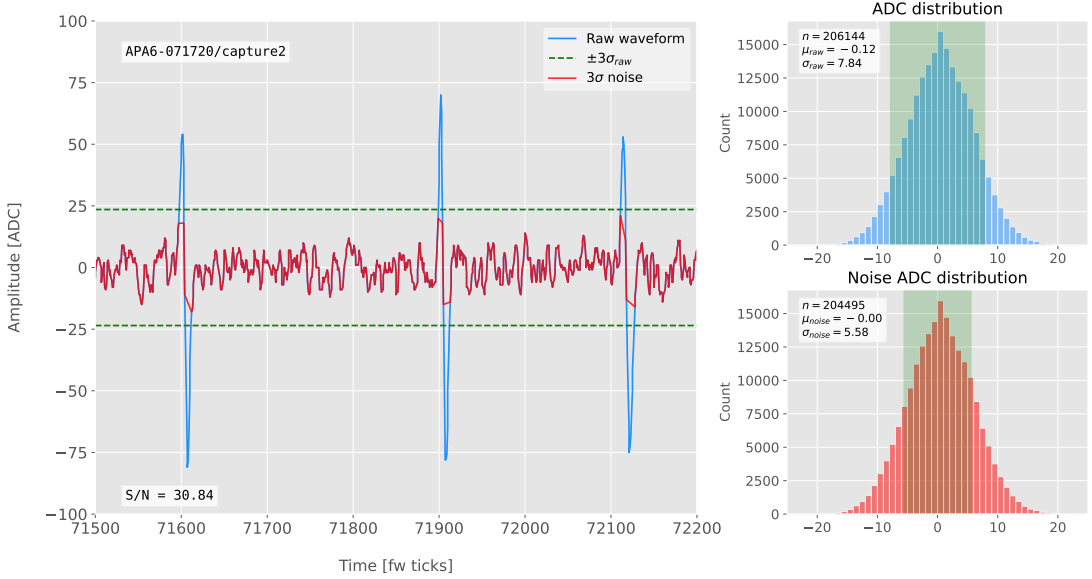


**Figure 4.2:** Left panel: Zoomed unfiltered waveform corresponding to channel 7840 from the ProtoDUNE-SP raw data capture `felix-2020-07-17-21:31:44` (blue line). The green dashed lines mark the region  $\pm 3\sigma_{\text{raw}}$ . The resulting noise waveform is also shown (red line). Top right panel: ADC distribution for channel 7840, where the green shaded region represents  $\pm \sigma_{\text{raw}}$ . Bottom right panel: noise ADC distribution for channel 7840, where the green shaded region represents  $\pm \sigma_{\text{noise}}$ .

1456 optimal filter performance for the induction wires.

## 1457 4.2 Signal-to-noise ratio definition

1458 I introduce the signal to noise ratio (S/N) as a measure of the FIR filter performance  
1459 and demonstrate how to extract its value for a set of ProtoDUNE-SP data. The S/N  
1460 metrics allow us to compare different filter implementations and serve as a basis for more  
1461 detailed studies presented later in this document. Specifically, I use the ADC capture  
1462 `felix-2020-07-17-21:31:44` (data capture taken for firmware validation purposes). I  
1463 defined S/N as the height of the signal peaks relative to the size of the noise peaks.  
1464 To quantify this quantity channel by channel one first need to estimate the standard  
1465 deviation of the ADC data for each channel,  $\sigma_{\text{ADC}}$ . Then, I define the corresponding  
1466 noise waveform to be the ADC values in the range  $\pm 3\sigma_{\text{ADC}}$ . From this new noise data  
1467 one can estimate again the mean and standard deviation,  $\mu_{\text{noise}}$  and  $\sigma_{\text{noise}}$ , so I can

## CHAPTER 4. MATCHED FILTER APPROACH TO TRIGGER PRIMITIVES

1468 write the S/N for any given channel as:

$$\text{S/N} = \frac{\max [ADC] - \mu_{noise}}{\sigma_{noise}}, \quad (4.2)$$

1469 where  $\max [ADC]$  is simply the maximum ADC value found in the corresponding channel.

1470 One can apply this definition of the S/N with a waveform from one of the channels  
1471 of the data capture<sup>1</sup>. Fig. 4.2 shows a zoomed region of the waveform corresponding to  
1472 channel 7840 (blue line), where one can clearly see three signal peaks and continuous  
1473 additive noise (we actually see 6 peaks, 3 positive and 3 negative, but, because by design  
1474 for induction channels the expected signal pulse shapes are bipolar, I treat them as a  
1475 collection of 3 individual signal peaks). I estimated the standard deviation of this raw  
1476 waveform to be  $\sigma_{raw} = 7.84$  ADC, so I am able to define the noise waveform (red line)  
1477 as the ADC values in the range  $\pm 23.52$  ADC. This way one obtains  $\mu_{noise} = 0$  and  
1478  $\sigma_{noise} = 5.58$  ADC, which gives  $\text{S/N} = 30.84$ .

1479 We can repeat this calculation now for the corresponding filtered waveform (using the  
1480 current firmware FIR filter). In Fig. 4.3 I plotted the same time window for the filtered  
1481 waveform from channel 7840 (blue line). In this case, the standard deviation of the  
1482 waveform is larger than before, giving  $\sigma_{raw} = 10.99$  ADC. The resulting noise waveform  
1483 (red line) results from selection the ADC values in the range  $\pm 32.91$  ADC, giving now  
1484  $\mu_{noise} = -0.47$  ADC and  $\sigma_{noise} = 7.03$  ADC. Finally, one obtains  $\text{S/N} = 24.68$ . Notice  
1485 that the value of S/N decreases after the filtering. Clearly, one can see that the noise  
1486 baseline has increased by a factor of 1.35 when we applied the FIR filter and at the same  
1487 time the amplitude of the signal peaks has remained almost unchanged, leading to this  
1488 poorer S/N value.

---

<sup>1</sup>All the original work was done within the `dtp-simulation` package [103], which offers a variety of tools to read raw data and emulate the TPG block (pedestal subtraction, filtering and hit finder). However, the results shown in this report were re-worked later using the C++ based `dtpemulator` package [104]. Its main purpose is the emulation of the TPG block and, in the same way as its predecessor, it has been cross-checked against the current firmware implementation.

### 4.3. LOW-PASS FIR FILTER DESIGN

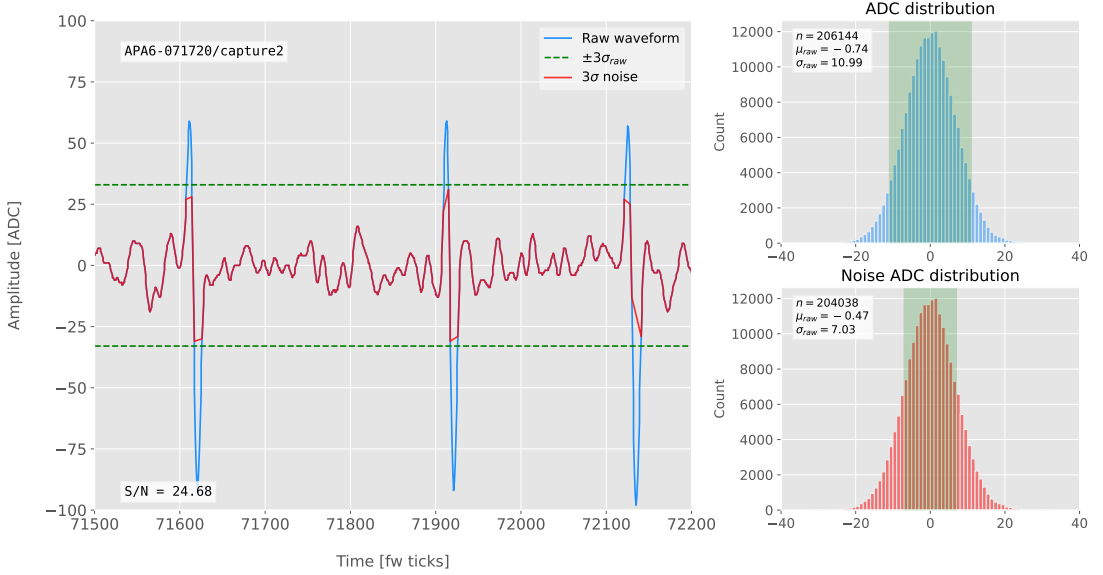


**Figure 4.3:** Left panel: Zoomed filtered waveform corresponding to channel 7840 from the ProtoDUNE-SP raw data capture `felix-2020-07-17-21:31:44` (blue line). The filter used was the current implementation of the low-pass FIR filter in `dtp-firmware`. The green dashed lines mark the region  $\pm 3\sigma_{\text{raw}}$ . The resulting noise waveform is also shown (red line). Top right panel: ADC distribution for channel 7840 after filtering, where the green shaded region represents  $\pm \sigma_{\text{raw}}$ . Bottom right panel: noise ADC distribution for channel 7840 after filtering, where the green shaded region represents  $\pm \sigma_{\text{noise}}$

## 1489 4.3 Low-pass FIR filter design

1490 In general, when one uses a method to optimize the frequency response of a digital filter,  
 1491 such as the Parks-McClellan algorithm, one finds a set of  $N$  real coefficients that give  
 1492 the best response for the specified pass-band and order of the filter [105].

1493 In our case, as the sampling frequency is defined as  $1 \text{ ticks}^{-1}$ , the Nyquist frequency  
 1494 will simply be  $1/2 \text{ ticks}^{-1}$ . The current implementation of the filter seems to have as  
 1495 pass-band the range  $[0, 0.1] \text{ ticks}^{-1}$ . This can be seen in Fig. 4.4, where I show the  
 1496 power spectrum, in decibels, of such filter implementation (blue solid line). For instance,  
 1497 the Park-McClellan algorithm finds the optimal Chebyshev FIR filter taking as input  
 1498 the boundaries of the target pass-band and stop-band, which can be written in the form:

$$\left\{ \begin{array}{l} [0, f_c] \\ [f_c + \delta f, f_N] \end{array} \right. , \quad (4.3)$$

## CHAPTER 4. MATCHED FILTER APPROACH TO TRIGGER PRIMITIVES

1499 where  $f_c$  is the cut-off frequency,  $\delta f$  is the transition width and  $f_N$  is the aforementioned  
 1500 Nyquist frequency. A similar behaviour to the one in the current filter can be obtained  
 1501 by setting  $f_c = 0$  and  $\delta f = 0.1 \text{ ticks}^{-1}$ . The response of the resulting filter is also shown  
 1502 in Fig. 4.4 (blue solid line). Notice that the suppression of the stop-band is enhanced for  
 1503 this optimal filter. For comparison I included the power response of the filter obtained  
 1504 by taking the integer part of the coefficients resulting from the Parks-McClellan method  
 1505 (red dashed line). One can see that it does not suppress that much the stop-band, in a  
 1506 similar way to the current implementation of the filter.

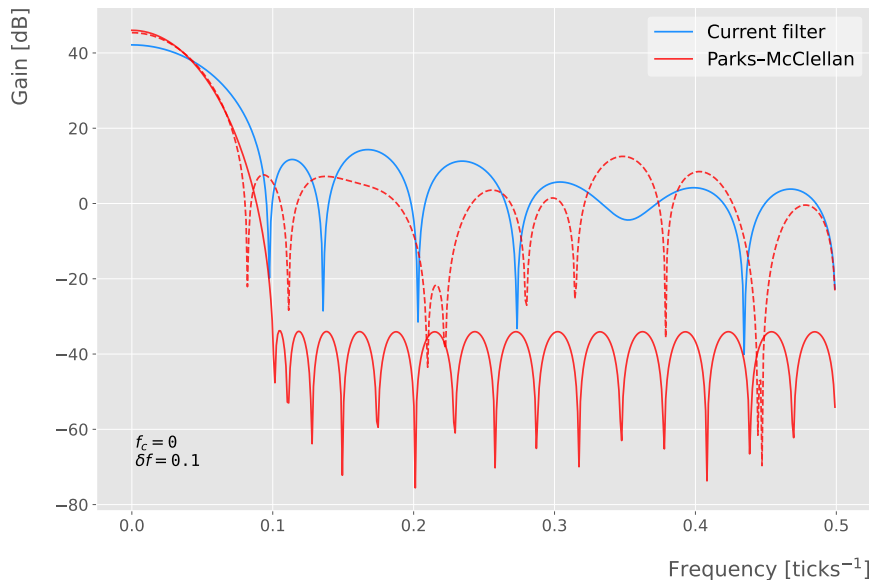


**Figure 4.4:** Power spectrum in decibels for the current implementation of the low-pass FIR filter in `dtp-firmware` (blue line), compared to the response of an optimal filter obtained using the Parks-McClellan algorithm for the same pass-band (red line). Also for comparison I include the spectrum of the optimal filter when taking only the integer part of the coefficients (red dashed line).

1507 At this point, I tried to improve the performance of the FIR filter using the Park-  
 1508 McClellan method, i.e. maximize the overall S/N, using the available data captures. I  
 1509 did so by varying the values of the two quantities that parametrize the pass-band and  
 1510 stop-band, the cut-off frequency  $f_c$  and the transition width  $\delta f$ .

1511 Fig. 4.5 shows the average relative change in the S/N (i.e. the ratio between the  
 1512 value of the S/N after and before the filtering) for capture `felix-2020-07-17-21:31:44`,

### 4.3. LOW-PASS FIR FILTER DESIGN

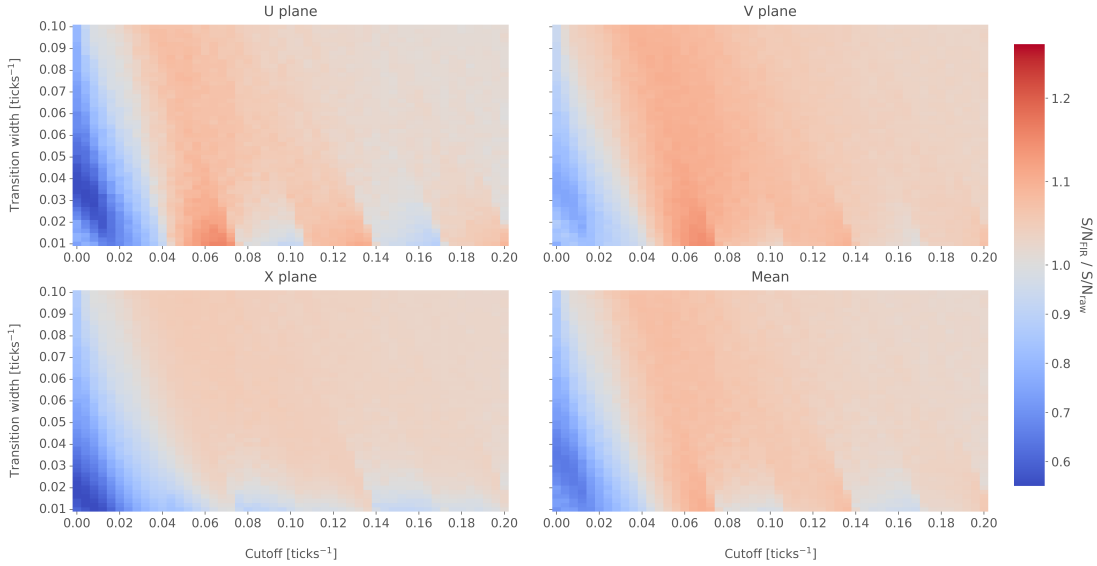


**Figure 4.5:** Relative change in the S/N for the ProtoDUNE-SP raw data capture `felix-2020-07-17-21:31:44`, using different values of the cutoff frequency  $f_c$  and the transition width  $\delta f$ . The optimal Chebyshev filters were applied using just the integer part of the coefficients given by the Parks-McClellan algorithm.

when using filters designed with the Parks-McClellan algorithm for the specified values of the cut-off frequency  $f_c$  and the transition width  $\delta f$ , restricted to integer values for the filter coefficients. One can clearly distinguish different regions where we get an improvement of up to a factor of 1.35 for the U plane. For large values of  $f_c + \delta f$  the ratio tends to 1, as expected (in that limit the width of the stop-band goes to 0, meaning that no frequencies are filtered out and thus the waveform remains the same).

Using the configuration which gives the best mean performance for the three planes (see bottom right panel of Fig. 4.5), i.e.  $f_c = 0.068 \text{ ticks}^{-1}$  and  $\delta f = 0.010 \text{ ticks}^{-1}$ , we can see how such filter affects the different channels. Fig. 4.6 shows the distribution of the S/N improvement values for all the channels in the raw ADC capture `felix-2020-07-17-21:31:44`, separated by wire plane, after the optimal Chebyshev filter was applied. One can see that there is a clear improvement for both U and V induction wire planes, obtaining a mean change of 1.25 and 1.30 for them respectively. However, in the case of the collection plane X the mean of this distribution is roughly 1, meaning that a good fraction of channels in that plane get a slightly worse S/N after the

## CHAPTER 4. MATCHED FILTER APPROACH TO TRIGGER PRIMITIVES

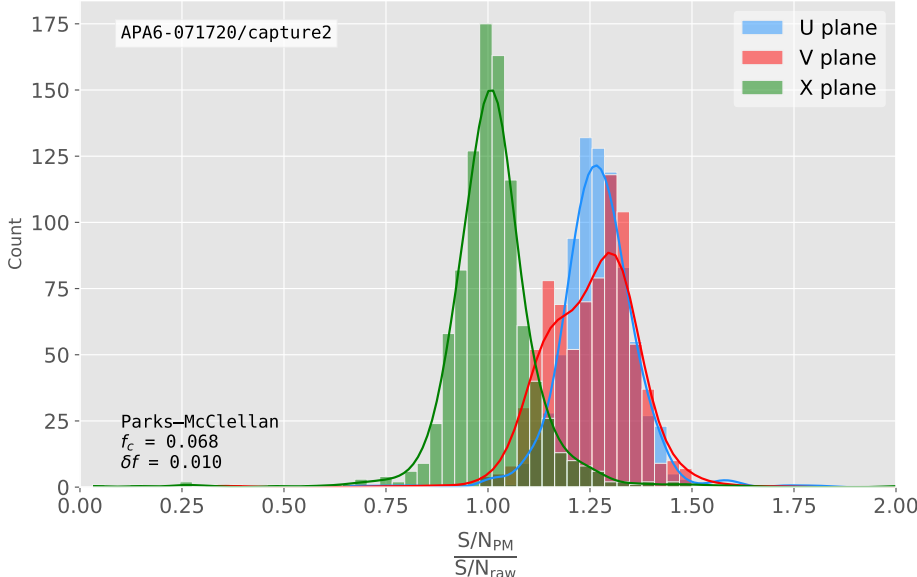


**Figure 4.6:** Distribution of the relative change of the S/N on the different wire planes from the ProtoDUNE-SP raw data capture *felix-2020-07-17-21:31:44* after the optimal Chebyshev filter was applied. The filter was computed with the Parks-McClellan algorithm using a cutoff of  $f_c = 0.068 \text{ ticks}^{-1}$  and a transition width  $\delta f = 0.010 \text{ ticks}^{-1}$ .

filter is applied. In any case, this is not a big issue as the S/N for collection channels is usually much higher than the one for induction channels.

The results I obtained optimising the low pass filter with the Parks-McClellan method are promising. Nonetheless, the improvement found is rather marginal so I wondered if there could be an alternative approach to the filtering problem which yields better outputs. At this point, I found a possible alternative in matched filters. By construction, this kind of filters offer the best improvement on the S/N.

## 4.4 Matched filters

In the context of signal processing, a matched filter is the optimal linear filter for maximising the signal-to-noise ratio (S/N) in the presence of additive noise, obtained by convolving a conjugated time-reversed known template with an unknown signal to detect the presence of the template in the signal [106].

Given a known signal sequence  $s(t)$  and another (a priori unknown) noise sequence

#### 4.4. MATCHED FILTERS

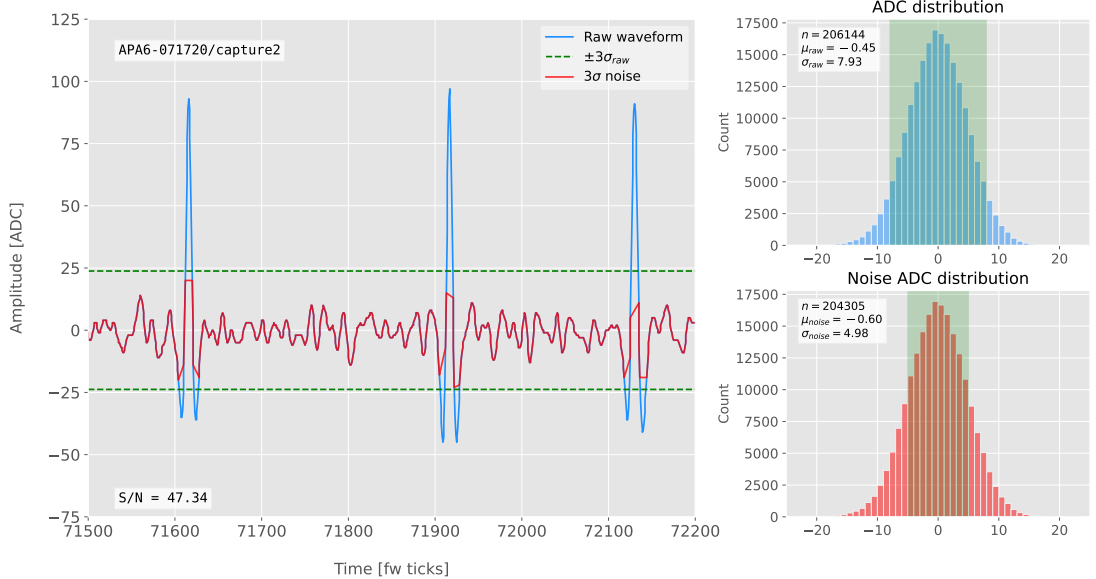


**Figure 4.7:** Left panel: Zoomed match filtered waveform corresponding to channel 7840 from the ProtoDUNE-SP raw data capture felix-2020-07-17-21:31:44 (blue line). The filter used was directly extracted from the data, being the 32 values around the first peak in the original waveform. The green dashed lines mark the region  $\pm 3\sigma_{raw}$ . The resulting noise waveform is also shown (red line). Top right panel: ADC distribution for channel 7840 after match filtering, where the green shaded region represents  $\pm \sigma_{raw}$ . Bottom right panel: noise ADC distribution for channel 7840 after match filtering, where the green shaded region represents  $\pm \sigma_{noise}$

1541  $n(t)$ , the input signal can be written as:

$$x(t) = s(t) + n(t). \quad (4.4)$$

1542 Now, considering a linear time-invariant filter, whose impulse-response function I  
1543 will refer to as  $h(t)$ , one can write the output signal as:

$$\begin{aligned} y(t) &= x(t) * h(t) \\ &= (s(t) + n(t)) * h(t) \\ &= y_s(t) + y_n(t), \end{aligned} \quad (4.5)$$

1544 where  $y_s(t)$  and  $y_n(t)$  are simply the outputs of the filter due to the signal and the noise  
1545 components respectively.

## CHAPTER 4. MATCHED FILTER APPROACH TO TRIGGER PRIMITIVES

1546 The goal of the matched filter is to detect the presence of the signal  $s(t)$  in the input  
 1547 sample  $x(t)$  at a certain time  $t_0$ , which effectively means we need to maximise the S/N.  
 1548 This way, what one wants is to have a filter which gives a much bigger output when the  
 1549 known signal is present than when it is not. Putting it in other words, the instantaneous  
 1550 power of the signal output  $y_s(t)$  should be much larger than the average power of the  
 1551 noise output  $y_n(t)$  at some time  $t_0$ .

1552 For the case of the filtered signal, one can easily re-write it as an inverse Fourier  
 1553 transform:

$$y_s(t) = \frac{1}{2\pi} \int_{-\infty}^{\infty} d\omega H(\omega)S(\omega)e^{i\omega t}, \quad (4.6)$$

1554 where  $H(\omega)$  and  $S(\omega)$  are the Fourier transforms of the impulse-response function (i.e.  
 1555 the transfer function of the filter) and of the input signal, respectively.

1556 Now focusing on the noise, we can use the Wiener-Khinchin theorem [107] to write  
 1557 the mean power of the noise after filtering as:

$$E|y_n(t)|^2 = \frac{1}{2\pi} \int_{-\infty}^{\infty} d\omega |H(\omega)|^2 S_n(\omega), \quad (4.7)$$

1558 where  $S_n(\omega)$  is the power spectral density of the noise.

1559 Having these, one can write the instantaneous S/N at time  $t_0$  as:

$$\begin{aligned} \left( \frac{S}{N} \right)_{t_0} &= \frac{|y_s|^2}{E|y_n(t)|^2} \\ &= \frac{1}{2\pi} \frac{\left| \int_{-\infty}^{\infty} d\omega H(\omega)S(\omega)e^{i\omega t_0} \right|^2}{\int_{-\infty}^{\infty} d\omega |H(\omega)|^2 S_n(\omega)}. \end{aligned} \quad (4.8)$$

1560 Once we have this expression, we need to find the upper limit of it to determine what  
 1561 would be the optimal choice for the transfer function. One can use the Cauchy-Schwarz  
 1562 inequality, which in the present case takes the form:

$$\left| \int_{-\infty}^{\infty} dx f(x)g(x) \right|^2 \leq \int_{-\infty}^{\infty} dx |f(x)|^2 + \int_{-\infty}^{\infty} dx |g(x)|^2, \quad (4.9)$$

#### 4.4. MATCHED FILTERS

1563 for any two analytical functions  $f(x)$  and  $g(x)$ . One can prove that making the choice:

$$\begin{aligned} f(x) &= H(\omega) \sqrt{S_n(\omega)} e^{i\omega t_0}, \\ g(x) &= \frac{S(\omega)}{\sqrt{S_n(\omega)}}, \end{aligned} \quad (4.10)$$

1564 leads to the following upper bound for the S/N:

$$\left( \frac{S}{N} \right)_{t_0} \leq \frac{1}{2\pi} \int_{-\infty}^{\infty} d\omega \frac{|S(\omega)|^2}{S_n(\omega)}. \quad (4.11)$$

1565 From Eqs. (4.8), (4.9) and (4.10) one can also derive the form of the transfer function

1566 such that the upper bound is exactly reached [108]:

$$H(\omega) \propto \frac{S^*(\omega) e^{-i\omega t_0}}{S_n(\omega)}. \quad (4.12)$$

1567 From this last expression we can clearly see the way the matched filter acts. As the  
1568 transfer function is proportional to the Fourier transform of the signal it will try to only  
1569 pick the frequencies present in the signal [109].

1570 The matched filter transfer function can be greatly simplified if the input noise is  
1571 Gaussian. In that case, the power spectral density of the noise is a constant, so it can be  
1572 re-absorbed in the overall normalisation of the transfer function. Moreover, considering  
1573 that the input signal is a real function, one can simply set  $S^*(\omega) = S(-\omega)$ , which gives:

$$H(\omega) \propto S(-\omega) e^{-i\omega t_0}. \quad (4.13)$$

1574 For a discrete signal, one can think of the input and impulse-response sequences as  
1575 vectors of  $\mathbb{R}^N$ . Then, the matched filter tries to maximise the inner product of the signal  
1576 and the filter while minimising the output due to the noise by choosing a filter vector  
1577 orthogonal to the later. In the case of additive noise, that leads to the impulse-response  
1578 vector:

$$h = \frac{1}{\sqrt{s^\dagger R_n^{-1} s}} R_n^{-1} s, \quad (4.14)$$

## CHAPTER 4. MATCHED FILTER APPROACH TO TRIGGER PRIMITIVES

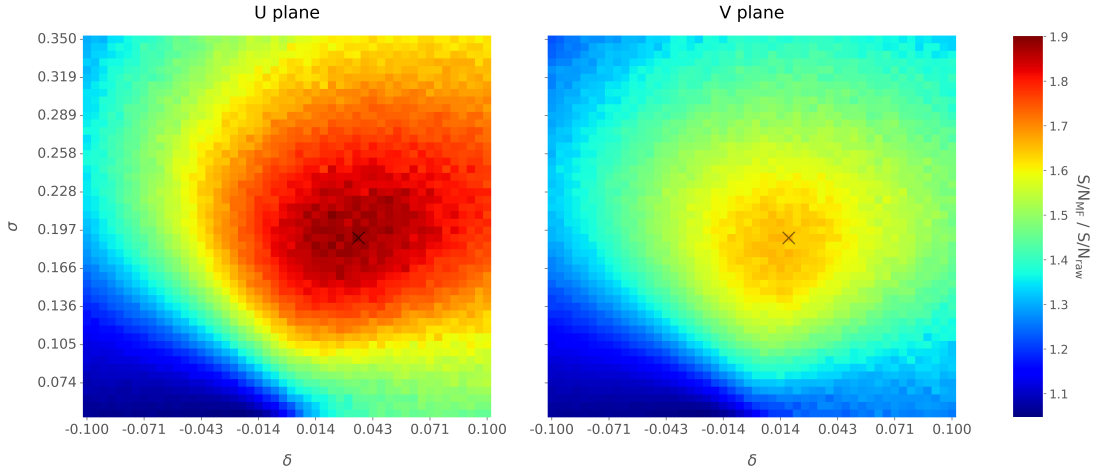


**Figure 4.8:** Relative improvement in the S/N for the raw data capture *felix-2020-07-17-21:31:44*, using the matched filter following the parametrisation in Eq. (4.17). The black crosses in both panels denote the location of the maximum ratio value.

1579 where  $s$  is a reversed signal template sequence of length  $N$  equal to the order of the filter  
 1580 and  $R_n$  is the covariance matrix associated with the noise sequence  $n$ . For the Gaussian  
 1581 noise case, the covariance matrix is simply the unit matrix, so the above expression  
 1582 simplifies again to:

$$h = \frac{s}{|s|}. \quad (4.15)$$

1583 For this first stage of the study, I use a definition of the S/N per channel given by:

$$\text{S/N} = \frac{\max [ADC] - \mu_{noise}}{\sigma_{noise}}, \quad (4.16)$$

1584 where the subscript *noise* refers to a subset of the data obtained by only taking into  
 1585 account waveform values within a  $\pm 3\sigma$  range around the mean of the data and  $\max [ADC]$   
 1586 is the maximum of the original waveform. This definition is further discussed in App.  
 1587 4.2, where I also show examples of its application to raw data and to a waveform filtered  
 1588 with the current low-pass FIR filter.

1589 To test whether this choice of filter is appropriate one needs to choose a signal  
 1590 template. As an example of how a matched filter would affect our signal, I simply took  
 1591 the filter coefficients to be the 32 ADC values around a signal peak present in the data.

#### 4.4. MATCHED FILTERS

1592 In Fig. 4.7 (left panel) I plotted a zoomed region for channel 7840 in the raw data capture  
1593 `felix-2020-07-17-21:31:44`, after applying the matched filter described before (blue  
1594 line). When compared to the raw and FIR filtered case (see App. 4.2), after applying  
1595 the match filter the standard deviation of the noise waveform (red line) decreases and at  
1596 the same time the signal peaks are enhanced. This leads to an improvement of the S/N  
1597 by a factor of 1.92 when compared to the raw waveform.

1598 In order to obtain the matched filter that is more suitable for our data, I explored  
1599 different configurations of signal templates. In order to perform this exploration, I  
1600 parametrised the signal using the bipolar function:

$$f(x) = -A(x + \delta) e^{-x^2/\sigma^2}, \quad (4.17)$$

1601 where the parameter  $\delta$  controls the asymmetry between the positive and negative peaks  
1602 and  $\sigma$  controls their width. The amplitude parameter  $A$  is set such that it keeps the  
1603 height of the biggest peak to be less than 200 ADC in absolute value.

1604 As this parametrisation is only adequate for bipolar signals I will focus exclusively  
1605 on the induction channels. Also, the optimal configurations I found for the U and V  
1606 plane will be kept separate, i.e. I will have two sets of coefficients that will be applied to  
1607 either the U and V planes of wires. I do so as I found this was the choice giving the  
1608 best performance. Even so, as I will discuss, the differences are not very pronounced. In  
1609 case it is not technically possible to separate channels in the firmware according to the  
1610 wire plane they come from and use different sets of filter coefficients for them, we can  
1611 just find a common unique set of coefficients. In such case, I do not expect our results  
1612 to change dramatically.

1613 In Fig. 4.8 I present the results of our parameter scan, for channels in the induction  
1614 planes U (left panel) and V (right panel). For each configuration of  $\sigma$  and  $\delta$  the resulting  
1615 matched filter was applied to all channels in the corresponding plane within the data  
1616 capture `felix-2020-07-17-21:31:44`, the S/N improvement was computed with respect  
1617 to the raw waveforms and then the S/N mean value was kept as a score for such filter.

## CHAPTER 4. MATCHED FILTER APPROACH TO TRIGGER PRIMITIVES

1618 One can see that the improvement obtained for the U plane is in general higher than the  
1619 one for the V plane. In any case, I got substantially higher ratios than the ones obtained  
1620 for the low-pass FIR filters. For the optimal configurations I attained improvements up  
1621 to a factor of 1.85 for the U plane and 1.65 for the V plane.

1622 The sets of optimal matched filter coefficients were obtained for the parameters  
1623  $\delta = 0.035$ ,  $\sigma = 0.191$  for the U plane and  $\delta = 0.018$ ,  $\sigma = 0.191$  for the V plane. I  
1624 show these two sets of coefficients in Fig. 4.9 (left panel). Also in Fig. 4.9 (right  
1625 panel) I plot the distribution of the S/N improvement after the optimal match filters  
1626 for the U and V were applied to the corresponding channels in the raw data capture  
1627 `felix-2020-07-17-21:31:44`. As mentioned before, the mean improvement achieved  
1628 for the U plane channels is slightly bigger than the one for the V channels. Note, however,  
1629 that the spread of the distribution for the V plane is also smaller than the one for the U  
1630 plane.

1631 I also performed a similar scan for the case of a low-pass FIR filter using the Parks-  
1632 McClellan algorithm. In that case, the parameters to check were the cutoff frequency  
1633 and the transition width of the filter. A summary of the results is given in App. 4.3.

1634 Overall, one can see that the improvements on the S/N are much more significant in  
1635 the case of the matched filter than it is for the low-pass FIR filters. The analysis of this  
1636 and other raw data captures from ProtoDUNE-SP suggest that matched filters increase  
1637 the S/N of induction channels by a factor of 1.5 more than the optimal low-pass FIR  
1638 filters.

1639 Although these results are by themselves great points in favour of the matched  
1640 filter, more studies are needed to completely assess the robustness of this approach. I  
1641 proceeded then to test the matched filter with simulated data samples.

## 1642 4.5 Using simulated samples

1643 In order to further test the matched filter, the next step was to generate and process  
1644 data samples using *LArSoft* [110]. In this way, one can control the particle content of

## 4.5. USING SIMULATED SAMPLES

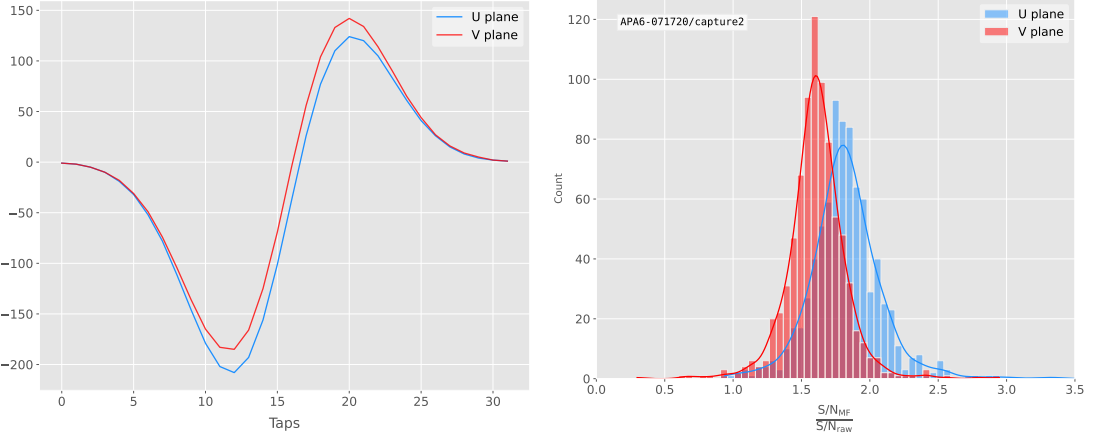


**Figure 4.9:** Left panel: Optimal matched filter coefficients for the U (blue line) and V (red line) planes. The filters were computed with our parametrisation in Eq. (4.17) for the parameter values  $\delta = 0.035$ ,  $\sigma = 0.191$  and  $\delta = 0.018$ ,  $\sigma = 0.191$  respectively. Right panel: Distribution of the relative change of the S/N on the two induction wire planes from the ProtoDUNE-SP raw data capture *felix-2020-07-17-21:31:44* after their respective optimal matched filters were applied.

the samples, the orientation of the tracks and their energy, and therefore see how the matched filter behaves in various situations.

To begin with, I prepared different monoenergetic and isotropic samples containing a single particle per event. Each sample contains a different particle species, namely electrons, muons, protons and neutral pions all with a kinetic energy of  $E_k = 100$  MeV. I chose these because of the fairly different topologies they generate in the liquid argon, ranging from shower-like to track-like. The procedure I followed to generate the samples and process them is discussed in detail in App. ??.

These were generated with the single particle gun and the Geant4 stage of the *LArSoft* simulation [110] was performed with the standard configuration for the DUNE FD 10kt module.

For simplicity, I restricted the particles to start drifting in a single TPC volume (in this case TPC 0), so I can focus exclusively on the signals coming from one APA. The chosen kinetic energy for all the particles in my first trial is  $E_k = 100$  MeV, so a necessary check is to see if all our tracks will be typically contained in one TPC volume. Fig. 4.10 (left panel) shows the distributions of the track lengths in the liquid argon

## CHAPTER 4. MATCHED FILTER APPROACH TO TRIGGER PRIMITIVES

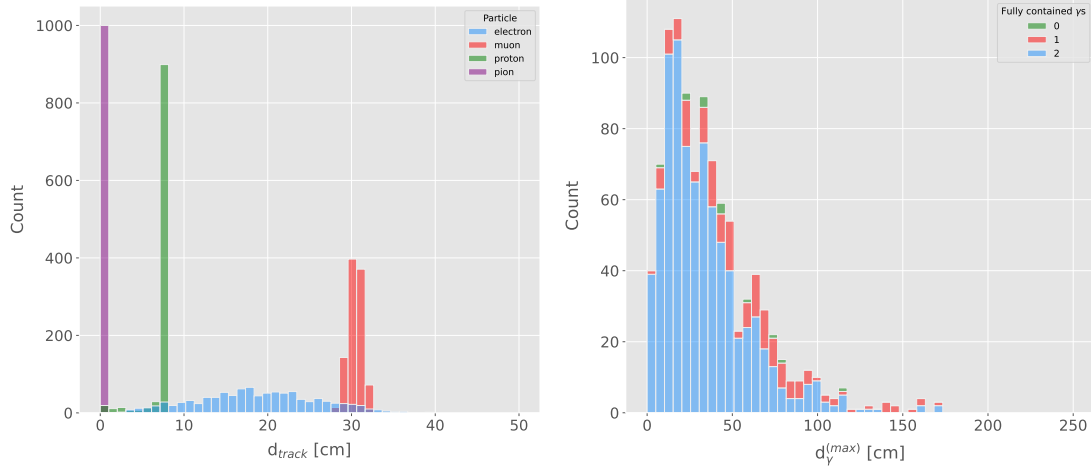


**Figure 4.10:** Left panel: distributions of the particles track length in the liquid argon for the generated  $E_k = 100$  MeV monoenergetic samples, electrons (blue), muons (red), protons (green) and neutral pions (purple). Right panel: distribution of the length of the longest photon in the neutral pion sample after the decay process  $\pi^0 \rightarrow \gamma\gamma$ .

of all generated particles with  $E_k = 100$  MeV. One can see that, in the case of the track-like particles (i.e. muons and protons), their length distributions are quite sharp and centered at relatively low distances (30 and 8 cm, respectively). For electrons, the distribution is quite broad but it does not extend past  $\sim 30$  cm. The case of neutral pions can be misleading, as they decay promptly the track length associated with the true Monte Carlo particle is always  $< 1$  cm. In Fig. 4.10 (right panel) I show the effective length distribution of the longest photon after the pion decays as  $\pi^0 \rightarrow \gamma\gamma$ , highlighting the number of fully contained photons in the TPC volume per event (either zero, one or both). One can see that the vast majority of events has both photons contained and that just a negligible number of them has none of them contained in the TPC volume. In any case, for the sake of caution, I will only keep the pion events with both photons contained.

Once I have prepared a sample at the Geant4 level, I need to process it through the detector simulation. In order to make adequate estimations of the noise levels and run the filtering and hit finder as I did with the ProtoDUNE data, one needs to turn off the default zero-suppression of the waveforms produced by the simulation. At this first stage I am only concerned with the waveforms with the noise added, so I keep the noise

## 4.5. USING SIMULATED SAMPLES

addition option as true in the configuration. However, for studies related to the hit finder performance one will also need to store the noiseless waveforms in order to retrieve the truth information of the hits. I will discuss this approach next.

After the detector simulation stage, one needs to extract the no zero-suppressed noisy waveforms, along with their offline channel numbers, and store them in a certain format to be analysed later. To reduce the amount of data that will go for processing, I used the information from the Geant4 step of the simulation to select only the active channels, i.e. the channels where some ionisation electrons arrive. Moreover, as said previously, I only extract the waveforms from APA 0 and exclusively the ones coming from induction channels. The resulting ROOT file contains a tree with two branches, one containing the waveforms for each event and channel and the other with the corresponding offline channel numbers.

Finally, to extract the truth values for the orientation of the tracks and the energies of the particles I used a modified analysis module. This gives a ROOT file with a single tree, containing several branches with different information such as the components of the initial momentum of the particles, initial and final  $xyz$  location, track length, etc.

For the analysis of the resulting waveforms and truth values I used a custom set of Python libraries (available at [???]). Among other functionalities, these enable the user to read the ROOT files, export the raw data as pandas objects, apply the filters and compute the S/N of both the raw and filtered signals. So far, the default configuration for the filtering uses the set of optimal matched filter coefficients that I found using the ProtoDUNE data samples.

Additionally, for the analysis of the samples it was necessary to use two different reference frames, to study separately the signals coming from the U and V induction wire planes. As I am focussing on a single APA, the U and V wires have a different orientation in the  $yz$  plane. In the case of U wires, these are tilted  $35.7^\circ$  clockwise from the vertical ( $y$  direction), whereas the V wires are at the same angle but in the counter clockwise direction. Because of this, the best option is to deal with two new coordinate systems rotated by  $\pm 35.7^\circ$  along the  $x$  axis, so the new  $y'$  and  $y''$  directions are aligned with the

## CHAPTER 4. MATCHED FILTER APPROACH TO TRIGGER PRIMITIVES

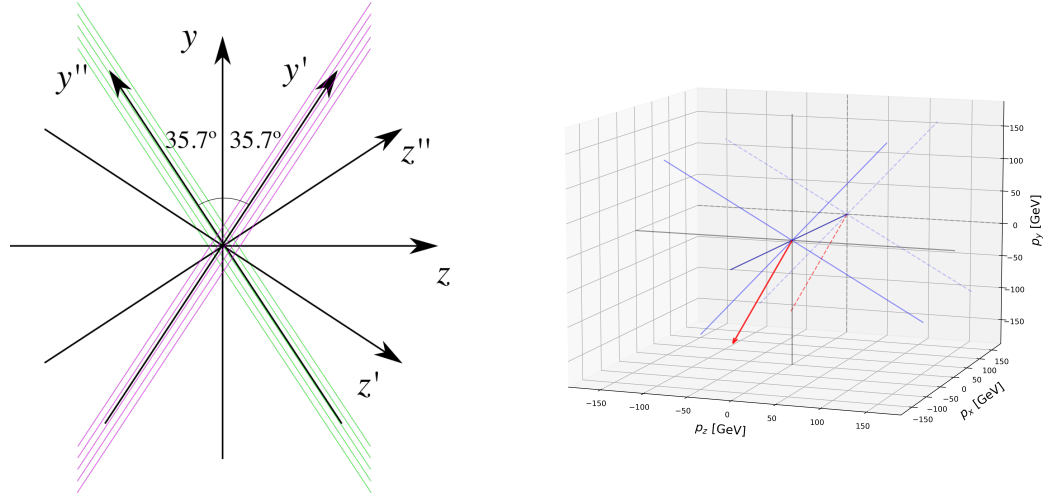


**Figure 4.11:** Left panel: schematic representation of the two new rotated reference frames used in this analysis (denoted as prime and double prime), viewed from the  $yz$  plane. The magenta stack of lines represent the wires in the  $U$  plane, whereas the green lines correspond to the wires in the  $V$  plane. Right panel: 3D representation of the momentum of one of the generated monoenergetic muons (red arrow) in the original reference frame (black lines), along with the new reference frame used for the  $U$  plane waveforms (blue lines). In the  $yz$  plane I added the projection of these three.

1707 U and V induction wires. Fig. 4.11 (left panel) shows a schematic representation of  
 1708 the original reference frame together with the two rotated ones (denoted by primed and  
 1709 double primed). This way, one can easily understand how parallel was a track to the  
 1710 wires in the two induction planes. Fig. 4.11 (right panel) shows a 3D representation of  
 1711 the momentum of a track (red arrow) in the original reference frame (black lines), along  
 1712 with the new reference frame for  $U$  wires (blue lines). I added the projection in the  $yz$   
 1713 plane of this three, to show the usefulness of the new reference frame to tell whether a  
 1714 track is parallel or normal to the wires in the induction plane.

1715 Fig. 4.12 shows the distribution of the average S/N improvement per event when one  
 1716 applies the optimal matched filters. I produced separate distributions for the channels  
 1717 in the  $U$  (red) and  $V$  (blue) induction wire planes. Notice that the S/N distributions  
 1718 for the track-like particles, i.e. muons (top left panel) and protons (bottom left panel),  
 1719 have significantly larger mean values than the distributions of the shower like particles,  
 1720 i.e. electrons (top right panel) and neutral pions (bottom right panel). An important

## 4.5. USING SIMULATED SAMPLES

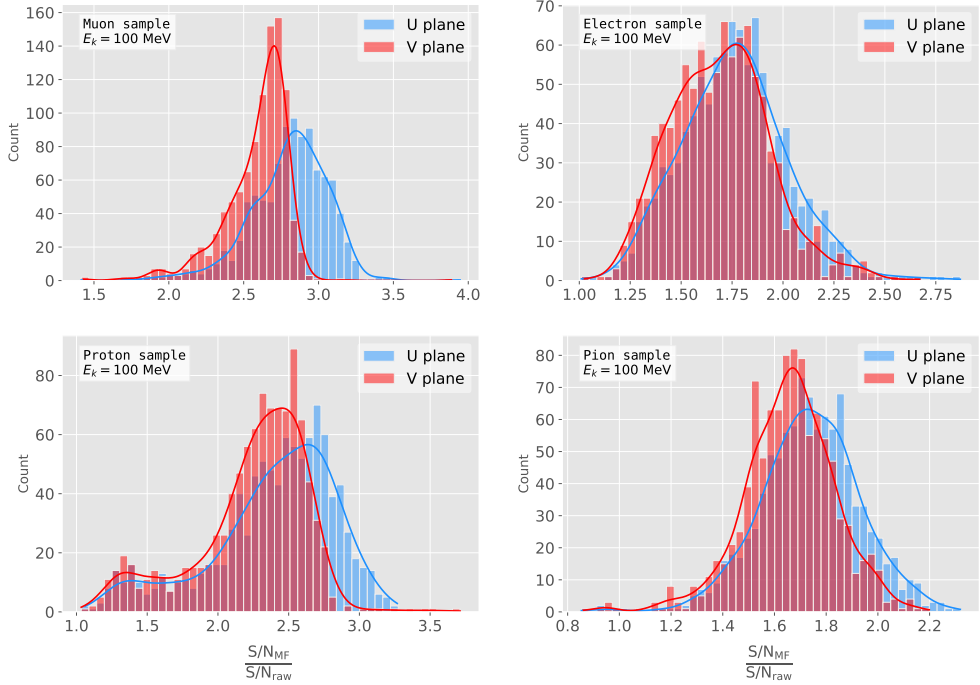


**Figure 4.12:** Distributions of the mean  $S/N$  improvement per event for the corresponding sample after applying the matched filters. Here I separated the change in the U plane (blue) and the V plane (red) channels. From top left to the right: muon, electron, proton and neutral pion. All the events have a fixed kinetic energy of  $E_k = 100 \text{ MeV}$ .

difference between these results and the ones seen before for ProtoDUNE data is that, overall, the improvements that I get for simulated data are bigger. This could be due either to the default noise model used in the *LArSoft* simulation or to the simulated hits having higher energy than the ones in the recorded data. Nonetheless, the concluding message is that the previously optimised matched filters give an overall significant improvement of the S/N for the different samples.

About the convention I followed for the plots and results, in the case of the raw and filtered S/N of each event in the sample I simply took the average of the quantities over all the active channels in the event. That is, if a certain event has  $N_{chan}$  active channels these two quantities are computed as:

$$(S/N_{fir})_{event} = \frac{\sum_{i=0}^{N_{chan}} (S/N_{fir})_i}{N_{chan}}, \quad (4.18)$$

$$(S/N_{raw})_{event} = \frac{\sum_{i=0}^{N_{chan}} (S/N_{raw})_i}{N_{chan}}.$$

## CHAPTER 4. MATCHED FILTER APPROACH TO TRIGGER PRIMITIVES

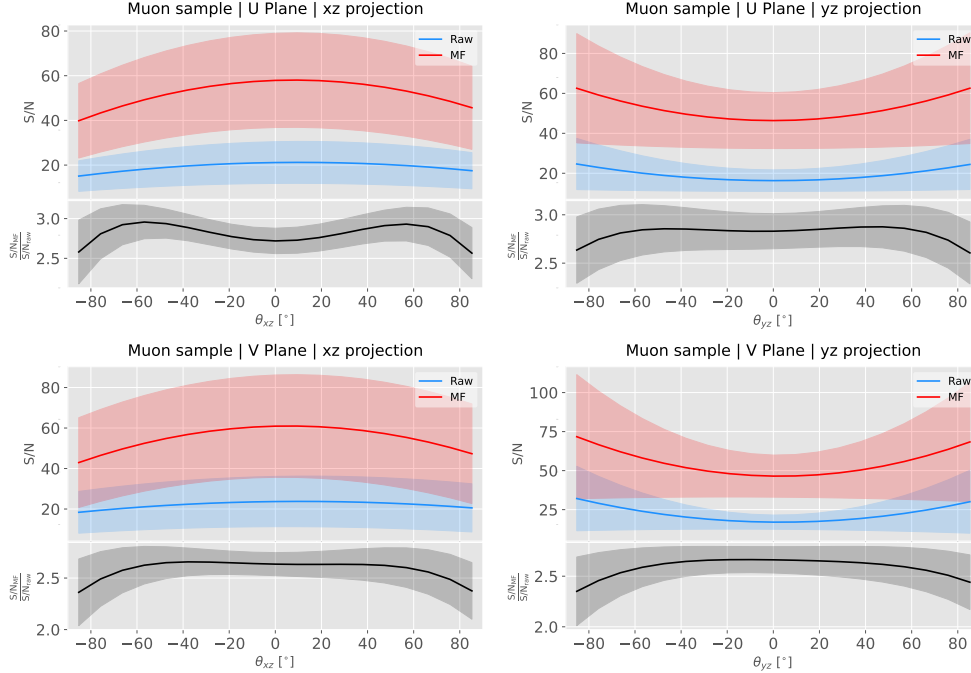


**Figure 4.13:** Angular dependence of the mean S/N and the S/N improvement, for the different monoenergetic samples considered (from top to bottom: electrons, muons, protons and neutral pions). The two columns on the left represent the values for the U plane waveforms. The top subplots show the mean S/N for raw (green) and filtered (red) waveforms whereas the bottom subplots depict the averaged S/N improvement (black).

1731 However, for the ratio of the raw and filtered S/N (what I called the S/N improvement)  
 1732 per event I am not just taking the ratio of the previous two quantities but computing  
 1733 the average of the individual ratios per channel in the event:

$$\left( \frac{S/N_{fir}}{S/N_{raw}} \right)_{event} = \frac{\sum_{i=0}^{N_{chan}} \left( \frac{S/N_{fir}}{S/N_{raw}} \right)_i}{N_{chan}}, \quad (4.19)$$

1734 and so:

$$\left( \frac{S/N_{fir}}{S/N_{raw}} \right)_{event} \neq \frac{(S/N_{fir})_{event}}{(S/N_{raw})_{event}}. \quad (4.20)$$

### 1735 4.5.1 Angular dependence

1736 Having these monoenergetic samples, one can also study the angular dependence of the  
 1737 performance of the matched filter. This is an important point, as it is a well established

## 4.5. USING SIMULATED SAMPLES

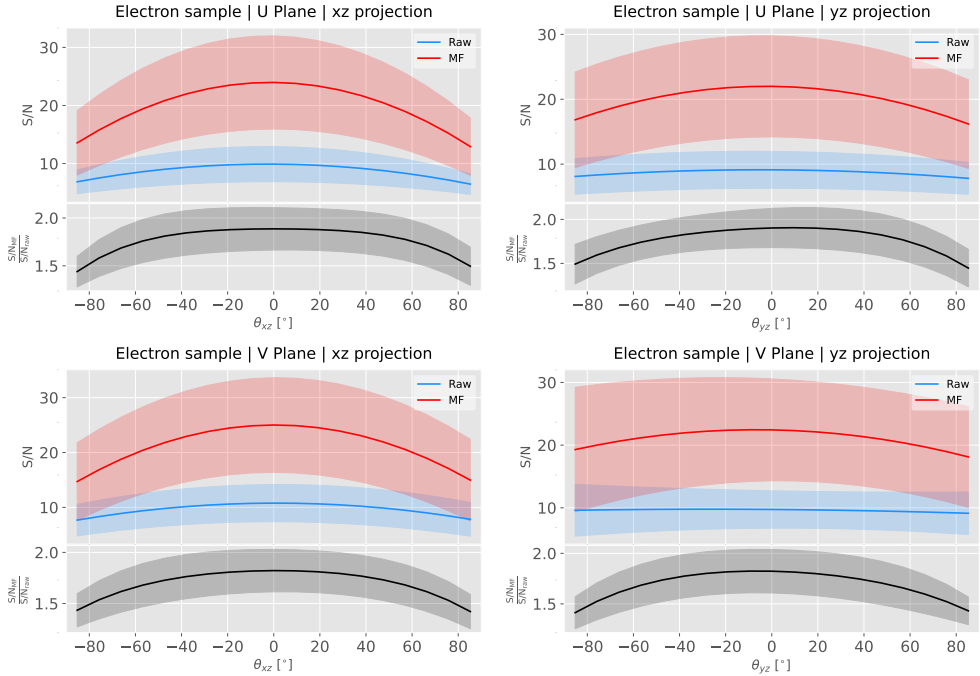


**Figure 4.14:** Angular dependence of the mean S/N and the S/N improvement, for the different monoenergetic samples considered (from top to bottom: electrons, muons, protons and neutral pions). The two columns on the left represent the values for the U plane waveforms. The top subplots show the mean S/N for raw (green) and filtered (red) waveforms whereas the bottom subplots depict the averaged S/N improvement (black).

fact that for certain configurations (an extreme case configuration being signals normal to the wire plane and perpendicular to the induction wires at the same time) the S/N is much lower than average as the corresponding waveforms are severely distorted. In this sense, I am interested to see how the matched filter behaves for these cases and how the S/N improvement on those compare to the average.

Fig. 4.13 shows the angular dependence of the S/N for the monoenergetic  $E_k = 100$  MeV isotropic muons, for the different induction wire planes and projections. The angles for each event are given by the components of the initial value of the momentum of the particles, taking the angles of the projections on the  $xz$  and  $yz$  planes with respect to the  $z$  axis (more accurately, one needs to compute these angles twice for each event, a pair for the  $xy'z'$  coordinate system and the other for the  $xy''z''$ ). The top row shows the dependence on the angles corresponding to the U plane, i.e.  $\theta_{xz'}$  and  $\theta_{y'z'}$ , whereas the bottom row shows the angular dependence viewed from the V plane,  $\theta_{xz''}$  and  $\theta_{y''z''}$ . In

## CHAPTER 4. MATCHED FILTER APPROACH TO TRIGGER PRIMITIVES

each plot, the top subplot represents the mean values of the S/N for the raw (blue) and matched filtered (red) signals, and the bottom subplot the averaged S/N improvement (black). The solid lines represent the mean value obtained for the corresponding angular value, whereas the semitransparent bands represent one standard deviation around the mean at each point.

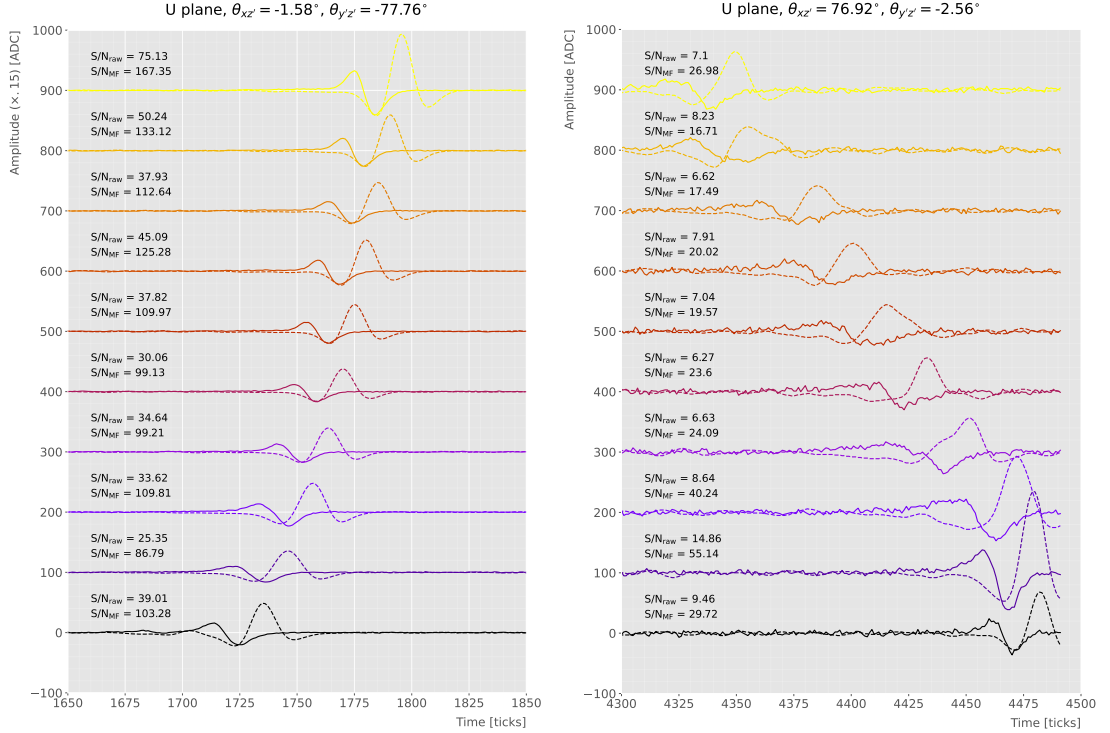
As expected, the S/N is in general higher when tracks are parallel to the APA (i.e.  $\theta_{xz} \sim 0$ ) and lower when it is normal to the plane ( $\theta_{xz} \sim \pm 90^\circ$ ). In the same way, tracks parallel to the wires ( $\theta_{yz} \sim \pm 90^\circ$ ) tend to have higher S/N than those perpendicular to these ( $\theta_{yz} \sim \pm 0$ ).

Fig. 4.14 shows the corresponding angular dependence information for the  $E_k = 100$  MeV electrons sample. Notice that, in this case, the S/N behaviour discussed above does not hold. A possible explanation can be that, because most hits in these events are produced by the secondary particles generated in the EM shower, the signal peaks whose S/N ratios were computed do not correspond to the directional information of the primary electron.

### 4.5.2 Distortion and peak asymmetry

As a little case of study, I selected two of the simulated  $E_k = 100$  MeV monoenergetic muon events. With respect to the U induction plane, one is parallel to the APA (low  $\theta_{xz'}$ ) and to the wires (high  $\theta_{y'z'}$ ) and the other is normal to the APA plane (high  $\theta_{xz'}$ ) and perpendicular to the wires (low  $\theta_{y'z'}$ ). As expected from the results on the angular dependence discussed above, the former has a higher S/N (before and after the filtering) when compared to the latter. An interesting thing to notice about these two samples is that, even though one has a much bigger S/N than the other, it is the one with the smallest S/N the one that got the biggest averaged S/N improvement. In Table 4.1 I included all the relevant parameters of these two  $E_k = 100$  MeV muon events I am considering, namely, the angles with respect to the  $xy'z'$  reference frame, the values of the S/N, the S/N improvement and also the so-called peak asymmetry  $\Delta_{peak}$  that I will discuss next.

## 4.5. USING SIMULATED SAMPLES



**Figure 4.15:** Selected consecutive waveforms corresponding to two monoenergetic  $E_k = 100$  MeV muon events, one is parallel to the APA and to the wires in the U plane (left panel) and the other is normal to the APA plane and perpendicular to the U plane wires (right panel). The solid lines represent the raw waveforms whereas the dashed lines correspond to the waveforms after the matched filter was applied. The waveforms on the left panel have been scaled by a factor of 0.15 to have similar amplitude to the ones on the right panel.

**Table 4.1:** Characteristic parameters of the two monoenergetic muon events selected, relative to the U plane: projected angles in the  $xz'$  and  $y'z'$  planes, S/N values for the raw and filtered waveforms, mean improvement of the S/N and peak asymmetry.

	$\theta_{xz'}$ (°)	$\theta_{y'z'}$ (°)	S/N <sub>raw</sub>	S/N <sub>MF</sub>	$\frac{S/N_{MF}}{S/N_{raw}}$	$\Delta_{peak}$ (ADC)
High ("parallel")	-1.58	-77.76	41.65	112.44	2.83	-35.73
Low ("normal")	76.92	-2.56	8.07	25.46	3.12	-10.38

1779 One can try to understand better what is going on with these two events by looking  
 1780 at the raw and filtered data from some of their active channels. Fig. 4.15 shows a  
 1781 selection of consecutive raw and filtered U plane waveforms from the event with high S/N  
 1782 (left panel) and the one with low S/N (right panel). Notice that to show both collections  
 1783 of waveforms at a similar scale I had to apply a factor of 0.15 to the waveforms with  
 1784 high S/N. Additionally, next to each waveform I included the values of the raw and

## CHAPTER 4. MATCHED FILTER APPROACH TO TRIGGER PRIMITIVES

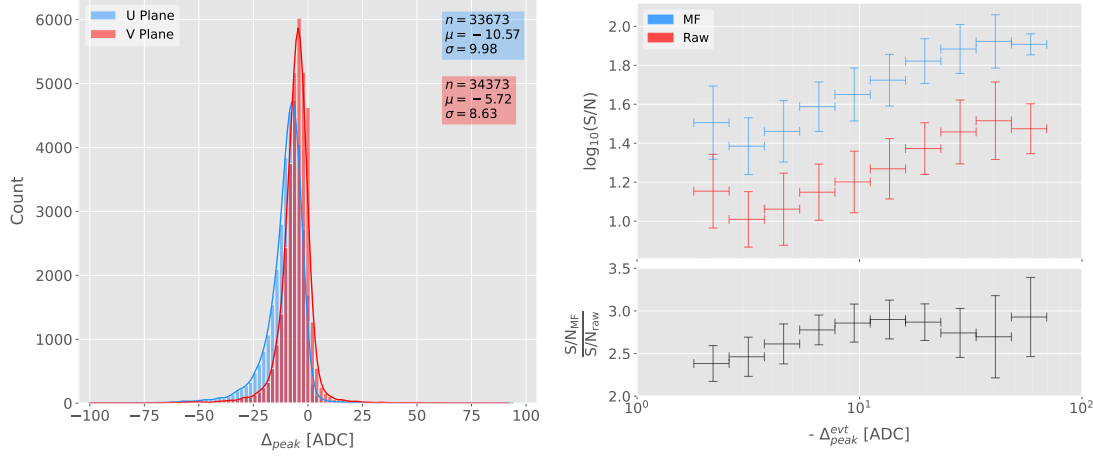


**Figure 4.16:** Left panel: peak asymmetry distribution for the case of the monoenergetic  $E_k = 100$  MeV muon sample. Each value corresponds to a single bipolar signal peak from a channel in any event. The blue distribution represents the peaks on U plane channels, whereas the red corresponds to signal peaks in V wires. Right panel: relation between the mean peak asymmetry per event with the S/N for U channel waveforms from the  $E_k = 100$  MeV muon sample. The top subplot shows the decimal logarithm of the mean S/N for the raw (red) and the matched filtered (blue) waveforms. The bottom subplot contains the mean S/N improvement ratio after the matched filter was applied.

1785 matched filtered S/N for the corresponding channel. The first thing to notice in this plot  
 1786 is that the amplitude of the signal peaks from the normal track have a much smaller  
 1787 amplitude, and also appear quite distorted when compared to the others. On the other  
 1788 hand, although the matched filtered S/N is still smaller, the relative improvement is  
 1789 bigger than in the parallel case.

1790 A way I found to quantify the difference between the shapes within these two events  
 1791 is their different peak asymmetry. One can define the peak asymmetry as the (signed)  
 1792 difference between the positive and the negative peaks of the bipolar shape, i.e.:

$$\Delta_{peak} \equiv h_+ - h_-, \quad (4.21)$$

1793 where both heights  $h_+$  and  $h_-$  are positive defined. Fig. 4.16 (left panel) shows the  
 1794 distribution of this peak asymmetry for all the waveforms corresponding to channels  
 1795 in the U (blue) and V (red) planes for the monoenergetic muon sample. One can  
 1796 see that these distributions are clearly shifted to negative values (with mean values

## 4.5. USING SIMULATED SAMPLES

1797  $\mu_{\Delta}^U = -10.57$  ADC and  $\mu_{\Delta}^V = -5.72$  ADC respectively). It is interesting to notice  
1798 that the peak asymmetry value of the sample with high S/N sits at the left tail of the  
1799 distribution whereas the corresponding value of the sample with low S/N lies around  
1800 the mean.

1801 Now, one can try to correlate the peak asymmetry with the S/N and the S/N change  
1802 per event. Fig. 4.16 (right panel) shows the result of comparing (minus) the mean  
1803 peak asymmetry per event to the averaged raw (red) and matched filtered (blue) S/N  
1804 per event (top subplot). The horizontal lines sit at the mean value obtained in the fit  
1805 and represent the width of the  $-\Delta_{peak}$  bins used, while the vertical lines indicate one  
1806 standard deviation around that mean value. Notice that, when taking decimal logarithm  
1807 on both, there is an approximate linear relation between these quantities, except for  
1808 peak asymmetry values bigger than  $-5$  ADC where the S/N remains constant.

1809 Also, in the bottom subplot of Fig. 4.16 (right panel) I show the relation between  
1810 the peak asymmetry and the mean S/N improvement. In this case, one see that there is  
1811 a maximum at  $\Delta_{peak} \sim -10$  ADC. As mentioned previously, this is also the value of the  
1812 mean of the peak asymmetry distribution. In fact, it is expected that our filter favours  
1813 the signal peaks with the most common values of the peak asymmetry, as this was one  
1814 of the features I target in our filter coefficient optimisation through the parameter  $\delta$ .

1815 These results suggest that events with poorer values of the mean S/N, usually  
1816 associated to non-favourable track orientations, tend to have smaller values of the mean  
1817 peak asymmetry (in absolute value). Nonetheless, because our matched filters have  
1818 been optimised to account for these asymmetries, the improvement on the S/N for these  
1819 events is sizeable if not better than the one for events which already had a high S/N.

### 1820 4.5.3 Hit sensitivity

1821 One of the advantages of the matched filter, directly related to increasing the S/N, is  
1822 the capability of picking hits that before fell below the threshold. For instance, Fig. 4.17  
1823 shows the raw ADC data from an example event (electron,  $E_k = 100$  MeV) with the  
1824 produced true hits superimposed (black boxes), together with the hits produced by the

## CHAPTER 4. MATCHED FILTER APPROACH TO TRIGGER PRIMITIVES

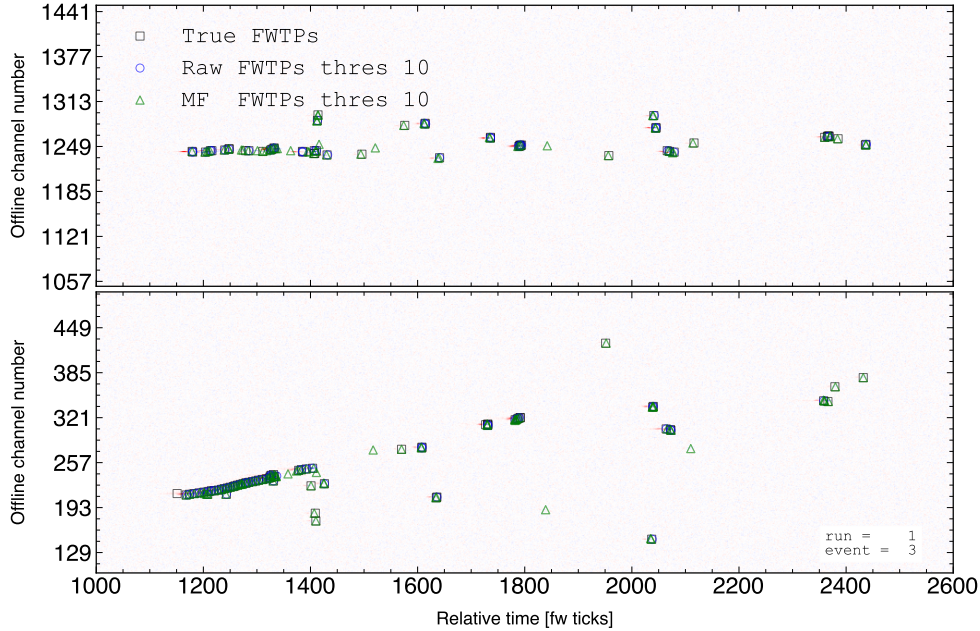


**Figure 4.17:** Raw data display in the plane time (in firmware ticks) vs. offline channel number for an  $E_k = 100$  MeV electron event. The produced true hits are superimposed (black boxes) as well as the hits coming from the standard hit finder chain (blue circles) and the hit finder using the matched filter (green triangles).

standard hit finder chain (blue circles), i.e. using the current FIR filter, and the hits obtained using the matched filters (green triangles). Both the standard and the matched filter hit finders were run with a threshold of 10 ADC. Notice that the standard hits match well the true ones at the initial part of the event (where we have a track-like object), but they miss most of the hits produced by the EM shower at later times. On the other hand, the hits produced with the matched filter have a better agreement with the true hits even for the more diffuse shower activity.

Notwithstanding that now I get more hits with this combination of matched filter and low threshold as a results of the enhancement of the signal peaks relative to the noise level, it is also true that I pick some spurious hits not related to any real activity if one lowers the thresholds too much. Therefore, some optimisation of the threshold is needed. Basically one will need to make a trade-off between precision and sensitivity.

Having this in mind, I tried to compare the produced hits one gets from the standard hit finder and the ones resulting from applying the matched filter with the true hits.

## 4.5. USING SIMULATED SAMPLES

1839 By running the hit finders on our samples with different values of the threshold one  
1840 can understand, for instance, how low one can set the threshold without getting mostly  
1841 spurious hits and then evaluate the gains obtained from this.

1842 Because now I am also interested in seeing how the hit sensitivity changes with the  
1843 energy, I prepared new isotropic samples with the same types of particles as before  
1844 (muons, electrons, protons and neutral pions) but with a flat kinetic energy distribution  
1845 ranging from 5 to 100 MeV.

1846 In order to estimate the hit sensitivity, given a certain sample, one needs to recover  
1847 the set of true hits to be able to compare these with the ones produced. To do so,  
1848 a modification in the procedure I was using to extract the raw waveforms is needed.  
1849 For this kind of study I run the detector simulation in two steps, first I produce the  
1850 waveforms without noise and extract them in the same format I used for the raw data,  
1851 then the noise is added and the noisy waveforms are then written to a file as well.

1852 To have a better comparison between the true hits and the ones produced from  
1853 the raw waveforms after applying the two filters, I applied also the FIR filter and the  
1854 matched filters to the noiseless waveforms and then I run the hit finder with a minimal  
1855 threshold (in this case I used 1 ADC) on these noiseless filtered waveforms. In this way  
1856 I generated two sets of true hits, I will refer to them as standard true hits (with the  
1857 current/default FIR filter) and matched filter true hits respectively. This allows a more  
1858 precise matching between the different groups of hits produced, as it will account for  
1859 any delays and distortions introduced by the FIR and the matched filters.

1860 In the case of the raw waveforms (with noise), I run the hit finder on them, with  
1861 different values of the threshold, after applying either the FIR or the matched filters. I  
1862 will name them simply standard hits and matched filter hits respectively. Then, I match  
1863 the generated hits to the true hits (the standard hits with the standard true hits and  
1864 the matched filter hits with the matched filter true hits). The matching is performed by  
1865 comparing the channel number and the timestamp of the hits. To count as a match,  
1866 I require that all hits with the same channel number and timestamp have overlapping  
1867 hit windows, i.e. the time windows between their hit end and hit start times need to

## CHAPTER 4. MATCHED FILTER APPROACH TO TRIGGER PRIMITIVES

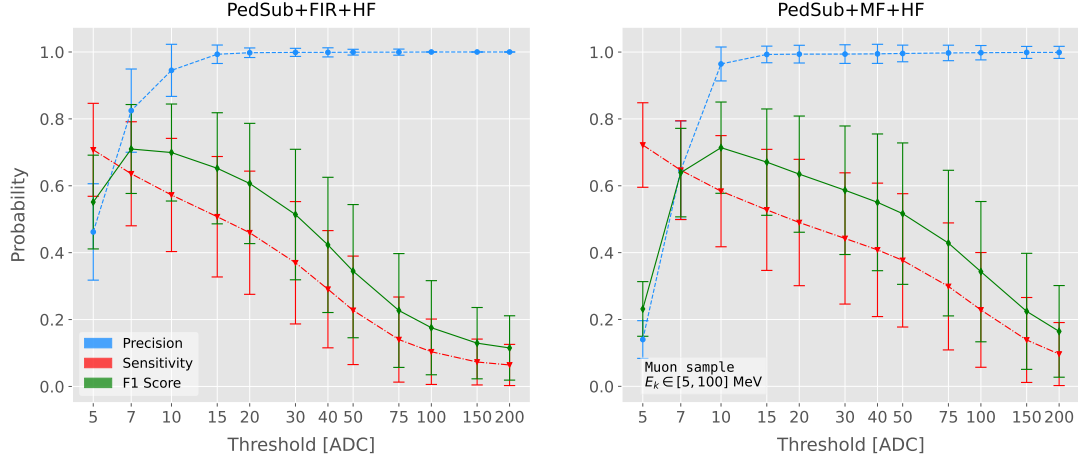


**Figure 4.18:** Dependence of the precision (blue), sensitivity (red) and  $F_1$  (green) scores on the threshold values used in the hit finder, for the FIR (left panel) and matched filter (right panel) cases. The results were obtained after matching the hits to the true hits in the case of the isotropic muon sample with kinetic energy in the range 5 to 100 MeV, taking only into account the induction plane channels. The points represent the mean value while the error bars indicate one standard deviation around that mean value.

overlap. If more than one hit in one of the groups have hit overlap with the same hit in the other group I only count the hit with closer hit peak time value.

The generation of the samples, the procedure to produce the standard hits (with the default FIR filter) and matched filter hits and the matching of these with the true hits is described in detail in App. ??.

To quantify the performance of the two hit finder approaches, I use a classical method from statistical classification known as confusion matrix [111]. This is basically a way of sorting the outputs of a binary classifier, considering the true values of the classification and the predicted values. It divides the outputs in four categories: true positive (TP, both true and predicted values are 1), false negative (FN, true value is 1 but predicted is 0), false positive (FP, true value is 0 but predicted is 1) and true negative (TN, both true and predicted values are 0)).

The contents of the confusion matrix allow us to compute other derived scores to judge the performance of our classifiers. In this study, I will make use of three of these

## 4.5. USING SIMULATED SAMPLES

1882 metrics, namely the precision or positive predictive value:

$$\text{PPV} = \frac{\text{TP}}{\text{TP} + \text{FP}}, \quad (4.22)$$

1883 the sensitivity or true positive rate:

$$\text{TPR} = \frac{\text{TP}}{\text{TP} + \text{FN}}, \quad (4.23)$$

1884 and the  $F_1$  score [112]:

$$F_1 = \frac{2\text{TP}}{2\text{TP} + \text{FP} + \text{FN}}, \quad (4.24)$$

1885 which is the harmonic mean of the precision and the sensitivity.

1886 In our specific case I am not going to make use of the true negative value, as its  
1887 definition in this context can be ambiguous because one does not have clear instances in  
1888 the classification process. This way, I will only count the number of true positives as the  
1889 total amount of hits I can match between true and raw populations, the number of false  
1890 negatives will be the number of missing true hits and the false positive the number of  
1891 hits which do not match any true hit.

1892 In Fig. 4.18 I show the precision (blue), sensitivity (red) and  $F_1$  (green) scores I  
1893 obtained for different values of the threshold used in the hit finder for the case of the  
1894 muon sample. Because the matched filters are only applied to induction channels, I only  
1895 consider here hits coming from the U and V planes. The panel on the left corresponds  
1896 to the scores I got when I ran the hit finder on the FIR filtered waveforms, whereas the  
1897 right panel contains the scores for the matched filter case. The points are centered at  
1898 the threshold value used and represent the mean value obtained for each score using all  
1899 the generated events, while the error bars indicate one standard deviation around the  
1900 mean value.

1901 One can see that the precision for the matched filter case is lower when the thresholds  
1902 are very low, as the noise baseline is slightly amplified, but then rises to high values  
1903 quicker than for the FIR case. The other difference one can spot is that the sensitivity

## CHAPTER 4. MATCHED FILTER APPROACH TO TRIGGER PRIMITIVES

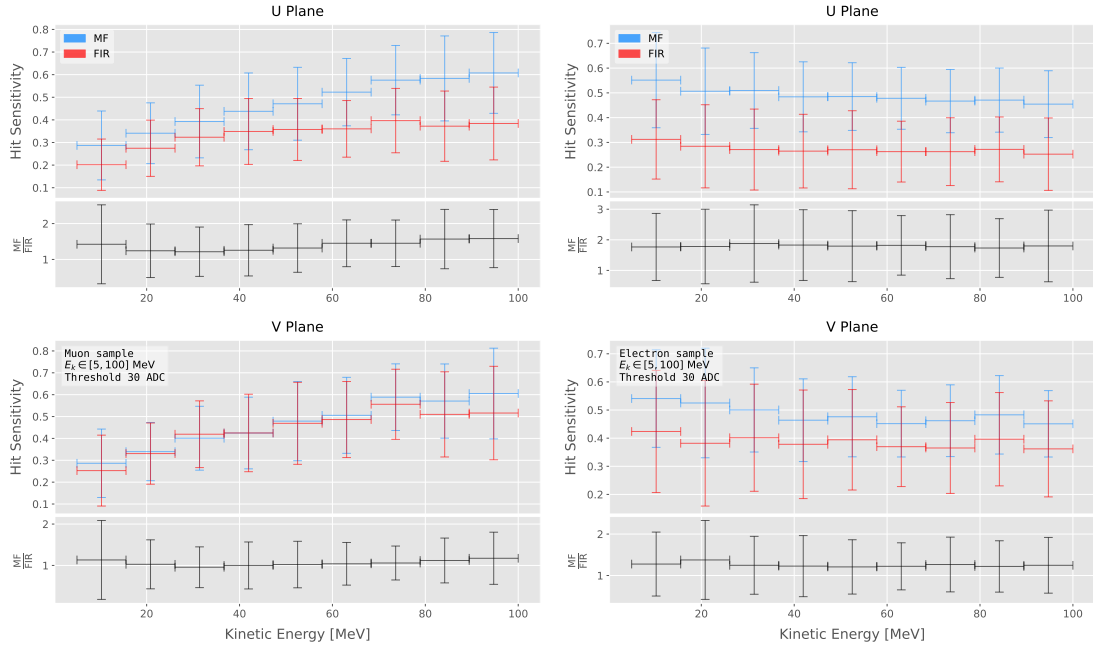


**Figure 4.19:** Dependence of the averaged hit sensitivity on the kinetic energy of the events for the matched filter (blue) and standard (red) hits, for the case of the muon (left panel) and electron (right panel) samples, separated between U (top plots) and V (bottom plots) induction wire planes. The top subplots contain the hit sensitivities for the two hit finder alternatives, while the bottom subplots show the ratio between the two. The horizontal lines sit at the mean value and represent the size of the energy bins, while the vertical error bars indicate one standard deviation around that mean value.

in the FIR case starts dropping faster at around the same threshold values where the precision stabilizes around 1, while in contrast for the matched filter this rapid decrease starts at higher threshold values. A similar scan for the same thresholds was performed for the electron sample in the same energy range, yielding similar results.

In Fig. 4.19 I show the averaged hit sensitivity versus the kinetic energy of the events, both for the matched filter hits (blue) and the standard hits (red). The left panel corresponds to the muon sample, whereas the one on the right corresponds to the electron sample, both with kinetic energies between 5 and 100 MeV. In each panel the top plot corresponds to hits in the U plane, while the bottom plot contains the same information for the V plane. Each plot contains two subplots, the one on the top shows the hit sensitivity values for the matched filter and standard hits separate, while the bottom subplot depicts the ratio between the matched filter and standard sensitivities.

## 4.5. USING SIMULATED SAMPLES

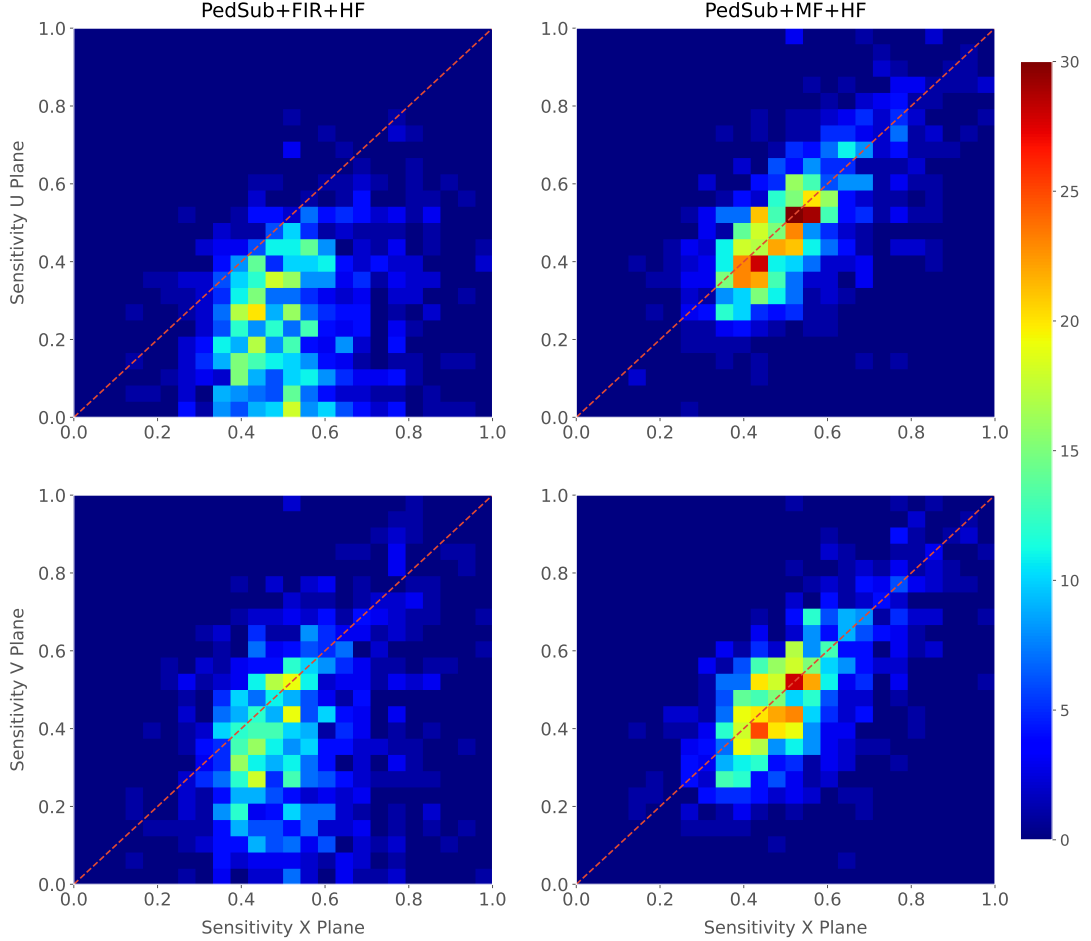


**Figure 4.20:** Distributions of the hit sensitivity in the  $U$  (top panels) and  $V$  (bottom panels) planes versus the hit sensitivity in the  $X$  plane, both for the standard hits (left panels) and the matched filter hits (right panels), in the case of the electron sample and a threshold of 30 ADC.

1916 The horizontal lines are placed at the mean value obtained in the fit and represent the  
 1917 width of the  $E_k$  bins used, while the vertical error bars indicate one standard deviation  
 1918 around that mean value. In both cases the threshold used was 30 ADC, as I required  
 1919 the precision to be higher than 0.99 for both matched filter and standard cases.

1920 One can see that, in general, the improvements are better for the  $U$  than for the  $V$   
 1921 plane. While for the  $U$  channels I achieved a mean improvement of 50% and 80% for  
 1922 muons and electrons respectively, the improvement in the  $V$  plane is stalled at 10% and  
 1923 25%. Nevertheless, if I look at the sensitivities for the matched filter hits in both planes  
 1924 one can see these have similar mean values for each energy bin, while on the contrary

## CHAPTER 4. MATCHED FILTER APPROACH TO TRIGGER PRIMITIVES

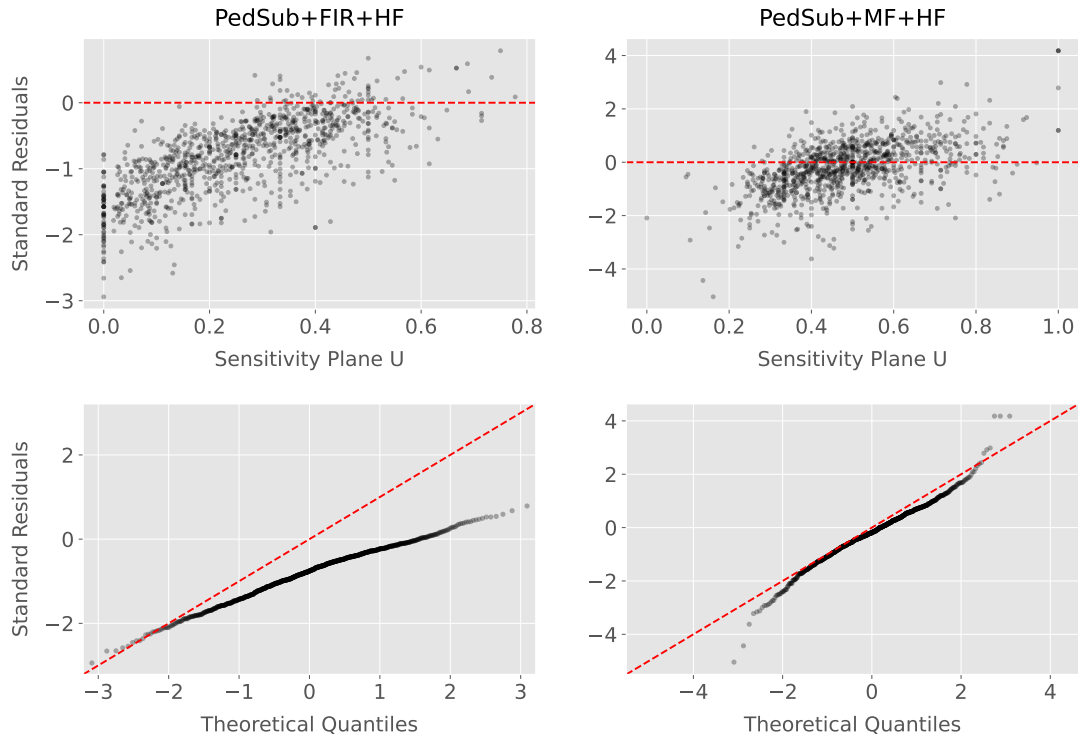


**Figure 4.21:** Top panels: standard residual plots of the hit sensitivities between the  $X$  and  $U$  planes. Bottom panels: quantile-quantile plots of the hit sensitivity standard residuals between the  $X$  and  $U$  planes. In all cases, the left panel corresponds to the standard hits while the right panel represents the matched filter case, all from the electron sample with a 30 ADC threshold.

for the standard hits the sensitivity remains relatively high for the  $V$  plane. This way, it looks there was a less significant gain because the hit sensitivity was already high.

Another interesting observation is the different behaviors for muons and electrons. While hit sensitivity for muons grows significantly with energy, in the case of electrons this slightly decreases the higher the kinetic energy of the event is. In any case, when it comes to the improvement on the sensitivities, this remains almost constant in all cases.

Furthermore, we can look at how the concurrence of hits between the different wire planes has changed. For any given event, I expect to have a similar number of hits in the three planes. As the ionisation electrons need to cross the  $U$  and  $V$  planes prior to reach the collection plane  $X$  they will induce current in those wire planes. A way to check the concurrence of hits across planes is looking at the relation between the hit sensitivities for each individual event. One cannot expect the sensitivities to be exactly equal across

## 4.5. USING SIMULATED SAMPLES

1937 planes, but ideally they should be normally distributed around the diagonal.

1938 Fig. 4.20 shows the hit sensitivity in the U (top panels) and V (bottom panels)  
1939 planes versus the hit sensitivity in the X plane, for the case of the standard hits (left  
1940 panels) and the matched filter hits (right panels). All plots were generated for the  
1941 electron sample and a threshold of 30 ADC. From these one can see a clear trend,  
1942 when I use the standard hit finder chain the sensitivities in the induction planes are  
1943 systematically lower than the hit sensitivity in the X plane, i.e. most of the points sit  
1944 below the diagonal (red dashed line). In contrast, when the matched filters are applied,  
1945 the majority of the events are distributed around the diagonal. This points out that the  
1946 concurrence of hits across planes has improved.

1947 To exemplify the improvement I obtained, one can consider the residuals of the hit  
1948 sensitivities for the X and U planes. Assuming the diagonal hypothesis, i.e. given a  
1949 dataset of the form  $(x, y)$  for any  $x$  I take the predicted  $y$  value to be equal to the value  
1950 of  $x$ , I can compute the standard residuals for the hit sensitivities in U given the ones for  
1951 X. In Fig. 4.21 (top panels) I show these standard residuals against the corresponding  
1952 values of the hit sensitivity in the U plane, for our electron sample with kinetic energy  
1953 between 5 and 100 MeV. If I compare the scatter points in the case of the standard  
1954 hits (left panel) and the matched filter hits (right panel), I see that the residuals of the  
1955 standard hit finder case follow a certain pattern and their mean deviates from 0.

1956 To see clearly if the residuals are normally distributed, in Fig. 4.21 (bottom panels)  
1957 I plot the corresponding quantile-quantile plot for both the standard (left panel) and  
1958 matched filter (right panel) standard residuals. One can clearly see that the points for  
1959 the standard case follow a strongly non-linear pattern, suggesting that the residuals  
1960 do not follow a normal distribution. In contrast, for the matched filter hits the points  
1961 conform to a roughly linear path, implying that in this case the normality condition is  
1962 fulfilled.

1963 All these results hint at the fact that the concurrence of hits across the wire planes  
1964 can be strengthened by applying the matched filters.



## 1966 DM searches with neutrinos from the Sun

### 1967 5.1 Motivation

1968 The idea of detecting neutrino signals coming from the Sun’s core to probe DM is not  
1969 new. The main focus of these searches has usually been high-energy neutrinos originated  
1970 from DM annihilations into heavy particles [113–116], although recent studies have  
1971 proposed to look at the low-energy neutrino flux arising from the decay of light mesons  
1972 at rest in the Sun [117–120] previously thought undetectable.

1973 In this chapter I try to demonstrate the capability of DUNE to constrain different  
1974 DM scenarios. I used the neutrino fluxes arising from DM annihilations in the core  
1975 of the Sun to compute the projected limits that DUNE would be able to set on the  
1976 annihilation rates in the Sun and the DM scattering cross sections.

### 1977 5.2 Gravitational capture of DM by the Sun

1978 The Sun and the centre of the Earth are possible sources of DM annihilations, specially  
1979 interesting because of their proximity. Their gravitational attraction ensured the capture  
1980 of DM from the local halo through repeated scatterings of DM particles crossing them.  
1981 Only neutrinos produced from DM annihilations can escape the dense interior of these  
1982 objects. Therefore, neutrino telescopes are the most useful experimental layouts to  
1983 pursue DM searches from their cores.

1984 The neutrino flux from DM annihilations inside the Sun depends on the DM capture

## CHAPTER 5. DM SEARCHES WITH NEUTRINOS FROM THE SUN

1985 rate, which is proportional to the DM scattering cross section, and the annihilation rate,  
 1986 which is proportional to the velocity-averaged DM annihilation cross-section. The total  
 1987 number of DM particles inside the Sun follows the Boltzmann equation [117]:

$$\frac{dN_{DM}}{dt} = C_\odot - A_\odot N_{DM}^2, \quad (5.1)$$

1988 where  $C_\odot$  and  $A_\odot$  are the total Sun DM capture and annihilation rates respectively.  
 1989 In this expression I neglected the evaporation term, proportional to  $N_{DM}$ , which only  
 1990 contribute for  $m_{DM} \lesssim 4$  GeV [121]. As the current threshold of neutrino telescopes  
 1991 is a few GeV, this region falls below the probed range but can be important in future  
 1992 low-energy projects.

1993 This equation has an equilibrium solution:

$$N_{DM}^{eq} = \sqrt{\frac{C_\odot}{A_\odot}}, \quad (5.2)$$

1994 which represents the amount of DM inside the Sun if the capture and annihilation have  
 1995 reached equilibrium. As the Sun is approximately 4.6 Gyr old, it is usually assumed that  
 1996 equilibrium has been achieved. Therefore, the anomalous neutrino flux from the Sun  
 1997 would only depend on the DM scattering cross section, enabling us to set limits on this  
 1998 quantity. If one does not assume equilibrium, some assumptions on the DM annihilation  
 1999 cross section are necessary to extract predictions from neutrino signals.

2000 Here, I am going to consider three possible scenarios for the DM interactions: DM  
 2001 scattering off electrons, spin-dependent (SD) and spin-independent interactions off nuclei.  
 2002 For the case of these last two, the cross sections will be given in terms of the SD and  
 2003 SI elastic scattering DM cross section off protons (assuming that DM interactions off  
 2004 protons and neutrons are identical),  $\sigma_p^{\text{SD}}$  and  $\sigma_p^{\text{SI}}$ , as [2, 117]:

$$\sigma_i^{\text{SD}} = \left( \frac{\tilde{\mu}_{A_i}}{\tilde{\mu}_p} \right)^2 \frac{4(J_i + 1)}{3J_i} |\langle S_{p,i} \rangle + \langle S_{n,i} \rangle|^2 \sigma_p^{\text{SD}}, \quad (5.3)$$

$$\sigma_i^{\text{SI}} = \left( \frac{\tilde{\mu}_{A_i}}{\tilde{\mu}_p} \right)^2 A_i^2 \sigma_p^{\text{SI}}, \quad (5.4)$$

## 5.2. GRAVITATIONAL CAPTURE OF DM BY THE SUN

2005 where  $\tilde{\mu}_{A_i}$  is the reduced mass of the DM-nucleus  $i$  system,  $\tilde{\mu}_p$  is the reduced mass of  
 2006 the DM-proton system,  $A_i$  and  $J_i$  the mass number and total angular momentum of  
 2007 nucleus  $i$  and  $\langle S_{p,i} \rangle$  and  $\langle S_{n,i} \rangle$  the expectation value of the spins of protons and neutrons  
 2008 averaged over all nucleons, respectively (see Ref. [122] for a review on spin expectation  
 2009 values).

2010 Since the Sun is mainly composed of Hydrogen, the capture of DM from the halo  
 2011 is expected to occur mainly through spin-dependent scattering. However, since the  
 2012 spin-independent cross section is proportional to the square of the atomic mass, heavy  
 2013 elements can contribute to the capture rate (even though they constitute less than 2%  
 2014 of the mass of the Sun). Heavy elements can also contribute to the spin-dependent cross  
 2015 section if the DM has also momentum-dependent interactions.

2016 DM particles can get captured by the Sun if after repeated scatterings off solar  
 2017 targets their final velocity is lower than the escape velocity of the Sun. In the limit of  
 2018 weak cross sections, this capture rate can be approximately written as [2]:

$$C_{\odot}^{\text{weak}} = \sum_i \int_0^{R_{\odot}} dr 4\pi r^2 \int_0^{\infty} du_{\chi} \frac{\rho_{\chi}}{m_{\chi}} \frac{f_{v_{\odot}}(u_{\chi})}{u_{\chi}} \omega(r) \int_0^{v_e(r)} dv R_i^-(\omega \rightarrow v) |F_i(q)|^2, \quad (5.5)$$

2019 where the summation extends over all possible nuclear targets. In this expression,  $R_{\odot}$   
 2020 is the radius of the Sun,  $\rho_{\chi}$  is the local DM density,  $m_{\chi}$  the mass of the DM particle,  
 2021  $f_{v_{\odot}}(u_{\chi})$  the DM velocity distribution seen from the Sun's reference frame,  $R_i^-(\omega \rightarrow v)$   
 2022 is the differential rate at which a DM particle with velocity  $v$  scatters a solar target of  
 2023 mass  $m_i$  to end up with a velocity  $\omega$  and  $|F_i(q)|$  is the nuclear form factor of target  $i$ .

2024 The differential scattering rate takes a rather simple form when considering velocity-  
 2025 independent and isotropic cross sections. In that case, this quantity is given by [2, 123]:

$$R_i^-(\omega \rightarrow v) = \frac{2}{\sqrt{\pi}} \frac{\mu_{i,+}^2}{\mu_i} \frac{v}{\omega} n_i(r) \sigma_i \left[ \chi(-\alpha_-, \alpha_+) + \chi(-\beta_-, \beta_+) e^{\mu_i(\omega^2 - v^2)/u_i^2(r)} \right], \quad (5.6)$$

## CHAPTER 5. DM SEARCHES WITH NEUTRINOS FROM THE SUN

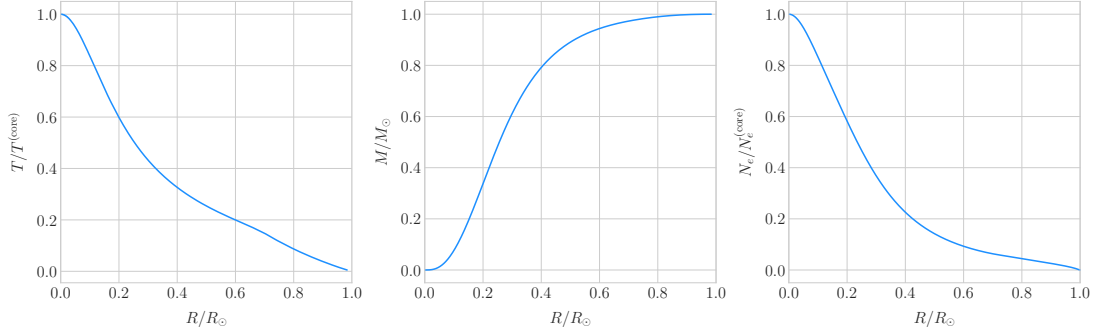


**Figure 5.1:** Input solar parameters used in our capture rate computation as functions of the Sun's radius, from left to right: temperature (with respect to the temperature at the core), mass (in solar masses) and electron number density (with respect to the electron density at the core). All quantities shown correspond to the standard solar model BS2005-OP [1].

2026 where  $\mu_i$  is the ratio between the DM mass and the mass of target  $i$ ,  $\mu_{i,\pm}$  is defined as:

$$\mu_{i,\pm} \equiv \frac{\mu_i \pm 1}{2}, \quad (5.7)$$

2027  $n_i(r)$  is the density profile of target  $i$  in the solar medium,  $u_i(r)$  is the most probable  
2028 velocity of target  $i$  given by:

$$u_i(r) = \sqrt{\frac{2T_\odot(r)}{m_i}}, \quad (5.8)$$

2029 where  $T_\odot(r)$  is the temperature of the Sun, the quantities  $\alpha_\pm$  and  $\beta_\pm$  are defined as:

$$\alpha_\pm \equiv \frac{\mu_{i,+}v \pm \mu_{i,-}\omega}{u_i(r)}, \quad (5.9)$$

$$\beta_\pm \equiv \frac{\mu_{i,-}v \pm \mu_{i,+}\omega}{u_i(r)}, \quad (5.10)$$

2030 and the function  $\chi(a, b)$  is a Gaussian integral of the form:

$$\chi(a, b) \equiv \int_a^b dx e^{-x^2}. \quad (5.11)$$

2031 Finally, if one assumes the DM halo velocity distribution in the galactic rest frame  
2032 to be a Maxwell-Boltzmann distribution, one can write the halo velocity distribution for

## 5.2. GRAVITATIONAL CAPTURE OF DM BY THE SUN

2033 an observer moving at the speed of the Sun with respect to the DM rest frame as:

$$f_{v_\odot}(u_\chi) = \sqrt{\frac{3}{2\pi}} \frac{u_\chi}{v_\odot v_d} \left( e^{-\frac{3(u_\chi - v_\odot)^2}{2v_d^2}} - e^{-\frac{3(u_\chi + v_\odot)^2}{2v_d^2}} \right), \quad (5.12)$$

2034 where:

$$\omega^2 = u_\chi^2 + v_e(r)^2, \quad (5.13)$$

2035 is the DM velocity squared,  $v_\odot$  the relative velocity of the Sun from the DM rest frame  
2036 and  $v_d \simeq \sqrt{3/2}v_\odot$  the velocity dispersion.

2037 For the case of strong scattering cross section, Eq. (5.5) ceases to be valid, as it  
2038 escalates indefinitely with the cross section. In that limit, the capture rate saturates to  
2039 the case where the probability of interaction is equal to one, which can be written as:

$$C_\odot^{\text{geom}} = \pi R_\odot^2 \left( \frac{\rho_\chi}{m_\chi} \right) \langle v \rangle \left( 1 + \frac{3}{2} \frac{v_e^2(R_\odot)}{v_d^2} \right) \xi(v_\odot, v_d), \quad (5.14)$$

2040 where  $v_d = \sqrt{8/3\pi}v_\odot$  is the mean velocity in the DM rest frame and the factor  $\xi(v_\odot, v_d)$   
2041 accounts for the suppression due to the motion of the Sun:

$$\xi(v_\odot, v_d) = \frac{v_d^2 e^{-\frac{3v_\odot^2}{2v_d^2}} + \sqrt{\frac{\pi}{6}} \frac{v_d}{v_\odot} (v_d^2 + 3v_e^2(R_\odot) + 3v_\odot^2) \operatorname{Erf} \left( \sqrt{\frac{3}{2}} \frac{v_\odot}{v_d} \right)}{2v_d^2 + 3v_e^2(R_\odot)}. \quad (5.15)$$

2042 Having these into account, one can write the total capture rate as a combination of  
2043 both contributions, allowing a smooth transition between the two, as:

$$C_\odot = C_\odot^{\text{weak}} \left( 1 - e^{C_\odot^{\text{geom}} / C_\odot^{\text{weak}}} \right). \quad (5.16)$$

2044 I computed the capture rate from Eq. (5.16) in the case of interactions with  
2045 electrons. To do so, I used the standard solar model BS2005-OP [1]. Fig. 5.1 shows the  
2046 three parameters from the solar model that are needed for the computation, the solar  
2047 temperature (left panel), mass (central panel) and electron density (right panel) profiles.

2048 For the case of the interactions off nuclei, the computations are more convoluted

## CHAPTER 5. DM SEARCHES WITH NEUTRINOS FROM THE SUN

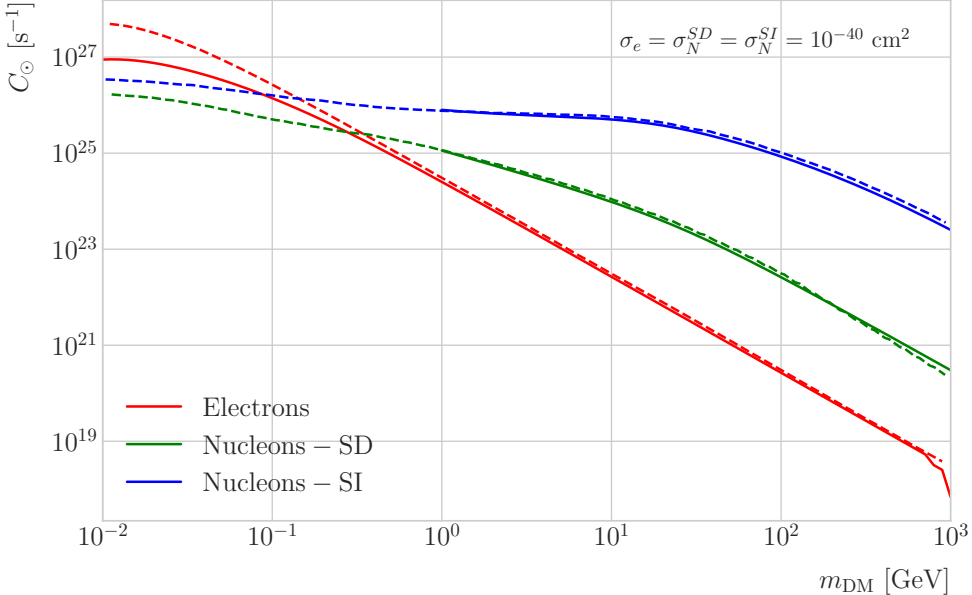


**Figure 5.2:** Capture rates as a function of the DM mass for the DM-electron interactions (red lines), SD DM-nucleons interactions (green lines) and SI DM-nucleons interactions (blue lines). Solid lines represent the values computed in this work while the dashed lines are the one given in Ref. [2]. All the rates are shown for a choice of scattering cross section of  $\sigma_i = 10^{-40} \text{ cm}^2$ .

as one needs to add up the contributions of the different most abundant nuclei in the Sun. Also, in contrast to the electron scenario where the form factor is trivially  $|F_e(q)|^2 = 1$ , for any nucleus  $i$  one would need to consider some appropriate nuclear density distribution (either a Gaussian approximation, a Woods-Saxon distribution, etc) which would complicate the calculations even further.

That is the reason why, at this stage of our study, I decided to take an alternative approach to the computation of the DM-nucleus capture rates. I used the **DarkSUSY** software, that allows us to compute these quantities performing a full numerical integration over the momentum transfer of the form factors. The default standard solar model used by **DarkSUSY** is BP2000<sup>1</sup> [124].

In Fig. 5.2 I show the results I obtained for the capture rates, for the case of interactions off electrons (red solid line), SD (green solid line) and SI (blue solid line)

<sup>1</sup>This is what they say in their manual, but I fear it is somewhat outdated. It appears to me this model is relatively old and do not see why they are not using others like [1]. Maybe one can double-check in the code to make sure.

## 5.2. GRAVITATIONAL CAPTURE OF DM BY THE SUN

interactions of nucleons. In all cases I used a value of the scattering cross sections of  $\sigma_i = 10^{-40} \text{ cm}^2$ . Note here one of the limitations of the **DarkSUSY** approach, one can not extend the computation below  $m_{\text{DM}} = 1 \text{ GeV}$ . Nevertheless, this is not something to worry about in this case, as I will discuss next. As a comparison, I added also the values computed in Ref. [2] (same color scheme, dashed lines). One can see there is good agreement between these and the **DarkSUSY** computation of the SD and SI interactions for  $m_{\text{DM}} \geq 1 \text{ GeV}$ . In this regime their computations also matches quite well our result for the electron capture rate. However, these start to differ significantly below  $m_{\text{DM}} = 1 \text{ GeV}$ , being their estimate up to a factor of 5 bigger than ours for low masses.

Let us comment briefly about the assumption I made before about not including an evaporation term in the Boltzmann equation. If I include this term in the equation (which will be proportional to the number of DM particles) the equilibrium solution takes the form:

$$N_{\text{DM}}^{\text{eq}} = \sqrt{\frac{C_{\odot}}{A_{\odot}}} \frac{1}{\kappa + \frac{1}{2} E_{\odot} \tau_{\text{eq}}}, \quad (5.17)$$

where  $E_{\odot}$  is the total evaporation rate,  $\tau_{\text{eq}}$  is the equilibrium time in the absence of evaporation:

$$\tau_{\text{eq}} = \frac{1}{\sqrt{C_{\odot} A_{\odot}}}, \quad (5.18)$$

and  $\kappa$  is defined as:

$$\kappa \equiv \sqrt{1 + \left( \frac{E_{\odot} \tau_{\text{eq}}}{2} \right)^2}. \quad (5.19)$$

Now, it is easy to proof that in case evaporation dominates  $\kappa \gg 1$  and therefore:

$$N_{\text{DM}}^{\text{eq}} \simeq \frac{C_{\odot}}{E_{\odot}}. \quad (5.20)$$

In contrast, if evaporation is irrelevant  $\kappa \simeq 1$  and one recovers Eq. (5.2).

In this way, one can define the evaporation mass as the mass for which the number of DM particles in equilibrium approaches Eq. (5.20) at 10% level:

$$\left| N_{\text{DM}}^{\text{eq}}(m_{\text{evap}}) - \frac{C_{\odot}(m_{\text{evap}})}{E_{\odot}(m_{\text{evap}})} \right| = 0.1 N_{\text{DM}}^{\text{eq}}(m_{\text{evap}}). \quad (5.21)$$

## CHAPTER 5. DM SEARCHES WITH NEUTRINOS FROM THE SUN

2081 This can be regarded as the minimum testable mass one can reach using the annihilation  
2082 products of the DM in the Sun.

2083 It was reported in Ref. [2] that, in the case of both SD and SI DM interactions  
2084 off nuclei, this value ranges from 2 to 4 GeV depending on the specific scattering  
2085 cross section value, compatible with the usual assumptions in the literature. What is  
2086 interesting is the case of the electron capture. It was found that, when one applies a  
2087 cutoff in the velocity distribution of the DM trapped in the Sun slightly below the escape  
2088 velocity, the evaporation mass for the DM-electron interaction decreases remarkably. For  
2089 a moderate choice of  $v_c(r) = 0.9v_e(r)$  one gets an evaporation mass of around 200 to  
2090 600 MeV. This possibility opens a region of the parameter space that could be tested  
2091 with neutrino detectors.

### 2092 5.3 Neutrino flux from DM annihilations

2093 When WIMPs annihilate inside the Sun a flux of high-energy neutrinos is expected from  
2094 heavy quarks, gauge bosons and  $\tau^+\tau^-$  final states, which decay before losing energy in  
2095 the dense solar medium, as they will produce a continuum spectra up to  $E_\nu \sim m_\chi$  (in  
2096 the case of direct annihilation to neutrinos one would have a line at  $E_\nu = m_\chi$ ) [118].  
2097 This kind of signal has been extensively studied in the literature, allowing to put strong  
2098 limits on the SD WIMP-proton cross section for large  $m_\chi$ . However, the number of  
2099 high-energy neutrinos per WIMP annihilation is small and the spectrum depends on the  
2100 unknown final state. Moreover, background rejection is easier for large  $m_\chi$  but neutrinos  
2101 with  $E_\nu \gtrsim 100$  GeV are significantly attenuated by interactions in the Sun.

2102 Nevertheless, most WIMP annihilation final states eventually produce a low-energy  
2103 neutrino spectrum. In this case one does not just consider the more massive final states  
2104 but also annihilations into  $e^+e^-$ ,  $\mu^+\mu^-$  and light quarks [117]. In particular, light  
2105 mesons would be produced and stopped in the dense medium, thus decaying at rest and  
2106 producing a monoenergetic neutrino signal. The decay-at-rest of kaons will produce  
2107 a  $E_\nu = 236$  MeV  $\nu_\mu$  while in the case of pions one would have a  $E_\nu = 29.8$  MeV  $\nu_\mu$ .

## 5.4. COMPUTING LIMITS FROM SOLAR NEUTRINO FLUXES

2108 In practice only  $K^+$  and  $\pi^+$  contribute to these signals, as  $K^-$  and  $\pi^-$  are usually  
 2109 Coulomb-captured in an atomic orbit and get absorbed by the nucleus. There is also a  
 2110 low-energy neutrino signal coming from muon decays, which are produced in kaon or  
 2111 pion decays, leptonic decays of other hadrons and heavy leptons or even directly from  
 2112 WIMP annihilations, which can decay at rest and contribute to the previous low-energy  
 2113 neutrino flux with a well known spectrum below 52.8 MeV.

2114 These monoenergetic MeV neutrinos were previously considered undetectable but,  
 2115 due to the large yield, the known spectra and the modern advances in the detector  
 2116 technology, these low-energy neutrino flux can be a good probe of the SD WIMP-proton  
 2117 cross-section in standard solar WIMP capture scenario, as it is sensitive to low WIMP  
 2118 masses and insensitive to the particular final state. A good place to look for these signals  
 2119 are next-generation neutrino experiments such as DUNE.

## 2120 5.4 Computing limits from solar neutrino fluxes

2121 In order to use the neutrino fluxes from DM annihilations in the Sun, the first thing I  
 2122 need to do is to determine the expected number of atmospheric background events, for  
 2123 a given exposure, after directionality selection has been applied. I can write this number  
 2124 as:

$$N_B = \eta_B \int d\Omega \int_{E_{min}}^{E_{max}} dE_\nu \frac{d^2\Phi_{atm}^\mu}{dE_\nu d\Omega} \times \left( A_{eff}^{(\mu)}(E_\nu) T \right), \quad (5.22)$$

2125 where  $\eta_B$  is the background efficiency,  $E_{min}$  and  $E_{max}$  the minimum and maximum  
 2126 energies to integrate over,  $d^2\Phi_{atm}^\mu/dE_\nu d\Omega$  the differential flux of atmospheric muon  
 2127 neutrinos,  $A_{eff}^{(\mu)}$  is the effective area of DUNE to muon neutrinos and  $T$  is the exposure  
 2128 time. The effective area can be expressed as the product of the neutrino-nucleus scattering  
 2129 cross section and the number of nuclei in the fiducial volume of the detector. This way  
 2130 for DUNE I can write:

$$A_{eff}^{(\mu)}(E_\nu) = (6.0 \times 10^{-10} \text{ m}^2) \left( \frac{\sigma_{\nu-\text{Ar}}^{(\mu)}(E_\nu)}{10^{-38} \text{ cm}^2} \right) \left( \frac{M_{target}}{40 \text{ kT}} \right), \quad (5.23)$$

## CHAPTER 5. DM SEARCHES WITH NEUTRINOS FROM THE SUN

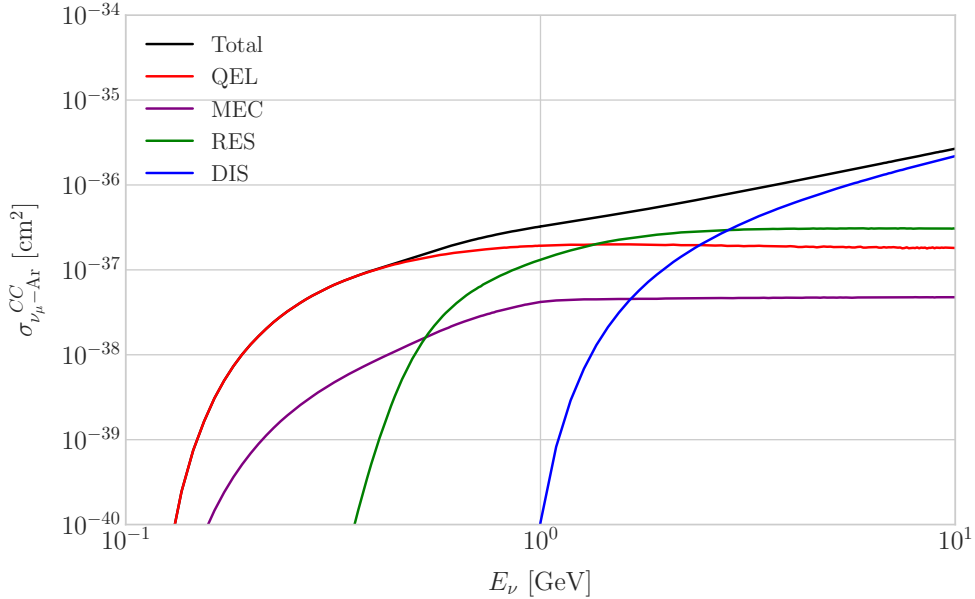


**Figure 5.3:** *NuWro* computed  $\nu_\mu - {}^{40}\text{Ar}$  charged-current scattering cross section as a function of the neutrino energy  $E_\mu$ . The black line shows to the total cross section, whereas the others correspond to the different contributions (in red quasi-elastic scattering, in green resonant pion exchange, in blue deep inelastic scattering and in purple meson exchange current).

where  $\sigma_{\nu_\mu - \text{Ar}}^{(\mu)}$  is the  $\nu_\mu - {}^{40}\text{Ar}$  charged-current scattering cross section. In Fig. 5.3 I show the computed value of this cross section as a function of the neutrino energy  $E_\nu$ , in the range of interest both for the atmospheric background and signal events. It was computed using the *NuWro* Monte Carlo neutrino event generator [125], including the charged-current contributions of the quasi-elastic scattering (red line), resonant pion exchange (green line), deep inelastic scattering (blue line) and meson exchange current (purple line).

The background rejection will depend on the resolution of the detector and the selection one applies on the events. A geometry argument can be used to estimate the maximum background rejection one can achieve in this case, considering one can efficiently discriminate all events coming from a direction different from that of the Sun. In that case, the optimal background efficiency will simply be the relative angular coverage of the Sun. Taking the angular diameter of the Sun as seen from the Earth to

## 5.4. COMPUTING LIMITS FROM SOLAR NEUTRINO FLUXES

2144 be  $0.5^\circ$ , I have:

$$\eta_B^{(opt)} \approx \frac{\pi \left(\frac{0.5}{2}\right)^2}{360 \times 180} \simeq 3.03 \times 10^{-6}. \quad (5.24)$$

2145 This value will give a very optimistic estimate of the number of background events.

2146 However, it can be regarded as an lower limit, as it represents the best case scenario.

2147 In Fig. 5.4 I show the fluxes of atmospheric neutrinos at the Homestake mine during  
2148 solar minimum, taken from Ref. [3]. The values are averaged over the two angular  
2149 directions. In blue I have the flux of muon neutrinos while in red I indicate the flux  
2150 of electron neutrinos. Additionally, the dashed lines correspond to both antineutrino  
2151 species.

2152 Using these values for the muon neutrino and the corresponding total CC cross  
2153 section, one can compute the number of expected background events by integrating over  
2154 the given energy range (as in this case the angular integral is trivial). As for the energy  
2155 range to integrate over, I choose the range for DUNE specified in [85],  $E_{min} = 10^{-1}$  GeV  
2156 and  $E_{max} = 10$  GeV. Taking all these into account, I found the number of background  
2157 events to be:

$$N_B \simeq \eta_B \times (3.827 \times 10^4) \times \left( \frac{\text{exposure}}{400 \text{ kT yr}} \right). \quad (5.25)$$

2158 In order to estimate the sensitivity of DUNE to this kind signal, one can consider a  
2159 hypothetical data set where the number of observed neutrinos is taken to be the expected  
2160 number of background events rounded to the nearest integer,  $N_{obs} = \text{round}(N_B)$  [126].  
2161 Now, if I assume that the number of signal and background events seen by DUNE are  
2162 given by Poisson distributions with means equal to the expected number of signal and  
2163 background events,  $N_S$  and  $N_B$ , one can denote by  $N_S^{90}$  to the number of expected  
2164 signal events such that the probability of having an experimental run with a number of  
2165 events greater than  $N_{obs}$  is 90%. This number can be obtained as the numerical solution  
2166 to the equation:

$$1 - \frac{\Gamma(N_{obs} + 1, N_S^{90} + N_B)}{N_{obs}!} = 0.9, \quad (5.26)$$

2167 where  $\Gamma(x, y)$  is the upper incomplete gamma function.

## CHAPTER 5. DM SEARCHES WITH NEUTRINOS FROM THE SUN

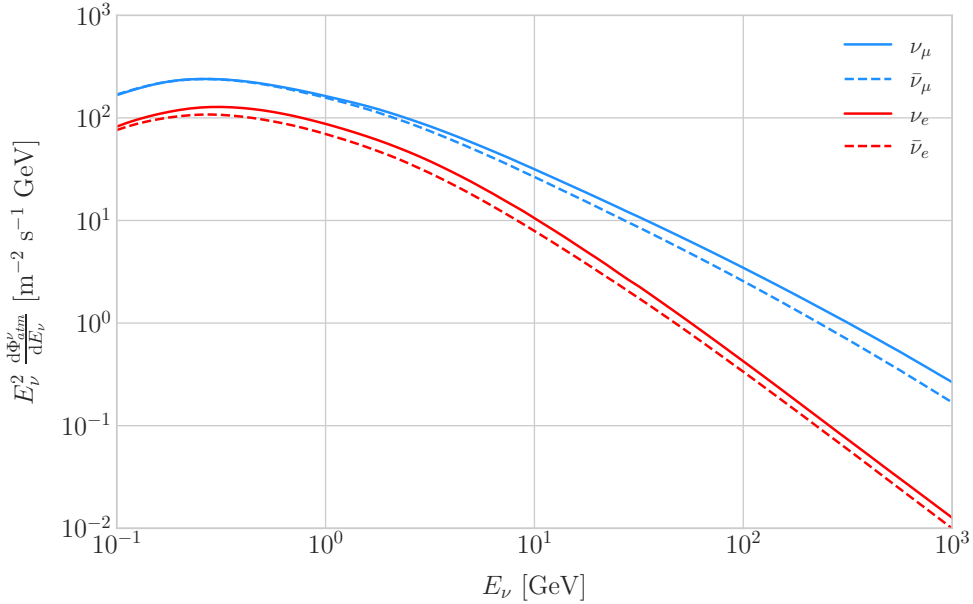


**Figure 5.4:** Expected atmospheric neutrino flux as a function of the neutrino energy  $E_\nu$  at Homestake at solar minimum, taken from Ref. [3]. The blue solid (dashed) line correspond to muon neutrinos (antineutrinos) and the red solid (dashed) line correspond to electron neutrinos (antineutrinos).

2168 The number of signal events is related to the neutrino flux from DM annihilations in  
 2169 a similar way as the background events to the atmospheric neutrino flux. In this case I  
 2170 have:

$$N_S = \eta_S \Gamma_A^{eq} \int_{z_{min}}^{z_{max}} dz \frac{dN_\nu}{dAdN_A dz} \times (A_{eff}^\mu(z)T), \quad (5.27)$$

2171 where  $\eta_S$  is the signal efficiency,  $\Gamma_A^{eq}$  is the total annihilation rate of DM particles at  
 2172 equilibrium,  $\Gamma_A^{eq} = A_\odot (N_{DM}^{eq})^2$ ,  $z_{min}$  and  $z_{max}$  the minimum and maximum relative  
 2173 energies to integrate over (in such a way that  $z_{min,max} \leq E_{min,max}/m_{DM}$  for each  $m_{DM}$ )  
 2174 and  $dN_\nu/dAdN_A dz$  the muon neutrino flux per DM annihilation in the Sun.

2175 Knowing  $N_S^{90}$  one can use the relation in Eq. (5.27) to obtain  $\Gamma_A^{eq,90}$  for different  
 2176 values of the DM mass. From there I can directly translate those values into the  
 2177 upper limits for DUNE on the DM scattering cross sections, for a given exposure. The  
 2178 relation between the annihilation rate and the DM-nucleon cross section comes from the  
 2179 equilibrium condition through the solar DM capture rate. The details of the evolution  
 2180 of the number of DM particles inside the Sun and the computation of the capture rates

## 5.5. EXAMPLE: KALUZA-KLEIN DARK MATTER

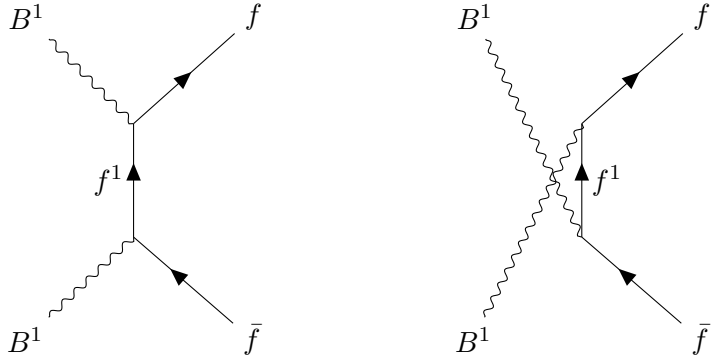


**Figure 5.5:** Feynman diagrams for  $B^1 B^1$  annihilation into SM fermions.

2181 are discussed in App. 5.2.

## 2182 5.5 Example: Kaluza-Klein Dark Matter

2183 Even though there are plenty of BSM theories which provide viable dark matter  
2184 candidates, Kaluza-Klein type of models [127, 128] within the universal extra dimensions  
2185 (UED) paradigm naturally predict the existence of a massive, stable particle that can  
2186 play the role of the dark matter. In the UED scenario all the SM fields can propagate  
2187 in one or more compact extra dimensions [129], as opposed to the idea of brane worlds  
2188 [130, 131], where just gravity can propagate in the bulk while SM particles live at fixed  
2189 points.

2190 Furthermore, in UED there is no violation of the translational invariance along the  
2191 extra dimensions, thus leading to degenerate KK modes masses and also the conservation  
2192 of the KK number in the effective four dimensional theory. At loop level, radiative  
2193 corrections and boundary terms shift the masses of the KK modes and break KK  
2194 number conservation into a KK parity. As a result, this theory only contains interactions  
2195 between an even number of odd KK modes and therefore the lightest among the first KK  
2196 excitations will be stable. This particle is usually denoted as the lightest Kaluza-Klein  
2197 particle (LKP) and its mass is proportional to  $1/R$ , being  $R$  the size of the extra  
2198 dimension.

2199 A viable DM candidate needs to be electrically neutral and non-baryonic, therefore

## CHAPTER 5. DM SEARCHES WITH NEUTRINOS FROM THE SUN

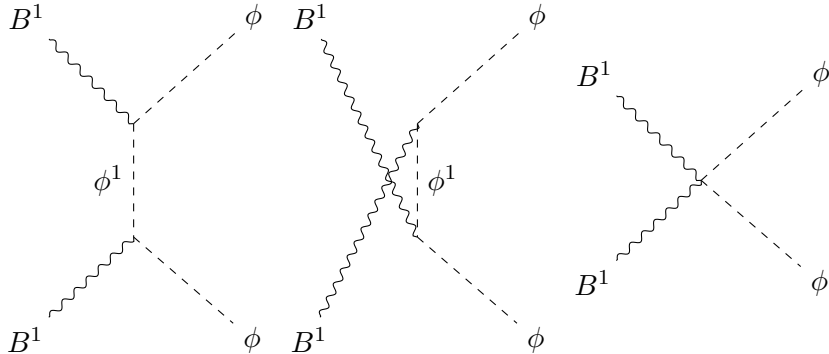


**Figure 5.6:** Feynman diagrams for  $B^1B^1$  annihilation into a Higgs boson pair.

2200 good candidates among the first Kaluza-Klein excitations would be the KK neutral  
 2201 gauge bosons and the KK neutrinos [132]. Another possible candidate is the first KK  
 2202 excitation of the graviton, which receives negligible radiative contributions and therefore  
 2203 has a mass almost equal to  $1/R$ , but it has been shown that the lightest eigenstate from  
 2204 the mixing of the gauge mass states  $(B^1, W_3^1)$  would be lighter, as  $B^1$  and  $W_3^1$  receive  
 2205 negative radiative corrections [133]. It is also understood that, when these corrections  
 2206 become sizeable, the eigenstates become approximately pure  $B^1$  and  $W_3^1$  states as the  
 2207 Weinberg mixing angle grows small with the KK number [133]. In that case, the LKP  
 2208 can be well-approximated as being entirely  $B^1$ .

2209 I need to compute the neutrino flux produced by the annihilations of the LKP in  
 2210 the core of the Sun, taking into account their propagation in the solar medium, as  
 2211 well as neutrino oscillations. To this end I used `WimpSim` [134, 135] to generate one  
 2212 million annihilation events in the Sun over a time span of four years and propagate  
 2213 them to the DUNE FD location ( $44^\circ 20' \text{ N}, 103^\circ 45' \text{ W}$ ), for different values of  $M_{\text{LKP}}$ .  
 2214 In Fig. 5.7 I show the obtained muon neutrino spectra arriving to the detector from  
 2215 LKP annihilations in the Sun, per unit area and per annihilation, plotted in relative  
 2216 energy units for different values of the mass. As one could expect the spectra get  
 2217 steeper the higher is the mass, due to the absorption of high-energy neutrinos in the  
 2218 solar medium. Also, one can see the peak at  $z = 1$  due to the direct annihilation into  
 2219 neutrinos  $\chi\chi \rightarrow \nu\bar{\nu}$ .

## 5.5. EXAMPLE: KALUZA-KLEIN DARK MATTER

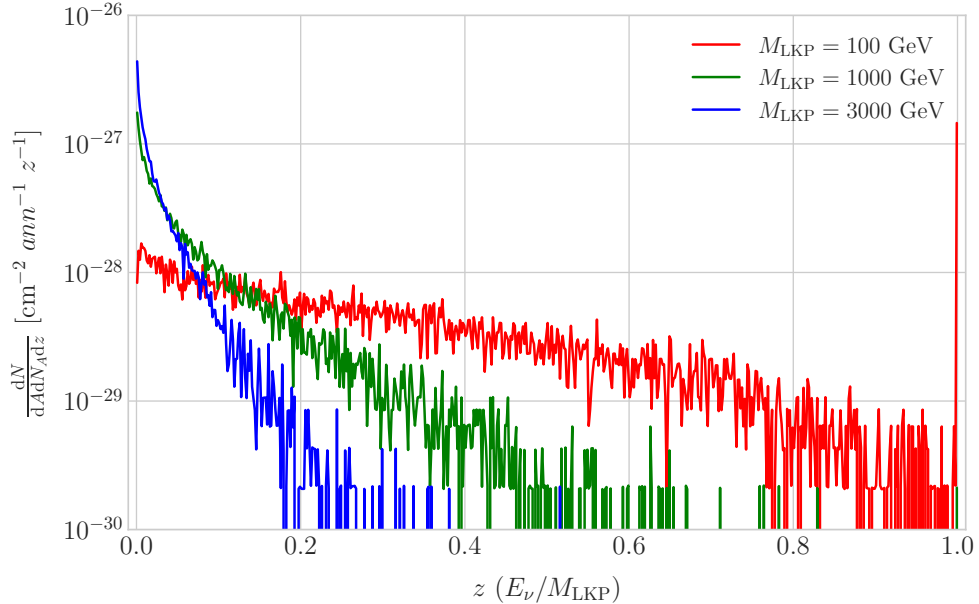


**Figure 5.7:** Computed spectra of muon neutrinos at the DUNE FD site from  $B^1$  annihilations in the Sun for three different values of  $M_{\text{LKP}}$ , plotted in relative energy units for legibility.

Now, one can estimate the sensitivity of DUNE to this particular model by using the methods I previously discussed. To begin with, I will use the optimistic estimation of the background efficiency in Eq. (5.24) to get our upper bound. Using it, one can directly compute the number of expected background events to be  $N_B = 0.1101$  for an exposure of 400 kT yr. Then, Eq. (5.26) give us a value of  $N_S^{90} = 2.20$  for the 90% exclusion number of expected signal events. By using the NuWro generated cross sections and the computed neutrino fluxes from  $B^1$  annihilations in the Sun I can estimate the limits on the SD and SI DM-nucleus cross section using the relation in Eq. (5.2) and the capture rates I computed with DarkSUSY.

In Fig. 5.8 I show the projected sensitive for DUNE on the spin-dependent  $B^1$ -proton scattering cross section versus the mass of the DM particle, for a exposure of 400 kT yr (green dots). I also include the previous results from IceCube [4] (blue line) and Antares [5] (red line). The shaded area represents the disfavoured region from combined searches for UED by ATLAS and CMS [6].

From the experimental point of view, this estimation lacked a detailed simulation of

## CHAPTER 5. DM SEARCHES WITH NEUTRINOS FROM THE SUN

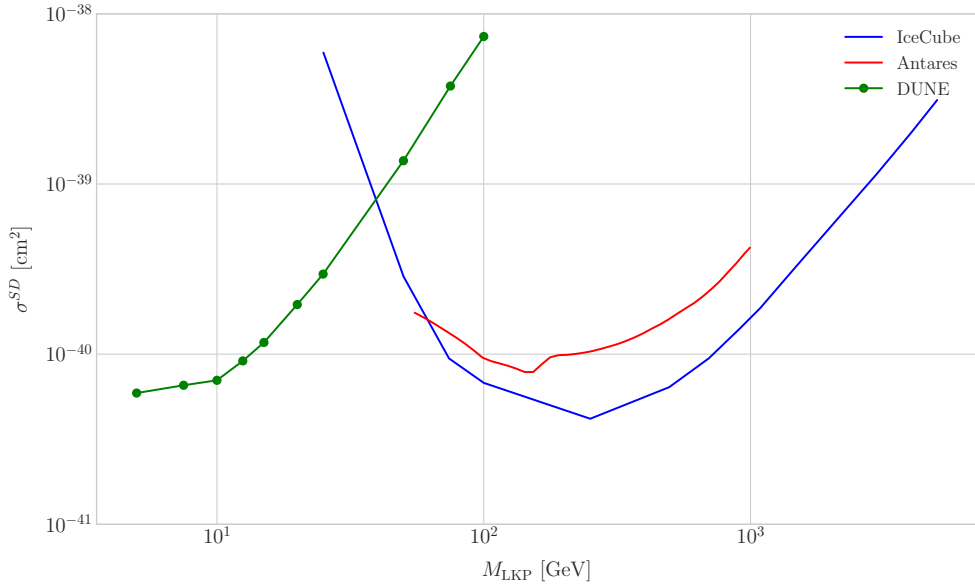


**Figure 5.8:** Projected 90% confidence level upper limit for DUNE (400 kT yr) on the spin-dependent  $B^1$ -proton scattering cross section as a function of  $M_{\text{LKP}}$  (green dots). I also show the previous limits from IceCube [4] (blue line) and Antares [5] (red line) on the LKP cross section. The shaded area represents the disfavoured region (at 95% confidence level) on the mass of the LKP from LHC data [6].

the detector response and thus this must be consider as a mere optimistic sensitivity computation. However, it shows the potential of DUNE to constrain this kind of exotic scenarios, showing the region where it will be in a position to compete with other neutrino telescopes. A more detailed analysis is needed if I am to make a realistic estimation. Even though the region of the parameter space where DUNE would be sensitive to this particular model is quite constrained by collider searches [6] and other rare decay measurements [136, 137], it still constitutes an alternative indirect probe.

## 5.6 High energy DM neutrino signals

To have better estimates on the capability of the DUNE FD to constrain the parameter space of DM using solar neutrino fluxes, I need to start accounting for the detector resolution effects and the topologies of the different signatures. As a starting point, I will focus on specific annihilation channels. For the case of DUNE, the relevant ones are mainly the hard channels  $\tau^+\tau^-$  and  $\nu\bar{\nu}$  and the soft channel  $b\bar{b}$ . These are the open

## 5.6. HIGH ENERGY DM NEUTRINO SIGNALS

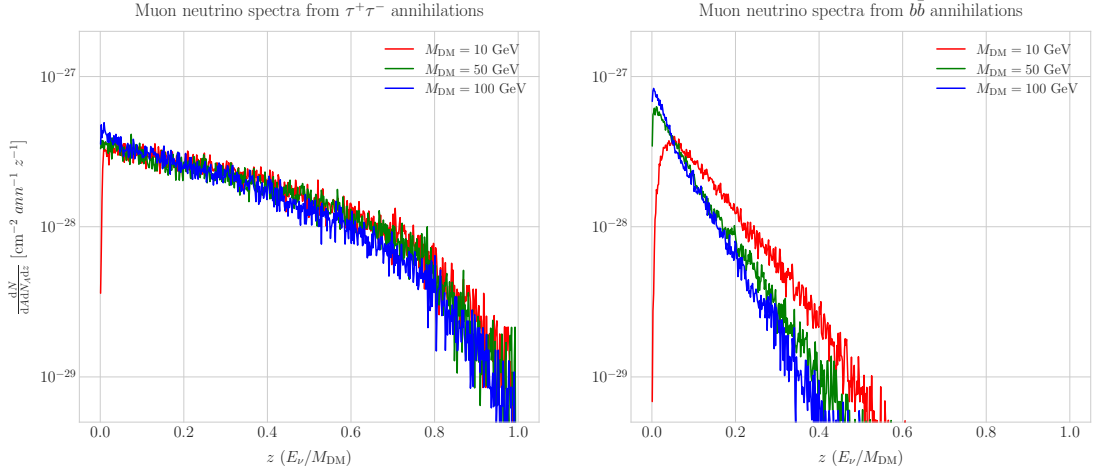


**Figure 5.9:** Computed spectra of muon neutrinos at the DUNE FD site from  $\tau^+\tau^-$  (left panel) and  $b\bar{b}$  (right panel) annihilations in the Sun for the DM masses  $m_{\text{DM}} = 10 \text{ GeV}$  (red line),  $50 \text{ GeV}$  (green line) and  $100 \text{ GeV}$  (blue line), plotted in relative energy units.

annihilation channels for relatively low mass WIMPs that will actually give neutrino fluxes. Other channels, like  $W^+W^-$  and  $ZZ$ , are open for more massive WIMPs, but those will produce usually a higher energy neutrino flux that will be out of reach for DUNE (usually the maximum neutrino energy is taken to be  $E_{\max} = 10 \text{ GeV}$ ).

In Fig. 5.9 I show the `WimpSim` [134, 135] generated muon neutrino spectra at the DUNE FD location ( $44^\circ 20' \text{ N}, 103^\circ 45' \text{ W}$ ) from  $\tau^+\tau^-$  (left panel) and  $b\bar{b}$  (right panel) annihilations in the core of the Sun, for different DM masses. Here, one can clearly see the meaning of the previous distinction between hard and soft channels. For the same DM mass value, the muon neutrino spectrum from the  $\tau^+\tau^-$  channel is more flat and reaches higher energies than the one from the  $b\bar{b}$  channel, which drops faster.

In this case, I prepared two sets of files, one for  $\tau^+\tau^-$  and the other for  $b\bar{b}$ , for DM masses in the range from 5 to 100 GeV (actually for  $b\bar{b}$  the first mass point I took is 7.5 GeV, as a WIMP with  $m_{\text{DM}} = 5 \text{ GeV}$  can not kinematically self annihilate into  $b\bar{b}$ ). Then, I prepared the `WimpSim` output fluxes in a specific way to use them as inputs to `NuWro`, which simulates the neutrino interaction with the argon.

Because `WimpSim` outputs an event list together with the fluxes, I can use the former to generate the events. The direction of these is given in terms of the azimuth and

## CHAPTER 5. DM SEARCHES WITH NEUTRINOS FROM THE SUN

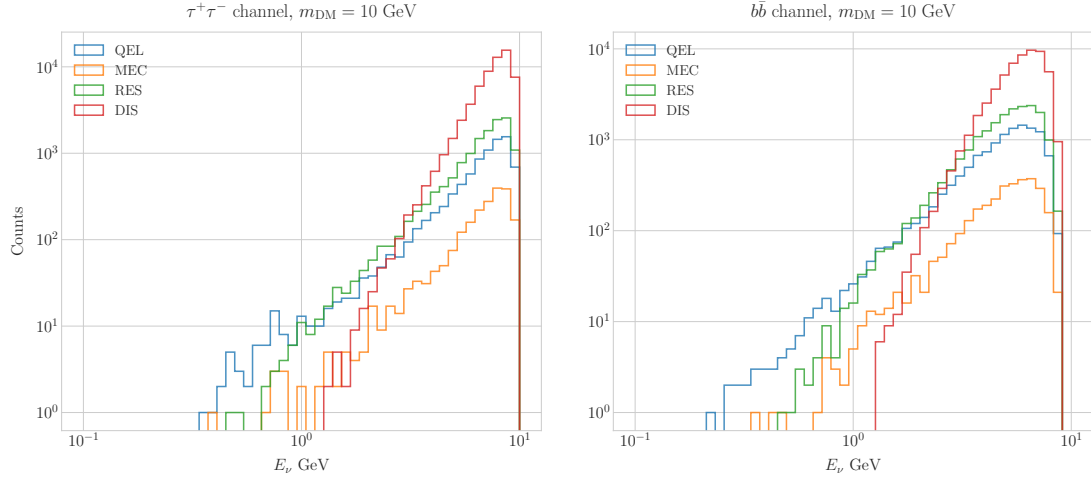


**Figure 5.10:** Distribution of the muon neutrino energies from the  $\tau^+\tau^-$  (left panel) and  $b\bar{b}$  (right panel) annihilation channels, for  $m_{\text{DM}} = 10 \text{ GeV}$ , separated by CC interaction type: QEL (blue), MEC (orange), RES (green) and DIS (red).

altitude angles viewed from the specified location, so first I need to convert these into the DUNE FD coordinates. Once I have done it, each event can be processed with `NuWro`. To increase the number of samples and optimise the computation time, I generate 100 interactions (i.e. `NuWro` events) for each `WimpSim` event<sup>2</sup>. I restrict the event generation to charged current interactions, but I allow all the different contributions to the CC cross section, i.e. quasielastic scattering (QEL), meson exchange current process (MEC), resonant pion production (RES) and deep inelastic scattering (DIS). I just take into account the CC contribution because I am only interested in final states with charged leptons, as we have better chances of reconstructing the kinematics of CC events.

For the atmospheric fluxes I follow a similar procedure, only that this time I do not have a set of events but the fluxes binned in azimuth and altitude angles. This way, I transform these to DUNE coordinates and process the fluxes for each bin separated with `NuWro`.

At this point, I have two sets of events with different energies and final states. In Fig. 5.10 one can see the distribution of the muon neutrino energies for the case

<sup>2</sup>This also solves a problem related with the generation of the neutrino interactions in `NuWro`, as if you only produce one event each time you launch `NuWro` it will always produce an interaction of the dominant interaction type for that particular energy.

## 5.6. HIGH ENERGY DM NEUTRINO SIGNALS

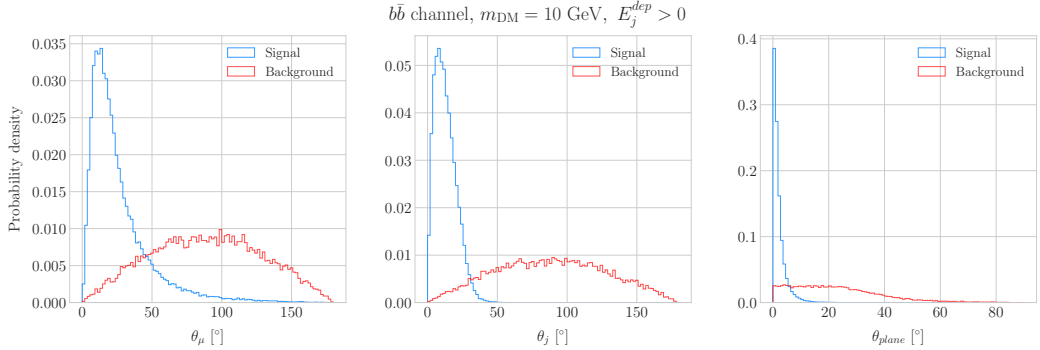


**Figure 5.11:** Distributions of  $\theta_\mu$  (left panel),  $\theta_j$  (central panel) and  $\theta_{\text{plane}}$  (right panel) for the  $b\bar{b}$  sample with  $m_{\text{DM}} = 10$  GeV (blue) and the atmospheric background (red).

2280  $m_{\text{DM}} = 10$  GeV, both for the  $\tau^+\tau^-$  (left panel) and  $b\bar{b}$  (right panel) channels, separated  
 2281 by interaction. One can clearly see that there are different energy regimes where the  
 2282 primary interaction type is different. This leads to a plurality of event topologies,  
 2283 therefore making it difficult to implement a general approach to the selection of events  
 2284 in detriment of the background. As a way to proceed, I decided to split our samples,  
 2285 based on the different interaction modes and contents of the final state, into a CC DIS  
 2286 sample and a single proton CC QEL sample.

### 2287 5.6.1 DIS events

2288 To begin with, I consider the high energy part of the spectrum. In this region DIS events  
 2289 dominate, i.e. interactions of the form  $\nu_\mu + q_d(\bar{q}_u) \rightarrow \mu^- + q_u(\bar{q}_d)$ . Therefore, our final  
 2290 estates will contain a muon and a hadronic jet from the fragmentation of the outgoing  
 2291 quark. As all these events have  $E_\nu \gtrsim 1$  GeV the momentum transfer to the remnant  
 2292 nucleus is negligible, for this reason the neutrino energy can be effectively reconstructed  
 2293 just taking into account the momenta of the muon and the jet. This technique was  
 2294 successfully used in Ref. [138] to select monoenergetic DM solar neutrino events from  
 2295  $\nu\bar{\nu}$  annihilation channels.

2296 Using momentum conservation one sees that the plane generated by the momenta  
 2297 of the muon and the jet needs to also contain the momentum of the neutrino. As we  
 2298 are interested in neutrinos coming from the Sun, the momentum of the neutrino can be

## CHAPTER 5. DM SEARCHES WITH NEUTRINOS FROM THE SUN

2299 regarded as known beforehand. This will allow us to define the angle of the outgoing  
 2300 muon and jet with respect to the incoming neutrino. Moreover, one can also use that  
 2301 information to reject poorly reconstructed jets, checking for deviations of these from the  
 2302 momentum conservation plane.

2303 To account for the limited angular resolution of the detector, I smeared the momenta  
 2304 of the muons and hadrons. In a liquid argon TPC muons are expected to be tracked with  
 2305 high precision, therefore I take the associated angular resolution to be  $1^\circ$ . In the case of  
 2306 jets, it is expected that for the hadrons dominating the cascade a detector like DUNE  
 2307 has an angular resolution between  $1^\circ$  to  $5^\circ$  [85], so I take the latter, more conservative,  
 2308 estimate.

2309 As a first selection step, I will just take into account particles with kinetic energies  
 2310 above the detection threshold of DUNE. For muons and photons the specified threshold  
 2311 energy is 30 MeV, for charged pions 100 MeV and for other hadrons 50 MeV [85]. This  
 2312 way, if the outgoing muon in a certain event has an energy lower than the required  
 2313 threshold I will drop such event. For the case of hadrons and photons, I will only require  
 2314 to have at least one particle above the energy threshold, so then one can compute the  
 2315 jet momentum using the (smeared) momenta of the  $N$  particles above threshold as:

$$\vec{p}_j = \sum_{i=1}^N \vec{p}_i. \quad (5.28)$$

2316 Additionally, I will also define an estimation of the deposited hadronic energy as:

$$E_j^{dep} = m_{^{39}\text{Ar}} - m_{^{40}\text{Ar}} + \sum_{i=1}^N \sqrt{|\vec{p}_i|^2 + m_i^2}. \quad (5.29)$$

2317 This quantity is useful to select events with enough hadronic visible energy in the  
 2318 detector. For events where most of the hadronic energy is scattered across plenty of  
 2319 hadrons with individual energies below the detection threshold, this estimation will  
 2320 give  $E_j^{dep} \leq 0$ . In these cases it could be expected that the jet momentum is poorly  
 2321 reconstructed, and therefore I require events to pass the cut  $E_j^{dep} > 0$ .

## 5.6. HIGH ENERGY DM NEUTRINO SIGNALS

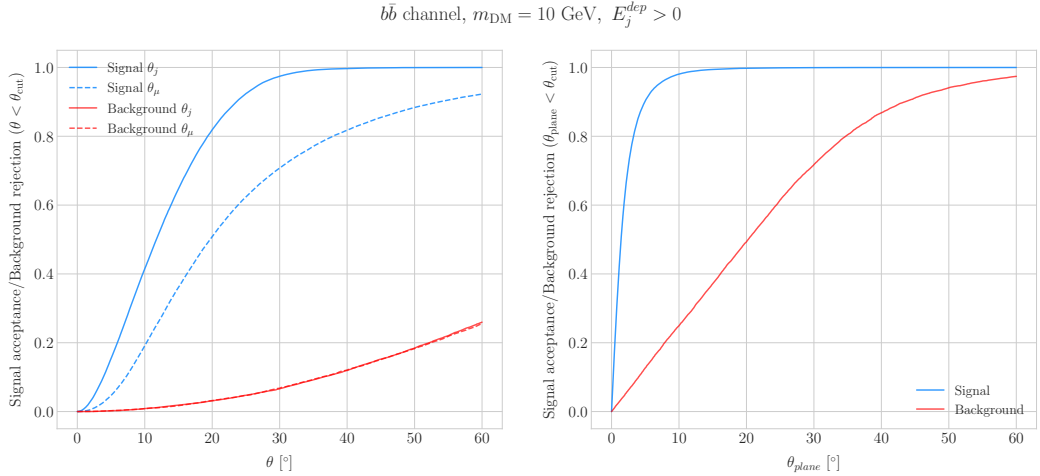


**Figure 5.12:** Left panel: signal efficiencies (blue lines) and background rejections (red lines) for events passing the cuts  $\theta < \theta_{\text{cut}}$  for the jet (solid lines) and muon (dashed lines) angles. Right panel: signal efficiency (blue line) and background rejection (red line) for events passing the cut  $\theta_{\text{plane}} < \theta_{\text{cut}}$  for the momentum conservation plane deviation.

2322 For the events I can compute the angles for the muon and jet with respect to the  
 2323 incoming neutrino as:

$$\cos \theta_\mu = \hat{p}_\nu \cdot \hat{p}_\mu, \quad (5.30)$$

$$\cos \theta_j = \hat{p}_\nu \cdot \hat{p}_j, \quad (5.31)$$

2324 and the deviation from the momentum conservation plane as:

$$\sin \theta_{\text{plane}} = \left| \frac{\hat{p}_\mu \times \hat{p}_\nu}{|\hat{p}_\mu \times \hat{p}_\nu|} \cdot \hat{p}_j \right|. \quad (5.32)$$

2325 In Fig. 5.11 I show some distributions of these quantities for the case of the  $b\bar{b}$  sample  
 2326 with  $m_{\text{DM}} = 10$  GeV (blue histograms) and for the atmospheric backgrounds (red).  
 2327 In order to select the atmospheric events I followed the same criteria as for the signal  
 2328 events. However, because in the signal case I used the true direction of the neutrino  
 2329 as input, as it should be that of the Sun at that time and therefore known, in the  
 2330 atmospheric case I used a set of solar positions as our ansatz for the neutrino direction.  
 2331 From the distributions, one can see that the muon and the jet for the signal events are

## CHAPTER 5. DM SEARCHES WITH NEUTRINOS FROM THE SUN

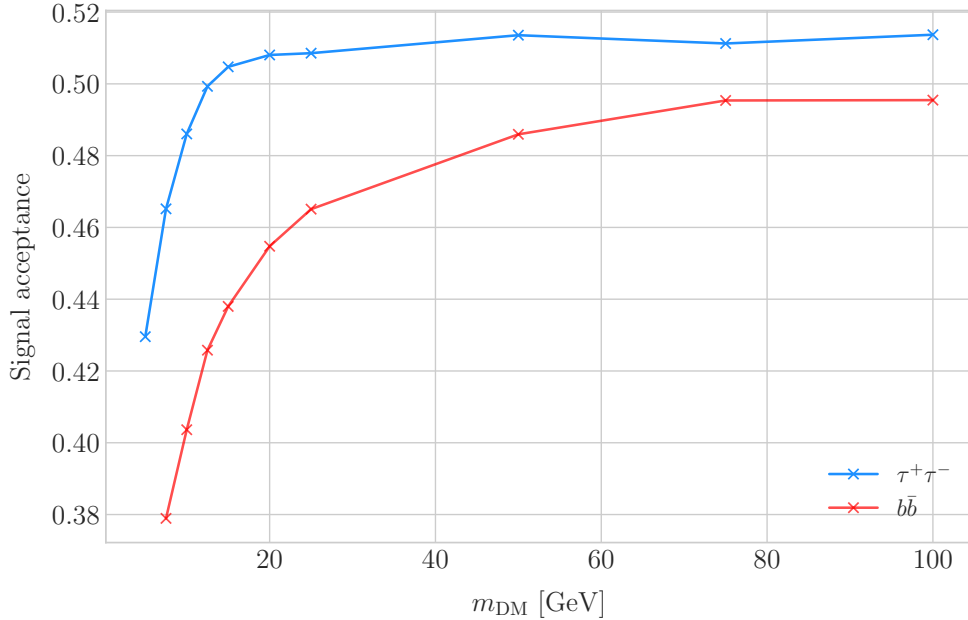


**Figure 5.13:** Signal efficiencies for the  $\tau^+\tau^-$  (blue line) and  $b\bar{b}$  (red line) DIS samples as functions of the DM mass,  $m_{\text{DM}}$ , obtained by applying the optimal angular cuts  $\theta_\mu < 27^\circ$ ,  $4^\circ < \theta_j < 26^\circ$  and  $\theta_{\text{plane}} < 3.5^\circ$ .

predominantly forward and also that the deviations from the momentum conservation plane are peaked at zero, as one should expect.

Now, I can start applying cuts to maximise our signal selection efficiency while at the same time I try to minimise the amount of atmospheric background events passing the selection. To this end, I will need to find some lower and upper cuts for  $\theta_j$  and  $\theta_\mu$  and an upper bound for  $\theta_{\text{plane}}$ . In Fig. 5.12 I show how upper bound cuts in the different angular variables affect the signal efficiency (blue lines) and the background rejection (red lines). Notice that the signal efficiency behaves in a quite different way when I apply cuts in the jet and the muon angles. On the contrary, the cuts on both variables have a similar effect on the background rejection.

In order to obtain the optimal set of cuts, I perform a multidimensional scan. I do this separately for the  $\tau^+\tau^-$  and the  $b\bar{b}$  samples. For each case, I scan the possible cuts for each mass point and then I take the mean value of the signal efficiency for each configuration, to get the mean efficiency for each set of cuts. I do a similar scan for the atmospheric sample independently. Then, I take the sets of cuts such that

## 5.6. HIGH ENERGY DM NEUTRINO SIGNALS

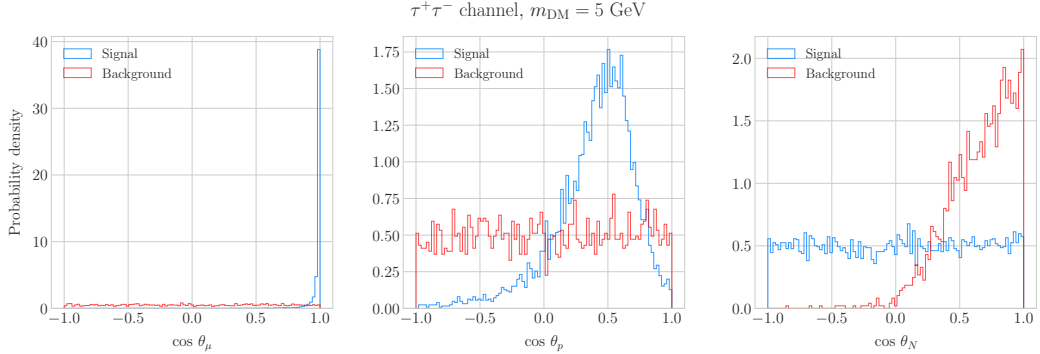


**Figure 5.14:** Distributions of  $\cos \theta_\mu$  (left panel),  $\cos \theta_p$  (central panel) and  $\cos \theta_N$  (right panel) for the  $\tau^+\tau^-$  QEL sample with  $m_{\text{DM}} = 5 \text{ GeV}$  (blue) and the atmospheric background (red).

the background rejection achieved is greater than 99.8% and search for the one which maximises the  $\tau^+\tau^-$  and  $b\bar{b}$  sample mean efficiencies. I found that with the cuts  $\theta_\mu < 27^\circ$ ,  $4^\circ < \theta_j < 26^\circ$  and  $\theta_{\text{plane}} < 3.5^\circ$  I get a background rejection of 99.80% while achieving a 49.40% and 44.92% mean signal efficiencies for the  $\tau^+\tau^-$  and  $b\bar{b}$  signals respectively.

In Fig. 5.13 I show the signal efficiencies as a function of the DM mass for the  $\tau^+\tau^-$  (blue line) and the  $b\bar{b}$  (red line) DIS events, after applying the cuts discussed above, as well as the energy threshold and hadronic visible energy selections. One can see that the efficiency grows with the mass, as annihilations of more massive DM particles will produce a neutrino spectrum centered at higher energies, where DIS events dominate. Notice also that the efficiency is higher for the  $\tau^+\tau^-$  case at every mass point, as in general this channel produces neutrinos at higher energies than the corresponding  $b\bar{b}$  channel.

### 5.6.2 Single proton QEL events

Now, one can try to explore the low energy tail of the neutrino energy distributions. This regime is dominated by the QEL interactions, i.e. events of the type  $\nu_\mu + n \rightarrow \mu^- + p$ . In this case, as the typical energies are  $E_\nu \lesssim 1 \text{ GeV}$ , the momentum transfer to the remnant nucleus is sizeable. Therefore, I can not make the approximation I did before and assume that the momentum of the muon and the proton will give an adequate

## CHAPTER 5. DM SEARCHES WITH NEUTRINOS FROM THE SUN

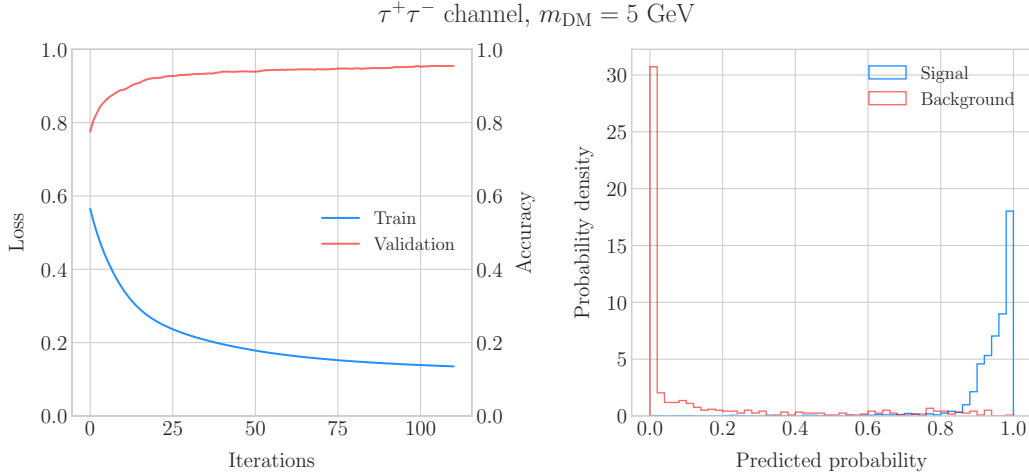


**Figure 5.15:** Left panel: value of the loss function for the training sample (blue line) and accuracy for the validation sample (red line) versus the number of iterations for the MLP classifier training. Right panel: distributions of the predicted probabilities assigned by the MLP classifier to the test sample for the  $\tau^+\tau^-$  QEL signal with  $m_{\text{DM}} = 5 \text{ GeV}$  (blue) and the atmospheric background (red).

2365 estimation of the reconstructed neutrino energy.

2366 In any case, as before, I can take the direction of the incoming neutrino as known.

2367 That way, one can estimate the energy of the neutrino as:

$$E_\nu^{reco} = E_\mu + E_p + m_{^{39}\text{Ar}} - m_{^{40}\text{Ar}}, \quad (5.33)$$

2368 and using momentum conservation I can write the momentum of the remnant nucleus

2369 as:

$$\vec{p}_N = \hat{p}_\nu (E_\mu + E_p + m_{^{39}\text{Ar}} - m_{^{40}\text{Ar}}) - \vec{p}_\mu - \vec{p}_p. \quad (5.34)$$

2370 As in the previous case, I need to drop the events where the muon or the proton fall  
 2371 below the kinetic energy detection threshold [85]. Also, I again apply a smearing to the  
 2372 momenta of the particles, a 1% for muons and 5% for protons.

2373 Having done that, one can compute the following angular variables for our selected  
 2374 events:

$$\cos \theta_\mu = \hat{p}_\nu \cdot \hat{p}_\mu, \quad (5.35)$$

## 5.6. HIGH ENERGY DM NEUTRINO SIGNALS

$$\cos \theta_p = \hat{p}_\nu \cdot \hat{p}_p, \quad (5.36)$$

$$\cos \theta_N = \hat{p}_\nu \cdot \hat{p}_N. \quad (5.37)$$

2375 Fig. 5.14 shows the distributions of these angular variables for the  $\tau^+\tau^-$  QEL  
 2376 sample with  $m_{\text{DM}} = 5$  GeV (blue) and the atmospheric background (red). Again, for  
 2377 the atmospheric events I used a random solar position as the ansatz for the incoming  
 2378 neutrino direction. Notice that now, opposed to the DIS case where the signal had very  
 2379 sharp distributions for the variables considered, the shapes of the angular distributions  
 2380 for signal and background are not that much different.

2381 This effectively means that the usual approach of applying simple angular cuts would  
 2382 not work as well as in the previous situation. Therefore, as a possible solution, I tried to  
 2383 use a multilayer perceptron (MLP) classifier to separate between signal and background  
 2384 events. Thus, the power of the hypothesis test will serve as an estimate of the signal  
 2385 efficiency, and in the same way one can take the size of the test to be our background  
 2386 rejection.

2387 For each DM mass value and channel, as well as for the background sample, I divide  
 2388 our events into training, validation and test samples. The input variables for the classifier  
 2389 were the reconstructed neutrino energy from Eq. (5.33) and the angular variables defined  
 2390 in Eqs. (5.35 - 5.37). I used the MLP classifier implemented in **scikit-learn** [139], with  
 2391 a total of five hidden layers, the rectified linear unit activation function and adaptive  
 2392 learning rate. In order to account for fluctuations due to artifacts in the training process I  
 2393 repeated the training a thousand times for each sample, redefining each time the training,  
 2394 validation and test subsets, so one can take as our signal efficiency and background  
 2395 rejection the mean values of the powers and sizes of the tests.

2396 The results of one of these training processes for the  $\tau^+\tau^-$  QEL signal with  $m_{\text{DM}} =$   
 2397 5 GeV is shown in Fig. 5.15. On the left panel I show the loss function values (blue) and  
 2398 accuracy (red) at each iteration for the training and the validation samples respectively.  
 2399 The training stops either when the maximum number of iterations is reached (1000 in  
 2400 this case) or when the accuracy for the validation sample reaches a certain tolerance

## CHAPTER 5. DM SEARCHES WITH NEUTRINOS FROM THE SUN

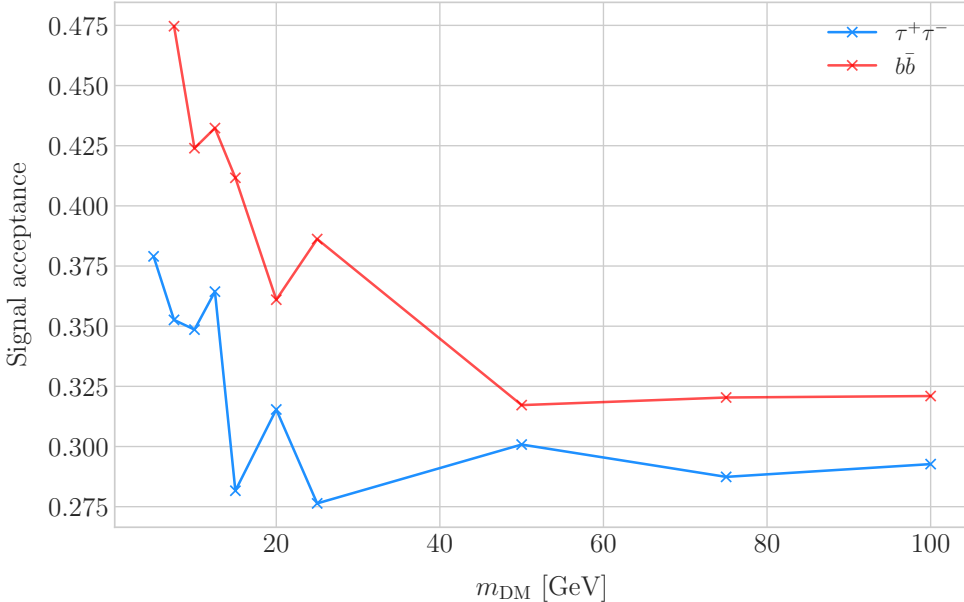


**Figure 5.16:** Signal efficiencies for the  $\tau^+\tau^-$  (blue line) and  $b\bar{b}$  (red line) single proton QEL samples as functions of the DM mass,  $m_{\text{DM}}$ , obtained by requiring a minimum predicted probability from the MLP classifier of 0.97 in order to achieve a background rejection greater than 99.8%.

(I chose  $10^{-4}$  as our tolerance). On the right panel I have the distributions for the predicted probability by the model, separated in true signal (blue) and background (red) events, for the test sample. One can see that both populations are well separated, obtaining a power of 44.97% and a size of 0.17% when I require a predicted probability greater than 0.97.

Applying this criteria for each sample, I obtain the mean signal efficiencies shown in Fig. 5.16. Notice that the efficiencies for the channel  $\tau^+\tau^-$  (blue line) are consistently lower than the ones for the  $b\bar{b}$  channel (red line). This can be due to the fact that, for each DM mass point, the neutrino spectrum coming from the  $b\bar{b}$  annihilation channel is centered at lower energies when compared to the  $\tau^+\tau^-$  spectrum. This directly translates into more low energy neutrinos undergoing QEL interactions, which give signals that can be easily separated from the atmospheric background. This explanation also help us understand why in both cases the signal acceptance drops when the DM mass increases. In all cases, the background rejection took values between 99.8% to 99.9%. I will assume

## 5.6. HIGH ENERGY DM NEUTRINO SIGNALS

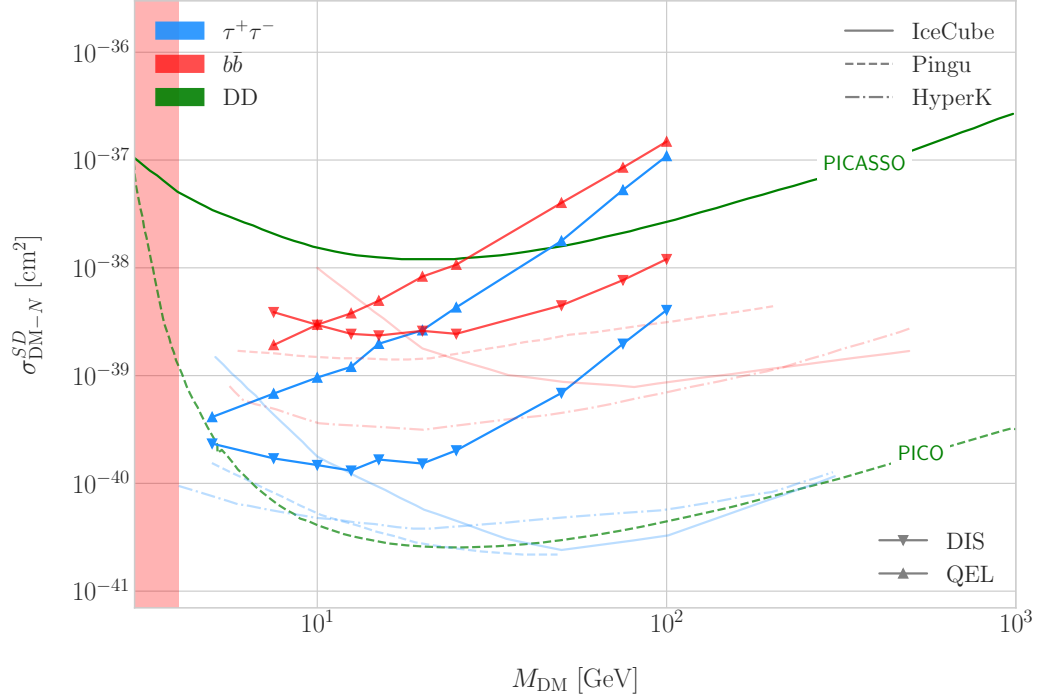


**Figure 5.17:** Projected 90% confidence level upper limit for DUNE (400 kT yr) on the spin-dependent DM-nucleon scattering cross section as a function of  $m_{\text{DM}}$ , for the annihilation channels  $\tau^+\tau^-$  (blue) and  $b\bar{b}$  (red) separated by interaction type (up triangles denote DIS interactions whereas down triangles represent QEL interactions). I also show the previous limits from IceCube [7] (solid lines) and the projected sensitivities for Pingu [8] (dashed lines) and Hyper-Kamiokande [9] (dash-dotted lines), as well as the direct detection limits from PICASSO [10] (solid green line) and PICO-60 C<sub>3</sub>F<sub>8</sub> [11] (dashed green line).

2415 a 99.8% background rejection value in all cases to keep our estimation conservative.

### 2416 5.6.3 Results

2417 In order to estimate the DM-nucleon cross section sensitivities in the present case I need  
 2418 again to compute the expected number of background events. As I am now separating  
 2419 events by interaction type Eq. (5.25) does not hold anymore, as in that case I integrated  
 2420 over the total neutrino-argon cross section. In this instance, the expected background  
 2421 events for DIS events is approximately given by:

$$N_B^{DIS} \simeq \eta_B^{DIS} \times (4.655 \times 10^3) \times \left( \frac{\text{exposure}}{400 \text{ kT yr}} \right), \quad (5.38)$$

## CHAPTER 5. DM SEARCHES WITH NEUTRINOS FROM THE SUN

2422 whereas for QEL events we have:

$$N_B^{QEL} \simeq \eta_B^{QEL} \times (2.248 \times 10^4) \times \left( \frac{\text{exposure}}{400 \text{ kT yr}} \right). \quad (5.39)$$

2423 Now, using these together with Eqs. (5.26) and (5.27) one can obtain the 90% C.L.  
2424 upper limit on the total annihilation rate at equilibrium for both kind of events. Then,  
2425 applying the computed DM-nucleons capture rates I can translate these into limits on  
2426 the DM-nucleon cross section by means of Eqs. (5.2), (5.5) and (5.6).

2427 Fig. 5.17 shows the obtained limits on the SD DM-nucleon cross section for DUNE,  
2428 using the DIS (up triangles) and QEL (down triangles) events both for the  $\tau^+\tau^-$  (blue)  
2429 and the  $b\bar{b}$  (red) samples, for an exposure of 400 kT yr. I also include the corresponding  
2430 current limits from IceCube [7] (solid lines), as well as the projected sensitivities of  
2431 Pingu [8] (dashed lines) and Hyper-Kamiokande [9] (dash-dotted lines). For comparison,  
2432 I also show the reported direct detection limits from PICASSO [10] (solid green line)  
2433 and PICO-60  $C_3F_8$  [11] (dashed green line).

2434 Notice that, for most of the mass range, the limits one can set by using the DIS  
2435 events are stronger than those of the QEL interactions, except for the low mass part  
2436 of both the  $\tau^+\tau^-$  and the  $b\bar{b}$  curves where the QEL events dominate. In general, the  
2437 expected sensitivity of DUNE for DM masses  $\lesssim 25$  GeV surpasses the stronger current  
2438 indirect limits. However, experiments like Hyper-Kamiokande are foreseen to have an  
2439 overall better sensitivity in this kind of searches, as they have a bigger active volume  
2440 and accept a broader energy range.

2441 A pending question is what happens when we add the RES and MEC charged-current  
2442 interaction contributions. In that case it would probably be more convenient to split  
2443 the samples by final state interaction topologies. Also, another necessary improvement  
2444 would be adding a full detector simulation and reconstructions. This will also require  
2445 considering the effect of poorly reconstructed events or final states containing neutral  
2446 particles such that they mimic the desired topology at the reconstruction level.

## 5.7. EXAMPLE: LEPTOPHILIC DARK MATTER

### **2447 5.7 Example: Leptophilic Dark Matter**

**2448** In general, the capture rate of DM particles by the Sun via interactions with electrons is  
**2449** several orders of magnitude smaller than the capture via DM-nucleus scattering. Thus,  
**2450** it would be sub-leading even when nucleon capture is loop suppressed. As I showed in  
**2451** Fig. 5.2, the capture rate via scattering off electrons only surpasses the capture rates  
**2452** via DM-nucleons interactions for DM masses  $\lesssim 100 - 500$  MeV.

**2453** However, if one considers a model where DM-nucleon interactions are forbidden even  
**2454** at loop level, then electron interactions will be the sole contributor to DM capture in  
**2455** the Sun. One can describe such scenario where the DM particles couple to leptons but  
**2456** not to the quark sector using effective operators.

**2457** In general, assuming that the DM particle is a Dirac fermion, the dimension six  
**2458** operators describing the interaction between two DM particles and two leptons can be  
**2459** written as:

$$\mathcal{L}_{eff} = G \sum_i (\bar{\chi} \Gamma^i \chi) (\bar{\ell} \Gamma^i \ell), \quad (5.40)$$

**2460** where  $G = 1/\Lambda^2$  is the effective coupling strength,  $\Lambda$  the cut-off of the effective field  
**2461** theory and  $\ell$  denotes any lepton. In principle, one should consider all the possible  
**2462** Lorentz structures  $\Gamma_f^i$  in order to have a complete set of effective operators.

**2463** However, some combinations will induce interactions with nucleons at loop level.  
**2464** As we are specifically interested in interactions which forbid any communication with  
**2465** the quark sector, I will not consider those [140]. In addition, some of the effective  
**2466** operators give rise to velocity-suppressed scattering cross sections between DM particles  
**2467** and leptons. I will also neglect those, as the suppression goes with the square of the DM  
**2468** halo velocity which in units of the speed of light is  $\sim 10^{-6}$ .

**2469** This way, the only Lorentz tensor structure that do not induce interactions with  
**2470** quarks at loop level and gives a contribution to the scattering cross section that is not  
**2471** velocity suppress is the axial-axial interaction. The effective Lagrangian is then given

## CHAPTER 5. DM SEARCHES WITH NEUTRINOS FROM THE SUN

2472 by:

$$\mathcal{L}_{eff} = \frac{c_A^\chi c_A^\ell}{\Lambda^2} (\bar{\chi} \gamma^\mu \gamma^5 \chi) (\bar{\ell} \gamma_\mu \gamma^5 \ell), \quad (5.41)$$

2473 where  $c_A^\chi$  and  $c_A^\ell$  are the couplings for the different species. As the DM coupling appears  
2474 as a common factor for any lepton choice, I will redefine the corresponding coupling  $c_A^\ell$   
2475 to absorb  $c_A^\chi$ . Also, for simplicity, I will assume that the couplings between the DM  
2476 particles and the leptons are flavour independent, i.e. I have just two couplings,  $c_A^e$  for  
2477 charged leptons and  $c_A^v$  for neutrinos.

2478 In the case of a scalar DM particle, the lowest order effective interaction with  
2479 leptons happens through a dimension five operator, generating scalar and pseudoscalar  
2480 interactions. However, the former induces interactions with quarks at two loop level  
2481 whereas the latter gives a velocity suppressed scattering cross section.

2482 From the effective Lagrangian in Eq. (5.41) it can be shown that the axial-axial  
2483 contribution to the scattering cross section for the fermionic DM and a charged lepton  
2484 is given by:

$$\sigma_{DM-e}^{AA} = 3 (c_A^e)^2 \frac{m_e^2}{\pi \Lambda^4}. \quad (5.42)$$

2485 If the DM interacts exclusively with fermions, then the only annihilation channels  
2486 that will give us a measurable neutrino flux coming out of the Sun are  $\tau^+ \tau^-$  and  $\nu \bar{\nu}$ . The  
2487 former channel, already explored previously in the more mainstream scenario of the DM  
2488 capture via scattering off nucleons, is open only for  $m_{DM} > m_\tau \simeq 1776.86 \pm 0.12$  MeV  
2489 [141], a mass region where the solar DM capture by electrons is at least one order of  
2490 magnitude smaller than the capture via interactions with nucleons. On the contrary, the  
2491 latter allows us to explore a region where the capture rate via scattering off electrons  
2492 dominates over the rest.

2493 One downside of focusing in such low mass range is that it falls below the usual  
2494 limit of  $m_{evap} \sim 4$  GeV usually explored in the literature. The pretext to explore this  
2495 region is the result discussed previously reported in Ref. [2], where DM evaporation in  
2496 the Sun for the case of capture via electron scattering could be negligible for masses  
2497 as low as  $m_{evap} \sim 200$  MeV. This result is quite sensitive to the high velocity tail of

## 5.7. EXAMPLE: LEPTOPHILIC DARK MATTER

the DM velocity distribution in equilibrium inside the Sun, and therefore full numerical simulations would be needed to asses the impact of this effect. However, this falls out of the scope of our work.

In this case, as I have an specific realisation of the interaction between the DM and leptons, one can estimate the relic density of our DM for different values of the couplings and the effective field theory scale  $\Lambda$ . The first step to do so is compute the self-annihilation cross section. Because I consider cold relics, at the freeze-out time our DM particles were non-relativistic and so one can expand the annihilation cross section in terms of the relative velocity  $v$  between two annihilating DM particles as [142]:

$$\sigma_{ann}^{AA}|v| \approx \frac{1}{2\pi\Lambda^4} \sum_{\ell} \left(c_A^{\ell}\right)^2 m_{\chi}^2 \sqrt{1 - \frac{m_{\ell}^2}{m_{\chi}^2} \left[ \frac{m_{\ell}^2}{m_{\chi}^2} + \frac{1}{12} \left(2 - \frac{m_{\ell}^2}{m_{\chi}^2}\right) v^2 \right]}, \quad (5.43)$$

where the sum includes all the possible lepton final states with mass  $m_{\ell}$ .

Solving the Boltzmann equation for the evolution of the DM density gives as a solution a relic density of:

$$\Omega_{\chi} h^2 \approx \frac{(1.04 \times 10^9) x_F}{M_{Pl} \sqrt{g_*} (a + 3b/x_F)}, \quad (5.44)$$

where  $x_F = m_{\chi}/T_F$  being  $T_F$  the freeze-out temperature,  $g_*$  the number of relativistic degrees of freedom at freeze-out and  $a$  and  $b$  the terms in the annihilation cross section expansion  $\sigma_{ann}|v| \approx a + bv^2 + \mathcal{O}(v^4)$ . Using the current best fit for the relic DM density  $\Omega_{\chi} h^2 = 0.1198 \pm 0.0012$  [143] one can use these relations to compute the required effective theory scale  $\Lambda$  at which the correct density is achieved for any combinations of  $m_{\chi}$  and  $c_A^{\ell}$ .

As discussed before, in the low DM mass region QEL interactions dominate. Moreover, if I focus on direct annihilation to neutrinos, the energy of the muon neutrino flux is known as it must be equal to the mass of the DM particle,  $E_{\nu} = m_{\chi}$ . That way, now I do not need to use Eq. (5.33) in order to estimate the momentum transfer to the

## CHAPTER 5. DM SEARCHES WITH NEUTRINOS FROM THE SUN

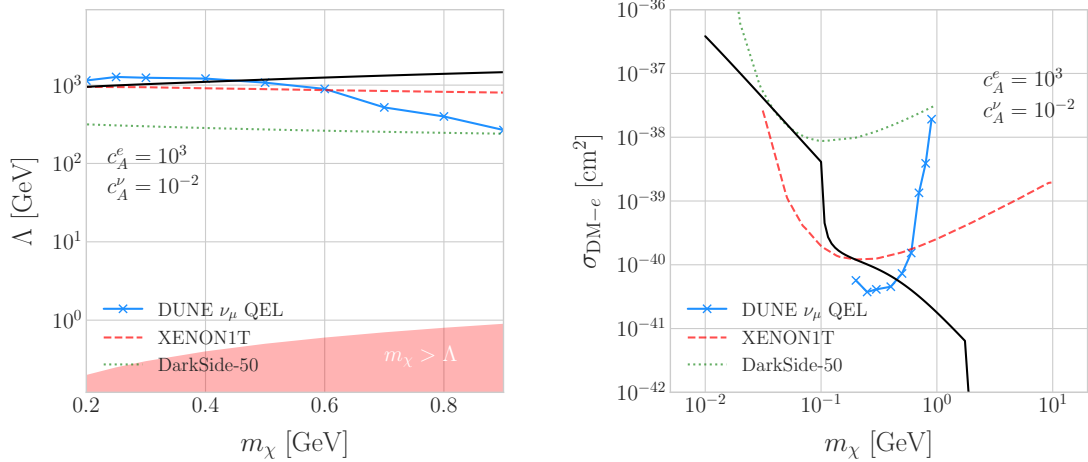


**Figure 5.18:** Left panel: Projected 90% confidence level sensitivity of DUNE (400 kT yr) to the scale  $\Lambda$  of an EFT containing only leptophilic DM axial-axial interactions (blue line). Right panel: In both cases the corresponding limits from DarkSide-50 [12] (dotted green line) and XENON1T [13] (dashed red line) are also shown, together with the configurations for which the correct relic density is achieved (black line), all for the coupling values  $c_A^e = 10^3$  and  $c_A^\nu = 10^{-2}$ .

2520 remnant nucleus, I can simply take:

$$\vec{p}_N = \hat{p}_\nu m_\chi - \vec{p}_\mu - \vec{p}_p. \quad (5.45)$$

2521 To estimate the signal efficiency and background rejection for this case I used again  
 2522 the MLP classifier from `scikit-learn`, using the same specifications as before. The  
 2523 only difference now is that I add also the reconstructed neutrino energy as one of the  
 2524 features to train the classifier with, because the characteristic monoenergetic flux for  
 2525 each  $m_\chi$  value will help to distinguish between signal and background events.

2526 In this case, for masses below  $\sim 500$  MeV I obtain a signal efficiency close to unity  
 2527 while keeping a background rejection of 99.9%. For bigger values of the mass, the signal  
 2528 efficiency drops significantly if I require to keep the background acceptance under 0.01%.  
 2529 However, because this kind of search is dominated by the background, sacrificing the  
 2530 signal acceptance to keep the background rejection to a minimum enhances the reach  
 2531 of the analysis. This way, for DM masses of the order of  $m_\chi \sim 1$  GeV I end up with  
 2532 efficiencies as low as 1%.

## 5.7. EXAMPLE: LEPTOPHILIC DARK MATTER

Now, estimating the number of background events using Eq. (5.39) one can go on and apply Eqs. (5.26) and (5.27) together with Eq. (5.42) to derive the sensitivity of DUNE to this kind of model. Fig. 5.18 (left panel) shows the potential reach of DUNE to constrain the EFT scale  $\Lambda$  this model containing only leptophilic DM axial-axial interactions (blue line), for a choice of couplings  $c_A^e = 10^3$  and  $c_A^\nu = 10^{-2}$ . I also included the current limits on the DM-electron scattering cross section from DarkSide-50 [12] (dotted green line) and XENON1T [13] (dashed red line), reworked with Eq. (5.42) to show their implications for the EFT scale. The values of  $\Lambda$  for which the correct DM relic density value is achieved for each mass are also shown (black line). This tells us that, for that specific choice of couplings, DUNE would be sensitive to DM configurations allowed by the relic density constraint up to a mass of  $m_\chi \sim 400$  MeV.

In Fig. 5.18 (right panel) I show the same upper limits but for the DM-electron scattering cross section. From this view one can see that DUNE would be able to offer complementary information to the low energy DM-electron interaction searches performed by direct detection experiments, in a slightly higher mass range.

With the present example, although it focuses on a very specific realisation of the DM interactions, I show the potential of DUNE to constrain exotic DM scenarios. Thanks to its low backgrounds and superb angular resolution DUNE will be able to help with the systematic searches for dark sectors physics.



2552

2553

## Particle ID in ND-GAr

2554 ND-GAr is a magnetised, high-pressure gaseous argon TPC (HPgTPC), surrounded by  
2555 an electromagnetic calorimeter (ECal) and a muon detector (commonly refer to as  $\mu$ ID).  
2556 A detailed discussion on the requirements, design, performance and physics of ND-GAr  
2557 can be found in the DUNE ND CDR [91] and the ND-GAr whitepaper (cite).

2558 In DUNE Phase II ND-GAr will fulfill the role of TMS, measuring the momentum  
2559 and sign of the charged particles exiting ND-LAr. Additionally, it will be able to measure  
2560 neutrino interactions inside the HPgTPC, achieving lower energy thresholds than those  
2561 of the ND and FD LArTPCs. By doing so ND-GAr will allow to constrain the relevant  
2562 systematic uncertainties for the LBL analysis even further.

2563 The goal of the present chapter is to review the requirements that the physics program  
2564 of DUNE impose on ND-GAr, present the current status of its design and describe the  
2565 GArSoft package, its simulation and reconstruction software.

2566 As decided during the DUNE Phase II workshop in June 2023 [reference], we want  
2567 to build ND-GAr physics case by showing:

- 2568 • That ND-GAr can constrain systematic uncertainties that ND-LAr might miss.
- 2569 • The impact on the neutrino oscillation results if such systematic uncertainties are  
2570 missed.
- 2571 • That ND-GAr is necessary to reach DUNE's main physics goals.

2572 This way, the design of ND-GAr will be physics driven.

## CHAPTER 6. PARTICLE ID IN ND-GAr

2573 In order to study the effects of final state interactions (FSI) in CC interactions,  
2574 ND-GAr should be able to measure the spectrum of protons and charged pions at low  
2575 energies. ND-GAr also needs to be able to measure the pion multiplicity, specially for  
2576 energies above 100 MeV as at these energies the pions shower in the LAr, to inform the  
2577 pion mass correction in the ND and FD LArTPCs.

2578 In order to correctly identify electrons, muons, pions, kaons and protons ND-GAr  
2579 can use a combination of:  $dE/dx$  measurements in the HPgTPC,  $E_{ECAL}/p$  using the  
2580 ECAL total energy and the momentum obtained from magnetic spectroscopy in the  
2581 HPgTPC and penetration information through the ECAL and muon tagger.

### 2582 6.1 GArSoft

2583 GArSoft is a software package developed for the simulation and reconstruction of events  
2584 in ND-GAr. It is inspired by the LArSoft toolkit used for the simulation of LArTPC  
2585 experiments, like the DUNE FD modules. It is based on `art`, the framework for event  
2586 processing in particle physics experiments [144]. Other of its main dependencies are  
2587 `ROOT`, `NuTools`, `GENIE` and `Geant4`. It allows the user to run all the steps of a generation-  
2588 simulation-reconstruction workflow using FHiCL configuration files.

#### 2589 6.1.1 Event generation

2590 The standard generator FHiCLs in GArSoft run the event generation and particle  
2591 propagation simulation (i.e. Geant4) in the same job by default. However, it is possible  
2592 to split them up if needed. The current version of GArSoft provides five different event  
2593 generators, each of them producing `simb::MCTruth` products defined in `NuTools`. The  
2594 available modules are:

- 2595 • **SingleGen**: particle gun generator. It produces the specified particles with a given  
2596 distribution of momenta, initial positions and angles.
- 2597 • **TextGen**: text file generator. The input file must follow the `hepevt` format<sup>1</sup>, the

---

<sup>1</sup>In brief, each event contains at least two lines. The first line contains two entries, the event number

## 6.1. GARSOFT

2598 module simply copies this to `simb::MCTruth` data products.

2599 • **GENIEGen**: GENIE neutrino event generator. The module runs the neutrino-nucleus  
2600 interaction generator using the options specified in the driver FHiCL file (flux file,  
2601 flavour composition, number of interactions per event,  $t_0$  distribution, ...). Current  
2602 default version is v3\_04\_00.

2603 • **RadioGen**: radiological generator. It produces a set list of particles to model  
2604 radiological decays. Not tested.

2605 • **CRYGen**: cosmic ray generator. The module runs the CRY event generator with a  
2606 configuration specified in the FHiCL file (latitude and altitude of detector, energy  
2607 threshold, ...). Not tested.

2608 The module **GArG4** searches for all the generated `simb::MCTruth` data products, using  
2609 them as inputs to the Geant4 simulation with the specified detector geometry. A constant  
2610 0.5 T magnetic field along the drift coordinate is assumed. The main outputs of this step  
2611 are `simb::MCParticle` objects for the generated Geant4 particles, `gar::EnergyDeposit`  
2612 data products for the energy deposits in the HPgTPC and `gar::CaloDeposit` data  
2613 products for the energy deposits in the ECal and muon system.

### 2614 6.1.2 Detector simulation

2615 The standard detector simulation step in GArSoft is all run with a single FHiCL, but  
2616 the different modules can be run independently as well. First the `IonizationReadout`  
2617 module simulates the charge readout of the HPgTPC, and later the `SiPMReadout` module  
2618 runs twice, once for the ECal and then for the muon system, with different configurations.

2619 The `IonizationAndScintillation` module collects all the `gar::EnergyDeposit`  
2620 data products, to compute the equivalent number of ionization electrons for each energy

---

and the number of particles in the event. Each following line contains 15 entries to describe each particle. The entries are: status code, pdg code for the particle, entry of the first mother for this particle, entry of the second mother for this particle, entry of the first daughter for this particle, entry of the second daughter for this particle, x component of the particle momentum, y component of the particle momentum, z component of the particle momentum, energy of the particle, mass of the particle, x component of the particle initial position, y component of the particle initial position, z component of the particle initial position and time of the particle production.

## CHAPTER 6. PARTICLE ID IN ND-GAr

deposit. The `ElectronDriftAlg` module simulates the electron diffusion numerically both in the longitudinal and transverse directions and applies an electron lifetime correction factor. The induced charge on the nearest and neighbouring readout pads is modeled using the provided pad response functions. The digitisation of the data is then simulated with the `TPCReadoutSimAlg` module. By default, the ADC sampling rate used is 50.505 MHz. The resulting raw waveforms for each channel are stored with zero-suppression, in order to save memory and CPU time. The algorithms keep blocks of ADC values above a certain threshold, plus some adjustable additional early and late tick counts. The results of these three steps are `gar::raw::RawDigit` data products.

For the ECal and the muon system the `SiPMReadout` module calls either the `ECALReadoutSimStandardAlg` or `MuIDReadoutSimStandardAlg` modules. These take all the `gar::CaloDeposit` data products in the corresponding detector and do the digitisation depending on whether the hit was in a tile or strip layer. They include single photon statistics, electronic noise, SiPM saturation and time smearing. The resulting objects are `gar::raw::CaloRawDigit` data products.

### 6.1.3 Reconstruction

The reconstruction in GArSoft is also run as a single job by default. It first runs the hit finding, clustering, track fitting and vertex identification in the HPgTPC, followed by the hit finding and clustering in the ECal and muon system. After those it produces the associations between the associations between the tracks and the ECal clusters.

Focusing first on the HPgTPC reconstruction, the `CompressedHitFinder` module takes the zero-suppressed ADCs from the `gar::raw::RawDigit` data products. The reconstructed hits largely correspond to the above threshold blocks, however the hit finder identifies waveforms with more than one maximum, diving them in multiple hits if they dip below a certain threshold. The data products produced are of the form `gar::rec::Hit`. These are the inputs to the clustering of hits in the `TPCHitCluster` module. Hits close in space and time are merged, and the resulting centroids are found. This module outputs `gar::rec::TPCClusters` objects and associations to the input

## 6.1. GARSOFT

2649 hits.

2650 The following step prior to the track fitting is pattern recognition. The module  
2651 called `tpcvechitfinder2` uses the `gar::rec::TPCClusters` data products to find track  
2652 segments, typically called vector hits. They are identified by performing linear 2D fits  
2653 to the positions of the clusters in a 10 cm radius, one fit for each coordinate pair. A  
2654 3D fit defines the line segment of the vector hit, using as independent variable the one  
2655 whose sum of (absolute value) slopes in the 2D fits is the smallest. The clusters are  
2656 merged to a given vector hit if they are less than 2 cm away from the line segment. The  
2657 outputs are `gar::rec::VecHit` data products, as well as associations to the clusters. The  
2658 `tpcpatrec2` module takes the `gar::rec::VecHit` objects to form the track candidates.  
2659 The vector hits are merged together if their direction matches, their centers are within  
2660 60 cm and their direction vectors point roughly to their respective centers. Once  
2661 the clusters of vector hits are formed they are used to make a first estimation of the  
2662 track parameters, simply taking three clusters along the track. The module produces  
2663 `gar::rec::Track` data products and associations between these tracks and the clusters  
2664 and vector hits.

2665 The track is fitted by means of a Kalman filter in the `tpctrackfit2` module, using  
2666 the position along the drift direction as the independent variable. Two different fits are  
2667 performed per track, a forward and a backwards fit, each starting from one of the track  
2668 ends. The Kalman filter state vector ( $y, z, R, \phi, \tan\lambda$ ) is estimated at each point along  
2669 the track using a Bayesian update. The track parameters reported in the forward and  
2670 backwards fits are the ones computed at the opposite end where the fit started. The  
2671 main outputs of the track fit are the `gar::rec::Track` objects. Additionally, the module  
2672 stores the fitted 3D positions along the track in the `gar::rec::TrackTrajectory` data  
2673 products and the total charge and step sizes for each point also get stored in the form of  
2674 `gar::rec::TrackIonization` objects.

2675 After the tracking step, the `vertexfinder1` module looks at the reconstructed  
2676 `gar::rec::Track` products, creating vertex candidates with the track ends that are  
2677 within 12 cm of each other. The vertices are then fitted using linear extrapolations from

## CHAPTER 6. PARTICLE ID IN ND-GAr

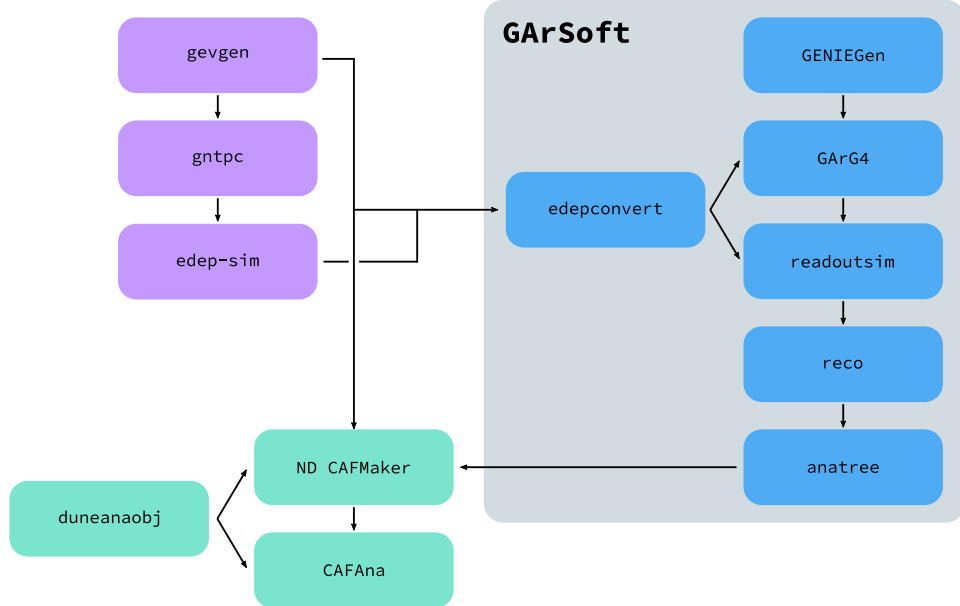


**Figure 6.1:** Schematic diagram showing the different modules involved in the ND-GAr production.

the different track ends associated. The results are `gar::rec::Vertex` data products, and associations to the tracks and corresponding track ends.

For the ECal and muon tagger, the `SiPMHitFinder` module runs twice with different configurations, adapted to the particular capabilities of both. The module simply takes the `gar::raw::CaloRawDigit` products, applies a calibration factor to convert the ADC counts to MeV and for the strip layer hits it calculates the position along the strip using the times recorded of both SiPMs. This module produces `gar::rec::CaloHit` data products. Next, these objects are used as inputs to the `CaloClustering` module. It merges the hits based on a simple nearest neighbours (NN) algorithm. For the resulting clusters it also computes the total energy and position of the centroid. The results are stored as `gar::rec::Cluster` data products, with associations to the hits.

The last step in the reconstruction is associating the reconstructed tracks in the HPgTPC to the clusters formed in the ECal and muon system. The `TPCECALAssociation` module checks first the position of the track end points, considering only the points that are at least 215 cm away from the cathode or have a radial distance to the center

## 6.2. $dE/dx$ MEASUREMENT IN THE TPC

2693 greater than 230 cm. The candidates are propagated up to the radial position, in the  
2694 case of clusters in the barrel, or the drift coordinate position, for the end cap cluster, of  
2695 the different clusters in the collection using the track parameters computed at the end  
2696 point. The end point is associated to the cluster if certain proximity criteria are met.  
2697 This module creates associations between the tracks, the end points and the clusters.  
2698 The criteria for the associations are slightly different for the ECal and the muon tagger.

### 2699 6.2 $dE/dx$ measurement in the TPC

2700 Among the parameters extracted from the track fitting, ionisation is particularly useful  
2701 for particle identification, as it is a function of the particle velocity. Although for the  
2702 case of relativistic particles this dependence is not very strong, measuring the track on  
2703 a large number of points may allow us to estimate the amount of ionisation accuratel.  
2704 This, paired with a measurement of the momentum, may allow us to identify the particle  
2705 type.

2706 The first calculation of the energy loss per unit length of relativistic particles using a  
2707 quantum-mechanical treatment is due to Bethe [145]. Using this approach, the mean  
2708 ionisation rate of a charged particle traveling through a material medium is (using  
2709 natural units  $G = \hbar = c = 1$ ):

$$\left\langle \frac{dE}{dx} \right\rangle = \frac{4\pi Ne^4}{m_e \beta^2} z^2 \left( \log \frac{2m_e \beta^2 \gamma^2}{I} - \beta^2 \right), \quad (6.1)$$

2710 where  $N$  is the number density of electrons in the medium,  $e$  the elementary charge,  $m_e$   
2711 is the electron mass,  $z$  the charge of the particle in units of  $e$ ,  $\beta$  is the velocity of the  
2712 particle,  $\gamma = (1 - \beta^2)^{-1}$  and  $I$  denotes the effective ionisation potential averaged over  
2713 all electrons. This relation is known as the Bethe-Bloch formula.

2714 From Eq. (6.1) one can see that the ionisation loss does not depend explicitly on  
2715 the mass of the charged particle, that for non-relativistic velocities it falls as  $\beta^{-2}$ , then  
2716 goes through a minimum and increases as the logarithm of  $\gamma$ . This behaviour at high  
2717 velocities is commonly known as the relativistic rise. The physical origin of this effect

## CHAPTER 6. PARTICLE ID IN ND-GAr

is partly due to the fact that the transverse electromagnetic field of the particle is proportional to  $\gamma$ , therefore as it increases so does the cross section.

It was later understood that the relativistic rise could not grow indefinitely with  $\gamma$ . A way to add this feature in the Bethe-Bloch formula is by introducing the so-called density effect term. It accounts for the polarisation effect of the atoms in the medium, which effectively shield the electromagnetic field of the charged particle halting any further increase of the energy loss [146]. Denoting the correction as  $\delta(\beta)$ , one can rewrite Eq. (6.1) as:

$$\left\langle \frac{dE}{dx} \right\rangle = \frac{4\pi Ne^4}{m_e \beta^2} z^2 \left( \log \frac{2m_e \beta^2 \gamma^2}{I} - \beta^2 - \frac{\delta(\beta)}{2} \right). \quad (6.2)$$

In general, the form of  $\delta(\beta)$  depends on the medium and its state of aggregation, involving the usage of tabulated parameters and implicit relations [147].

Another standard method to compute the amount of ionisation a charged particle produces is the so-called photo-absorption ionisation (PAI) model proposed by Allison and Cobb [148]. Within their approach, the mean ionisation is evaluated using a semiclassical calculation in which one characterises the continuum material medium by means of a complex dielectric constant  $\epsilon(k, \omega)$ . However, in order to model the dielectric constant they rely on the quantum-mechanical picture of photon absorption and collision. Therefore, in the PAI model the computation of the ionisation loss involves a numerical integration of the measured photo-absorption cross-section for the relevant material.

In a particle physics experiment, the typical way of determining the energy loss per unit length as a function of the particle velocity is studying identified particles over a range of momenta. Once we have established this relation we can use it for other, unknown particles. In this sense, it makes sense to have a regular mathematical expression for this relation that one can use.

It happens that neither the Bethe-Bloch theory nor the PAI model from Allison and Cobb offer a close mathematical form for the ionisation curve. This is the reason why a full parametrisation of the ionisation curves can be useful. A parametrisation originally proposed for the ALEPH TPC [149] and later used by the ALICE TPC [150] group that

## 6.2. dE/dx MEASUREMENT IN THE TPC

2745 manages to capture the features of the ionisation energy loss is:

$$f(\beta\gamma) = \frac{P_1}{\beta^{P_4}} \left( P_2 - \beta^{P_4} - \log \left[ P_3 + \frac{1}{(\beta\gamma)^{P_5}} \right] \right), \quad (6.3)$$

2746 where  $P_i$  are five free parameters. Hereafter, we will refer to Eq. (6.3) as the ALEPH

2747 dE/dx parametrisation.

### 2748 6.2.1 Energy calibration

2749 In order to obtain the amount of energy loss by a charged particle due to ionisation  
2750 in our TPC we need to determine the conversion between the charge deposited in our  
2751 readout planes and the actual energy depositions. This procedure is known as energy  
2752 calibration.

2753 In a general, the first step of the calibration involves a non-uniformity correction,  
2754 to make sure that the detector response is uniform throughout the TPC. These are  
2755 typically divided into three categories, non-uniformities in the transverse  $YZ$  plane,  
2756 non-uniformities along the drift direction  $X$  and variations of the detector response  
2757 over time (would not apply to us as the detector is not built yet). These would correct  
2758 for effects such as electron diffusion and attenuation, space charge effects or channel  
2759 misconfiguration. However, because at the moment I am only interested in making sure  
2760 we recover a sensible result from our simulation, I will not apply uniformity corrections  
2761 to our charge deposits.

2762 Other effects, like electron-ion recombination or ADC saturation, lead to a non-linear  
2763 relation between the observed charge and the deposited energy in the detector, with the  
2764 observed readout charge saturating at high ionisation energies. In this case, because we  
2765 are dealing with gaseous argon and therefore recombination is not as important as in  
2766 liquid, we do not simulate recombination effects in the TPC. Even so, the simulation of  
2767 the electronic response will still introduce charge saturation, and one needs to correct  
2768 for it in order to obtain the exact amount of energy loss due to ionisation.

2769 By default, the track fitting algorithm in GArSoft provides a `TrackIonization`

## CHAPTER 6. PARTICLE ID IN ND-GAr

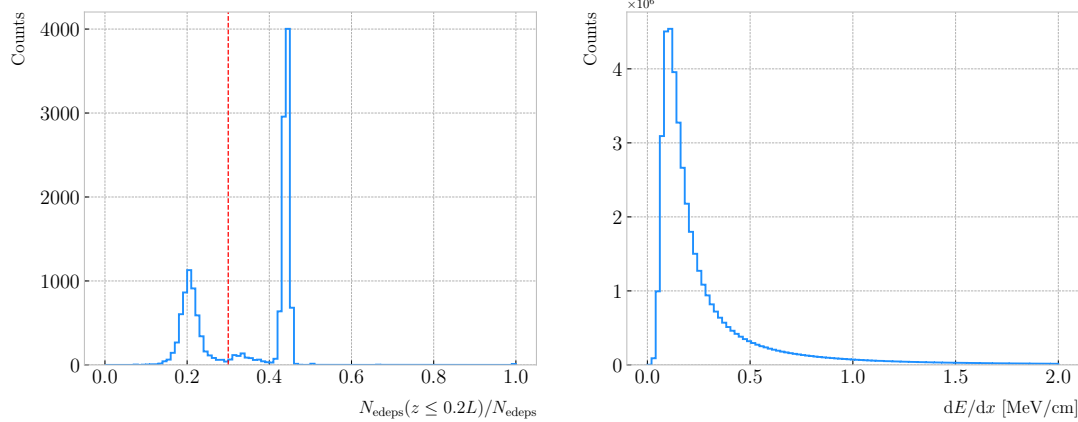


**Figure 6.2:** Left panel: distribution of the fraction of Geant4-level energy deposits per track with residual range less than 20% of the total track length, for the isotropic proton sample. Right panel: distribution of the ionisation per unit length of the energy deposits in the proton sample after removing the tracks with less than 30% of their energy deposits in the last 20% of the track.

object associated to each reconstructed track. It contains two collections of charge deposits, one for each fitting direction, consisting on pairs of charge values ( $dQ$ , in ADC) and step sizes ( $dx$ , in cm).

In order to estimate the ionisation loss in the ND-GAr TPC, I have used an MC sample consisting of single, isotropic protons propagating in the TPC. The starting points of the protons were sampled inside a  $50 \times 50 \times 25$  cm box centered at  $(100, -150, 1250)$ , and their momenta are uniformly distributed in the range  $0.25 - 1.75$  GeV. I ran the simulated sample through GArSoft's default detector simulation and reconstruction, and then a custom analyser module that extracts the ionisation data together with other reconstructed track information from the Kalman fit.

For studying the energy loss of the protons I select the reconstructed tracks that range out (i.e. slow down to rest) inside the TPC. A characteristic feature of the energy loss profile of any stopping ionising particle is the so-called Bragg peak, a pronounced peak that occurs immediately before the particle comes to rest. From Eq. (6.1) we can see that this behaviour is expected, as the energy loss for non-relativistic particles is inversely proportional to  $\beta^2$ . In data, a way of identifying the Bragg peak, and thus select the stopping particles, is checking the number of energy deposits towards the

## 6.2. $dE/dx$ MEASUREMENT IN THE TPC

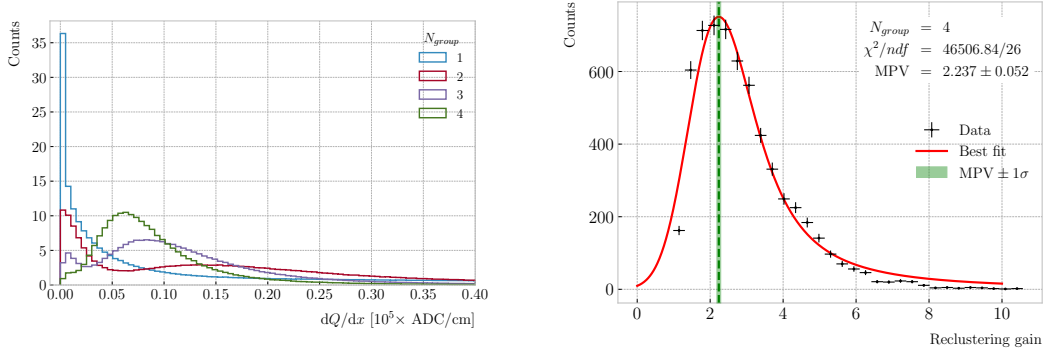


**Figure 6.3:** Left panel: distribution of the reconstructed ionisation charge per unit length for our MC stopping proton sample. The different colors indicate how many consecutive  $dQ/dx$  pairs were grouped together. Right panel: distribution of the median change in  $dQ/dx$  per track after  $N_{group} = 4$  clusters were reclustered together.

end of the track. In this case, I count the fraction of the Geant4 simulated energy deposits with a residual range value (the distance from a given energy deposit to the last deposit in the track trajectory) less than a 20% of the corresponding track length<sup>2</sup>. The distribution of this fraction of energy deposits for our proton sample is shown in Fig. 6.2 (left panel). We can clearly see two well separated peaks in this distribution, one centered at 0.2 and another, narrower, one centered at a higher value. The first one corresponds to non-stopping protons, as in that case the number of energy deposits towards the end of the track is uniformly distributed due to the absence of the Bragg peak. In that way, I apply a cut in this distribution, requiring that at least 30% of the simulated energy deposits sit in the last 20% of the tracks, to ensure that the Bragg peak is present.

Figure 6.2 (right panel) shows the distribution of the energy loss per unit length for the Geant4 simulated energy deposits of the selected stopping protons. We can see that it follows the expected shape of a Landau distribution, which describes the fluctuations of the ionisation energy losses [151]. This distribution has a characteristic asymmetric PDF, with a long right tail that translates into a high probability for high-energy ionisation losses. The origin of these fluctuations is mainly the possibility of transferring a high

<sup>2</sup>As we are applying this selection at the Geant4 level we could have simply selected the stopping protons using the `EndProcess` labels from the simulation. However, the Bragg peak identification method displayed here could serve as a starting point for a selection of stopping protons in real data.

## CHAPTER 6. PARTICLE ID IN ND-GAr

2804 enough energy to an electron, so it becomes a ionising particle itself.

2805 Now, from the point of view of the reconstruction, the objects that we have available  
 2806 to extract the ionisation information for the different reconstructed tracks are the  
 2807 collections of  $dQ$  and  $dx$  pairs, as stated before. The  $dQ$  values come from adding up  
 2808 the amplitude of all the reconstructed hits in a cluster, which is the input object to the  
 2809 Kalman fit.

2810 Figure 6.3 (left panel) shows the distribution of the ionisation charge deposits  
 2811 per unit length for the track in the stopping proton sample (blue line). As one can  
 2812 notice, this distribution does not resemble the expected shape of the Landau PDF. This  
 2813 distribution peaks sharply at 0 and has a heavy tailed behaviour. Notice, however, how  
 2814 the distribution changes its shape as we group together  $N_{group}$  consecutive charge deposit  
 2815 pairs (red, purple and green lines). The distribution in the  $N_{group} = 4$  case already has  
 2816 a shape which resembles that of the Geant4-level ionisation per unit length, so I will  
 2817 proceed using this amount of reclustering for the reconstruction-level depositions.

2818 An extra factor I need to account for, when reclustering is applied, is how the overall  
 2819  $dQ/dx$  per track changes. To do so, we can look at the ratio between the median  $dQ/dx$   
 2820 after and before the reclustering. Figure 6.3 (right panel) shows the median enhancement  
 2821 in  $dQ/dx$  per track for the stopping proton sample in the case  $N_{group} = 4$ . Fitting a  
 2822 Landau distribution convolved with a Gaussian<sup>3</sup>, I estimate the most probable value of  
 2823 this ratio to be  $G_{group} = 2.24 \pm 0.05$ .

2824 At this point, I am left with determining the conversion between the charge deposits  
 2825 per unit length  $dQ/dx$  and the energy deposits per unit length  $dE/dx$ . To this end, we  
 2826 need a way of comparing the two. I can use the residual range  $z$  to get a prediction of  
 2827 the most probable  $dE/dx$  by using the following empirical parametrisation [152]:

$$\frac{dE}{dx}(z) = \frac{z^{\frac{1}{p}-1}}{p\Lambda^{\frac{1}{p}}}, \quad (6.4)$$

2828 which is quoted in the literature as the Bragg-Kleeman formula. In order to obtain the

---

<sup>3</sup>In the literature, this distribution is often referred to as Landau+Gaussian or langau. In the following, I will use LanGauss to refer to such PDF.

## 6.2. $dE/dx$ MEASUREMENT IN THE TPC

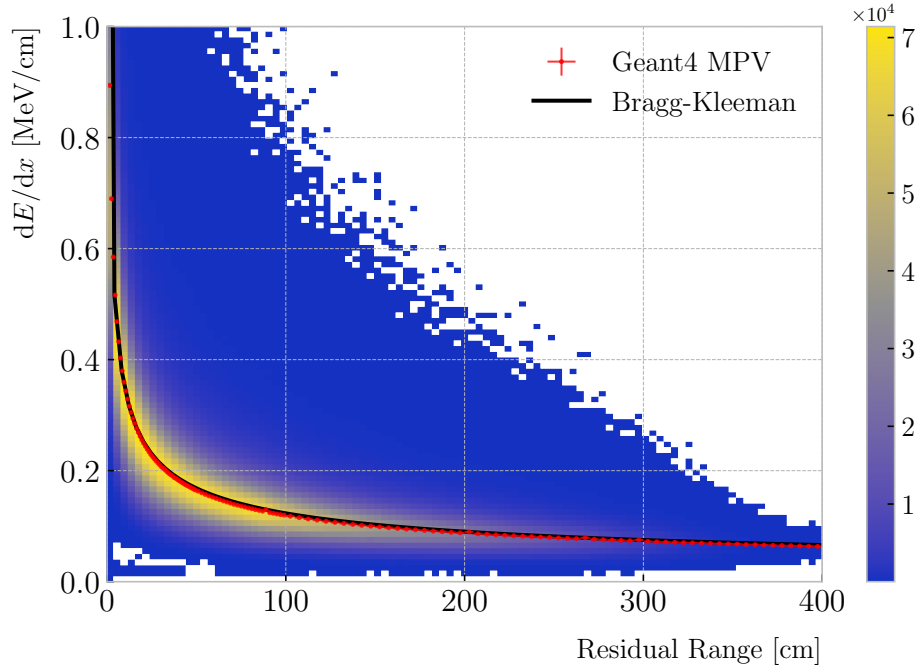


**Figure 6.4:** Distribution of the Geant4-simulated energy losses per unit length versus residual range for the stopping proton sample. The overlaid points represent the fitted most probable value of the  $dE/dx$  distribution in each residual range bin, whereas the curve is their best fit to the Bragg-Kleeman formula from Eq. (6.4).

2829  $p$  and  $\Lambda$  parameters I perform a fit using the energy losses and the residual ranges given  
 2830 by the Geant4 stage of our proton sample.

2831 Within our simulation, the residual range is sampled with a maximum size of  
 2832 5 mm. Therefore, to perform the fit to the Bragg-Kleeman formula, we can use a  
 2833 fine-grained residual range binning. For each of the residual range bins I extract the  
 2834  $dE/dx$  distribution and fit it to a LanGauss distribution, to obtain the value of the  
 2835 most probable  $dE/dx$  in the bin together with a statistical uncertainty. I then fit Eq.  
 2836 (6.4) to these most probable values and the centres of the residual range bins. This  
 2837 procedure is depicted in Fig. 6.4, where I show the distribution of the energy loss per  
 2838 unit length versus the residual range, together with the most probable  $dE/dx$  values  
 2839 and their uncertainty in each bin (red points) and the curve with the best fit of the  
 2840 Bragg-Kleeman relation to those values (black line). The best fit is obtained for the

## CHAPTER 6. PARTICLE ID IN ND-GAr

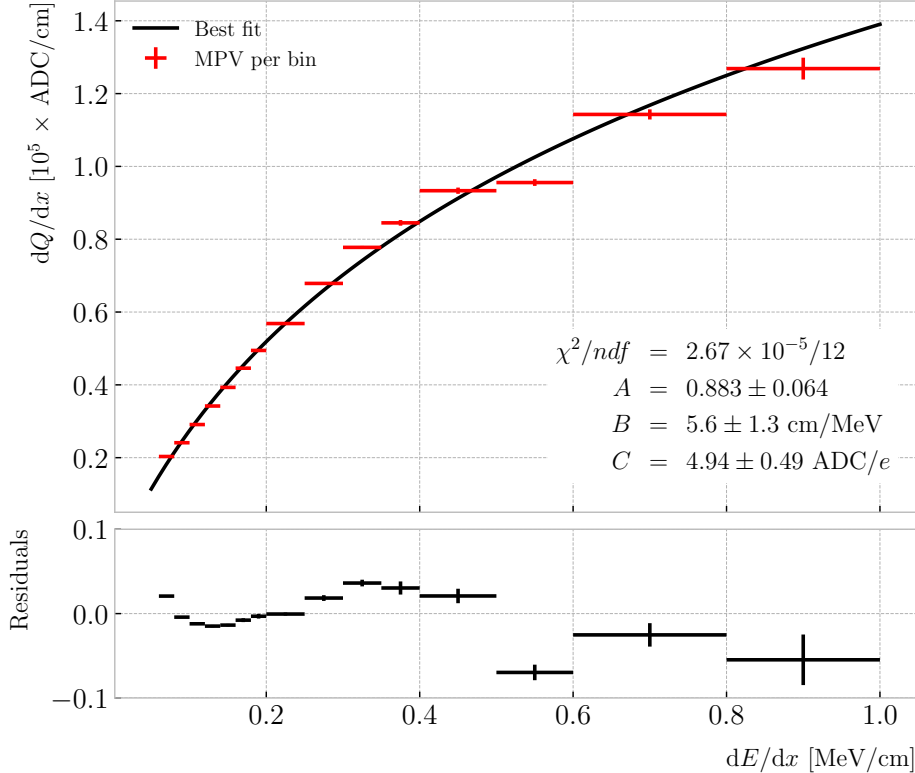


**Figure 6.5:** Fitted most probable  $dQ/dx$  values for each  $dE/dx$  bin (red points), obtained from the stopping proton sample. The overlaid curve (black line) represents the best fit to the logarithmic calibration function from Eq. (6.5).

2841 parameter values  $p = 1.8192 \pm 0.0005$  and  $\Lambda = 0.3497 \pm 0.0008 \text{ cm}/\text{MeV}^{p^4}$ .

2842 Having an analytical expression that relates the residual range to  $dE/dx$ , I can take  
 2843 our reconstruction-level residual ranges from the stopping proton sample and compute  
 2844 the most probable energy loss associated.

2845 In order to parametrise the charge saturation, we can use the following logarithmic  
 2846 function inspired by the modified box model for recombination:

$$\frac{dE}{dx} = \frac{e^{\frac{dQ}{dx} B \frac{W_{ion}}{G_{group} C}} - A}{B}, \quad (6.5)$$

2847 where  $A$  and  $B$  are the calibration parameters we need to determine,  $W_{ion}$  is the average  
 2848 energy to produce an electron-ion pair,  $G_{group}$  is the gain from the reclustering discussed

---

<sup>4</sup>These strange units for  $\Lambda$  come from dimensional analysis, just to keep the Bragg-Kleeman formula (6.4) consistent.

## 6.2. $dE/dx$ MEASUREMENT IN THE TPC

**Table 6.1:** Calibration parameters obtained from the fit of the ND-GAr simulated stopping proton sample to the calibration function from Eq. (6.5). The fits were performed for the 10, 12, and 16-bit ADC limits.

	$\chi^2/ndf$	Best fit $\pm 1\sigma$		
		$A$	$B$ (cm/MeV)	$C$ (ADC/e)
10-bit	$1.83 \times 10^{-6}/12$	$-9.3 \pm 3.9$	$270 \pm 69$	$27.1 \pm 5.4$
12-bit	$2.67 \times 10^{-5}/12$	$0.883 \pm 0.064$	$5.6 \pm 1.3$	$4.94 \pm 0.49$
16-bit	$1.44 \times 10^{-5}/12$	$0.949 \pm 0.024$	$3.53 \pm 0.58$	$4.52 \pm 0.29$

above and  $C$  is the calibration constant to convert number of electrons to ADC counts, commonly refer to as gain (also to be obtained in the fit). In this case, I use a value for the electron-ion production energy of  $W_{ion} = 26.4$  eV [153]. This value, used in our simulation as well, was measured for gaseous argon in normal conditions, and therefore should be checked in the future to describe correctly the high-pressure argon-CH<sub>4</sub> mixture of ND-GAr.

For the calibration fit I follow a procedure similar to the previous one for Eq. (6.4). Binning the  $dE/dx$  range, I fit a LanGauss distribution to the corresponding  $dQ/dx$  distribution to obtain the most probable value. The resulting data points (red bars) are shown in Fig. 6.5 (top panel), the horizontal error bars depict the width of the  $dE/dx$  bin whereas the vertical bars represent the error associated to the most probable value estimation. A fit to the logarithmic function in Eq. (6.5) is also shown (black line). For this I weighted the data points using the inverse of their relative error, obtaining a reduced chi-square value of  $\chi^2/ndf = 2.22 \times 10^{-6}$ . The best fit parameters I found from this fit are  $A = 0.883 \pm 0.064$ ,  $B = 5.6 \pm 1.3$  cm/MeV and  $C = 4.94 \pm 0.49$  ADC/e. Figure 6.5 (bottom panel) shows the residuals between the data points and the fit.

The value for the gain I obtained from the fit is in reasonable agreement with our expectation. This value is set in GArSoft to 5 ADC/e by default.

One interesting thing to check is what induces this non-linear relation between charge and energy. The only effects that modify the amount of electrons reaching the readout planes in the simulation are the transverse diffusion and the finite electron lifetime. Once the electrons reach the readout chambers, the pad response functions are applied,

## CHAPTER 6. PARTICLE ID IN ND-GAr

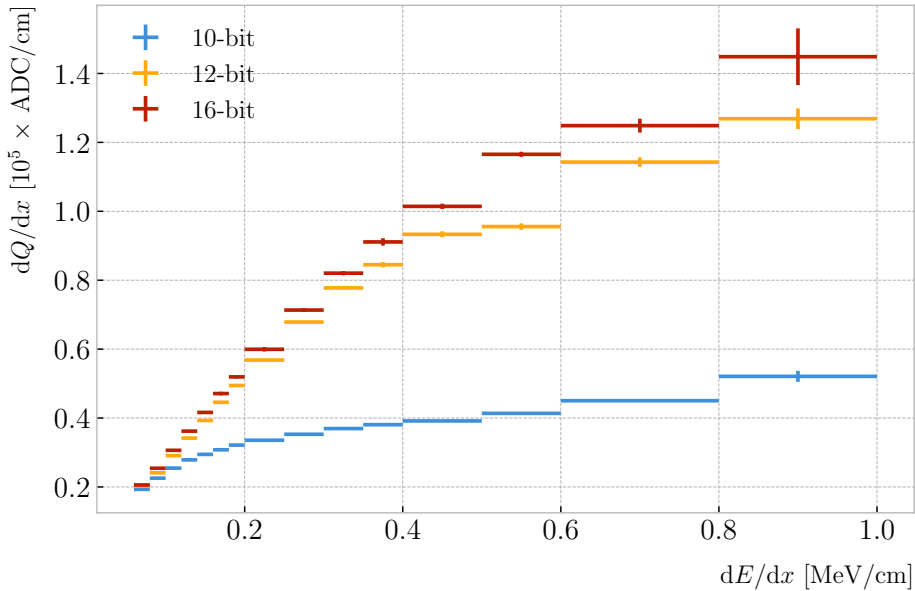


**Figure 6.6:** Fitted most probable  $dQ/dx$  values for each  $dE/dx$  bin for three different ADC bit limits, 10 (blue points), 12 (default, yellow points) and 16-bit (red points).

2871 together with an electrons-to-ADC conversion and the ADC saturation limit.

2872 By default, GArSot applies a 12-bit ADC limit, which can be changed in the  
 2873 simulation configuration. However, it can only be increased up to 16-bit, as we represent  
 2874 the ADC collection as a `std::vector<short>`. This way, I tried to change the saturation  
 2875 parameter to see how it affects the relation between reconstructed charge and energy.  
 2876 Figure 6.6 shows a comparison between the most probable  $dQ/dx$  for 10, 12 and 16-  
 2877 bit ADC limits. As expected, the lower the limit is the sooner the charge saturates.  
 2878 For higher ADC limits the relation between energy and charge remains linear up to  
 2879 higher  $dE/dx$  values, but even for the 16-bit limit the saturation is noticeable for values  
 2880  $\gtrsim 0.5$  MeV/cm.

2881 Table 6.1 shows the results of fitting the samples with 10 and 16-bits ADC limits to  
 2882 the calibration function from Eq. (6.5), using the weights based on their relative error  
 2883 as described previously. One interesting feature to notice is how different the best fit  
 2884 points look for the 10-bit ADC saturation when compared to the other two, which are  
 2885 consistent with each other.

2886 At this point we can compare the  $dE/dx$  distribution one gets from Geant4, i.e. the

## 6.2. $dE/dx$ MEASUREMENT IN THE TPC

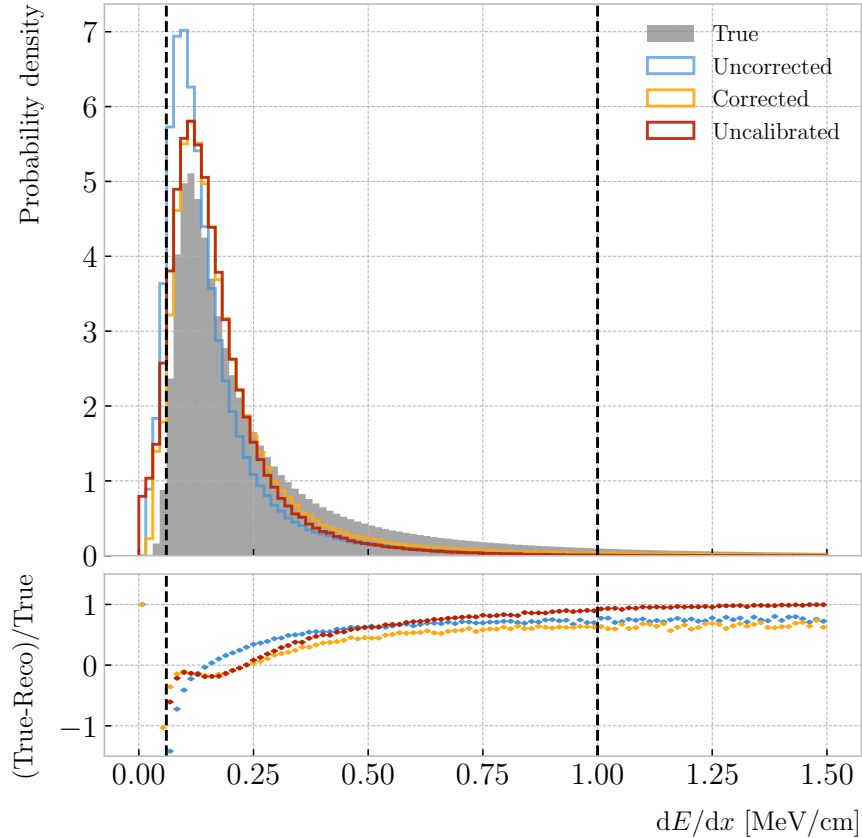


**Figure 6.7:** Top panel: area normalised  $dE/dx$  distributions for the true (solid grey) and the reconstructed energy deposits in the stopping proton sample, both after applying the calibration (blue) and the calibration and the normalisation correction (yellow). Also shown is the distribution obtained by applying a correction factor to the  $dQ/dx$  values but not the calibration (red). Bottom panel: fractional residuals for the uncorrected (blue), corrected (yellow) and uncalibrated (red) samples.

2887 true energy loss distribution, and the distribution I found by applying the calibration  
 2888 function to our collection of reconstructed  $dQ/dx$  values. Figure 6.7 (top panel) shows  
 2889 the true (solid grey) and reconstructed (blue, labeled as uncorrected) distributions  
 2890 together. The dashed vertical lines indicate the region of validity of the calibration fit, i.e.  
 2891 the left and right edges of the first and last  $dE/dx$  bin respectively. Notice that these  
 2892 histograms are area-normalised, as the total number of true energy deposits is much  
 2893 higher than the number of reconstructed charge deposits. This is due to a combination  
 2894 of effects, like the finite spatial resolution of the detector, the hit clustering used in the  
 2895 track fitting and the reclustering we have applied here.

## CHAPTER 6. PARTICLE ID IN ND-GAr

2896        The two distributions are significantly different. That can be seen clearly when  
2897        looking at the fractional residuals, shown in Fig. 6.7 (bottom panel). In particular,  
2898        the position of the peak is off, which could bias the mean energy loss predictions. It  
2899        seems like the difference between these may be due to an overall scaling factor. One  
2900        possibility is to scale the most probable value of the reconstructed distribution to  
2901        the most probable value predicted by Geant4. I do this by fitting both distributions  
2902        using a LanGauss function, obtaining  $dE/dx_{MPV, true} = 0.1145 \pm 0.0005$  MeV/cm and  
2903         $dE/dx_{MPV, reco} = 0.0928 \pm 0.0005$  MeV/cm for the true and reconstructed most probable  
2904        values respectively. These can be translated into an scaling factor  $S = 0.579 \pm 0.006$ .

2905        The result of applying the scaling correction can be seen in Fig. 6.7 (top panel).  
2906        The corrected  $dE/dx$  distribution (yellow, labeled as corrected) peaks around the same  
2907        value the true distribution does, as expected. Moreover, the high energy region is also  
2908        slightly better described. For low ionisations, below the lower limit of the calibration  
2909        fit, the differences between true and reconstructed are still significant. This low energy  
2910        excess may be migration of some events from the peak region. The overall effect of the  
2911        correction can be seen in the fractional residual plot in Fig. 6.7 (bottom panel).

2912        One can also check what happens if instead of applying the logarithmic calibration we  
2913        simply scale the  $dQ/dx$  distribution (post reclustering) to have the same most probable  
2914        value as the true  $dE/dx$  distribution. In this case, following an analogous procedure to the  
2915        one described earlier, I found the scaling factor  $S_{uncalibrated} = 0.414 \pm 0.002$  MeV/ADC<sup>5</sup>.  
2916        The resulting distribution (red, labeled as uncalibrated) is also shown in in Fig. 6.7 (top  
2917        panel). The behaviour of the new distribution is similar to the corrected case at low  
2918        energy losses, around the peak of the true distribution, but it is worse at describing the  
2919        high energy tail. This is expected, it is in the high ionisation regime where saturation  
2920        effects apply and therefore calibration is needed.

## 6.2. $dE/dx$ MEASUREMENT IN THE TPC

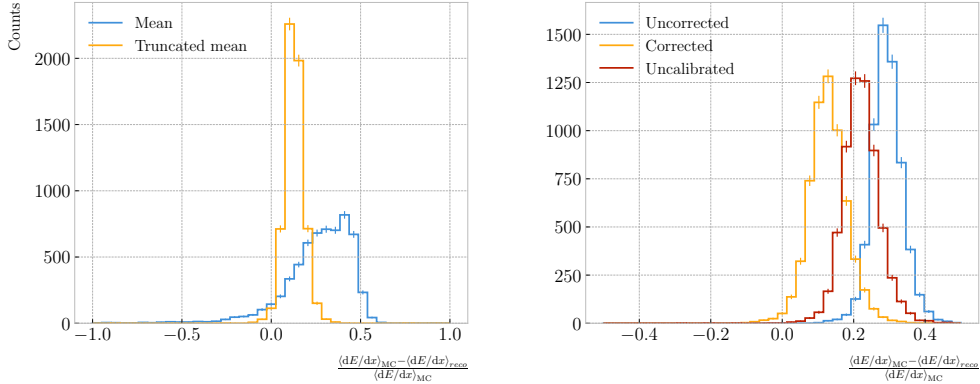


**Figure 6.8:** Left panel: fractional residuals between the true and the corrected  $dE/dx$  means (blue) and the 60% truncated means (yellow), for each event in the stopping proton sample. Right panel: fractional residuals between the true and the uncorrected (blue), corrected (yellow) and uncalibrated (red)  $dE/dx$  60% truncated means, for each event in the stopping proton sample.

### 2921 6.2.2 Truncated $dE/dx$ mean

2922 Once we have a collection of  $dE/dx$  values for each reconstructed track, we can compute  
 2923 the corresponding most probable ionisation loss per unit length of the particle. This  
 2924 is the value predicted by the Bethe-Bloch or the PAI models, and together with a  
 2925 measurement of the momentum it allows for particle identification.

2926 However, estimating the most probable  $dE/dx$  value for each reconstructed track  
 2927 is not a trivial task. As mentioned before, the  $dE/dx$  distributions follow Landau-like  
 2928 distributions. Therefore, one should perform e.g. a LanGauss fit to correctly estimate  
 2929 the most probable values. Automating this kind of fits is often problematic, as they  
 2930 usually incur in convergence problems. Moreover, the reconstructed  $dE/dx$  distributions  
 2931 we obtain tend to have relatively small statistics, which may also produce poor fits. In  
 2932 practice, doing these unsupervised fits may degrade our performance, and a more robust  
 2933 method is preferred.

2934 A possibility could be taking the mean of the reconstructed  $dE/dx$  distribution for  
 2935 each particle. The problem with this approach is that the high energy Landau tail,  
 2936 combined with our limited statistics, can induce large fluctuations in the computation

---

<sup>5</sup>Notice that now the scaling factor is not dimensionless, as it acts more like a conversion factor here.

## CHAPTER 6. PARTICLE ID IN ND-GAr

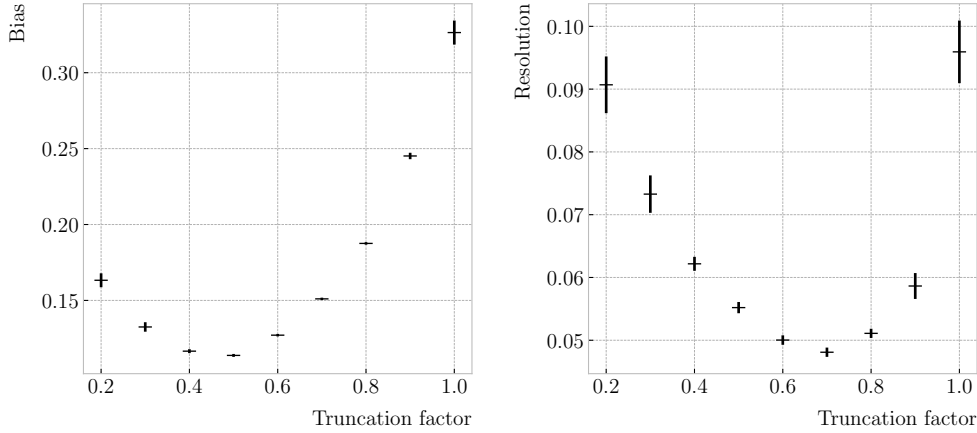


**Figure 6.9:** Estimated values of the mean  $dE/dx$  bias (left panel) and resolution (right panel) obtained using the corrected data from the stopping proton sample, for different values of the truncation factor.

2937 of the mean. Imagine you have two protons with the same kinetic energy, but due to  
 2938 reconstruction problems in one case you did not get as many charge deposits reconstructed  
 2939 in its high ionisation loss region. If you do not remove the tails the computed  $dE/dx$   
 2940 means will be significantly different.

2941 In order to avoid those fluctuations, one can compute the mean of a truncated  $dE/dx$   
 2942 distribution instead. By keeping only a given fraction of the lowest energy deposits  
 2943 we obtain an estimate of the mean energy loss that is more resilient to reconstruction  
 2944 inefficiencies and statistical effects. Figure 6.8 (left panel) shows a comparison between  
 2945 the  $\langle dE/dx \rangle$  computed by taking the mean of the full distribution (blue line) and the  
 2946 60% lowest energy clusters (yellow line), for the stopping proton sample. The fractional  
 2947 residuals are computed for each proton, taking the corresponding means using their  
 2948 collections of true and reconstructed energy deposits. One can see that using the simple  
 2949 mean translates into a high bias and uncertainty in the  $\langle dE/dx \rangle$  estimation, whereas  
 2950 applying the truncation reduces both significantly.

2951 Additionally, I performed a comparison between the 60% truncated mean  $dE/dx$   
 2952 obtained using the different calibration methods discussed earlier, namely the uncorrected  
 2953 (blue), corrected (yellow) and uncalibrated (red) distributions. The results are shown  
 2954 in Fig. 6.8 (right panel). While the widths of these distributions are similar, the bias

## 6.2. $dE/dx$ MEASUREMENT IN THE TPC

2955 obtained for the corrected sample, i.e. calibration function and correction factor applied,  
 2956 is a factor of  $\sim 2$  lower than in the uncalibrated case and almost three times smaller  
 2957 than for the uncorrected sample.

2958 The next step is to optimise the level of truncation we are going to apply to our  
 2959 data. To do so, I used different truncation factors, i.e. the percentage of energy-ordered  
 2960 reconstructed energy deposits we keep to compute the mean, on the corrected  $dE/dx$   
 2961 sample of the stopping protons. Then, following the same procedure of computing the  
 2962 fractional residuals as before, I fitted the resulting histograms using a double Gaussian  
 2963 function. This is simply the sum of two Gaussian functions of the type:

$$g(x; \mu, \sigma, A) = A e^{-\frac{(x-\mu)^2}{2\sigma^2}}. \quad (6.6)$$

2964 I do not add the classical normalisation factor of the Gaussian,  $1/\sqrt{2\pi}\sigma$ , therefore  
 2965 the amplitude  $A$  simply represents the maximum of the function. One of the two  
 2966 Gaussian functions describes the core part of the distribution, while the other captures  
 2967 the behaviour of the tails.

2968 For each truncation factor, I look at the bias and the resolution I obtain. I define  
 2969 these as the weighted means of the corresponding parameters in the fits:

$$\bar{x} = \frac{A_{core} x_{core} + A_{tail} x_{tail}}{A_{core} + A_{tail}}, \quad (6.7)$$

2970 where  $A_{core}$  and  $A_{tail}$  are the amplitudes of the core and tail distributions respectively  
 2971 and  $x$  is either the mean  $\mu$  or the width  $\sigma$  of said distributions.

2972 Figure 6.9 shows the bias (left panel) and the resolution (right panel) I obtained  
 2973 for the stopping proton sample, using different values of the truncation. From these, it  
 2974 can be seen that a truncation factor of 50% minimises the bias in the estimation, while  
 2975 70% gives the best resolution. That way, I settled on the intermediate value of 60%  
 2976 truncation, which yields a  $\langle dE/dx \rangle$  resolution of  $5.00 \pm 0.08$  % for stopping protons.

## CHAPTER 6. PARTICLE ID IN ND-GAr

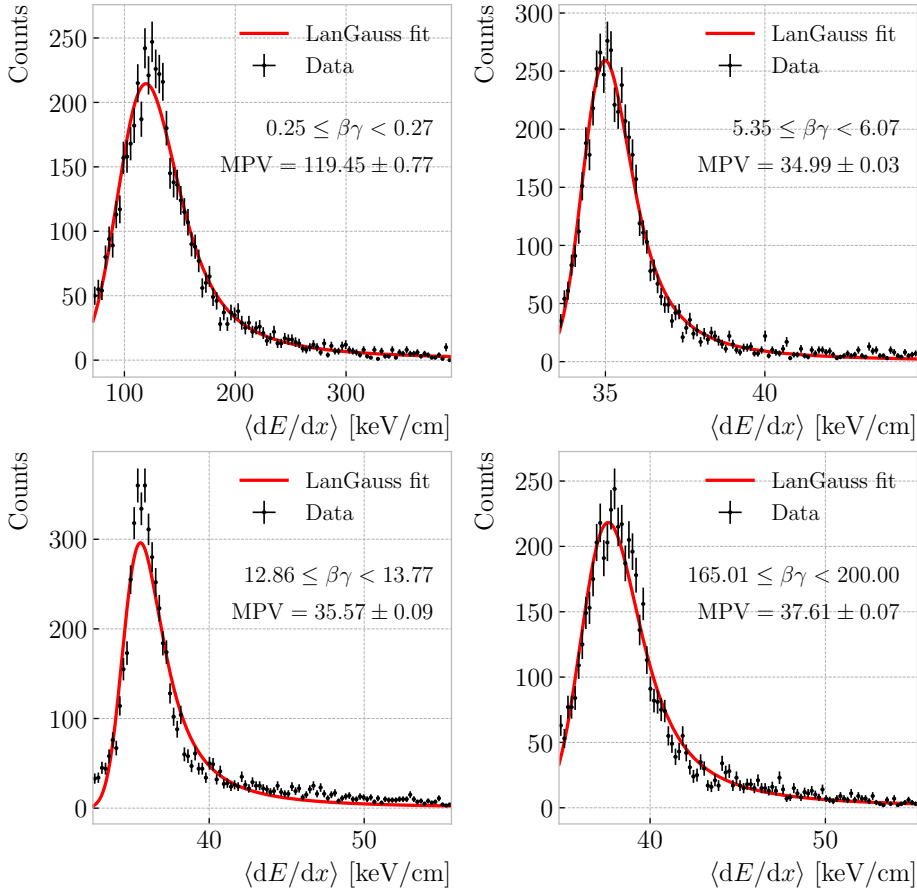


**Figure 6.10:** Examples of the truncated mean  $dE/dx$  LanGauss fits for various  $\beta\gamma$  bins, from a simulated FHC neutrino sample.

### 6.2.3 Mean $dE/dx$ parametrisation

Now that we have a way to estimate the mean energy loss of a particle in the HPgTPC, we can determine the value of the free parameters in the ALEPH formula, Eq. (6.3). For this, I used a sample of  $10^5$  reconstructed FHC neutrino events inside ND-GAr. In this case I cannot use the stopping proton sample, as we need to cover the full kinematic range of interest for the neutrino interactions in our detector.

The original data does not contain an estimation of the velocity of the tracks, instead the tracks have a value for the reconstructed momentum and the associated PDG code of the Geant4-level particle that created the track. Therefore, one can select some of the particles in the data, in this case I selected electrons, muons, pions and protons, and

## 6.2. $dE/dx$ MEASUREMENT IN THE TPC

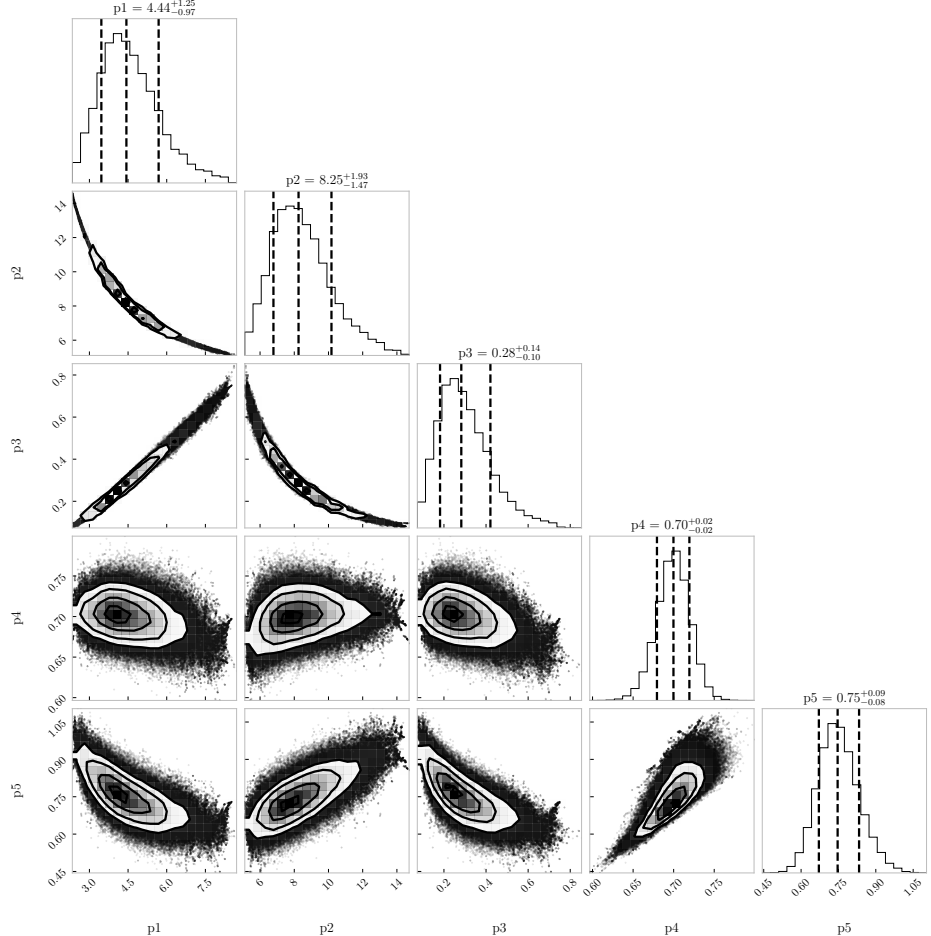


**Figure 6.11:** Resulting one and two dimensional projections of the posterior probability distributions of the ALEPH  $\langle dE/dx \rangle$  parameters obtained by fitting the 60% truncated mean  $dE/dx$  values from a FHC neutrino sample in ND-GAr. The vertical dashed lines in the 1D distributions represent the 16th, 50th and 84th percentiles.

2987 compute  $\beta$  and  $\gamma$  using the reconstructed momentum and their mass. In terms of  $\beta\gamma$   
 2988 the mean  $dE/dx$  does not depend on the particle species, so one can consider all the  
 2989 dataset as a whole. For this fit, I will express  $\beta$  in terms of the  $\beta\gamma$  product as:

$$\beta = \frac{\beta\gamma}{\sqrt{1 + (\beta\gamma)^2}}, \quad (6.8)$$

2990 which can be easily proven from the definition of  $\gamma$ .

2991 Next, I bin the data in  $\beta\gamma$ . I chose a fine binning so as to capture the different  
 2992 features of the ionisation curve. Instead of fixing the bin width, I select them so each one

## CHAPTER 6. PARTICLE ID IN ND-GAr

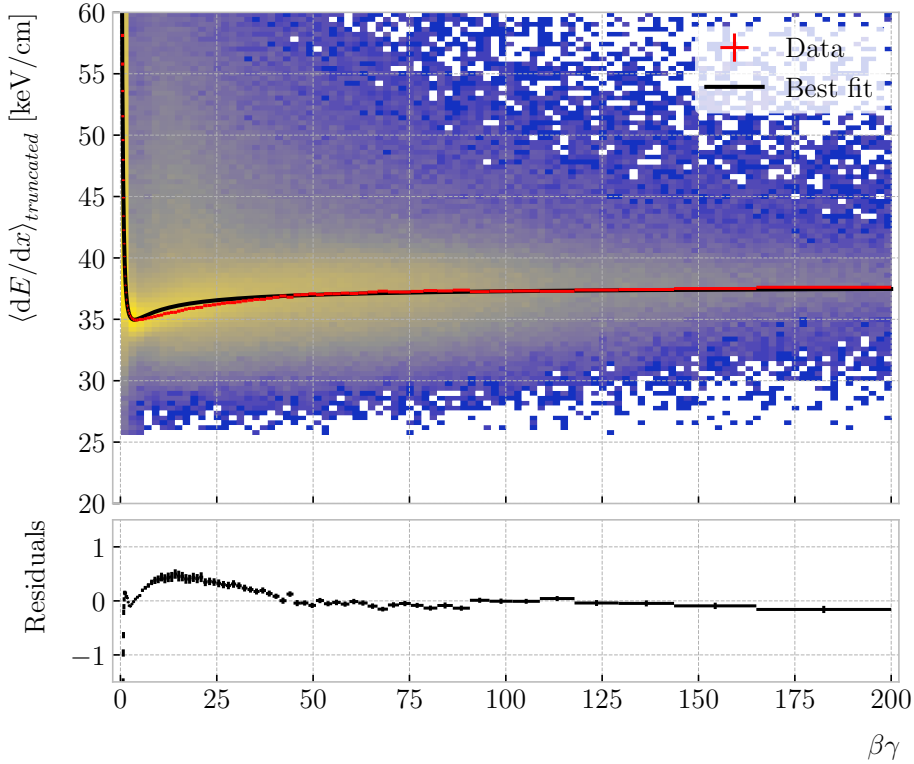


**Figure 6.12:** Truncated mean  $dE/dx$  obtained for the FHC neutrino sample as a function of the  $\beta\gamma$  product (upper panel). Also shown are the fitted most probable values for each  $\beta\gamma$  bin (red points) and the best fit obtained using the ALEPH parametrisation (black line). The residuals resulting from the fit are shown in the lower panel.

2993 has approximately the same statistics. Then, for each  $\beta\gamma$  slice, I compute the median  
 2994 and the interquartile range (IQR) of the  $\langle dE/dx \rangle$  distribution. Using these, I make a  
 2995 histogram in the range [median – IQR, median + 5 IQR], which I fit to a LanGauss  
 2996 function in order to extract the MPV. Using this range accounts for the asymmetric  
 2997 nature of the distributions, while also helps avoiding a second, lower maximum present  
 2998 at low  $\beta\gamma$ , probably a result of reconstruction failures.

2999 A few examples of these fits are shown in Fig. 6.10. The chosen values of  $\beta\gamma$  sit in  
 3000 very distinct points along the  $\langle dE/dx \rangle$  curve, going from the high ionisation region at  
 3001 low velocities (top left panel), to the minimum point (top right panel), the beginning of  
 3002 the relativistic rise (bottom left panel), and the plateau produced by the density effect  
 3003 (bottom right panel).

## 6.2. $dE/dx$ MEASUREMENT IN THE TPC

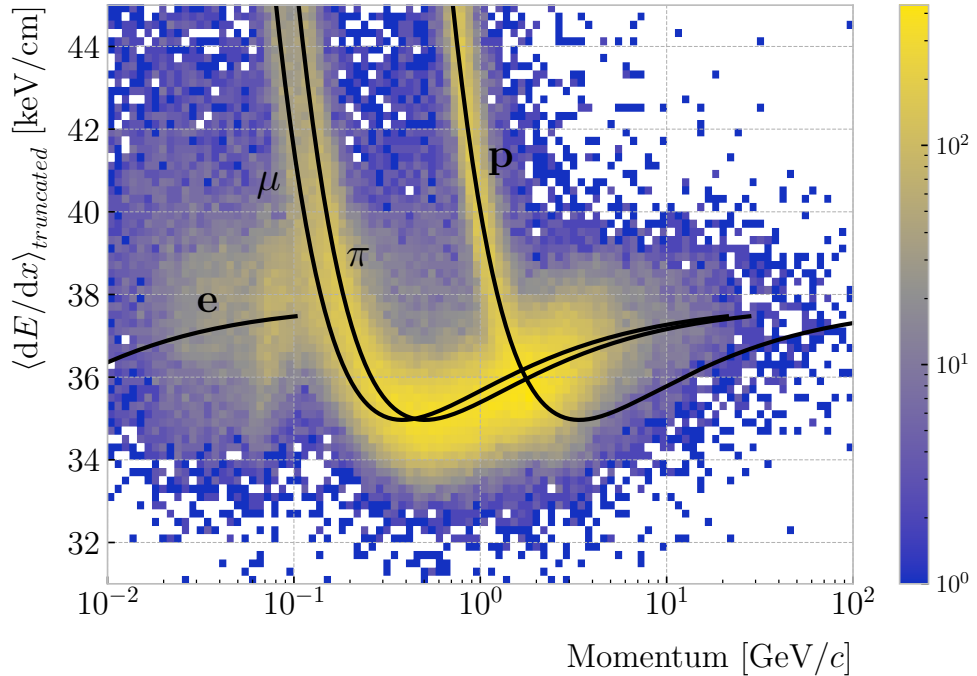


**Figure 6.13:** Distribution of the 60% truncated mean  $dE/dx$  versus reconstructed momentum for the FHC neutrino sample. The black lines indicate the predictions of the ALEPH parametrisation for electrons, muons, charged pions and protons.

3004 I used the resulting most probable  $\langle dE/dx \rangle$  values and the centres of the  $\beta\gamma$  bins as  
 3005 the points to fit to the ALEPH formula. For this particular fit I used the least-squares  
 3006 method to get a first estimation of the ALEPH parameters. Applying some uniform  
 3007 priors, I then used these values as the starting point of a 100000 steps MCMC. Figure 6.11  
 3008 shows the posterior probability distributions I obtain for each parameter. The reported  
 3009 best fit points are based on the 16th, 50th, and 84th percentiles in the marginalised  
 3010 distributions.

3011 The resulting fit (black line), compared to the data points (red points) and the  
 3012 underlying distribution is shown in Fig. 6.12 (top panel). The overall fit is good, with a  
 3013 reduced chi-squared of  $\chi^2/ndf = 1.02$ . However, there are some regions where the fit  
 3014 does not describe the data correctly, like the very low  $\beta\gamma$  regime, where the fit severely  
 3015 underestimates for energy losses  $\gtrsim 50$  keV/cm, and the start of the relativistic raise,  
 3016 where we have a slight overestimation. This is a result of those points having a larger  
 3017 uncertainty when compared to the ones around the dip or the plateau areas. These

## CHAPTER 6. PARTICLE ID IN ND-GAr

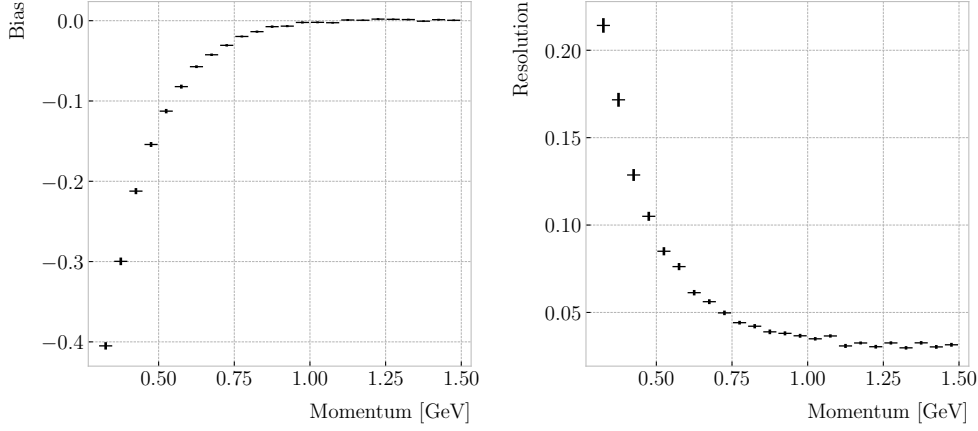


**Figure 6.14:** Estimated values of the mean  $dE/dx$  bias (left panel) and resolution (right panel) obtained for the true protons in a FHC neutrino sample.

3018 differences can be better seen in the residual plot, Fig. 6.12 (bottom panel).

### 3019 6.2.4 Particle identification

## 3020 6.3 Muon and pion separation in the ECal and MuID

3021 As it could be seen from Fig. 6.13, it is not possible to separate muons and charged pions  
 3022 in the HPgTPC using  $dE/dx$  for momenta  $\gtrsim 300 \text{ MeV}/c$ . In ND-GAr, approximately  
 3023 70% of the interactions in FHC mode will be  $\nu_\mu$  CC (compared to the 47% of  $\bar{\nu}_\mu$  CC  
 3024 interactions when operating in RHC mode), while 24% are neutral currents. Out of  
 3025 these, around 53% and 47% of them will produce at least one charged pion in the final  
 3026 state, respectively. Figure 6.15 shows a comparison between the spectra of the primary  
 3027 muons and the charged pions for  $\nu_\mu$  CC interactions in ND-GAr producing one or more  
 3028 charged pions. From this, one can see that (i) the majority of muons and charged pions  
 3029 are not going to be distinguishable with a  $\langle dE/dx \rangle$  measurement, and that (ii) particle  
 3030 identification is necessary both to classify correctly the  $\nu_\mu$  CC events and identify the  
 3031 primary muon within them.

3032 ND-GAr features two other subdetectors which can provide additional information  
 3033 for this task, namely the ECal and MuID. The current ECal design, described in (ref  
 3034 section), consists of 42 layers, made of 5 mm of Pb, 7 mm of plastic scintillator and a

### 6.3. MUON AND PION SEPARATION IN THE ECAL AND MUID

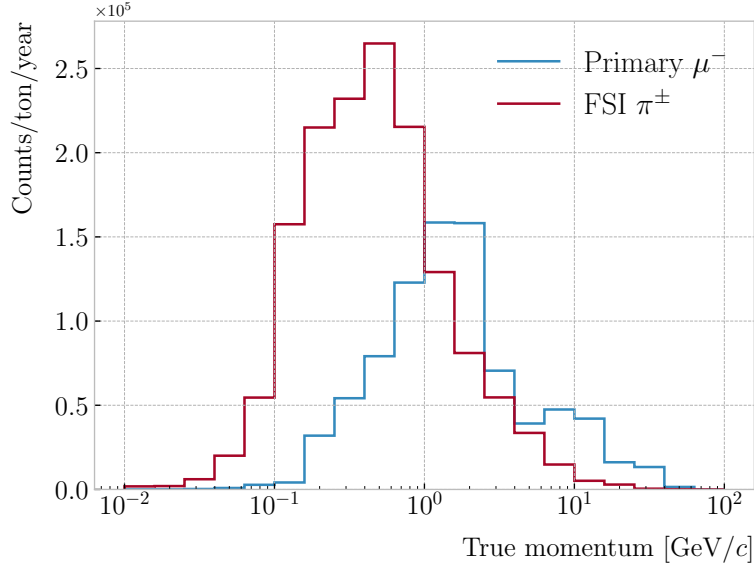


**Figure 6.15:** True momentum distribution for the primary muon in  $\nu_\mu$  CC  $N\pi^\pm$  interactions inside the fiducial volume of ND-GAr (blue line), compared to the post FSI charged pion spectrum (red line).

3035 1 mm PCB board. The total thickness of this calorimeter is 1.66 nuclear interaction  
 3036 lengths or 1.39 pion interaction lengths. The Muid design is in a more conceptual  
 3037 stage, however it is envisioned to feature layers with 10 cm of Fe and 2 cm of plastic  
 3038 scintillator<sup>6</sup>. With its three layers, it will have a thickness of 1.87 or 1.53 nuclear or pion  
 3039 interaction lengths, respectively.

3040 Because pion showers are dominated by inelastic nuclear interactions, the signatures  
 3041 of these particles in the calorimeter will look significantly different from those of muons.  
 3042 Although our ECal is not thick enough to fully contain the hadronic showers of the  
 3043 charged pions at their typical energies in FHC neutrino interactions, they can still be  
 3044 used to understand whether the original particle was more hadron-like or MIP-like. In  
 3045 Fig. 6.16 I show two examples of energy distributions created by a muon (left panel)  
 3046 and a charged pion (right panel) of similar momenta interacting in the ECal. These  
 3047 figures represent the transverse development of the interactions. For each of them, I  
 3048 computed the principal component and centre of mass of the interaction, projecting

<sup>6</sup>It is not mentioned anywhere, but I assume that there should also be another layer of PCB board of 1 mm. However, in this case its contribution to the total thickness of the sampling calorimeter would be negligible.

## CHAPTER 6. PARTICLE ID IN ND-GAr

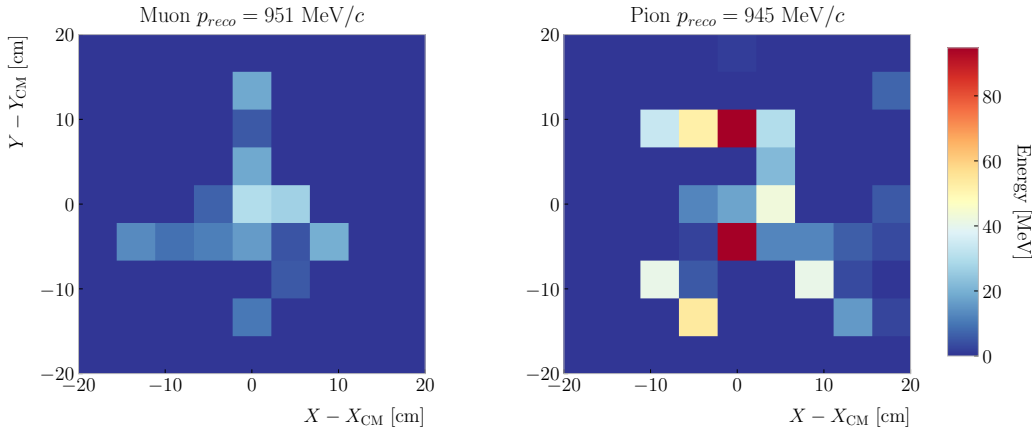


**Figure 6.16:** Distributions of energy deposits in the ECal for a muon (left panel) and a charged pion (right panel) with similar momenta. The energy is projected onto the plane perpendicular to the principal component of the hits, and the positions are relative to the center of the interaction.

3049 the position of the hits onto the plane perpendicular to that direction, and taking the  
 3050 distances relative to the centre. It can be seen that the muon follows an almost MIP-like  
 3051 behaviour, being the central bin in the histogram the one with the highest deposited  
 3052 energy. On the other hand, the pion not only deposits more energy overall, but also this  
 3053 energy is more spread-out among the different hits. It is this kind of information that  
 3054 would allow us to tell apart muons from pions.

3055 This way, I identify three main action points that need to be addressed if one wants  
 3056 to use these detectors to distinguish between muons and charged pions. These are:

- 3057 1. the way we make the associations between tracks in the HPgTPC to the activities  
 3058 (what in GArSoft we call clusters) in the ECal and the MuID,
- 3059 2. what variables or features one can extract from the calorimeters that encapsulate  
 3060 the information we are interested about,
- 3061 3. and how to carry out the classification problem.

### 6.3. MUON AND PION SEPARATION IN THE ECAL AND MUID

#### 3062 6.3.1 Track-ECal matching

3063 One of the main players in the muon and pion separation is the way we associate clusters  
3064 in the ECal to reconstructed tracks in the TPC. Missing some associations or making  
3065 wrong ones can bias the ECal quantities that we can use for classifying particles. The  
3066 current algorithm in GArSoft provides precise associations, i.e. most of the associations  
3067 that it produces are correct, but it appears to miss an important number of associations  
3068 (at least when using the default configuration).

3069 The current TPC track-ECal cluster association algorithm is divided in four parts.  
3070 It first checks whether the track end point fulfils certain conditions to be extrapolated.  
3071 There are two cut values in this step, one for the drift direction and other radial.

3072 If the point can be extrapolated, the code computes the coordinates of the centre  
3073 of curvature using the Kalman fit estimates at the track end ( $y$ ,  $z$ ,  $1/R$ ,  $\phi$ ,  $\tan\lambda$ ). It  
3074 then compares the distance between this and the cluster in the  $(z, y)$  plane with  $R$ . This  
3075 introduces another cut in the perpendicular direction.

3076 The next step is different for clusters in the barrel or in one of the end caps. If it  
3077 is a barrel cluster the algorithm extrapolates the track up to the radial distance of the  
3078 cluster. There are three possible outcomes, the extrapolated helix can cut the cylinder  
3079 of radius  $r_{clus}$  two, one or zero times. I get the cut point that is closer to the cluster and  
3080 check that it is either in the barrel or the end caps. Computing the difference between  
3081 the  $x$  coordinates of the cluster and the extrapolated point, the module checks that this  
3082 is not greater than a certain cut. If the cluster is in an end cap, I propagate the track  
3083 up to the  $x$  position of the cluster. Then, the algorithm computes the angle in the  $(z, y)$   
3084 plane between the centre of curvature and the cluster,  $\alpha$ , and the centre of curvature  
3085 and the propagated point,  $\alpha'$ . A cut is applied to the quantity  $(\alpha - \alpha')R$ .

3086 If the cluster contains more than a certain number  $N$  of hits, I apply an extra cut to  
3087 the dot product of the direction of the track at the propagated  $x$  value and the cluster  
3088 direction.

3089 The code makes sure to only associate one end of the track (if any) to a cluster.

## CHAPTER 6. PARTICLE ID IN ND-GAr

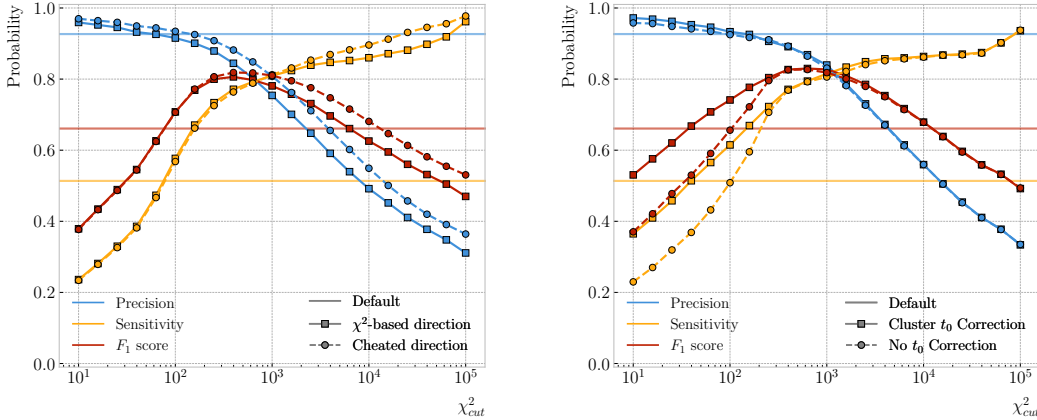


**Figure 6.17:** Left panel: comparison between the precision (blue), sensitivity (yellow) and  $F_1$  score (red) obtained for the default (horizontal lines) and new algorithms, both with the  $\chi^2$ -based direction estimator (squares) and cheating the directions (circles), for different values of the  $chi^2$  cut. Right panel: comparison of the performance of the new algorithm when applying the cluster  $t_0$  correction (squares) and when (circles).

3090 However, it can associate more than one track to the same cluster. This makes sense,  
3091 as different particles can contribute to the same cluster in the ECal, but it makes it  
3092 difficult to quantify the relative contributions of the tracks to a certain cluster.

3093 As a way of comparing the performance of this algorithm, a new, simpler association  
3094 module was written. The goal was to have a simple and robust algorithm, which depends  
3095 on as few parameters as possible and that can produce a one-to-one matching between  
3096 tracks and ECal clusters.

3097 For each reconstructed track, the new algorithms applies the same procedure to the  
3098 forward and the backward fits irrespective of their end point positions. It first gets the  
3099 Kalman fit parameters at the corresponding end point together with the  $X$  position,  $x_0$ ,  
3100 ( $y_0$ ,  $z_0$ ,  $1/R$ ,  $\phi_0$ ,  $\tan\lambda$ ).

3101 For each ECal cluster, I compute the radial distance to the centre of the TPC and  
3102 find the  $\phi$  value in the range  $[\phi_0, \phi_0 + \text{sign}(R)\phi_{max}]$  that makes the propagated helix  
3103 intersect with the circle defined with such radius. The  $(x, y, z)$  position of the helix for  
3104 the  $\phi$  value found (if any) is then computed. In case there are two intersections, I keep  
3105 the one that minimises the distance between  $(y, z)$  and  $(y_c, z_c)$ .

3106 I then calculate  $\chi^2$  value based on the Euclidean distance between the propagated

### 6.3. MUON AND PION SEPARATION IN THE ECAL AND MUID

3107 point and the cluster:

$$\chi^2/ndf = \frac{\sum_{n=0}^2 (x^{(n)} - x_c^{(n)})^2}{3}. \quad (6.9)$$

3108 If there was no intersection I store a  $-1$  instead. In the end, for each reconstructed track  
3109 in the event one ends up with two collections of  $\chi^2$  values, one for each ECal cluster  
3110 and fit directions.

3111 The current code only supports having ECal clusters associated to one end of each  
3112 track. We have two options to decide what track end to keep. The first one tries to  
3113 cheat the selection, looking at the distance between the two track ends and the true  
3114 start position of the associated MC particle. The second one keeps the track end with  
3115 more  $\chi^2$  entries below the cut.

3116 This feature of only considering one track end limits the algorithm, making it not  
3117 suitable for reconstructing events with particles originating outside the TPC. However,  
3118 as for the moment the main concern of the group is the study of neutrino interactions  
3119 off the gaseous argon, this is an acceptable assumption.

3120 In order to associate a cluster to a track, I take all clusters with a  $\chi^2$  value in the  
3121 range  $[0, \chi_{cut}^2]$ . If a cluster has been assigned to more than one track we leave it with  
3122 the one with the lowest  $\chi^2$ .

3123 This default behaviour of the algorithm can be modified to associate more than one  
3124 track to each cluster. Not only that, but the  $\chi^2$  values can be used to assign relative  
3125 weights to the different contributions.

3126 To evaluate the performance of the association method, I use a binary classification  
3127 approach. In this case, I check the leading MC Track IDs associated to the reconstructed  
3128 tracks and ECal clusters. I count an association as true positive (TP) if both Track  
3129 IDs coincide. An association is considered false positive (FP) when the Track IDs are  
3130 different. If a cluster has not been associated to any track but it shares the Track ID  
3131 with a reconstructed track it is counted as a false negative (FN).

3132 For the testing, I used a sample of 10000 FHC neutrino events inside the HPgTPC.  
3133 Figure 6.17 (left panel) shows the precision (blue line), sensitivity (yellow line), and  $F_1$

## CHAPTER 6. PARTICLE ID IN ND-GAr

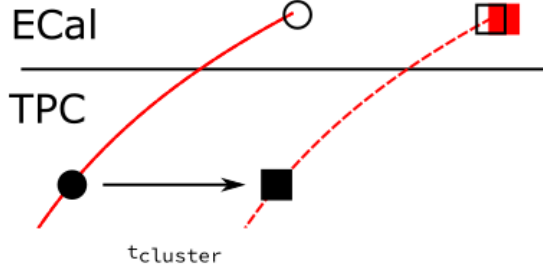


**Figure 6.18:** Schematics of a possible option to deal with track-ECal associations in non-zero  $t_0$  neutrino interaction events, trying to correct for the drift direction uncertainty in a cluster-by-cluster basis using the cluster time,  $t_{cluster}$ .

3134 score (red line) I obtained for different values of  $\chi^2_{cut}$ . For comparison, the same metrics  
 3135 computed for the default algorithm with the current configuration are also shown (dashed  
 3136 lines). In the case of the new algorithm, I used both the  $\chi^2$ -based method to estimate  
 3137 the track direction described earlier (square markers) and the cheated direction from the  
 3138 Geant-level information (circle markers). For either of these we achieve similar values of  
 3139 the precision compared to the old code, while having a considerably higher sensitivity.  
 3140 It can be seen that cheating the direction of the tracks only makes a difference at high  
 3141  $\chi^2_{cut}$ , past the optimal value of the cut around the  $F_1$  score maximum. Therefore, I set  
 3142 the  $\chi^2$  method as the default.

3143 One of the possible weak points of this approach is that it relies on the position along  
 3144 the drift direction to make the decisions. Within the current ND-GAr design implemented  
 3145 in GArSoft, the timing information is provided by the ECal. That effectively means  
 3146 that prior to make the track-ECal associations the reconstructed  $x$  positions of the track  
 3147 trajectories differ from the simulated ones by an amount:

$$x_{reco}^{(n)} - x_{sim}^{(n)} = v_{drift} t_0, \quad (6.10)$$

3148 where  $v_{drift}$  is the mean drift velocity in our medium and the initial time is in the range  
 3149  $t_0 \in [0, t_{spill}]$  where  $t_{spill}$  is the spill length. For a 10  $\mu\text{s}$  spill this translates into a  
 3150 maximum 30 cm uncertainty on the drift direction position.

3151 The current default in GArSoft sets  $t_0 = 0$ , but the functionality to randomly sample

### 6.3. MUON AND PION SEPARATION IN THE ECAL AND MUID

3152 this within the spill time is in place. Therefore, we need to understand what is the impact  
3153 of a non-zero  $t_0$  on the associations algorithm and foresee possible ways of minimising a  
3154 loss in performance.

3155 Figure 6.18 represents a possible option to tackle the association problem when  
3156 having events with a non-zero initial time  $t_0$ . The black and white circles represent the  
3157 original points, whereas the squares indicate the corrected positions. The end points of  
3158 the track and the propagated points up to the cluster radius are indicated using filled  
3159 and unfilled markers respectively. The red square represents the position of the cluster.

3160 Here I try to correct for the drift coordinate position using the time associated to the  
3161 cluster. Assuming that the drift time is much larger than the propagation time,  $t_{cluster}$   
3162 could be used as a good estimation of the  $t_0$ . An alternative can be using the earliest  
3163 time associated to a hit in said cluster. Doing this for each cluster before computing  
3164 the  $\chi^2$  value could be used as an alternative to knowing the specific value of the  $t_0$ , as  
3165 when the association is correct this will provide the right correction but its impact is  
3166 small enough to not change the position significantly in the case the cluster does not  
3167 correspond to a given track.

3168 I tested the effect of this correction again using a sample of 10000 FHC neutrino  
3169 events. Figure 6.17 (right panel) shows the precision (blue line), sensitivity (yellow line),  
3170 and  $F_1$  score (red line) for the case the cluster  $t_0$  correction is applied (square markers)  
3171 and for the no correction case (circle markers), as a function of  $\chi^2_{cut}$ . In this case, the  
3172 differences are particularly notorious at low values of the cut. It makes sense, as the  $t_0$   
3173 effect becomes subdominant when the distance we consider grows large. Overall, the  
3174 correction increases the sensitivity while keeping the precision almost unchanged. As a  
3175 result, I apply the  $t_0$  correction to the generated samples as the default.

#### 3176 6.3.2 Classification strategy

3177 The problem of the muon and charged pion separation has to be viewed in the broader  
3178 context of the particle identification in our detector. Focusing on the beam neutrino  
3179 interactions, it is clear that we are going to have muons and pions spanning a broad

## CHAPTER 6. PARTICLE ID IN ND-GAr

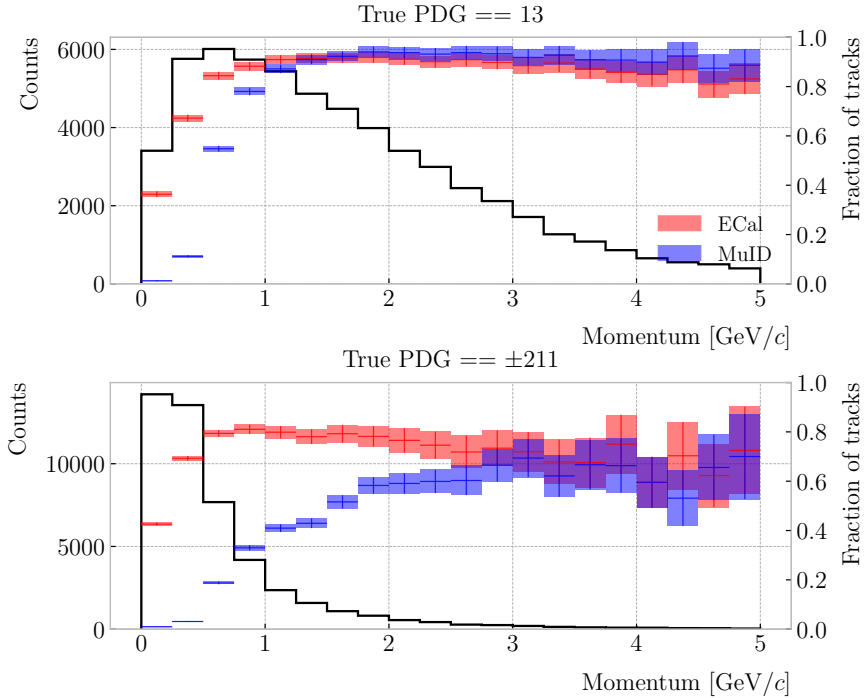


**Figure 6.19:** Momentum distribution for the reconstructed muons (top panel) and charged pions (bottom panel) in a FHC neutrino sample, together with the fraction of them reaching the ECal (red) and MuID (blue). Each entry corresponds to a reconstructed track, backtracked to a true muon or pion which has not produced any other reconstructed track.

momentum range. Not only that, but we will also have other particles with similar characteristics that will make the classification even more challenging. Therefore, we are presented with a task that will depend heavily on the kinematic range we are looking at each time, as both the available information and the possible impurities of other particle species vary.

For instance, distinguishing muons from pions could be difficult at low momenta, as a great number of them do not reach the ECal. Therefore, we could think of tailoring a version of the classification for that particular case, which could be complemented with a  $dE/dx$  measurement. Likewise, for momenta  $\gtrsim 1$  GeV muons and pions reach the calorimeters efficiently, but so do protons. Because of this, one can try to train another classifier for this energy range, and rely on other methods to remove as many of the protons as possible.

### 6.3. MUON AND PION SEPARATION IN THE ECAL AND MUID

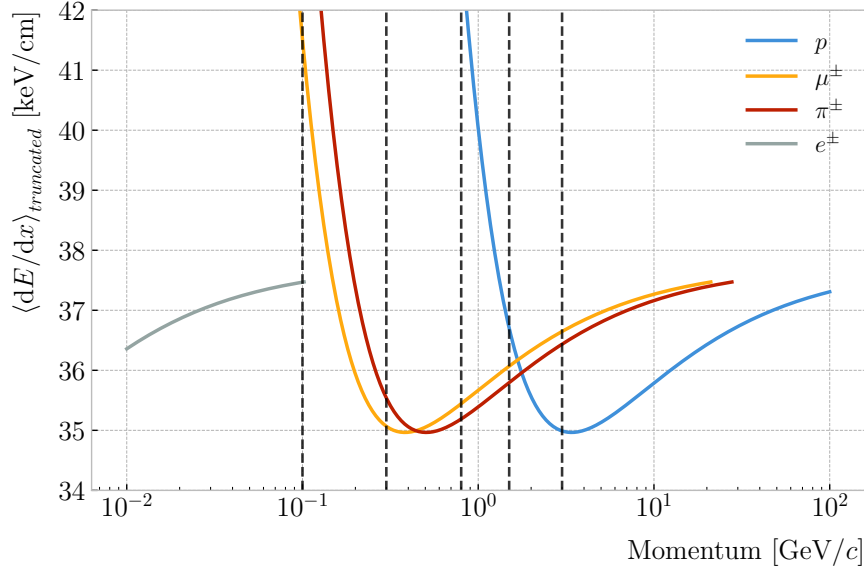


**Figure 6.20:** Predicted truncated mean  $dE/dx$  versus momentum, for electrons, muons, charged pions and protons, obtained using the ALEPH parametrisation. The vertical dashed lines represent the boundaries of the six regions used for the muon and pion classification training.

3192       Figure 6.19 shows the momentum distribution of the reconstructed muons (top) and  
 3193       pions (bottom) in a FHC sample. It also contains the fraction of particles reaching the  
 3194       ECal (red) and MuID (blue), for the different momentum bins. In Fig. 6.20 I show the  
 3195       mean  $dE/dx$  of different particles as a function of the momentum, computed using the  
 3196       ALEPH parametrisation with the best fit parameters found in Subsec. 6.2.2.

3197       Using these two figures as references, I decided to approach the classification by  
 3198       dividing the problem into six different momentum regions. A summary of these can be  
 3199       found in Tab. 6.2. The basic idea is to exploit all the information that is available in  
 3200       each region and . For the problem at hand, I prepared separated samples of isotropic  
 3201       single muons and pions, with momenta uniformly distributed along the corresponding  
 3202       momentum range. Each sample contains 50000 events of the corresponding particle  
 3203       species. I did not generate samples for the first region, as it is assumed that the separation  
 3204       can be achieved using  $dE/dx$  only. For the last region, I generated particles up to a  
 3205       momentum of 10  $\text{GeV}/c$ , as that is well above the typical energies of muons and pions  
 3206       from FHC neutrino interactions in ND-GAr.

## CHAPTER 6. PARTICLE ID IN ND-GAr

**Table 6.2:** Momentum ranges and description of the PID approach assumed for the muon and pion classification task.

Momentum range	Description
$< 0.1 \text{ GeV}/c$	All tracks can be separated with $dE/dx$
$[0.1, 0.3) \text{ GeV}/c$	Use ECal for reaching muons and pions, $dE/dx$ for the rest
$[0.3, 0.8) \text{ GeV}/c$	Use ECal for muons and pions, $dE/dx$ for protons
$[0.8, 1.5) \text{ GeV}/c$	Use ECal and MuID for muons and pions, $dE/dx$ for protons
$[1.5, 3.0) \text{ GeV}/c$	Use ECal and MuID for muons and pions, ToF for protons
$\geq 3.0 \text{ GeV}/c$	Use ECal and MuID for muons and pions, $dE/dx$ and ToF for protons

3207     Additionally, I prepared another sample of 100000 FHC neutrino events. For each  
 3208    interaction, I select the reconstructed particles which were backtracked to true muons or  
 3209    charged pions. I use this dataset to perform validation checks, to see how the models  
 3210    trained with the single particle data generalise to a more realistic scenario.

3211     To tackle this classification problem, I make use of Boosted Decision Trees (BDT). A  
 3212    decision tree uses a flowchart-like structure to make decisions based on some input data.  
 3213    It starts from a root node, which represents the complete dataset, and then it splits  
 3214    this based on the variable or feature which gives the best separation between classes,  
 3215    creating two new nodes. The process repeats for each node until it reaches a certain  
 3216    limit, like a maximum number of splits or some tolerance criteria. The last set of nodes  
 3217    are often called leave nodes, and represent the final prediction of the classifier.

3218     Boosting refers to a family of methods to combine the predictions from multiple  
 3219    classifiers, following a sequential approach where each new model learns from the errors  
 3220    of the previous one. The process starts with a simple decision tree, which is used to  
 3221    make predictions on the training data. Then, the data points misclassified by the first  
 3222    model are assigned higher weights, and another decision tree is trained on the data with  
 3223    adjusted weights. The predictions of the two trees are then combined, and the cycle  
 3224    repeats for a predefined number of iterations. Gradient boosting uses the direction of  
 3225    the steepest error descent to guide the learning process and improve the accuracy with  
 3226    each iteration.

### 6.3. MUON AND PION SEPARATION IN THE ECal AND MuID

#### 3227 6.3.3 Feature selection and importance

3228 Using the reconstructed tracks as a starting point, I compute a number of ECal and  
3229 MuID variables for each of them. As there can be more than one cluster associated to a  
3230 track, what I do is collect all associated clusters and compute these variables from the  
3231 complete collection of associated hits. For the MuID, because it only features three layers  
3232 and typically there will be less hits, I also allow single hits to be associated with tracks<sup>7</sup>.  
3233 I can roughly divide the variables in three types: energy-related, geometry-related and  
3234 statistical. In the following, I briefly describe the variables related exclusively to the  
3235 ECal:

##### 3236 • Energy-related ECal

- 3237 – ECal total energy (ClusterTotalEnergy): sum of the energy of all the ECal  
3238 hits.
- 3239 – Mean ECal hit energy (HitMeanEnergy): mean of the hit energy distribution.
- 3240 – Standard deviation ECal hit energy (HitStdEnergy): standard deviation of  
3241 the hit energy distribution.
- 3242 – Maximum ECal hit energy (HitMaxEnergy): maximum of the hit energy  
3243 distribution.

##### 3244 • Geometry-related ECal

- 3245 – Mean distance hit-to-cluster (DistHitClusterMean): mean of the distance  
3246 distribution between the hits and the corresponding cluster's main axis.
- 3247 – RMS distance hit-to-cluster (DistHitClusterRMS): root mean square of the  
3248 distance distribution between the hits and the corresponding cluster's main  
3249 axis.

---

<sup>7</sup>At the reconstruction level what happens is that non-clustered hits are put into single hit clusters, instead of being thrown away. This is necessary to keep the consistency of the track-cluster association code.

## CHAPTER 6. PARTICLE ID IN ND-GAr

- 3250        – Maximum distance hit-to-centre (DistHitCenterMax): maximum of the  
3251                  distance distribution between the hits and the centre of the TPC.  
  
3252        – Time-of-Flight velocity (TOFVelocity): slope obtained when fitting a straight  
3253                  line to the hit time versus hit distance to the centre (i.e.  $d = v \times t$ ).

### 3254        • Energy and geometry ECal

- 3255        – Radius 90% energy (Radius90E): distance in the hit-to-cluster distribution  
3256                  for which 90% of the total energy is contained in the hits that are closer to  
3257                  the axis (i.e. radius that contains 90% of the energy).

### 3258        • Statistical ECal

- 3259        – Number of hits (NHits): total number of hits associated to the track.  
3260        – Number of layers with hits (NLayers): not really a count of all layers with  
3261                  hits but the difference between the last and the first layer with hits.

3262        Figure 6.21 shows the distributions of three different ECal variables, separating true  
3263                  muons (blue) and charged pions (red), for the five momentum ranges considered. I chose  
3264                  to show one feature from each category, namely the mean energy per hit (left column),  
3265                  the mean distance between the hits and the centre of the cluster (middle column), and  
3266                  the number of ECal layers with hits (right column). These give an idea of the separating  
3267                  power of the different features, and how it changes considerably with the energy. In  
3268                  the number of layers with hits distributions, the peak at 6 is due to the fact that the  
3269                  first six ECal layers sit inside the pressure vessel<sup>8</sup>. Therefore, some of the particles get  
3270                  stopped crossing it, never making it to the seventh layer.

3271        In the case of the MuID, because at low momenta a significant fraction of the particles  
3272                  do not make it past the ECal, I only consider the information coming from this detector  
3273                  for momenta  $\geq 0.8$  GeV/c, i.e. for the last three momentum regions. The variables I  
3274                  extract from it are the following:

---

<sup>8</sup>Note to self: check this. I thought the ECal barrel had 8 layers of tiles, and that all of them were inside the pressure vessel.

### 6.3. MUON AND PION SEPARATION IN THE ECAL AND MUID

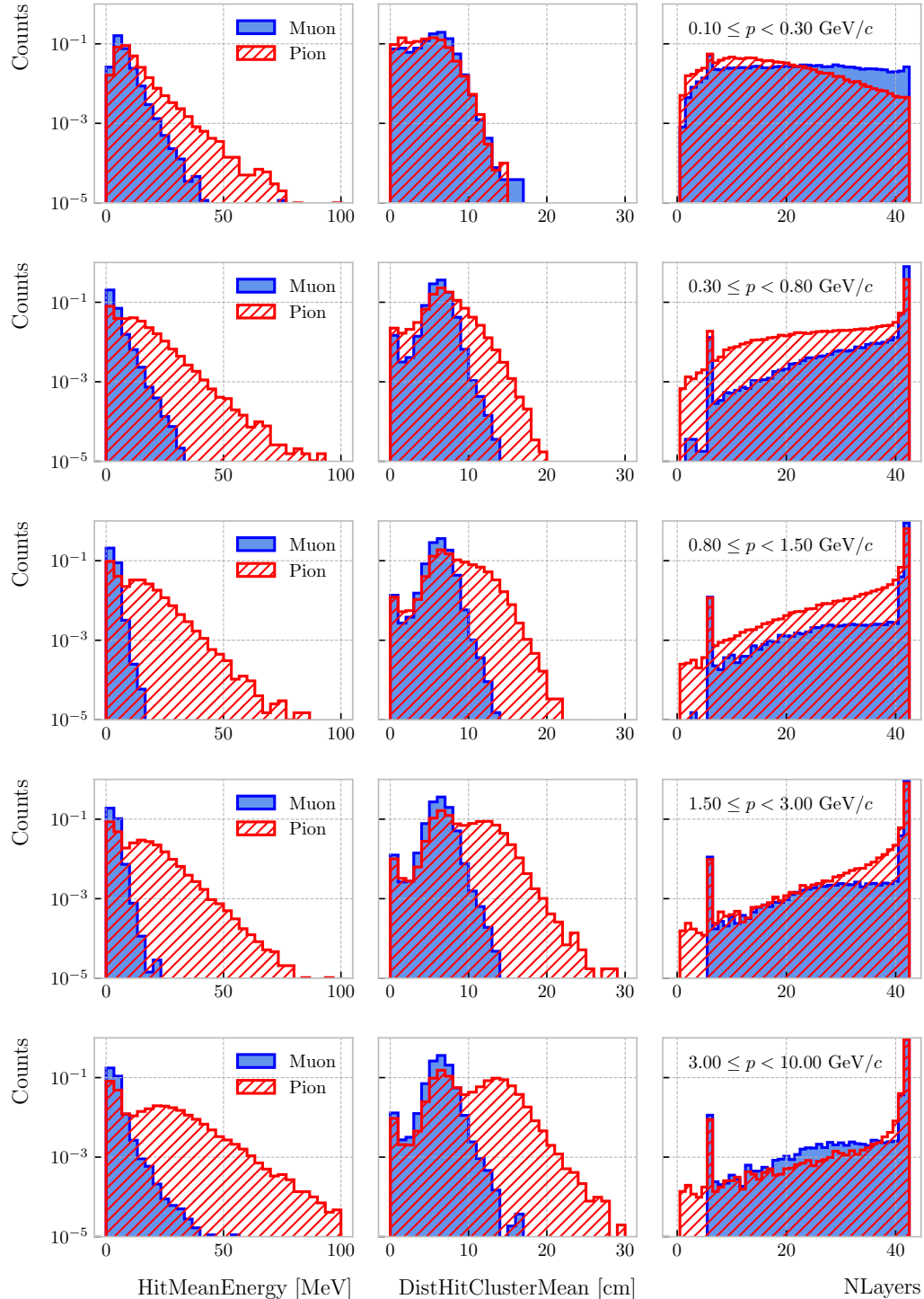


**Figure 6.21:** Example ECal feature distributions for muons (blue) and charged pions (red) in the five different momentum ranges considered (from top to bottom, in ascending momentum order). From left to right: mean hit energy, mean distance hit-to-cluster, and number of layers with hits.

## CHAPTER 6. PARTICLE ID IN ND-GAr

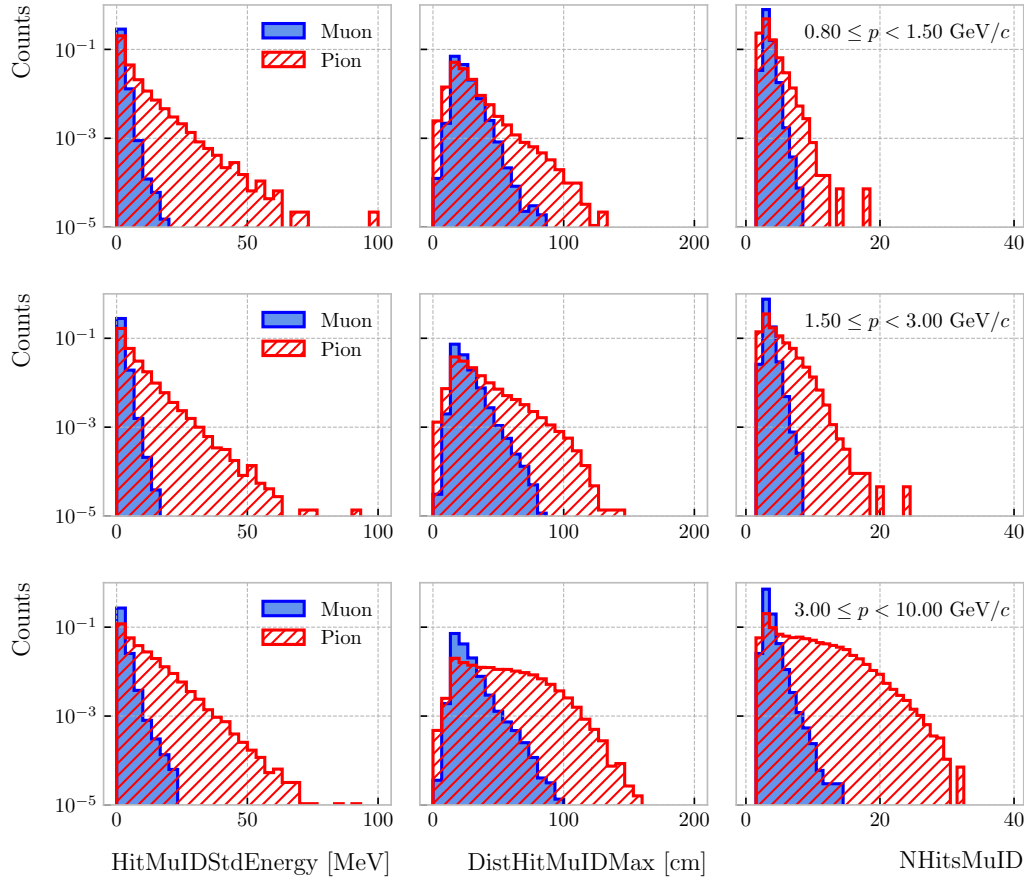


**Figure 6.22:** Example MuID feature distributions for muons (blue) and charged pions (red) in the three different momentum ranges considered (from top to bottom, in ascending momentum order). From left to right: standard deviation hit energy, maximum distance hit-to-hit, and number of hits.

3275

- Energy-related MuID

3276

- MuID total energy (ClusterMuIDTotalEnergy): sum of the energy of all the MuID hits.

3277

- Mean MuID hit energy (HitMuIDMeanEnergy): mean of the MuID hit energy distribution.

3278

- Standard deviation MuID hit energy (HitMuIDStdEnergy): standard deviation of the MuID hit energy distribution.

3279

- Maximum MuID hit energy (HitMuIDMaxEnergy): maximum of the MuID hit energy distribution.

3280

3281

3282

3283

### 6.3. MUON AND PION SEPARATION IN THE ECAL AND MUID

#### • Geometry-related MuID

- 3285        – Maximum distance MuID hit-to-hit (DistHitMuIDMax): maximum distance
- 3286              between pairs of MuID hits (not sure this is a good variable, distribution
- 3287              looks nuts).
- 3288        – Maximum distance MuID hit-to-centre (DistHitCenterMuIDMax): maximum
- 3289              of the distance distribution between the MuID hits and the centre of the
- 3290              TPC.

#### • Statistical MuID

- 3292        – Number of hits (NHitsMuID): total number of MuID hits associated to the
- 3293              track.
- 3294        – Number of layers with hits (NLayersMuID): not really a count of all layers
- 3295              with MuID hits but the difference between the last and the first layer with
- 3296              MuIDhits.

3297        Figure 6.22 shows the distributions of three different MuID variables, separating true  
3298        muons (blue) and charged pions (red), for the three momentum ranges which use the  
3299        muon tagger information. In this case I decided to standard deviation of the MuID hit  
3300        energy distribution (left column), the maximum distance between the MuID hit pairs  
3301        (middle column), and the number of MuID hits (right column). These variables are used  
3302        together with the ECal features at high momenta, providing additional disambiguation  
3303        power.

3304        Once our features have been defined, one can do some exploratory analysis to  
3305        understand how well the variables describe the target class, and avoid the black-box  
3306        approach by what features are most relevant for the learning process. This way, I  
3307        performed a feature analysis for each of the momentum ranges I divided this classification  
3308        problem into. It follows three steps: first a principal component analysis (PCA), followed  
3309        by a feature importance study using Gini and Shapley values, and finally a feature  
3310        permutation importance analysis.

## CHAPTER 6. PARTICLE ID IN ND-GAr

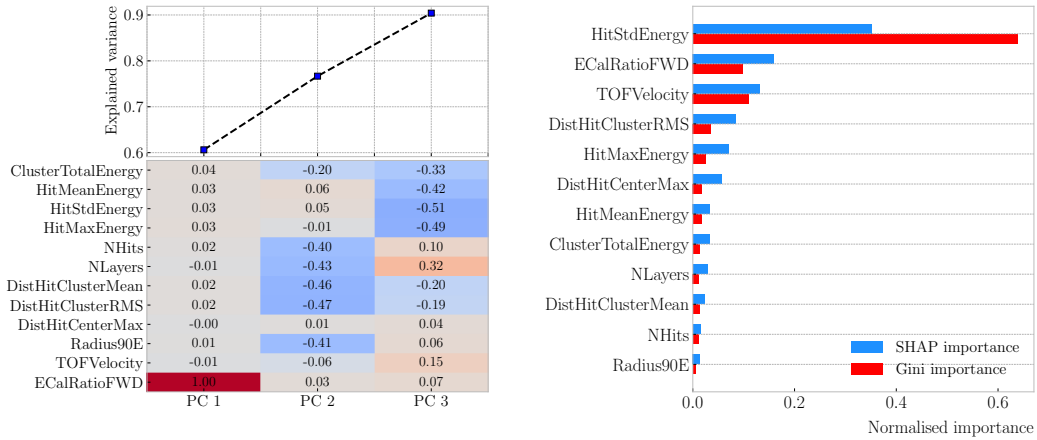


**Figure 6.23:** Left panel: cumulative explained variance for the first three principal components (top panel) and contribution of the different features to the principal axes in feature space (bottom panel). Right panel: Shapley (blue) and Gini (red) feature importances for the different input features. Both figures correspond to the samples in the momentum range  $0.3 \leq p < 0.8 \text{ GeV}/c$ .

The PCA is useful to understand the variance of the feature space. It is an unsupervised machine learning technique that allows the user to perform a dimensionality reduction. It uses a singular value decomposition of the input features to project them into a lower dimensional space. The idea is to find the matrix  $\mathbf{C}_m$ , whose columns are the first  $m$  orthonormal eigenvectors of the input covariance matrix. Consider the  $n \times p$  real matrix of input data  $\mathbf{X}$ , where  $n$  is the number of samples and  $p$  the number of features. If  $\mathbf{X}$  is centred, i.e. the means of its columns are equal to zero, we can write the covariance matrix of  $\mathbf{X}$  as  $\mathbf{C} = \mathbf{X}^\top \mathbf{X} / (n - 1)$ . This matrix can be diagonalised, yielding:

$$\mathbf{C} = \mathbf{V} \mathbf{L} \mathbf{V}^\top, \quad (6.11)$$

where  $\mathbf{V}$  is a matrix of eigenvectors and  $\mathbf{L}$  a diagonal matrix with eigenvalues  $\lambda_i$ . Then, performing SVD on  $\mathbf{X}$  gives us:

$$\mathbf{X} = \mathbf{U} \mathbf{S} \mathbf{W}^\top, \quad (6.12)$$

where  $\mathbf{U}$  is a unitary matrix, whose columns are called left singular vectors,  $\mathbf{S}$  is a diagonal matrix of single values  $s_i$ , and  $\mathbf{W}$  is another unitary matrix, its columns known

### 6.3. MUON AND PION SEPARATION IN THE ECAL AND MUID

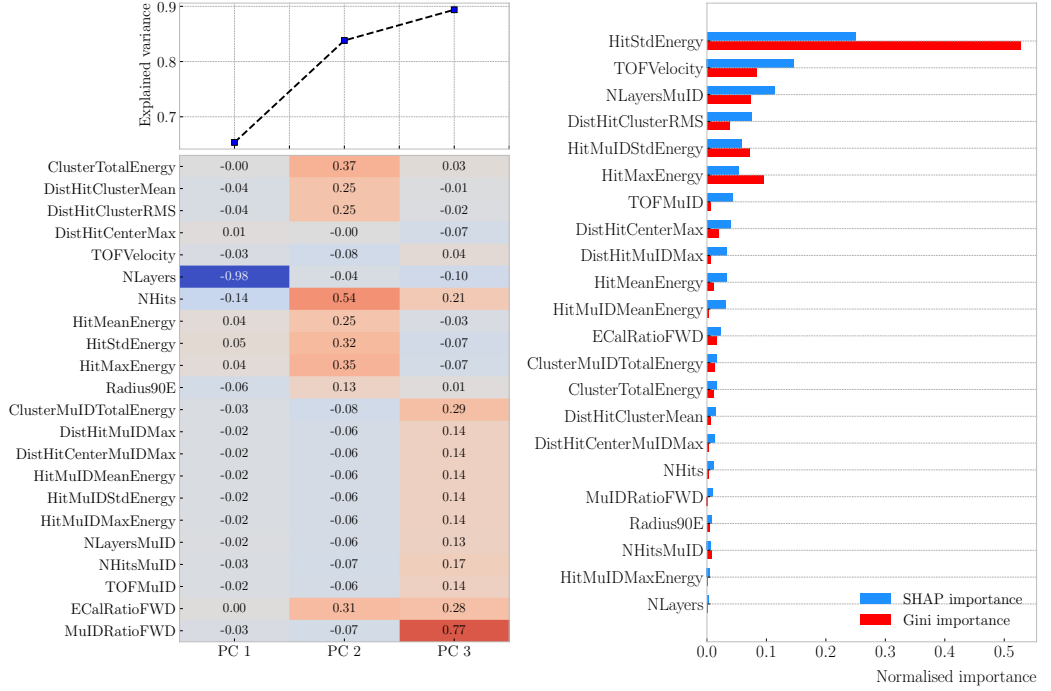


**Figure 6.24:** Left panel: cumulative explained variance for the first three principal components (top panel) and contribution of the different features to the principal axes in feature space (bottom panel). Right panel: Shapley (blue) and Gini (red) feature importances for the different input features. Both figures correspond to the samples in the momentum range  $0.8 \leq p < 1.5$  GeV/c.

as right singular vectors. This way, we can write:

$$\mathbf{C} = \mathbf{W}\mathbf{S}\mathbf{U}^\top\mathbf{U}\mathbf{S}\mathbf{W}^\top/(n-1) = \mathbf{W}\frac{\mathbf{S}^2}{n-1}\mathbf{W}^\top. \quad (6.13)$$

meaning that the right singular vectors are also the eigenvectors of the covariance matrix.

The SVD can be computed numerically following an iterative approach.

This way, taking an input data vector  $X \in \mathbb{R}^n$ , the resulting feature vector  $Y \in \mathbb{R}^m$

is given by:

$$Y = \mathbf{C}_m^\top X. \quad (6.14)$$

The new features capture most of the variance of the original sample, while being lower

dimensional, as  $m < n$ .

Before applying the PCA reduction one needs to centre and scale the input data.

## CHAPTER 6. PARTICLE ID IN ND-GAR

3331 Centring is necessary when using SVD to obtain the eigenvectors of the covariance  
3332 matrix, as only in that case we can do the identification with the right singular vectors  
3333 from the input data. Scaling is needed when variables are on different scales, as some  
3334 can then dominate the PCA procedure.

3335 I used the PCA module of `scikit-learn`, together with the `RobustScaler`, which  
3336 centres the data and scales it based on the interquartile range. In Fig. 6.23 (left panel)  
3337 and Fig. 6.24 (left panel) I show the results I obtained from the PCA for the momentum  
3338 ranges  $0.3 \leq p < 0.8 \text{ GeV}/c$  and  $0.8 \leq p < 1.5 \text{ GeV}/c$ , respectively. Notice that in  
3339 the second case the number of features increases considerably, as this is the first region  
3340 which uses the MuID variables. I found that, in all the cases, adding a fourth PC does  
3341 not add additional information. As it can be seen in the top panels of the figures, the  
3342 cumulative explained variance is already over 80% with three PCs.

3343 The bottom panels show the contribution of the variables to the principal axes. For  
3344 the two first momentum regions, I observe a tendency of the energy-related and the  
3345 geometry-related ECal variables to be clustered together. For the other ranges, when  
3346 I include the MuID variables, there seems to be a division between ECal and MuID  
3347 variables. For these, it seems like the number of ECal layers with hits also plays an  
3348 important role.

3349 The next step in the analysis is to quantify the importance of the features based on  
3350 two additional metrics, namely the Gini and the Shapley values. The Gini importance,  
3351 often called mean decrease impurity, is based on how much a feature contributes to the  
3352 purity improvement at the splits in each decision tree. The purity is measured in terms  
3353 of the Gini impurity index, defined as:

$$I_G = 1 - \sum_i f_i, \quad (6.15)$$

3354 where  $f_i$  is the fractional abundance of the  $i$ -th class. Then, for each split one can

### 6.3. MUON AND PION SEPARATION IN THE ECAL AND MUID

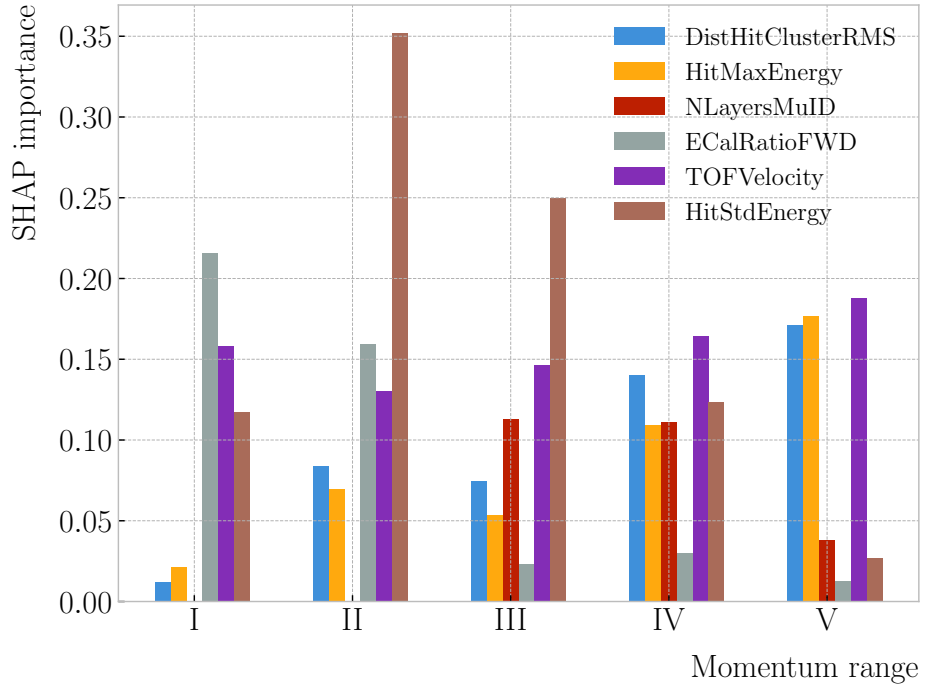


**Figure 6.25:** Evolution of the SHAP importance for the top six most important features across all five momentum ranges.

3355 compute the weighted decrease in impurity as:

$$\Delta_G = \frac{N_t}{N} \left( I_G - \frac{N_t^R}{N_t} I_G^R - \frac{N_t^L}{N_t} I_G^L \right), \quad (6.16)$$

3356 where  $N$  represents the total number of samples,  $N_t$  the number of samples at the current  
 3357 node,  $N_t^R$  and  $N_t^L$  the number of samples in the right and left children respectively,  
 3358  $I_G$  is the Gini impurity at the current node, and  $I_G^R$  and  $I_G^L$  the Gini impurities of the  
 3359 resulting right and left children.

3360 For each decision tree, one will have a normalised vector with the accumulated  
 3361 decrease in Gini impurity for each feature. In the case of a BDT, the feature importances  
 3362 are simply the mean for all the estimators in the ensemble<sup>9</sup>.

3363 The concept of Shapley values originated in the context of game theory, and it  
 3364 measures the marginal contribution of a feature in enhancing the accuracy of a classifier.

---

<sup>9</sup>Note to self: this appears not to be the case. If you get the `feature_importance` for each tree in the BDT and take the average, the result is not the same to be one reported in the `feature_importance` attribute of the BDT.

## CHAPTER 6. PARTICLE ID IN ND-GAr

3365 Take  $F$  to be the set of all features in a problem, and  $S \subseteq F$  the subset of features. To  
 3366 compute the Shapley value of the  $i$ -th feature, one has to train a model with that feature  
 3367 present,  $f_{S \cup \{i\}}$ , and another model trained without it,  $f_S$ . This has to be repeated for  
 3368 all possible combinations of subsets  $S \subset F \setminus \{i\}$ , and evaluating the models predictions  
 3369 on the appropriate sets of data  $x_S$ . This way, the Shapley value results:

$$\varphi_i = \sum_{S \subset F \setminus \{i\}} \frac{|S|! (|F| - |S| - 1)!}{|F|!} [f_{S \cup \{i\}}(x_{S \cup \{i\}}) - f_S(x_S)]. \quad (6.17)$$

3370 I trained the `GradientBoostingClassifier` from `scikit-learn` with the default  
 3371 configuration in order to evaluate both the Gini and Shapley importances. The Gini  
 3372 scores are automatically computed by `scikit-learn`, using the training data. For the  
 3373 Shapley importance, I used the implementation from the `SHAP` package, computing  
 3374 it using the test sample. The results can be seen in Fig. 6.23 (right panel) and  
 3375 Fig. 6.24 (right panel), again for the momentum ranges  $0.3 \leq p < 0.8 \text{ GeV}/c$  and  
 3376  $0.8 \leq p < 1.5 \text{ GeV}/c$ . The length of the bars denote either the SHAP (blue) or the Gini  
 3377 (red) importance of the feature. One interesting thing to notice is that, when looking at  
 3378 the Gini importance, there is always one feature that dominates over the rest. This is  
 3379 not the case for the SHAP importance, where importances tend to be more balanced.

3380 Across all momentum ranges, I observe that the most important features are. For  
 3381 the five momentum ranges considered, only six variables sit in the top five at least once.  
 3382 Figure 6.25 shows the evolution of the SHAP importance of these six features. It is  
 3383 interesting to see that the time-of-flight variable keeps its importance almost unchanged  
 3384 for all momenta. Also, it looks like the ECal energy ratio gets less relevant the higher the  
 3385 momentum is, but the RMS of the hit-to-cluster distance distribution and the maximum  
 3386 ECal hit energy become more important in the last momentum ranges.

3387 The last step in the feature selection analysis is the feature permutation. This  
 3388 technique measures the contribution of each feature to the performance of a model by  
 3389 randomly shuffling its values and checking how some scores degrade. For the present  
 3390 case, I am interested in the precision or purity, and the sensitivity or efficiency, as these

### 6.3. MUON AND PION SEPARATION IN THE ECAL AND MUID

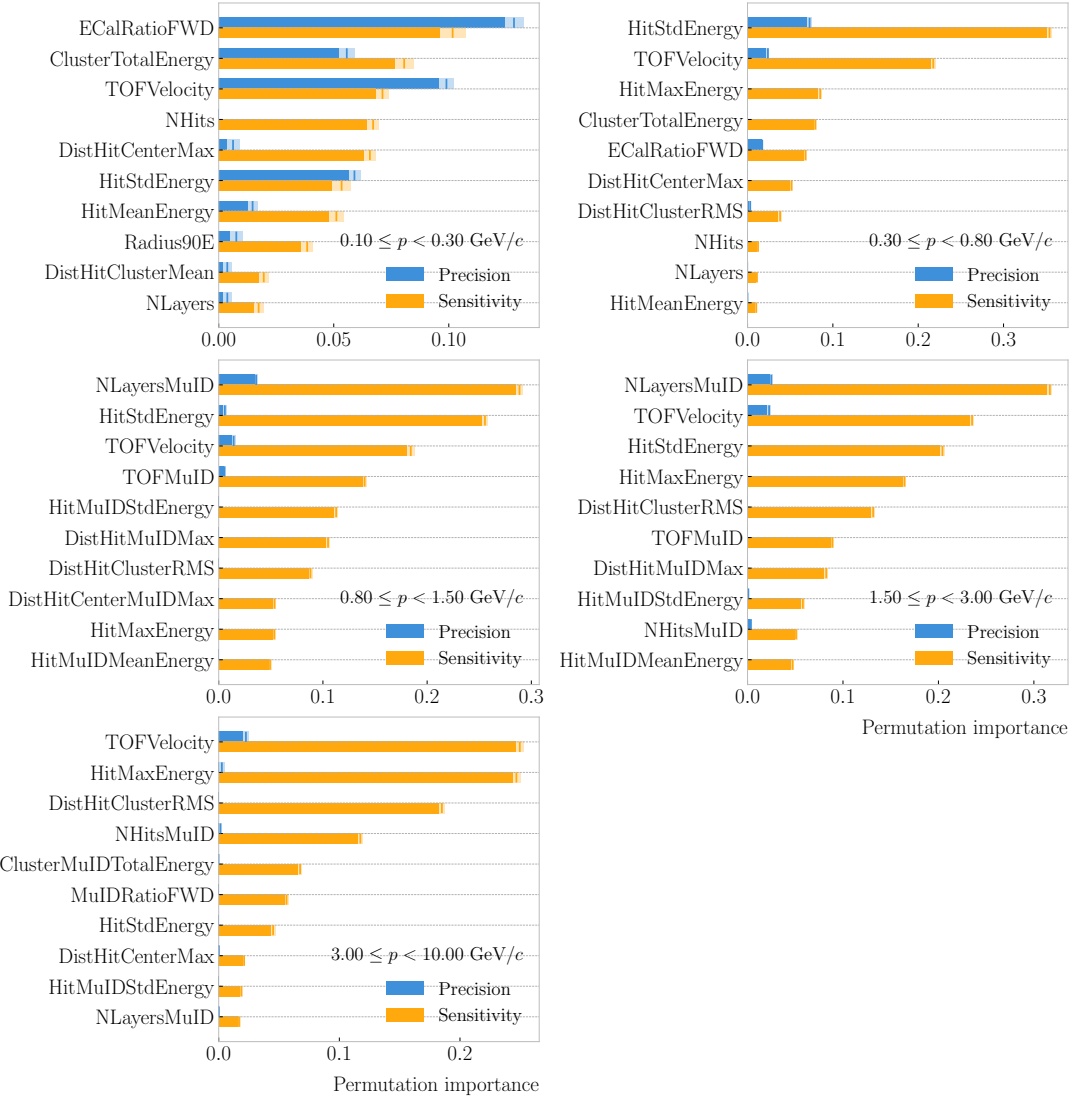


**Figure 6.26:** Permutation importances for the ten most important features in the different momentum ranges (from left to right, top to bottom, in increasing momentum order). The bars indicate the effect that permutations of each feature have on the purity (blue) and the sensitivity (yellow), the translucent regions representing one standard deviation around the central value.

## CHAPTER 6. PARTICLE ID IN ND-GAR

3391 two are the most relevant metrics from a physics point of view. The `scikit-learn`  
3392 module provides the user with a method to perform the permutation scans.

3393 The results of these are shown in Fig. 6.26. For the different momentum ranges  
3394 I show the permutation importances for the ten most important features. For each  
3395 of the variables I report the effect the permutations have on the precision (blue) and  
3396 sensitivity (yellow) of the models. The bars indicate the importance value, with the  
3397 lighter part representing one standard deviation around the mean (hinted as an additional  
3398 vertical line). Something to notice is that, in the first momentum region, the feature  
3399 permutations have an effect on both the precision and the sensitivity. However, for the  
3400 rest the precision is almost unaffected, while the sensitivity changes are considerably  
3401 larger.

3402 It is also interesting to see that most of the variables identified as important here  
3403 are the same I found when looking at the Shapley values. The behaviour of these across  
3404 the momentum ranges is also similar, with the same patterns of some features being  
3405 important at low momenta and then dropping in importance for the high momentum  
3406 ranges.

3407 Wit this, I conclude the study of the features. I have prepared the training and  
3408 testing datasets and understood what features are likely to have the largest impact on  
3409 the performance of the classifiers.

### 3410 6.3.4 Hyperparameter optimisation

3411 Any BDT requires the user to specify a number of parameters that will dictate its  
3412 behaviour. They can be divided into two categories: (i) tree-specific parameters, which  
3413 affect each individual tree in the model, and (ii) boosting parameters, which control the  
3414 boosting operation in the model. The value of these so-called hyperparameters affect the  
3415 performance and predictive power of the models. Therefore, one needs to carefully select  
3416 their optimal values in order to extract as much information as possible from the data.

3417 From all the parameters used to define a tree in the `scikit-learn` implementation  
3418 of the BDT classifier, I only consider a subset of them. This is due to the fact that some

### 6.3. MUON AND PION SEPARATION IN THE ECAL AND MUID

3419 are mutually exclusive, but also because I noticed that others have little effect on the  
3420 problem at hand. Therefore, the parameters I investigate are the following:

- 3421 • `min_samples_split`: defines the minimum number of samples required in a node  
3422 to be considered for splitting. Higher values prevent a model from learning relations  
3423 which might be highly specific to the particular sample, but may lead to under-fitting  
3424 if the value is too low.
- 3425 • `min_samples_leaf`: defines the minimum samples required in a leaf node. For  
3426 imbalanced problems it should take a low value, as there will not be many cases  
3427 where the minority class dominates.
- 3428 • `max_depth`: maximum depth of a tree. Useful to prevent over-fitting, as higher  
3429 depth will allow a model to learn relations specific to the training sample.

3430 In the case of the boosting parameters, the ones I look at are:

- 3431 • `learning_rate`: determines the impact of each tree on the final outcome. Low  
3432 values make the model robust to the specific characteristics of a tree, and thus  
3433 allow it to generalise well. However, that usually requires a large number of trees  
3434 to model the data properly.
- 3435 • `n_estimators`: number of sequential trees to be trained. In general, BDTs are  
3436 fairly robust at higher number of trees but it can still overfit at a point.
- 3437 • `subsample`: fraction of observations to be selected for each tree. Values slightly  
3438 less than 1 make the model robust by reducing the variance.

3439 In general, hyperparameters depend on each other. Thus, it is not possible to  
3440 optimise them independently. In the literature, we find two main strategies to explore  
3441 the hyperparameter space. We could use a grid search, in which one discretises a  
3442 portion of the space of hyperparameters and evaluates the model at each point. Another  
3443 approach is the randomised search, where a certain number of random configurations of  
3444 hyperparameters are explored.

## CHAPTER 6. PARTICLE ID IN ND-GAR

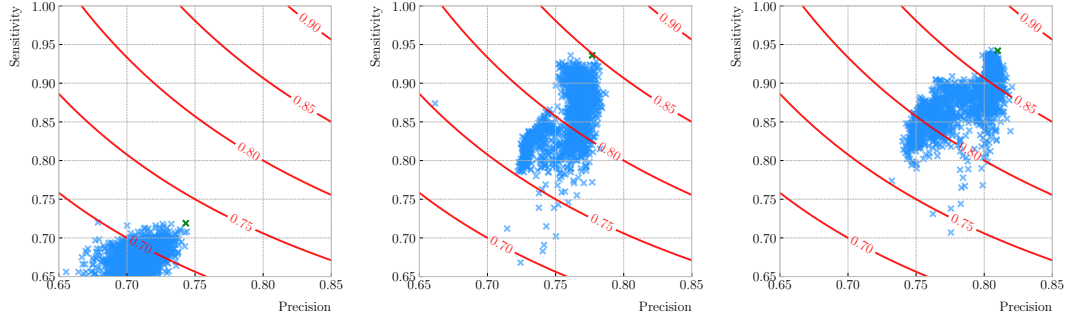


**Figure 6.27:** Values of the precision and sensitivity obtained for 10000 BDT hyperparameter configurations, for the momentum regions I, III and V. The red contours indicate the curves of equal  $F_1$ -score, while the green crosses are the selected configurations.

3445 In this case, I used the random search to scan the hyperparameter space. Also,  
 3446 because it is not guaranteed that a set of hyperparameters can be efficiently applied  
 3447 across different datasets, I perform the optimisation for each of the momentum ranges  
 3448 considered. Table 6.3 shows the list of hyperparameters considered, and the range within  
 3449 which I let them vary. I decided to fix the number of estimators to 400 in all cases, as  
 3450 its value is correlated with that of the learning rate.

3451 I evaluate 10000 different hyperparameter configurations for each momentum range.  
 3452 For the hyperparameter tuning, I used subsamples containing 10% of the full datasets,  
 3453 keeping the original proportions between classes, in order to reduce the computational  
 3454 load. The performance of the models was assessed using a stratified 3-fold cross-validation  
 3455 with replacement. Cross-validation involves dividing the data in a number of subsets,  
 3456 training the model using some of them, and testing it with the rest. In our case, I  
 3457 divide the data in 3 equal-sized subsets, maintaining the class proportions of the original  
 3458 dataset. Then, for 3 consecutive iterations, I train the models using 2 of the subsets  
 3459 while I compute the precision and sensitivity scores with the other. This approach  
 3460 provides a more robust estimate of the performance on unseen data.

3461 Figure 6.27 shows the results in the precision versus sensitivity plane, for the  
 3462 momentum regions I, III and V (from left to right). The contours represent the curves  
 3463 of equal  $F_1$ -score, i.e. the harmonic mean of the precision and the sensitivity. In order

### 6.3. MUON AND PION SEPARATION IN THE ECAL AND MUID

**Table 6.3:** Optimal values of the hyperparameters used by the BDT, for each momentum range.

Hyperparameter	Range	Best value				
		I	II	III	IV	V
<code>min_samples_split</code>	[0.001, 1]	0.10	0.06	0.05	0.27	0.06
<code>min_samples_leaf</code>	[0.001, 1]	0.02	0.03	0.01	0.02	0.07
<code>max_depth</code>	{2, 3, ..., 8}	8	2	4	2	7
<code>learning_rate</code>	[0.05, 1]	0.10	0.23	0.07	0.13	0.09
<code>subsample</code>	[0.01, 1]	0.75	0.65	0.79	0.86	0.95

**Table 6.4:** Performance metrics of the BDTs with optimal hyperparameters, for the different momentum ranges.

Metric	Value $\pm 1\sigma$				
	I	II	III	IV	V
Accuracy	$0.779 \pm 0.003$	$0.812 \pm 0.003$	$0.846 \pm 0.002$	$0.861 \pm 0.003$	$0.874 \pm 0.002$
Precision	$0.769 \pm 0.003$	$0.752 \pm 0.005$	$0.788 \pm 0.002$	$0.805 \pm 0.003$	$0.815 \pm 0.003$
Sensitivity	$0.745 \pm 0.009$	$0.921 \pm 0.006$	$0.965 \pm 0.002$	$0.967 \pm 0.002$	$0.976 \pm 0.001$
$F_1$ -score	$0.757 \pm 0.004$	$0.828 \pm 0.003$	$0.867 \pm 0.002$	$0.879 \pm 0.002$	$0.889 \pm 0.002$
ROC AUC	$0.868 \pm 0.003$	$0.865 \pm 0.003$	$0.899 \pm 0.002$	$0.902 \pm 0.002$	$0.911 \pm 0.001$

3464 to select the optimal configurations (indicated in the plots with a green cross), I chose  
3465 the point with the highest  $F_1$ -score.

3466 The results for the different momentum ranges are summarised in Tab. 6.3. One  
3467 can see some consistency in hyperparameter choices, with models generally preferring  
3468 small values for the tree-specific parameters, small learning rate, and relatively large  
3469 subsample sizes.

3470 Now that I have obtained the optimal values of the hyperparameters, I can train  
3471 the different BDTs. In this case I use the complete datasets, keeping 20% of the data  
3472 for testing. Table 6.4 shows the values of the different performance metrics obtained  
3473 using the selected hyperparameters and 5-fold cross-validation. The last row indicates  
3474 the value of the area under the receiver operating characteristic (ROC) curve. This  
3475 represents the sensitivity of a model as a function of the false positive rate. I have

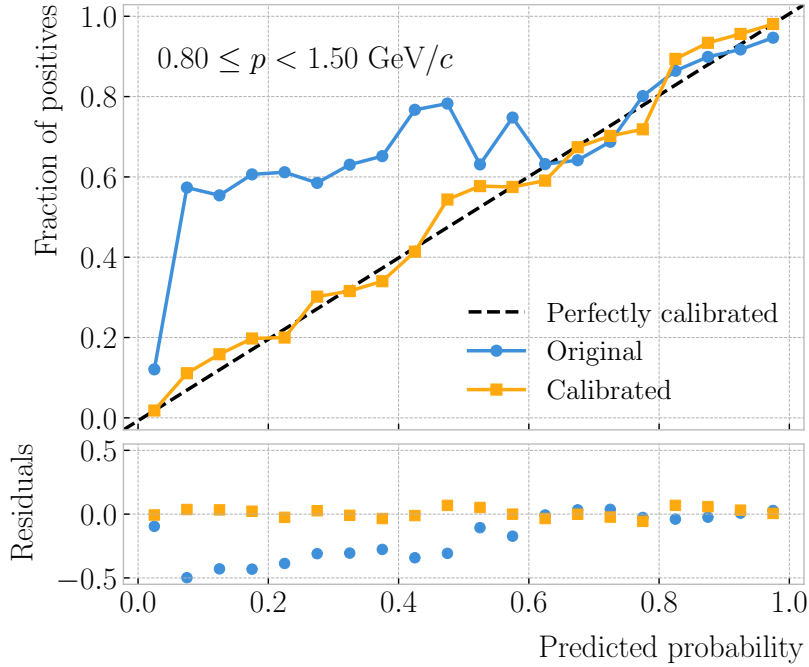


**Figure 6.28:** Reliability diagrams for the BDT classifier used in the momentum range  $0.3 \leq p < 0.8 \text{ GeV}/c$ , both for the original (blue circles) and calibrated (yellow squares) responses. For reference, the response of a perfectly calibrated classifier is also shown (black dashed line).

3476 included it here as it is a classic model metric used in the machine learning community.

3477 Overall, there is a clear trend of models performing better at higher momentum.

### 3478 6.3.5 Probability calibration

3479 So far, the trained BDTs are able to provide predictions of the class labels. Ideally,  
3480 one would like the output of a classifier to give a confidence level about the prediction.  
3481 However, it is not straightforward to interpret the outputs of our BDTs in terms of  
3482 probabilities.

3483 A way to visualise how well the predictions of a classifier are calibrated is using  
3484 reliability diagrams [154]. They represent the probability of the positive label versus the  
3485 probability predicted by the classifier. These can be obtained by binning the predicted  
3486 probabilities, and then compute the conditional probability  $P(y_{true} = 1 | y_i \leq y_{pred} <$   
3487  $y_{i+1})$  by checking the fraction of true positive instances in each bin. The reliability

### 6.3. MUON AND PION SEPARATION IN THE ECAL AND MUID

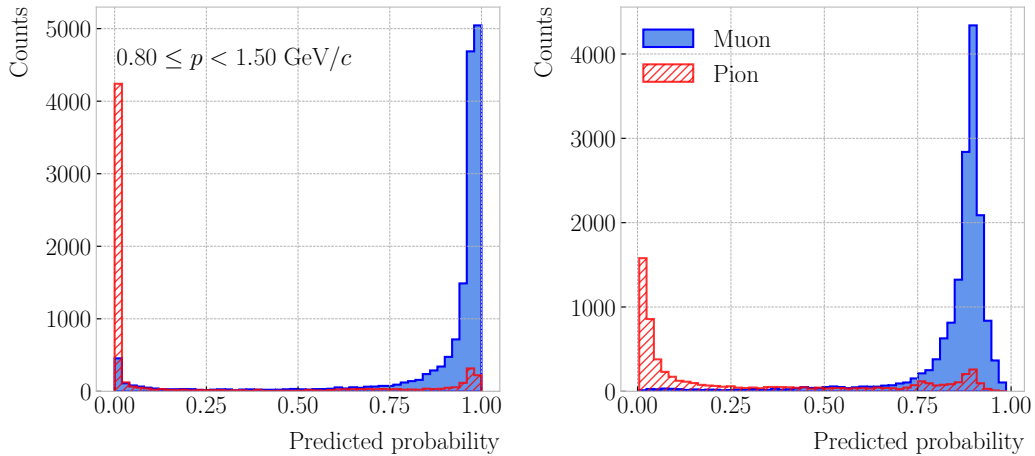


**Figure 6.29:** Uncalibrated (left panel) and calibrated (right panel) predicted probabilities assigned by the BDT classifiers for true muons (blue) and charged pions (red) in the momentum range  $0.3 \leq p < 0.8 \text{ GeV}/c$ .

3488 diagram of a perfectly calibrated classifier would be a diagonal line.

3489 In this case, I try to correct the raw response of the classifiers by applying a sigmoid  
3490 function:

$$\sigma(x; A, B) = \frac{1}{1 + e^{Ax+B}}, \quad (6.18)$$

3491 where the parameters  $A$  and  $B$  are real numbers determined using the method of least  
3492 squares.

3493 For each classifier, I perform a grid search to obtain the optimal values of  $A$  and  $B$ .  
3494 For any pair, I compute the predicted probabilities as  $y_{pred} = \sigma(y_{raw}; A, B)$ , where  $y_{raw}$   
3495 are the raw predictions of the classifier<sup>10</sup>. Then, I calculate the corresponding reliability  
3496 curve, and take the sum of the squared residuals between it and the response of the  
3497 perfectly calibrated classifier.

3498 Figure 6.28 shows the reliability diagrams for the original (blue) and calibrated  
3499 (yellow) probability predictions of the classifier for the III momentum range,  $0.3 \leq p <$   
3500  $0.8 \text{ GeV}/c$ . The original response of the classifier is given by  $y_{pred} = \sigma(y_{raw}; -2, 0)$ ,  
3501 which is the transformation applied by `scikit-learn` to produce the probability estimate.  
3502 Notice how the calibrated prediction matches the ideal response much better than the

---

<sup>10</sup>In `scikit-learn` these correspond to the outputs of the `decision_function` method.

## CHAPTER 6. PARTICLE ID IN ND-GAr

3503 original, across all the probability range.

3504 One can also compare the responses of the uncalibrated and calibrated classifiers  
3505 broken down by true particle type, as shown in Fig. 6.29. It can be seen that the  
3506 distributions for both muons (blue) and charged pions (red) smoothen after calibration,  
3507 but still the separating power of the classifier remains unchanged.

3508 At this point, having the trained classifiers and the probability calibration parameters,  
3509 I am able to assess the performance of the classification strategy in a physics-relevant  
3510 case.

### 3511 6.3.6 Performance

## 3512 6.4 ECal time-of-flight

3513 Looking at Fig. 6.20, it is clear that for momentum values in the range  $1.0 - 3.0 \text{ GeV}/c$   
3514 it is not possible to separate pions and protons using a  $\langle dE/dx \rangle$  measurement in the  
3515 HPgTPC. However, in the previous section I assumed that protons at those energies  
3516 could be identified by other means, and therefore were not an issue for the muon and  
3517 pion discrimination.

3518 Some detectors, like ALICE [155] or the ILD concept [156], complement the PID  
3519 capabilities of their gaseous trackers with time-of-flight measurements. The use of  
3520 fast timing silicon sensors, with hit time resolutions under 100 ps, would allow for the  
3521 identification of charged hadrons via a ToF measurement up to  $5.0 \text{ GeV}/c$ . In the case  
3522 of ND-GAr, one could think of using the inner layers of the ECal, the ones consisting of  
3523 high-granularity tiles, to obtain a ToF-based PID, with some inputs from the TPC.

3524 Measuring the momentum and the velocity of a charged particle allows for a  
3525 determination of the mass through the relativistic momentum formula:

$$m = \frac{p}{\beta} \sqrt{1 - \beta^2}. \quad (6.19)$$

3526 In our case, the momentum is measured in the TPC, using the curvature and the dip

## 6.4. ECAL TIME-OF-FLIGHT

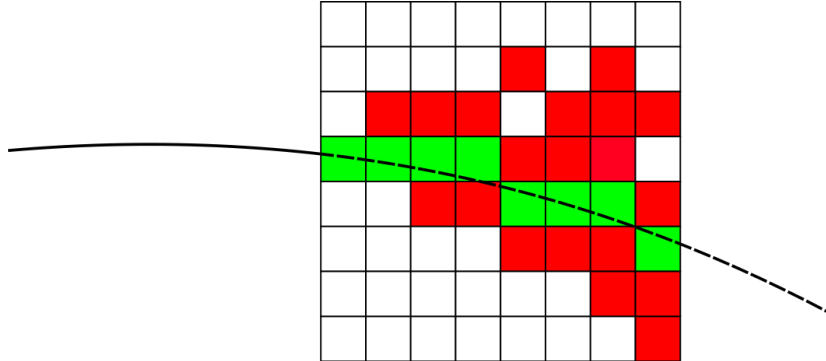


**Figure 6.30:** Schematic of the hit selection used for the ToF measurement. The grid represents the layers of the inner ECAL, with coloured squares indicating the tiles with hits. Green squares indicate the selected hits.

angle of the helix inside the magnetic field. The velocity of the particle can be written as:

$$\beta = \frac{\ell_{track}}{c\tau}, \quad (6.20)$$

where  $\ell_{track}$  is the length of the track, and  $\tau$  the arrival time to the ECAL.

In GArSoft, the track length is computed at the Kalman filter stage. It is simply the sum of the line segments along the track, either in the forward or backward fit. In this case, because we are only interested in the particles that make it to the ECAL, I choose the fit direction based on the results of the track-cluster associations.

Additionally, because the last 30 cm of the TPC radius are uninstrumented<sup>11</sup>, I need to correct for the length of the tracks. Using the track fit parameters to propagate the helix to its entry point in the ECAL, one can write the total track length as:

$$\ell_{track} = \ell + \left| \frac{\phi_{EP} - \phi}{R^{-1}} \right| \sqrt{1 + \tan^2 \lambda}, \quad (6.21)$$

where  $\phi_{EP}$  is the angle of rotation at the entry point to the calorimeter, and  $\ell$ ,  $\phi$ ,  $R$  and  $\lambda$  are the track length, angle of rotation, radius of curvature and dip angle at the last point in the fit, respectively.

To test the idea of performing a ToF measurement with the inner ECAL, I generated

---

<sup>11</sup>Note to self: check this number.

## CHAPTER 6. PARTICLE ID IN ND-GAr

3541 two data samples. Each consists of 10000 single particle events, either charged pions or  
3542 protons. Their momenta are uniformly distributed in the range  $0.5 - 5.0 \text{ GeV}/c$ , and  
3543 their directions are isotropic. I process each sample using different values of the time  
3544 resolution, from  $\Delta\tau = 0$ , the perfect time resolution case for comparison, to the current  
3545 nominal value of  $\Delta\tau = 0.7 \text{ ns}$ , and the worse scenario of  $\Delta\tau = 1.0 \text{ ns}$ .

### 3546 6.4.1 Arrival time estimations

3547 In the simulation, the limited time resolution of the ECal is taken into account by  
3548 applying a Gaussian smearing to the true hit times. Other effects, like the digitisation  
3549 of the signals, are not taken into account and fall beyond the scope of this study. After  
3550 the track-cluster, one ends up with a collection of ECal hits associated to each particle.  
3551 From these, the arrival time of the particle to the ECal can be extracted.

3552 The simplest possibilities are to either take the time of the earliest hit or the hit  
3553 closest to the entry point. Because these two coincide, in general, I focused only in  
3554 the earliest hit time. However, this needs to be corrected, to account for the distance  
3555 travelled from the entry point to the position of the hit:

$$\tau_{earliest} = \tau_{hit} - \frac{d_{EP-hit}}{c}, \quad (6.22)$$

3556 where  $\tau_{hit}$  is the time of the earliest hit, and  $d_{EP-hit}$  is the distance between that hit  
3557 and the entry point of the particle to the ECal. This is computed as the arc length  
3558 between the entry point and the point of the extrapolated helix up to the layer of the  
3559 hit. This way of correcting the time assumes  $c$  for the propagation of the particle, which  
3560 may lead to biased estimates.

3561 I also tried to estimate the arrival times using information from the rest of the hits.  
3562 In order to do this, as a simplifying assumption, I approximate the hadronic shower  
3563 considering only its MIP component. For each layer, I keep only the hit in the tile closest  
3564 to the point of the extrapolated track up to that layer. Figure 6.30 shows an example of  
3565 how this hit selection works. The dashed line represents the extrapolated track, while

## 6.4. ECAL TIME-OF-FLIGHT

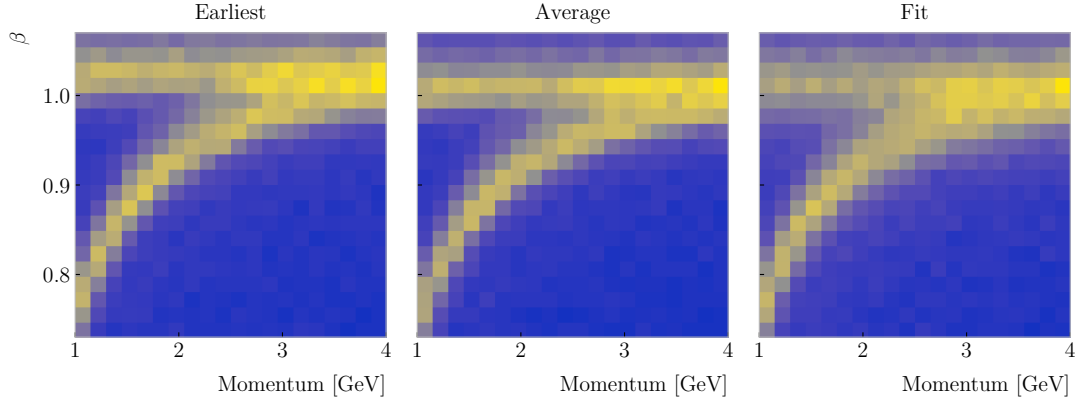


**Figure 6.31:** Particle velocity versus momentum measured with different ECal arrival time estimations. From left to right: earliest hit time, average hit time, and fitted hit time. In all cases the time resolution is  $\Delta\tau = 0.1$  ns.

3566 the coloured squares are the tiles containing hits. Green indicates the tiles closer to the  
 3567 track in each layer (in the sketch they correspond to the grid columns).

3568 Now, I can use these collections of hits to estimate the arrival times. A possibility  
 3569 is to take the average of the times of the selected hits, denoted  $\tau_{average}$ . For that to  
 3570 work, one needs to correct these times, in a similar way as in Eq. (6.22), before taking  
 3571 the average. However, as before, this correction assumes that the particle travels at the  
 3572 speed of light inside the ECal. Another option is to perform a linear fit to the hit times  
 3573 and the distances to the entry point. In that case, the arrival time would be the fitted  
 3574 value of the intercept,  $\tau_{fit}$ . This method would not assume a speed of light propagation.

3575 Figure 6.31 shows the velocity estimations as a function of the particle momentum,  
 3576 for the earliest hit time (left panel), average hit time (middle panel), and fitted hit time  
 3577 (right panel). The two bands correspond to the  $\pi^\pm$  and the  $p$  particles.  $\Delta\tau = 0.1$  ns.  
 3578 Notice how, for the earliest hit time method, the velocities are significantly biased  
 3579 towards larger values. For the multi-hit methods, the  $\tau_{fit}$  estimate appears to produce a  
 3580 larger variance than when using the  $\tau_{average}$  method.

## CHAPTER 6. PARTICLE ID IN ND-GAr

### 3581 6.4.2 Proton and pion separation

3582 Once we have the velocities of the particles, one can estimate their masses through  
3583 Eq. (6.19). The resulting mass spectra are shown in Fig. 6.32. I computed the masses  
3584 for the three arrival time estimates discussed above, and three different values of the  
3585 time resolution:  $\Delta\tau = 0.00$  (perfect time resolution),  $\Delta\tau = 0.10$  ns, and  $\Delta\tau = 0.70$  ns.  
3586 Although in all cases we have the same number of events, it appears as if the entries  
3587 in the histograms decrease as the time resolution increases. Sometimes, the particles  
3588 get unphysical values of  $\beta > 1$ , and in turn they do not contribute to the mass spectra.  
3589 This is more likely to happen for higher values of  $\Delta\tau$ .

3590 As noted before, the average hit time method produces the most robust estimates  
3591 when increasing  $\Delta\tau$ . Intuitively this makes sense, as by taking the mean one averages  
3592 out the effect of the Gaussian smearing. Going forward, I will use this arrival time  
3593 estimator, as it appears to be the best performing one.

3594 It is possible to use the velocity estimations to select a sample of protons. In this  
3595 case, I do so by dividing the relevant momentum range in bins of  $0.1 \text{ GeV}/c$ . For each  
3596 momentum bin, I compute the expected velocity for the protons via the inverse of Eq.  
3597 (6.19), and then take the fractional residuals of the measured velocities. Using that  
3598 distribution, I choose the cut that maximises the  $F_1$ -score of the proton selection.

3599 The results can be seen in Fig. 6.33, for the case  $\Delta\tau = 0.10$  ns. As expected from  
3600 Fig. 6.31, the performance of the selection degrades rapidly with increasing momentum.  
3601 However, the purity is still around 75% at  $3.0 \text{ GeV}/c$ . This is likely to be sufficient, as  
3602 we do not expect protons or charged pions with higher energies from the beam neutrino  
3603 interactions.

3604 Figure 6.34

### 3605 6.5 Charged pion decay in flight

3606 As discussed previously, in GArSoft the TPC tracks are formed after a pattern recognition  
3607 algorithm and a Kalman filter are applied to the TPC clusters. These two steps can

## 6.5. CHARGED PION DECAY IN FLIGHT

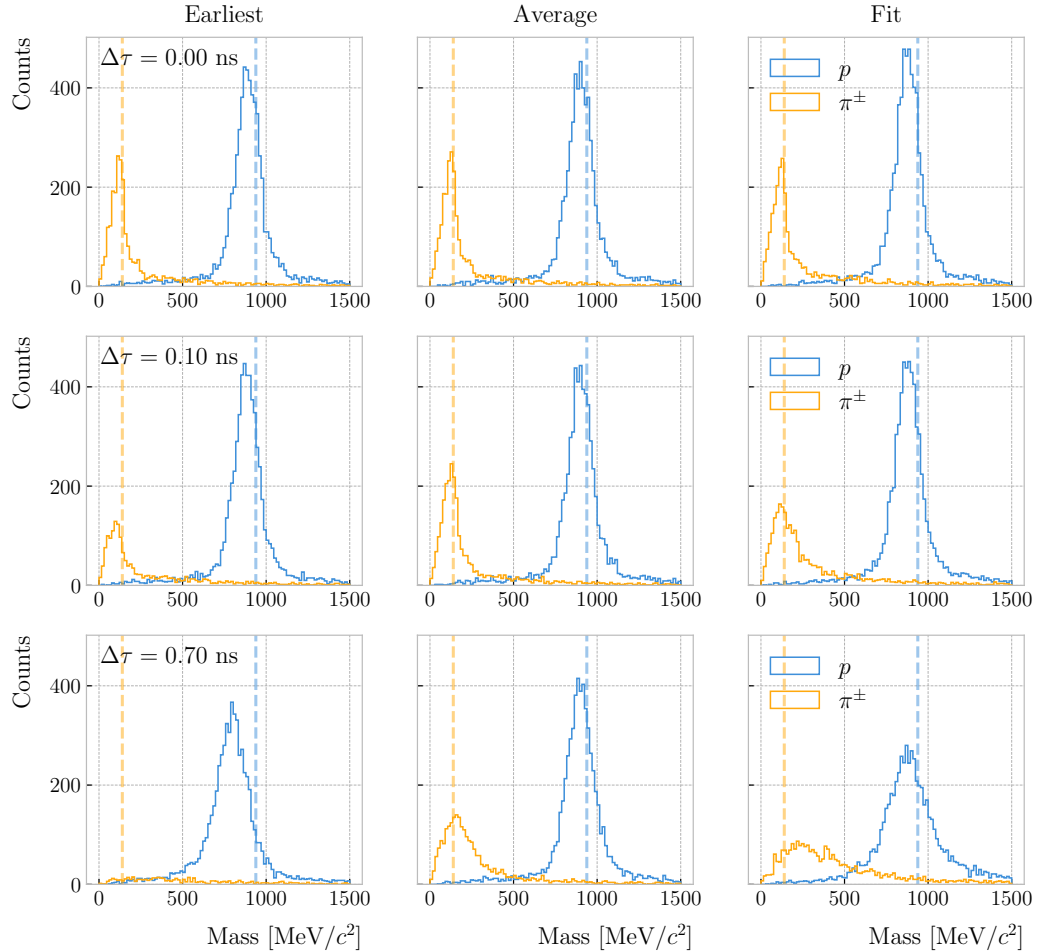


**Figure 6.32:** Mass spectra for  $p$  (blue) and  $\pi^\pm$  (yellow) particles, using different ECal time resolution values (from top to bottom, in ascending order), and arrival time estimates. From left to right: earliest hit time, average hit time, and fitted hit time. The dashed lines indicate the true masses of the particles.

3608 find discontinuities in the track candidates (e.g. due to a particle decay) when these  
 3609 so-called breakpoints are large enough. However, for some, more subtle, cases they may  
 3610 miss them and form a single reconstructed track. It has been noted in the literature  
 3611 that Kalman filters offer, as a by-product, additional information to form test statistics  
 3612 to identify these breakpoints [157, 158].

3613 Considering the mean life of the charged pion,  $\tau = (2.6033 \pm 0.0005) \times 10^{-8}$  s, one  
 3614 can estimate that about 12% of the pions with momentum  $p \sim \mathcal{O}(500 \text{ MeV}/c)$  (roughly  
 3615 the peak of the pion momentum distribution in  $\nu_\mu$  CC interactions off argon) decay

## CHAPTER 6. PARTICLE ID IN ND-GAr

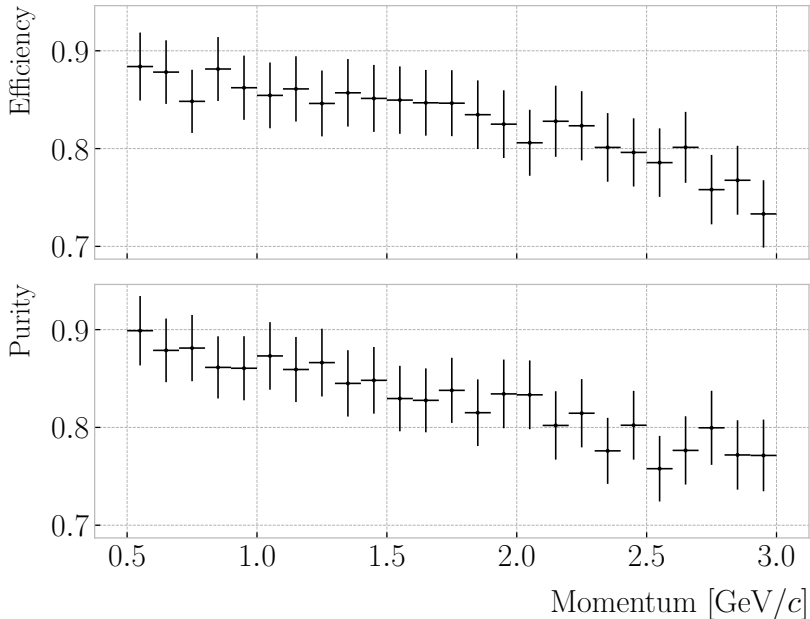


**Figure 6.33:** Efficiency (top panel) and purity (bottom panel) for the proton selection as a function of the momentum, for  $\Delta\tau = 0.10$  ns.

3616     inside the TPC. Figure 6.35 (left panel) shows the amount of charged pions decaying in  
 3617     the full TPC and fiducial volumes from an isotropic, monoenergetic sample of 100000  
 3618     negatively charged pions with  $p = 500$  MeV/ $c$ . We see that about 10% of those decayed,  
 3619     with more than half of them decaying inside the TPC fiducial volume.

3620       Figure 6.35 (right panel) shows an example event display of a charged pion (magenta  
 3621       line) decays in flight inside the TPC, but because the angle of the muon (blue line) is  
 3622       small both were reconstructed as one single track (black line). In this case, the composite  
 3623       track reaches the ECal, where it undergoes a muon-like interaction, thus being classified  
 3624       as a muon.

3625       A way to understand what decaying pion tracks were totally or partially reconstructed  
 3626       together with the daughter muon is looking at the relative energy contributions to the  
 3627       reconstructed track. In order to select a sample of such events, I require that a minimum  
 3628       50% of the total energy comes from the pion and at least 20% from the muon.

## 6.5. CHARGED PION DECAY IN FLIGHT

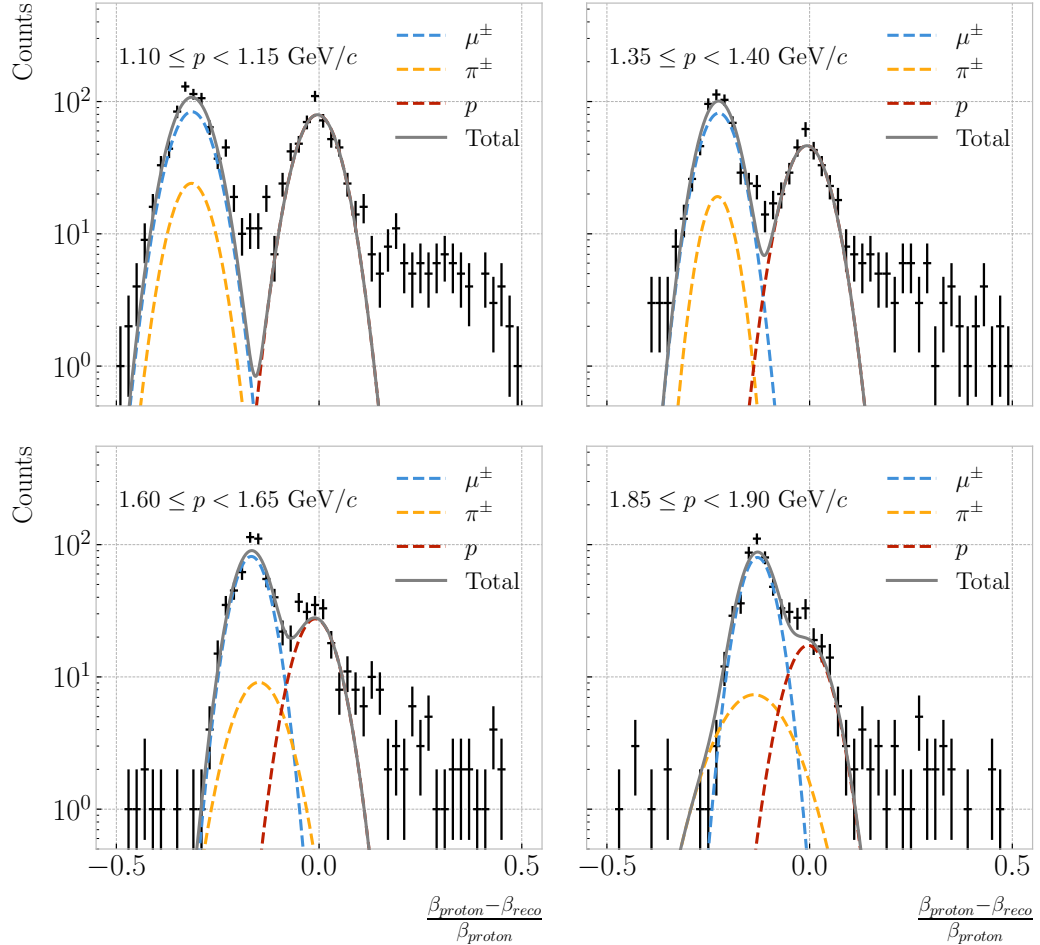


**Figure 6.34:** Distributions of the velocities measured by ToF with the inner ECal, for different momentum bins, in a FHC neutrino interaction sample. The Gaussian fits are performed around the maxima for each particle species.

### 3629 6.5.1 Track breakpoints

3630 To identify potential decays we can use the information we obtain from the Kalman  
 3631 filter at each step of the fitted track. The simplest test we can think about is computing  
 3632 the  $\chi^2$  of the mismatch between all the parameters in the forward and the backward fits:

$$\chi_k^{2 (FB)} = (\hat{x}_k^B - \hat{x}_k^F)^T [V^{(\hat{x}_k, B)} + V^{(\hat{x}_k, F)}]^{-1} (\hat{x}_k^B - \hat{x}_k^F), \quad (6.23)$$

3633 where  $\hat{x}_k^F$ ,  $\hat{x}_k^B$  are the Kalman filter state vector estimates at step  $k$  in the forward and  
 3634 backward fits and  $V^{(\hat{x}_k, F)}$ ,  $V^{(\hat{x}_k, B)}$  the covariance matrices of  $\hat{x}_k^F$  and  $\hat{x}_k^B$  respectively.

## CHAPTER 6. PARTICLE ID IN ND-GAr

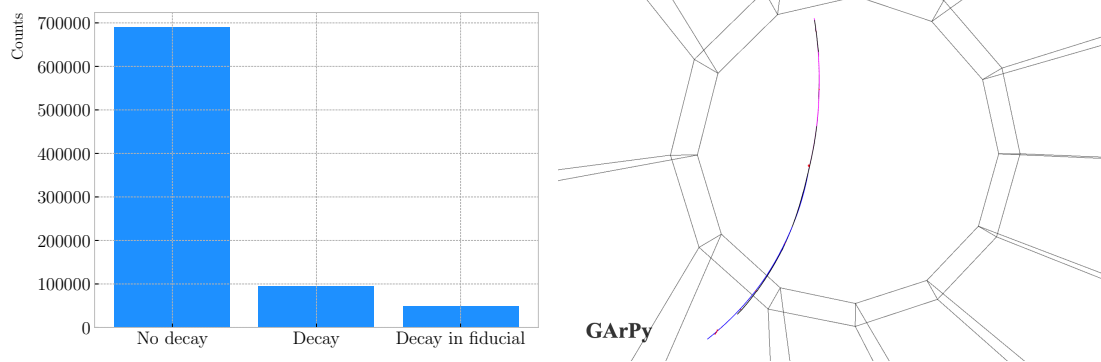


**Figure 6.35:** Left panel: number of non-decaying, decaying and decaying in the fiducial volume pions for a MC sample of 100000,  $p = 500$  MeV/c isotropic positively charged pions inside the TPC. Right panel: event display for a positive pion decaying inside the fiducial volume, with a single reconstructed track for the pion and muon system.

3635 Using the values of the  $\chi^2$  at measurement  $k$  for the forward and backward fits we can  
 3636 compute another  $\chi^2$  value that characterises the overall track fit:

$$\chi_{track}^2 = \chi_k^{2(F)} + \chi_k^{2(B)} + \chi_k^{2(FB)}, \quad (6.24)$$

3637 which remains approximately constant for all  $k$ .

3638 An alternative approach proposed in the context of the NOMAD experiment was  
 3639 using a fit with a more elaborate breakpoint hypothesis, so we can perform a comparison  
 3640 of the  $\chi^2$  with and without breakpoints. This can be achieved by using some alternative  
 3641 parametrisation with extra parameters, which allows some of the track parameters to  
 3642 be discontinuous at certain points. A decay changes the momentum magnitude and  
 3643 direction, so we can use the new state vector:

$$\alpha = (y, z, 1/R_F, 1/R_B, \phi_F, \phi_B, \tan\lambda_F, \tan\lambda_B)^T. \quad (6.25)$$

3644 As we already have the estimates from the standard Kalman filter and their  
 3645 covariance matrices at each point, we do not need to repeat the Kalman fit for the new  
 3646 parametrisation. Instead, I can compute the values of  $\alpha$  at each point  $k$  that minimise

## 6.5. CHARGED PION DECAY IN FLIGHT

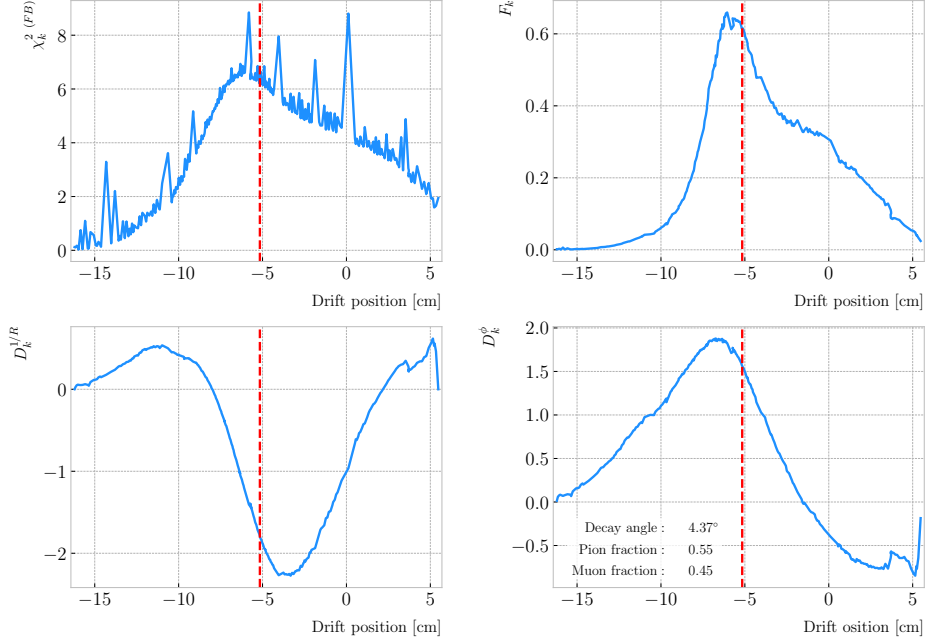


**Figure 6.36:** Values of  $\chi_k^2(FB)$  (top left panel),  $F_k$  (top right panel),  $D_k^{1/R}$  (bottom left panel) and  $D_k^\phi$  (bottom right panel) versus position along the drift direction for a reconstructed track in a positive pion decay event. The vertical red dashed line indicates the true location of the decay point.

3647 the  $\chi^2$  resulting from comparing them to  $\{\hat{x}_k^B, \hat{x}_k^F\}$ . Introducing the two  $5 \times 8$  matrices:

$$H^F = \begin{pmatrix} 1 & 0 & 0 & 0 & 0 & 0 & 0 & 0 \\ 0 & 1 & 0 & 0 & 0 & 0 & 0 & 0 \\ 0 & 0 & 1 & 0 & 0 & 0 & 0 & 0 \\ 0 & 0 & 0 & 0 & 1 & 0 & 0 & 0 \\ 0 & 0 & 0 & 0 & 0 & 0 & 1 & 0 \end{pmatrix}, \quad H^B = \begin{pmatrix} 1 & 0 & 0 & 0 & 0 & 0 & 0 & 0 \\ 0 & 1 & 0 & 0 & 0 & 0 & 0 & 0 \\ 0 & 0 & 0 & 1 & 0 & 0 & 0 & 0 \\ 0 & 0 & 0 & 0 & 0 & 1 & 0 & 0 \\ 0 & 0 & 0 & 0 & 0 & 0 & 0 & 1 \end{pmatrix}, \quad (6.26)$$

3648 we can write this as:

$$\begin{aligned} \chi_k^2(FB)(\alpha) &= (\hat{x}_k^F - H^F \alpha)^T \left[ V^{(\hat{x}_k, F)} \right]^{-1} (\hat{x}_k^F - H^F \alpha) \\ &\quad + (\hat{x}_k^B - H^B \alpha)^T \left[ V^{(\hat{x}_k, B)} \right]^{-1} (\hat{x}_k^B - H^B \alpha). \end{aligned} \quad (6.27)$$

3649 The minimum of  $\chi_k^2(FB)(\alpha)$  is found when the measured new state vector takes the  
3650 value:

$$\hat{\alpha}_k = V^{(\hat{\alpha}_k)} H^T (V^{(\hat{x}_k)})^{-1} \hat{X}, \quad (6.28)$$

## CHAPTER 6. PARTICLE ID IN ND-GAr

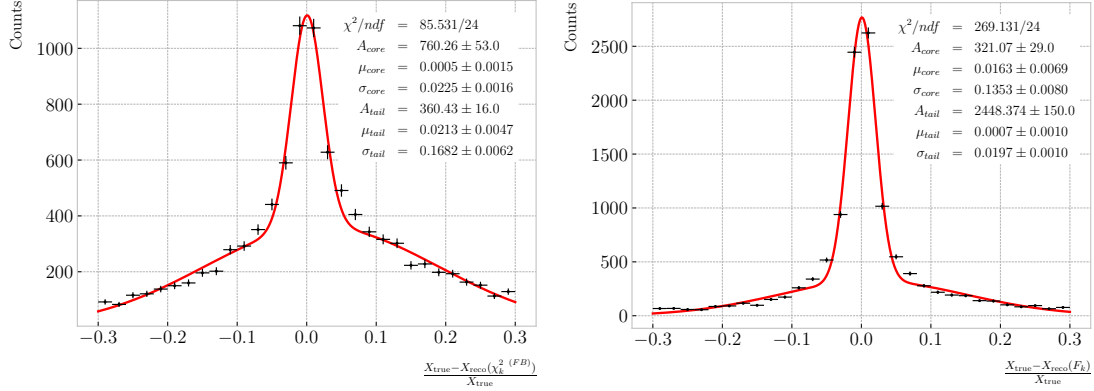


**Figure 6.37:** Fractional residual distributions of the true and reconstructed decay position along the drift coordinate, using the position of the maximum of  $\chi_k^2(FB)$  (left panel) and  $F_k$  (right panel) as estimates of the decay position. Also shown are double Gaussian fits to these points (red lines).

where  $\hat{\mathbf{X}} = \{\hat{\mathbf{x}}_k^B, \hat{\mathbf{x}}_k^F\}$ ,  $V^{(\hat{\mathbf{x}}_k)}$  is the block diagonal matrix formed by  $V^{(\hat{\mathbf{x}}_k, F)}$  and  $V^{(\hat{\mathbf{x}}_k, B)}$  and  $V^{(\hat{\alpha}_k)}$  is the covariance matrix of  $\hat{\alpha}_k$ , given by:

$$V^{(\hat{\alpha}_k)} = \left( H^T (V^{(\hat{\mathbf{x}}_k)})^{-1} H \right)^{-1}. \quad (6.29)$$

From these new fit estimates we can compute the  $F$  statistic, which tells us whether the model with breakpoint provides a statistically significant better fit:

$$F_k = \left( \frac{\chi_{\text{track},k}^2 - \chi_{\text{full},k}^2}{8 - 5} \right) / \left( \frac{\chi_{\text{full},k}^2}{N - 8} \right). \quad (6.30)$$

One can also compute the signed difference of the duplicated variables divided by their standard deviation at each point. These represent how significant the discontinuity in each variable is. For any variable  $\eta$  we can write it as:

$$D_k^\eta = \frac{\hat{\eta}_k^B - \hat{\eta}_k^F}{\sqrt{\text{Var}[\hat{\eta}_k^F] + \text{Var}[\hat{\eta}_k^B] - 2\text{Cov}[\hat{\eta}_k^F, \hat{\eta}_k^B]}}. \quad (6.31)$$

In our case, the relevant ones to look at are  $D_k^{1/R}$  and  $D_k^\phi$ .

Figure 6.36 shows the values of  $\chi_k^2(FB)$ ,  $F_k$ ,  $D_k^{1/R}$  and  $D_k^\phi$  as functions of the position along the drift direction, for an example reconstructed track with 55.5% of the energy

## 6.5. CHARGED PION DECAY IN FLIGHT

3661 coming from the charged pion and 45.5% from the daughter muon. The true position of  
 3662 the decay is indicated (dashed red lines). Notice how  $\chi_k^2(FB)$  and  $F_k$ ,  $D_k^{1/R}$  reach their  
 3663 maxima near the decay point. In the former case this indicates a large forward-backward  
 3664 difference in the track fit. In the later it represents that the extended state vector  
 3665 improves the fit particularly around that point.

3666 I can estimate the decay position finding resolution by computing the difference  
 3667 between the  $X$  position of the maxima of  $\chi_k^2(FB)$  and  $F_k$  and the  $X$  position of the  
 3668 true decay. Figure 6.37 represent the the fractional residual distributions for both  
 3669 cases, from the sample of tracks containing pion decays. Fitting a double Gaussian to  
 3670 the distributions (red lines) I find a resolution of  $(3.31 \pm 0.15)\%$  and  $(6.94 \pm 0.31)\%$   
 3671 respectively.

3672 In principle, the  $F$ -statistic should follow a Fisher distribution with  $(8 - 5)$  and  
 3673  $(N - 8)$  degrees of freedom under the null hypothesis. In most of our cases  $N \sim \mathcal{O}(100)$ ,  
 3674 so the probability density functions will look very similar. In this case, it is safe to take  
 3675 the limit  $N \rightarrow \infty$  in the Fisher PDF:

$$\begin{aligned}\tilde{f}(x; a - b) &= \lim_{N \rightarrow \infty} f(x; a - b, N - a) \\ &= \frac{2^{-\frac{a-b}{2}}}{\Gamma\left(\frac{a-b}{2}\right)} (a - b)^{\frac{a-b}{2}} x^{\frac{a-b}{2}-1} e^{-\frac{a-b}{2}x}.\end{aligned}\tag{6.32}$$

3676 In our case  $a - b = 8 - 5 = 3$ , so we would obtain a p-value of 0.05 at  $x = 2.60$ .

3677 Figure 6.38 contains the distributions of the maxima of  $\chi_k^2(FB)$ ,  $F_k$  and  $D_k^\phi$  and the  
 3678 minima of  $D_k^{1/R}$  for a sample of non-decaying pion tracks (blue) and another sample of  
 3679 reconstructed tracks containing part of the pion and the daughter muon from a decay  
 3680 inside the fiducial volume (red). Notice that, even though the values of  $F_k^{(max)}$  for the  
 3681 decay sample are typically larger than for the non-decaying one, just a small fraction of  
 3682 the events go beyond the aforementioned value of  $F = 2.60$ . Therefore, from a practical  
 3683 point of view, it is not the most efficient variable to use for selecting the decay events.

3684 However, looking at the  $D_k^{1/R \text{ (min)}}$  distribution we can see there is a big difference  
 3685 between non-decaying and decaying events in this variable. One can use a combination

## CHAPTER 6. PARTICLE ID IN ND-GAR

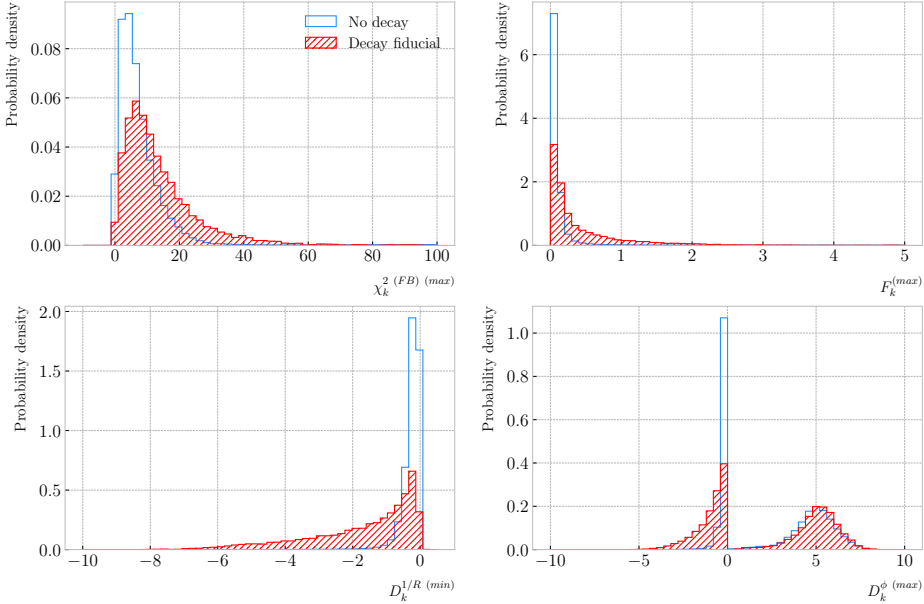


**Figure 6.38:** Distributions of the extreme values of  $\chi_k^2 (FB)$  (top left panel),  $F_k$  (top right panel),  $D_k^{1/R}$  (bottom left panel) and  $D_k^\phi$  (bottom right panel) for non-decaying reconstructed pion tracks (blue) and tracks which include the decay inside the fiducial volume (red).

3686 of these four variables to distinguish between the pion decay events (signal) and the  
 3687 non-decaying pions (background).

3688 An approach to this classification could be using a boosted decision tree (BDT). One  
 3689 of the advantages of BDTs is that they are easy to interpret and identify the relative  
 3690 importance of the different input variables. Training a BDT with 400 estimators and a  
 3691 maximum depth of 4 I can obtain an efficient classification without overtraining. Figure  
 3692 6.39 (left panel) shows the distribution of probabilities predicted by the BDT for a test  
 3693 sample. The signal efficiency as a function of background acceptance, the so-called ROC  
 3694 curve, is shown in Fig. 6.39 (right panel). With a relative importance of 0.83, the most  
 3695 important variable turned out to be  $D_k^{1/R} (min)$ .

3696 One thing we can check is how the resolution to the decay and the signal efficiency in  
 3697 the classification changes with the true decay angle. Using an equal-frequency binning  
 3698 for the decay angles, we can repeat the previous steps for each bin.

3699 Figure 6.40 (left panel) shows the dependence on the decay angle of the decay finding

## 6.5. CHARGED PION DECAY IN FLIGHT

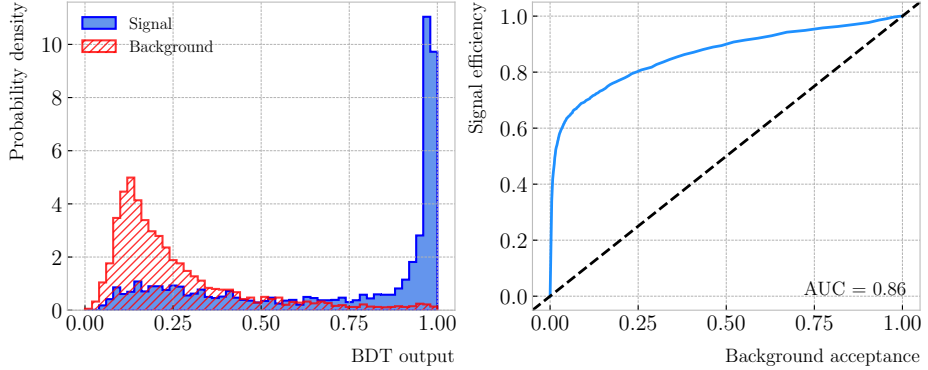


**Figure 6.39:** Left panel: distributions of the predicted probabilities assigned by the BDT classifier to a test sample of decaying pion+muon tracks (blue) and non-decaying pion tracks (red). Left: signal efficiency versus background acceptance (ROC curve) obtained from the BDT for the test sample.

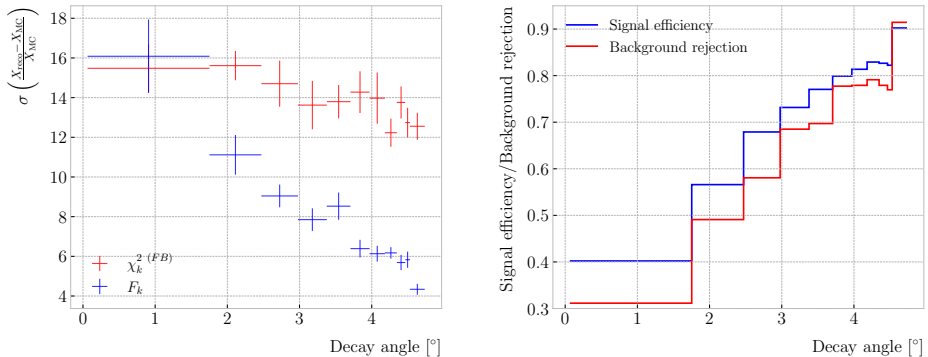


**Figure 6.40:** Left panel: dependence of the decay position finding resolution on the true value of the decay angle for the  $\chi_k^2(FB)$  (red) and  $F_k$  (blue) methods. Right panel: signal efficiency (blue line) and background rejection (red line) from the BDT classifier versus true decay angle.

resolution. We can see that for the  $\chi_k^2(FB)$  maximum location method the resolution consistently lies between 12 to 16%. However, the  $F_k^{(\max)}$  approach gives a significantly better resolution for high angle values, reaching the 4 – 6% range for decay angles  $\geq 4^\circ$ .

For the classification dependence on the angle, I use the same classifier I trained before but evaluating the test sample for each individual angular bin. I compute the signal efficiency in each bin for a fixed value of the background rejection, in this case 90%. Similarly, for the background rejection estimation I use a fixed signal efficiency value of 90%. Figure 6.40 (right panel) represents the change in signal efficiency (blue)

## CHAPTER 6. PARTICLE ID IN ND-GAr

3708 and background rejection (red) with the value of the true decay angles.

### 3709 6.6 Neutral particle identification

#### 3710 6.6.1 ECal clustering

3711 Another important reconstruction item is the clustering algorithm of ECal hits in  
3712 GArSoft. The default module features a NN algorithm that treats all hits in the same  
3713 way, independently of the layer each hit comes from. However, the current ECal design  
3714 of ND-GAr has two very different types of scintillator layers. The inner layers are made  
3715 out of tiles, which provide excellent angular and timing resolutions. On the other hand,  
3716 the outer layers are cross scintillator strips. That way, an algorithm that treats hits  
3717 from both kinds of layers differently may be able to improve the current performance.

3718 Inspired by the reconstruction of T2K’s ND280 downstream ECal [159], the idea  
3719 was to put together a clustering module that first builds clusters for the different ECal  
3720 views (tiles, strips segmented in the  $X$  direction and strips segmented in  $Y$  direction),  
3721 and then tries to match them together to form the final clusters.

3722 Working on a module-by-module basis, the algorithm first separates the hits depending  
3723 on the layer type they come from. Then, it performs a NN clustering for the 3 sets of  
3724 hits separately. For the tile hits it clusters together all the hits which are in nearest-  
3725 neighbouring tiles and nearest-neighbouring layers, for strip hits it looks at nearest-  
3726 neighbouring strips and next-to-nearest-neighbouring layers (as the layers with strips  
3727 along the two directions are alternated). For strip clusters an additional cut in the  
3728 direction along the strip length is needed.

3729 After this first clustering I then apply a recursive re-clustering for each collection  
3730 of strip clusters based on a PCA method. In each case, we loop over the clusters with  
3731  $N_{hits} \geq 2$ , computing the centre of mass and three principal components. Propagating  
3732 these axes up to the layers of the rest of the clusters, we check if the propagated point  
3733 and the centre of mass of the second cluster are within next-to-nearest-neighbouring  
3734 strips. An additional cut in the direction along the strip length is also needed. Moreover,

## 6.6. NEUTRAL PARTICLE IDENTIFICATION

3735 I require that the two closest hits across the two clusters are at most in next-to-nearest-  
3736 neighbouring strips. I merge the clusters if these three conditions are satisfied. The  
3737 re-clustering is repeated until no more cluster pairs pass the cuts.

3738 The clusters in each strip view are combined if their centres of mass are close enough  
3739 and they point in the same direction. An alternative approach for the strip cluster  
3740 merging could be to compute the overlap between the ellipsoids defined by the principal  
3741 axes of the clusters, and then merge the pair if the overlap exceeds some threshold.  
3742 Further study is needed to understand if this change would have an impact in the overall  
3743 clustering performance.

3744 To merge the tile clusters to the combined strip clusters I propagate the principal  
3745 axis of the strip cluster towards the inner layers, up to the centre of mass layer of the  
3746 tile cluster. I merge the clusters if the distance between the propagated point and the  
3747 centre of mass is below a certain cut.

3748 The last step is to check if clusters in neighbouring modules should be merged  
3749 together, both across two barrel modules, across end cap modules and between barrel  
3750 end cap modules. I check the distance between the two closest hits in the pair of clusters  
3751 and merge them if it passes this and an additional direction cut.

3752 Figure ?? presents an example of the clustering steps relevant for strip layer hits, from  
3753 the input hits (top left panel) to the NN clustering (top right panel) and re-clustering  
3754 (bottom left panel) for each strip view and the final merging strip clusters (bottom  
3755 right panel). It shows the hits from a single ECal barrel module in a  $\nu_\mu$  CC interaction  
3756 event with a neutral pion and a proton in the final state. The two clusters on the left  
3757 correspond to the photon pair from the  $\pi^0$  decay and the one on the upper right corner  
3758 is associated to the proton.

3759 This algorithm has a total number of eight free parameters that need to be optimised.  
3760 I used a sample of 1000  $\nu_\mu$  CC interactions in order to obtain the optimal configuration of  
3761 clustering parameters. This sample was generated up to the default ECal hit clustering  
3762 level, so then I could run the new clustering algorithm each time with a different  
3763 configuration of parameters. As the number of parameters is relatively large, I only

## CHAPTER 6. PARTICLE ID IN ND-GAr

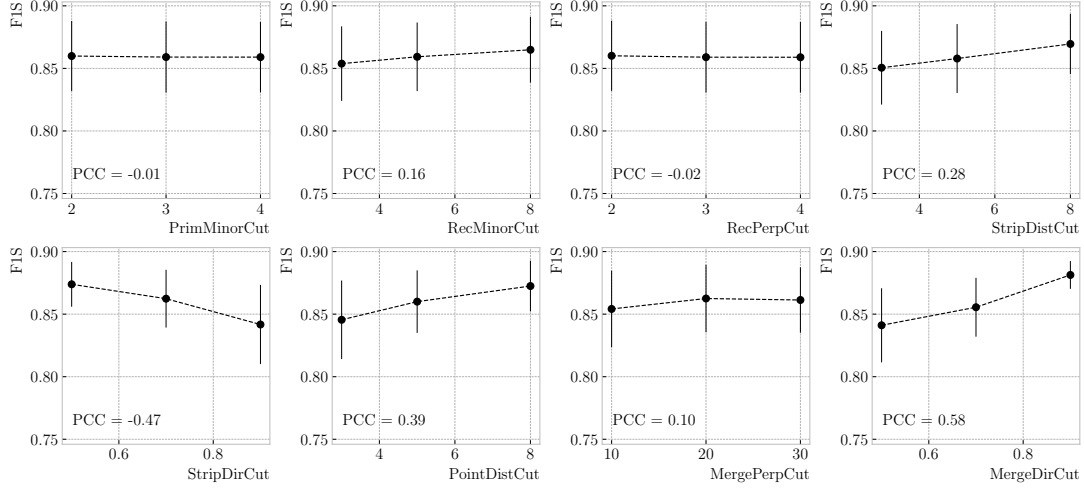


**Figure 6.41:** Mean values of the  $F_1$ -score marginal distributions for the different free parameters of the new clustering algorithm, with the error bars representing one standard deviation around the mean. The  $F_1$ -score values were computed for the 6561 possible parameter configurations using 1000  $\nu_\mu$  CC interaction events.

**Table 6.5:** Summary of parameters and sampled values used in the optimisation of the clustering algorithm.

Name	Units	Sampled values	Description
PrimMinorCut	strips	2, 3, 4	Distance along strip length in NN clustering
RecMinorCut	strips	3, 5, 8	Distance between propagated point and CM along strip length in re-clustering
RecPerpCut	strips	2, 3, 4	Closest hit pair distance in re-clustering
StripDistCut	strips	3, 5, 8	Distance between CMs in strip cluster merging
StripDirCut	cos	0.5, 0.7, 0.9	Main axes direction cut in strip cluster merging
PointDistCut	tiles	3, 5, 8	Distance between propagated point and CM in strip-tile matching
MergePerpCut	cm	10, 20, 30	Closest hit pair distance in module merging
MergeDirCut	cos	0.5, 0.7, 0.9	Main axes direction cut in module merging

3764 performed a coarse-grained scan of the parameter space. Sampling each of the eight  
 3765 parameters at three different points each I obtain 6561 different configurations. These  
 3766 parameters, together with the used values, are summarised in Tab. 6.5.

3767 In order to measure the performance of the clustering, I use a binary classification  
 3768 approach. For each formed cluster, I identify the Geant4 Track ID of the matching MC  
 3769 particle and the energy fraction of each hit. Then, I assign to each cluster the Track ID  
 3770 with the highest total energy fraction. For each of the different Track IDs associated to

## 6.6. NEUTRAL PARTICLE IDENTIFICATION

3771 the clusters, I select the cluster with the highest energy (only from the hits with the  
3772 same Track ID). I identify such a cluster as the main cluster for that Track ID. I count  
3773 as true positives (TPs) the hits with the correct Track ID in each main cluster. False  
3774 positives (FPs) are the hits with the incorrect Track ID for the cluster they are in, not  
3775 only main clusters. The false negatives (FNs) are the hits with the correct Track ID in  
3776 clusters other than the main.

3777 Figure 6.41 shows the computed  $F_1$ -score values for the different cuts. In each case,  
3778 the central value represents the mean of the  $F_1$ -score distribution for the specified value  
3779 of the corresponding variable and the vertical error bar represents one standard deviation  
3780 around the mean. Also shown are the Pearson correlation coefficients of these central  
3781 values. We can see that five of the variables have a sizeable effect on the  $F_1$ -score, with  
3782 an absolute difference between the last and first values as big as 4%.

3783 The working configuration is obtained as follows. I first select all configurations  
3784 with purity  $\geq 90\%$ . Among those, I choose the combinations that yield the maximum  
3785  $F_1$ -score. If more than one configuration remains I select the one with the highest  
3786 sensitivity. Doing so, I end up with a parameter configuration with an efficiency of 88%  
3787 and a 90% purity. Compared with the default algorithm, which gives an efficiency of  
3788 76% and a purity of 91% for the same sample, I have managed to improve the efficiency  
3789 by a factor of 1.16.

### 3790 6.6.2 $\pi^0$ reconstruction

3791 One of the potential applications of the new ECal hit clustering is the reconstruction of  
3792 neutral particles, in particular pions. Neutral pions decay promptly after being produced,  
3793 through the  $\pi^0 \rightarrow \gamma\gamma$  channel ( $98.823 \pm 0.034\%$ ) of the time. The photon pair does  
3794 not leave any traces in the HPgTPC (unless one or both of them converts into an  
3795 electron-positron pair), but each of them will produce an electromagnetic shower in  
3796 the ECal.

3797 To test the potential impact of the new algorithm in  $\pi^0$  reconstruction, I generated  
3798 a MC sample of single, isotropic neutral pions inside the HPgTPC. All pions were

## CHAPTER 6. PARTICLE ID IN ND-GAr

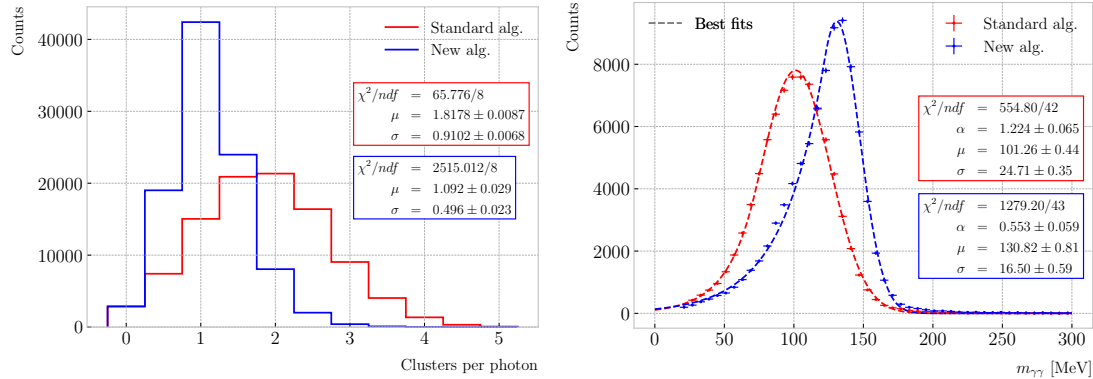


**Figure 6.42:** Left panel: distributions of the number of ECal clusters per photon from  $\pi^0$  decays for the standard (red) and new (blue) clustering algorithms. Right panel: reconstructed invariant mass distributions for photon pairs from single  $\pi^0$  events using the standard (red) and new (blue) ECal clustering algorithms.

3799 generated with a momentum  $p = 500$  MeV and their initial positions were uniformly  
 3800 sampled inside a  $2 \times 2 \times 2$  m box aligned with the centre of the TPC. I ran both the  
 3801 default and the new clustering algorithms, using for the latter the optimised configuration  
 3802 discussed above.

3803 The first thing to notice is that the number of clusters produced per photon has  
 3804 decreased. Figure 6.42 (left panel) shows these distributions for the default (red) and  
 3805 new (blue) algorithms. Using a simple Gaussian fit, we see that the mean number of  
 3806 ECal clusters per photon went from  $1.82 \pm 0.01$  to  $1.09 \pm 0.03$ . This effectively means that  
 3807 with the new algorithm the ECal activity of one true particle is typically reconstructed  
 3808 as a single object. From the reconstruction point of view this can be an advantage. As  
 3809 now most of the photon energy ends up in a single ECal cluster, I can simply use cluster  
 3810 pairs to identify the  $\pi^0$  decay.

3811 In general, one calculates the invariant mass of the photon pair as:

$$m_{\gamma\gamma} = \sqrt{2E_1E_2(1 - \cos \theta)}, \quad (6.33)$$

3812 where  $E_i$  are the energies of the photons and  $\theta$  the opening angle between them. In this  
 3813 case I can use the energies deposited in the ECal and their incident directions. This  
 3814 quantity is computed for all possible pairs of clusters, using their position together with

## 6.6. NEUTRAL PARTICLE IDENTIFICATION

3815 the true decay point. In a more realistic scenario, e.g.  $\nu_\mu$  CC interaction, one could use  
 3816 the position of the reconstructed primary vertex instead. I also tried to use the principal  
 3817 direction of the clusters, but that approach gave considerably worse results. For each  
 3818 event I only keep the pair with an invariant mass closer to the true  $\pi^0$  mass value.

3819 Figure 6.42 (right panel) shows the invariant mass distributions for the photon pairs  
 3820 we get using the default (red) and the new (blue) ECal clustering algorithms. For the fit  
 3821 I used a modified version of the Crystal Ball function [160], obtained by taking the limit  
 3822 where the parameter controlling the power-law tail goes to infinity:

$$f(x; N, \mu, \sigma, \alpha) = N \cdot \begin{cases} e^{\frac{\alpha(2x-2\mu+\alpha\sigma)}{2\sigma}}; & x \leq \mu - \alpha\sigma, \\ e^{-\frac{(x-\mu)^2}{2\sigma^2}}; & x > \mu - \alpha\sigma. \end{cases} \quad (6.34)$$

3823 Comparing the fitted mean and standard deviation values for the Gaussian cores, we  
 3824 see that the distribution for the new algorithm is a 67% narrower and also peaks much  
 3825 closer to the true  $m_{\pi^0}$  value, going from  $101.3 \pm 0.4$  MeV to  $130.8 \pm 0.6$  MeV.



3826

3827

# Event selection in ND-GAr

3828 **7.1 Data sample**3829 **7.2  $\nu_\mu$  CC selection**

3830 In a  $\nu_\mu$  CC inclusive selection, the signal topology we look for is a neutrino-induced  
 3831 muon with or without other final state particles. Here, I also require the neutrino vertex  
 3832 to be located inside the fiducial volume (FV) of ND-GAr.

3833 The FV is defined as a smaller cylinder within the cylindrical volume of the HPgTPC.  
 3834 The FV has a radius  $R_{\text{FV}}$  and a half-length  $L_{\text{FV}}$ . For a particle position to lie within  
 3835 the FV it must satisfy:

$$\vec{x}_i \in \left\{ \vec{x} \in \mathbb{R}^3 \mid |x_0| \leq L_{\text{FV}} \text{ \& } \sqrt{x_1^2 + x_2^2} \leq R_{\text{FV}} \right\}, \quad (7.1)$$

3836 in the reference frame of the HPgTPC. For convenience, I define:

$$\Delta R_{\text{FV}} = R_{\text{HPgTPC}} - R_{\text{FV}}, \quad (7.2)$$

$$\Delta L_{\text{FV}} = L_{\text{HPgTPC}} - L_{\text{FV}},$$

3837 where  $R_{\text{HPgTPC}}$  and  $L_{\text{HPgTPC}}$  refer to the radius and the half-length of the HPgTPC,  
 3838 respectively. Figure 7.1 shows the HPgTPC volume with the FV inside of it. In that  
 3839 representation, the FV is defined as  $\Delta L_{\text{FV}} = 30.0$  cm and  $\Delta R_{\text{FV}} = 30.0$  cm. Also shown  
 3840 is the HPgTPC reference frame, with  $x$  being the drift direction and  $z$  aligned along the

## CHAPTER 7. EVENT SELECTION IN ND-GAr

**Table 7.1:** Event rates in ND-GAr.

Process	Events/ton/year	
	$1.1 \times 10^{21}$ POT/year	$1.9 \times 10^{21}$ POT/year
All $\nu_\mu$ -CC	$1.60 \times 10^6$	$2.83 \times 10^6$
CC $0\pi$	$5.28 \times 10^5$	$9.35 \times 10^5$
CC $1\pi^\pm$	$3.02 \times 10^5$	$5.34 \times 10^5$
CC $1\pi^0$	$1.65 \times 10^5$	$2.92 \times 10^5$
CC $2\pi$	$3.18 \times 10^5$	$5.63 \times 10^5$
CC $3\pi$	$1.36 \times 10^5$	$2.41 \times 10^5$
CC other	$1.52 \times 10^5$	$2.69 \times 10^5$
All $\bar{\nu}_\mu$ -CC	$7.54 \times 10^4$	$1.33 \times 10^5$
All NC	$5.50 \times 10^5$	$9.73 \times 10^5$
All $\nu_e$ -CC	$2.70 \times 10^4$	$4.78 \times 10^4$

3841 beam direction.

3842 In some cases, it is interesting to divide the signal events in different categories  
3843 based on their true interaction mode. In this work, I will distinguish between charged-  
3844 current quasi-elastic (CCQE), coherent (CCCOH), resonant (CCRES), and deep-inelastic  
3845 (CCDIS) interactions. I also use a separate category for the interactions not included in  
3846 any of the other categories (CCOther).

3847 Any other events are considered backgrounds. For this selection, I use the following  
3848 categorisation of background events:

- 3849 • Out of FV: if the true neutrino vertex lies outside the defined FV.
- 3850 • NC: if the event is a true neutral-current event.
- 3851 •  $\bar{\nu}_\mu$  CC: if the true neutrino candidate is of muon antineutrino flavour.
- 3852 • Other: if the event is not signal nor falls in any of the other background categories.

3853 The key to the CC selection is the identification of a primary muon candidate.  
3854 Typically, this is the longest track in the event. However, sometimes protons and pions  
3855 leave tracks longer than that of the muon. This is particularly important in the GAr

## 7.2. $\nu_\mu$ CC SELECTION

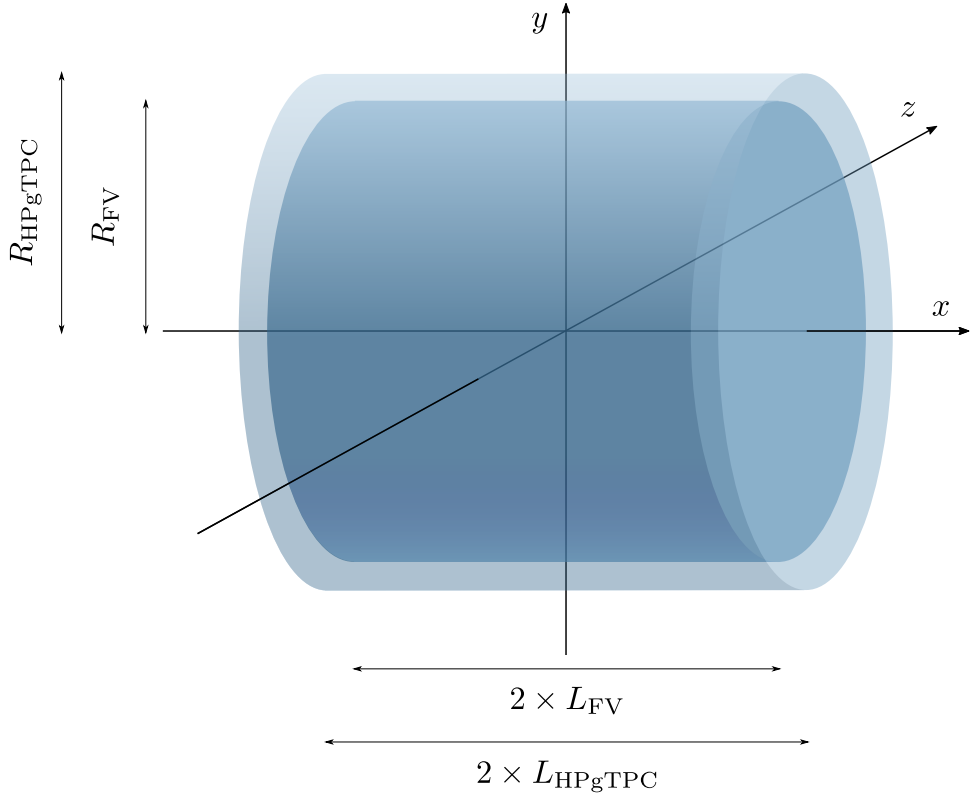


**Figure 7.1:** Schematic diagram of the HPgTPC including the fiducial volume (FV). In this case the FV is given by  $\Delta L_{\text{FV}} = 30.0$  cm and  $\Delta R_{\text{FV}} = 30.0$  cm.

3856 medium, considerably less dense than the LAr. For this reason, the muon identification  
 3857 in ND-GAr relies heavily on the capabilities of the ECal.

3858 The selection strategy proposed combines the information coming from the three  
 3859 main detection systems of ND-GAr: the HPgTPC charge readout, and the ECal and  
 3860  $\mu$ ID detectors. It consists of five steps:

- 3861 1. Event contains reconstructed particles.
- 3862 2. Select particles with reconstructed negative charge,  $q_{\text{reco}} = -1$ .
- 3863 3. Select particles passing the muon score cut,  $\mu_{\text{score}} \geq \mu_{\text{score}}^{\text{cut}}$ .
- 3864 4. Keep reconstructed particle with the highest momentum,  $\max [p_{\text{reco}}]$ .
- 3865 5. Check that the remaining particle starts within the FV.

## CHAPTER 7. EVENT SELECTION IN ND-GAR

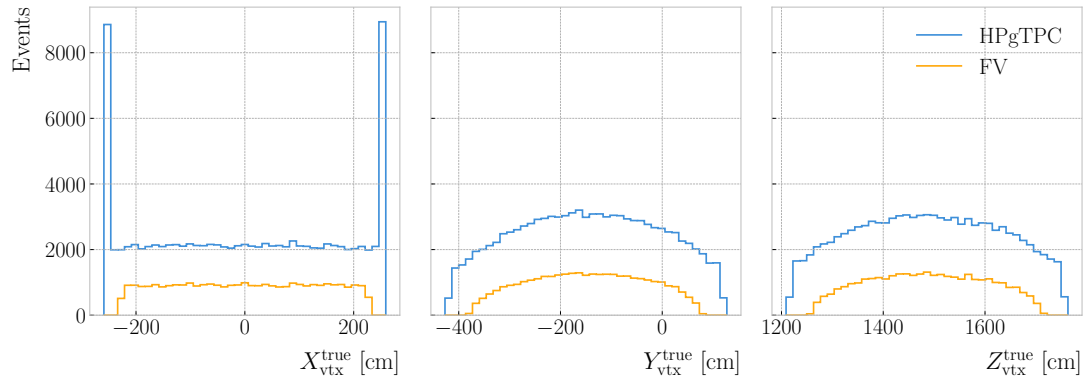


**Figure 7.2:** Distributions of the true  $\nu_\mu$  CC vertex positions for the full HPgTPC volume (blue) and the optimised FV (yellow), given by  $\Delta L_{\text{FV}} = 30.0$  cm and  $\Delta R_{\text{FV}} = 50.0$  cm.

3866 All the events passing these cuts are classified as signal, and the selected particle is  
 3867 regarded as the primary muon candidate.

3868 **7.2.1 Selection optimisation**

3869 I performed an optimisation of the selection . For the muon selection, I varied the value  
 3870 of  $\mu_{\text{score}}^{\text{cut}}$  from 0.05 to 0.95, using a step size of 0.05. Additionally, to optimise the FV, I  
 3871 systematically explored a number of different parameter configurations, moving within  
 3872 the 10.0 – 70.0 cm range for  $\Delta L_{\text{FV}}$  and 25.0 – 75.0 cm for  $\Delta R_{\text{FV}}$ , in increments of  
 3873 10.0 cm and 5.0 cm respectively.

3874 For each parameter configuration, I extract three different true neutrino energy  
 3875 distributions. These are built combining the results of the selection described previously,  
 3876 which we can refer to as the “reco” selection, and a “true” selection. The later identifies  
 3877 the true  $\nu_\mu$  CC events using the GENIE event records, and checks that the true neutrino  
 3878 vertices are contained in the FV.

3879 The first distribution consists of the events passing both selections, i.e., these are the  
 3880 true  $\nu_\mu$  CC events which pass the “reco” selection. The second distribution of the events  
 3881 passing the “reco” selection but failing the “true” selection. These are the background  
 3882 events that the selection misidentifies. Finally, the third distribution corresponds to the  
 3883 events

### 7.3. CHARGED PION IDENTIFICATION

**Table 7.2:** Step-by-step  $\nu_\mu$  CC selection cuts and cumulative passing rates. Relative passing rates are indicated in parentheses.

Cut #	Selection cut	Events	Passing rates
0	Total number of events (No cuts)	100000	100.00% (100.00%)
1	At least one reconstructed particle	85680	85.68% (85.68%)
2	Negatively charged particles only	62054	62.05% (72.43%)
3	$\mu_{\text{score}} \geq \mu_{\text{score}}^{\text{cut}}$	45035	45.03% (72.57%)
4	Candidate $\vec{x}_{\text{start}}$ in FDV	31212	31.21% (69.31%)

3884 **7.2.2 Primary muon kinematics**

3885 **7.3 Charged pion identification**

3886 **7.3.1  $\nu_\mu$  CC  $1\pi^\pm$  selection**

CHAPTER 7. EVENT SELECTION IN ND-GAR

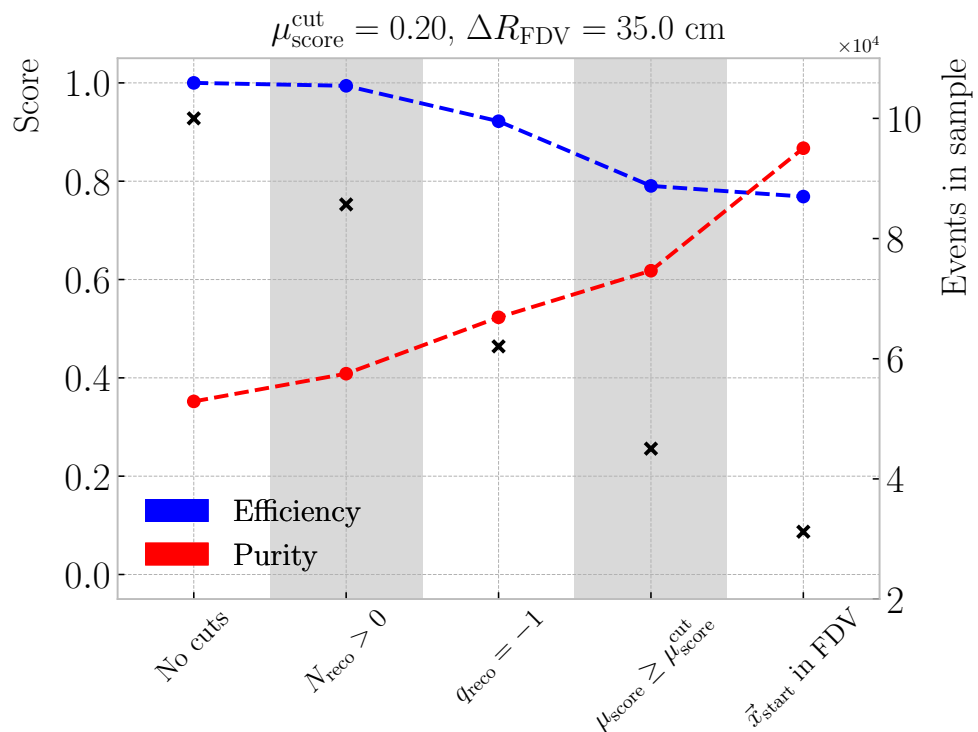


**Figure 7.3:** Cumulative efficiency (blue) and purity (red) of the  $\nu_\mu$  CC selection. Also indicated is the number of events in the sample after each cut (black crosses).

8

3887

## Conclusions

3888



3889

A [REDACTED]

3890

An appendix



## Bibliography

- 3892 [1] J.N. Bahcall, A.M. Serenelli and S. Basu, *New solar opacities, abundances,*  
 3893 *helioseismology, and neutrino fluxes*, *Astrophys. J. Lett.* **621** (2005) L85  
 3894 [[astro-ph/0412440](#)]. 22, 42, 124, 125, 126
- 3895 [2] R. Garani and S. Palomares-Ruiz, *Dark matter in the Sun: scattering off electrons*  
 3896 *vs nucleons*, *JCAP* **05** (2017) 007 [[1702.02768](#)]. 22, 122, 123, 126, 127, 128, 150
- 3897 [3] M. Honda, M. Sajjad Athar, T. Kajita, K. Kasahara and S. Midorikawa,  
 3898 *Atmospheric neutrino flux calculation using the NRLMSISE-00 atmospheric model*,  
 3899 *Phys. Rev. D* **92** (2015) 023004 [[1502.03916](#)]. 22, 131, 132
- 3900 [4] M. Colom i Bernadich and C. Pérez de los Heros, *Limits on Kaluza-Klein dark*  
 3901 *matter annihilation in the Sun from recent IceCube results*, *Eur. Phys. J. C*, **80** 2  
 3902 (2020) 129 **80** (2019) [[1912.04585](#)]. 23, 135, 136
- 3903 [5] ANTARES collaboration, *Search for Dark Matter in the Sun with the ANTARES*  
 3904 *Neutrino Telescope in the CMSSM and mUED frameworks*, *Nucl. Instrum. Meth.*  
 3905 *A* **725** (2013) 76 [[1204.5290](#)]. 23, 135, 136
- 3906 [6] N. Deutschmann, T. Flacke and J.S. Kim, *Current LHC Constraints on Minimal*  
 3907 *Universal Extra Dimensions*, *Phys. Lett. B* **771** (2017) 515 [[1702.00410](#)]. 23, 135,  
 3908 136
- 3909 [7] ICECUBE collaboration, *Search for GeV-scale dark matter annihilation in the Sun*  
 3910 *with IceCube DeepCore*, *Phys. Rev. D* **105** (2022) 062004 [[2111.09970](#)]. 24, 147,  
 3911 148

## BIBLIOGRAPHY

- 3912 [8] C.-S. Chen, F.-F. Lee, G.-L. Lin and Y.-H. Lin, *Probing Dark Matter*  
3913 *Self-Interaction in the Sun with IceCube-PINGU*, *JCAP* **10** (2014) 049  
3914 [1408.5471]. 24, 147, 148
- 3915 [9] N.F. Bell, M.J. Dolan and S. Robles, *Searching for dark matter in the Sun using*  
3916 *Hyper-Kamiokande*, *JCAP* **11** (2021) 004 [2107.04216]. 24, 147, 148
- 3917 [10] E. Behnke et al., *Final Results of the PICASSO Dark Matter Search Experiment*,  
3918 *Astropart. Phys.* **90** (2017) 85 [1611.01499]. 24, 147, 148
- 3919 [11] PICO collaboration, *Dark Matter Search Results from the Complete Exposure of*  
3920 *the PICO-60 C<sub>3</sub>F<sub>8</sub> Bubble Chamber*, *Phys. Rev. D* **100** (2019) 022001  
3921 [1902.04031]. 24, 147, 148
- 3922 [12] DARKSIDE collaboration, *Constraints on Sub-GeV Dark-Matter–Electron*  
3923 *Scattering from the DarkSide-50 Experiment*, *Phys. Rev. Lett.* **121** (2018) 111303  
3924 [1802.06998]. 24, 152, 153
- 3925 [13] XENON collaboration, *Light Dark Matter Search with Ionization Signals in*  
3926 *XENON1T*, *Phys. Rev. Lett.* **123** (2019) 251801 [1907.11485]. 24, 152, 153
- 3927 [14] P.F. de Salas, D.V. Forero, S. Gariazzo, P. Martínez-Miravé, O. Mena,  
3928 C.A. Ternes et al., *2020 global reassessment of the neutrino oscillation picture*,  
3929 *JHEP* **02** (2021) 071 [2006.11237]. 31, 55, 63
- 3930 [15] W. Pauli, *Dear radioactive ladies and gentlemen*, *Phys. Today* **31N9** (1978) 27. 37
- 3931 [16] F. Reines and C.L. Cowan, *Detection of the free neutrino*, *Phys. Rev.* **92** (1953)  
3932 830. 37
- 3933 [17] S.L. Glashow, *Partial-symmetries of weak interactions*, *Nuclear Physics* **22** 579. 37
- 3934 [18] S. Weinberg, *A model of leptons*, *Physical Review Letters* **19** 1264. 37
- 3935 [19] A. Salam, *Weak and Electromagnetic Interactions*, *Conf. Proc. C* **680519** (1968)  
3936 367. 37

## BIBLIOGRAPHY

- 3937 [20] A. Pich, *The Standard Model of Electroweak Interactions*, in *2010 European  
3938 School of High Energy Physics*, pp. 1–50, 1, 2012 [[1201.0537](#)]. 38
- 3939 [21] ALEPH, DELPHI, L3, OPAL, SLD, LEP ELECTROWEAK WORKING GROUP,  
3940 SLD ELECTROWEAK GROUP, SLD HEAVY FLAVOUR GROUP collaboration,  
3941 *Precision electroweak measurements on the Z resonance*, *Phys. Rept.* **427** (2006)  
3942 257 [[hep-ex/0509008](#)]. 41
- 3943 [22] R. Davis, D.S. Harmer and K.C. Hoffman, *Search for neutrinos from the sun*,  
3944 *Physical Review Letters* **20** 1205. 42
- 3945 [23] J.N. Bahcall, N.A. Bahcall and G. Shaviv, *Present Status of the Theoretical  
3946 Predictions for the  $^{37}\text{Cl}$  Solar-Neutrino Experiment*, . 42
- 3947 [24] B.T. Cleveland, T. Daily, R. Davis, Jr., J.R. Distel, K. Lande, C.K. Lee et al.,  
3948 *Measurement of the solar electron neutrino flux with the Homestake chlorine  
3949 detector*, *Astrophys. J.* **496** (1998) 505. 42
- 3950 [25] SAGE collaboration, *Measurement of the solar neutrino capture rate with gallium  
3951 metal. III: Results for the 2002–2007 data-taking period*, *Phys. Rev. C* **80** (2009)  
3952 015807 [[0901.2200](#)]. 42, 54
- 3953 [26] F. Kaether, W. Hampel, G. Heusser, J. Kiko and T. Kirsten, *Reanalysis of the  
3954 GALLEX solar neutrino flux and source experiments*, *Phys. Lett. B* **685** (2010) 47  
3955 [[1001.2731](#)]. 42, 54
- 3956 [27] Q.R. Ahmad, R.C. Allen, T.C. Andersen, J.D. Anglin, G. Bühler, J.C. Barton  
3957 et al., *Measurement of the Rate of  $\nu_e + d \rightarrow p + p + e^-$  Interactions Produced by  
3958  $^8\text{B}$  Solar Neutrinos at the Sudbury Neutrino Observatory*, . 43
- 3959 [28] Q.R. Ahmad, R.C. Allen, T.C. Andersen, J. D. Anglin, J.C. Barton, E.W. Beier  
3960 et al., *Direct Evidence for Neutrino Flavor Transformation from Neutral-Current  
3961 Interactions in the Sudbury Neutrino Observatory*, . 43
- 3962 [29] T.K. Gaisser and M. Honda, *Flux of atmospheric neutrinos*, . 43

## BIBLIOGRAPHY

- 3963 [30] K. Hirata, T. Kajita, M. Koshiba, M. Nakahata, S. Ohara, Y. Oyama et al.,  
3964 *Experimental study of the atmospheric neutrino flux*, . 44
- 3965 [31] D. Casper, R. Becker-Szendy, C.B. Bratton, D.R. Cady, R. Claus, S.T. Dye et al.,  
3966 *Measurement of atmospheric neutrino composition with the imb-3 detector*, . 44
- 3967 [32] M. Ambrosio, R. Antolini, C. Aramo, G. Auriemma, A. Baldini, G. C. Barbarino  
3968 et al., *Measurement of the atmospheric neutrino-induced upgoing muon flux using*  
3969 *macro*, . 44
- 3970 [33] W. Allison, G. Alner, D. Ayres, W. Barrett, C. Bode, P. Border et al.,  
3971 *Measurement of the atmospheric neutrino flavour composition in soudan 2*, . 44
- 3972 [34] SUPER-KAMIOKANDE collaboration, *Evidence for oscillation of atmospheric*  
3973 *neutrinos*, *Phys. Rev. Lett.* **81** (1998) 1562 [[hep-ex/9807003](#)]. 44
- 3974 [35] P. Minkowski,  $\mu \rightarrow e\gamma$  at a Rate of One Out of  $10^9$  Muon Decays?, *Phys. Lett. B*  
3975 **67** (1977) 421. 47
- 3976 [36] M. Gell-Mann, P. Ramond and R. Slansky, *Complex Spinors and Unified Theories*,  
3977 *Conf. Proc. C* **790927** (1979) 315 [[1306.4669](#)]. 47
- 3978 [37] T. Yanagida, *Horizontal gauge symmetry and masses of neutrinos*, *Conf. Proc. C*  
3979 **7902131** (1979) 95. 47
- 3980 [38] R.N. Mohapatra and G. Senjanovic, *Neutrino Mass and Spontaneous Parity*  
3981 *Nonconservation*, *Phys. Rev. Lett.* **44** (1980) 912. 47
- 3982 [39] J. Schechter and J.W.F. Valle, *Neutrino Masses in  $SU(2) \times U(1)$  Theories*, *Phys.*  
3983 *Rev. D* **22** (1980) 2227. 47
- 3984 [40] B. Pontecorvo, *Mesonium and anti-mesonium*, *Sov. Phys. JETP* **6** (1957) 429. 47
- 3985 [41] M. Gell-Mann and A. Pais, *Behavior of neutral particles under charge conjugation*,  
3986 . 47

## BIBLIOGRAPHY

- 3987 [42] B. Pontecorvo, *Neutrino Experiments and the Problem of Conservation of  
Leptonic Charge*, *Zh. Eksp. Teor. Fiz.* **53** (1967) 1717. 48
- 3988
- 3989 [43] B. Pontecorvo, *Inverse beta processes and nonconservation of lepton charge*, *Zh.  
Eksp. Teor. Fiz.* **34** (1957) 247. 49
- 3990
- 3991 [44] Z. Maki, M. Nakagawa and S. Sakata, *Remarks on the unified model of elementary  
particles*, *Prog. Theor. Phys.* **28** (1962) 870. 49
- 3992
- 3993 [45] PARTICLE DATA GROUP collaboration, *Review of particle physics*, *Phys. Rev. D*  
**110** (2024) 030001. 51
- 3994
- 3995 [46] L. Wolfenstein, *Neutrino Oscillations in Matter*, *Phys. Rev. D* **17** (1978) 2369. 52
- 3996
- 3997 [47] B.T. Cleveland, T. Daily, R. Davis, Jr., J.R. Distel, K. Lande, C.K. Lee et al.,  
*Measurement of the solar electron neutrino flux with the Homestake chlorine  
detector*, *Astrophys. J.* **496** (1998) 505. 54
- 3998
- 3999 [48] G. Bellini et al., *Precision measurement of the  $^{7}\text{Be}$  solar neutrino interaction rate  
in Borexino*, *Phys. Rev. Lett.* **107** (2011) 141302 [[1104.1816](#)]. 54
- 4000
- 4001 [49] SUPER-KAMIOKANDE collaboration, *Solar neutrino measurements in  
super-Kamiokande-I*, *Phys. Rev. D* **73** (2006) 112001 [[hep-ex/0508053](#)]. 54
- 4002
- 4003 [50] SNO collaboration, *Combined Analysis of all Three Phases of Solar Neutrino  
Data from the Sudbury Neutrino Observatory*, *Phys. Rev. C* **88** (2013) 025501  
[[1109.0763](#)]. 54
- 4004
- 4005
- 4006 [51] SUPER-KAMIOKANDE collaboration, *Atmospheric neutrino oscillation analysis  
with external constraints in Super-Kamiokande I-IV*, *Phys. Rev. D* **97** (2018)  
072001 [[1710.09126](#)]. 54
- 4007
- 4008
- 4009 [52] ICECUBE collaboration, *Measurement of Atmospheric Neutrino Oscillations at  
6–56 GeV with IceCube DeepCore*, *Phys. Rev. Lett.* **120** (2018) 071801  
[[1707.07081](#)]. 54
- 4010
- 4011

## BIBLIOGRAPHY

- 4012 [53] KamLAND collaboration, *Reactor On-Off Antineutrino Measurement with*  
4013 *KamLAND*, *Phys. Rev. D* **88** (2013) 033001 [[1303.4667](#)]. 55
- 4014 [54] RENO collaboration, *Measurement of Reactor Antineutrino Oscillation Amplitude*  
4015 *and Frequency at RENO*, *Phys. Rev. Lett.* **121** (2018) 201801 [[1806.00248](#)]. 55
- 4016 [55] DAYA BAY collaboration, *Measurement of the Electron Antineutrino Oscillation*  
4017 *with 1958 Days of Operation at Daya Bay*, *Phys. Rev. Lett.* **121** (2018) 241805  
4018 [[1809.02261](#)]. 55
- 4019 [56] K.J. Kelly, P.A.N. Machado, S.J. Parke, Y.F. Perez-Gonzalez and R.Z. Funchal,  
4020 *Neutrino mass ordering in light of recent data*, *Phys. Rev. D* **103** (2021) 013004.  
4021 55
- 4022 [57] P. Dunne, “Latest Neutrino Oscillation Results from T2K.” Jul, 2020. 55
- 4023 [58] MINOS collaboration, *Combined analysis of  $\nu_\mu$  disappearance and  $\nu_\mu \rightarrow \nu_e$*   
4024 *appearance in MINOS using accelerator and atmospheric neutrinos*, *Phys. Rev.*  
4025 *Lett.* **112** (2014) 191801 [[1403.0867](#)]. 55
- 4026 [59] OPERA collaboration, *Final Results of the OPERA Experiment on  $\nu_\tau$*   
4027 *Appearance in the CNGS Neutrino Beam*, *Phys. Rev. Lett.* **120** (2018) 211801  
4028 [[1804.04912](#)]. 55
- 4029 [60] K2K collaboration, *Measurement of Neutrino Oscillation by the K2K Experiment*,  
4030 *Phys. Rev. D* **74** (2006) 072003 [[hep-ex/0606032](#)]. 55
- 4031 [61] DUNE collaboration, *Long-baseline neutrino oscillation physics potential of the*  
4032 *DUNE experiment*, *Eur. Phys. J. C* **80** (2020) 978 [[2006.16043](#)]. 55
- 4033 [62] HYPER-KAMIOKANDE collaboration, *Physics potential of Hyper-Kamiokande for*  
4034 *neutrino oscillation measurements*, *PoS NuFact2019* (2019) 040. 55
- 4035 [63] SUPERNEMO collaboration, *Probing New Physics Models of Neutrinoless Double*  
4036 *Beta Decay with SuperNEMO*, *Eur. Phys. J. C* **70** (2010) 927 [[1005.1241](#)]. 56

## BIBLIOGRAPHY

- 4037 [64] SNO+ collaboration, *Current Status and Future Prospects of the SNO+*  
 4038 *Experiment, Adv. High Energy Phys.* **2016** (2016) 6194250 [[1508.05759](#)]. 56
- 4039 [65] NEXT collaboration, *Sensitivity of a tonne-scale NEXT detector for neutrinoless*  
 4040 *double beta decay searches, JHEP* **2021** (2021) 164 [[2005.06467](#)]. 56
- 4041 [66] P. Coloma and P. Huber, *Impact of nuclear effects on the extraction of neutrino*  
 4042 *oscillation parameters, Phys. Rev. Lett.* **111** (2013) 221802 [[1307.1243](#)]. 57
- 4043 [67] P. Coloma, P. Huber, C.-M. Jen and C. Mariani, *Neutrino-nucleus interaction*  
 4044 *models and their impact on oscillation analyses, Phys. Rev. D* **89** (2014) 073015  
 4045 [[1311.4506](#)]. 57
- 4046 [68] U. Mosel, *Neutrino Interactions with Nucleons and Nuclei: Importance for*  
 4047 *Long-Baseline Experiments, Ann. Rev. Nucl. Part. Sci.* **66** (2016) 171  
 4048 [[1602.00696](#)]. 57
- 4049 [69] J.A. Formaggio and G.P. Zeller, *From ev to eev: Neutrino cross sections across*  
 4050 *energy scales, Rev. Mod. Phys.* **84** (2012) 1307 [[1305.7513](#)]. 58
- 4051 [70] L. Bathe-Peters, S. Gardiner and R. Guenette, *Comparing generator predictions*  
 4052 *of transverse kinematic imbalance in neutrino-argon scattering,* [2201.04664](#). 59
- 4053 [71] R.A. Smith and E.J. Moniz, *Neutrino reactions on nuclear targets, Nucl. Phys. B*  
 4054 **43** (1972) 605. 59
- 4055 [72] H. Nakamura and R. Seki, *Quasi-elastic neutrino-nucleus scattering and spectral*  
 4056 *function, Nuclear Physics B - Proceedings Supplements* **112** 197. 59
- 4057 [73] V. Pandey, N. Jachowicz, T. Van Cuyck, J. Ryckebusch and M. Martini,  
 4058 *Low-energy excitations and quasielastic contribution to electron-nucleus and*  
 4059 *neutrino-nucleus scattering in the continuum random-phase approximation, Phys.*  
 4060 *Rev. C* **92** (2015) 024606 [[1412.4624](#)]. 59

## BIBLIOGRAPHY

- 4061 [74] A. Nikolakopoulos, R. González-Jiménez, N. Jachowicz, K. Niewczas, F. Sánchez  
4062 and J.M. Udías, *Benchmarking intranuclear cascade models for neutrino*  
4063 *scattering with relativistic optical potentials*, *Phys. Rev. C* **105** (2022) 054603  
4064 [2202.01689]. 59
- 4065 [75] MINIBooNE collaboration, *First Measurement of the Muon Neutrino Charged*  
4066 *Current Quasielastic Double Differential Cross Section*, *Phys. Rev. D* **81** (2010)  
4067 092005 [1002.2680]. 60
- 4068 [76] MINERvA collaboration, *Measurements of the Inclusive Neutrino and*  
4069 *Antineutrino Charged Current Cross Sections in MINERvA Using the Low- $\nu$  Flux*  
4070 *Method*, *Phys. Rev. D* **94** (2016) 112007 [1610.04746]. 60
- 4071 [77] MICROBooNE collaboration, *First Measurement of Energy-Dependent Inclusive*  
4072 *Muon Neutrino Charged-Current Cross Sections on Argon with the MicroBooNE*  
4073 *Detector*, *Phys. Rev. Lett.* **128** (2022) 151801 [2110.14023]. 60
- 4074 [78] SBND collaboration, *Neutrino cross-section measurement prospects with SBND*,  
4075 *PoS NuFact2017* (2018) 067. 60
- 4076 [79] NOvA collaboration, *Measurement of the double-differential muon-neutrino*  
4077 *charged-current inclusive cross section in the NOvA near detector*, *Phys. Rev. D*  
4078 **107** (2023) 052011 [2109.12220]. 60
- 4079 [80] T2K collaboration, *Measurement of the  $\nu_\mu$  charged-current cross sections on*  
4080 *water, hydrocarbon, iron, and their ratios with the T2K on-axis detectors*, *PTEP*  
4081 **2019** (2019) 093C02 [1904.09611]. 60
- 4082 [81] \$NU\$PRISM collaboration,  *$\nu$ PRISM: A new way of probing neutrino*  
4083 *interactions*, *PoS NUFAC2014* (2015) 046. 60
- 4084 [82] C. Hasnip, *DUNE-PRISM – A New Method to Measure Neutrino Oscillations*,  
4085 Ph.D. thesis, Oxford U., 2023. 60

## BIBLIOGRAPHY

- 4086 [83] DUNE collaboration, *Deep Underground Neutrino Experiment (DUNE), Far*  
 4087 *Detector Technical Design Report, Volume I Introduction to DUNE*, JINST **15**  
 4088 (2020) T08008 [2002.02967]. 61, 62, 63, 68, 69, 79, 80, 81, 82
- 4089 [84] DUNE collaboration, *Snowmass Neutrino Frontier: DUNE Physics Summary*,  
 4090 2203.06100. 63
- 4091 [85] DUNE collaboration, *Deep Underground Neutrino Experiment (DUNE), Far*  
 4092 *Detector Technical Design Report, Volume II: DUNE Physics*, 2002.03005. 64, 65,  
 4093 66, 73, 131, 140, 144
- 4094 [86] SUPER-KAMIOKANDE collaboration, *Search for Proton Decay via  $p \rightarrow e^+ \pi_0$  and*  
 4095  *$p \rightarrow \mu^+ \pi_0$  in a Large Water Cherenkov Detector*, Phys. Rev. Lett. **102** (2009)  
 4096 141801 [0903.0676]. 64
- 4097 [87] S. Raby, *Grand Unified Theories*, in *2nd World Summit: Physics Beyond the*  
 4098 *Standard Model*, 8, 2006 [[hep-ph/0608183](#)]. 64
- 4099 [88] KAMIOKANDE-II collaboration, *Observation of a Neutrino Burst from the*  
 4100 *Supernova SN 1987a*, Phys. Rev. Lett. **58** (1987) 1490. 64
- 4101 [89] R.M. Bionta et al., *Observation of a Neutrino Burst in Coincidence with*  
 4102 *Supernova SN 1987a in the Large Magellanic Cloud*, Phys. Rev. Lett. **58** (1987)  
 4103 1494. 64
- 4104 [90] J. Strait, E. McCluskey, T. Lundin, J. Willhite, T. Hamernik, V. Papadimitriou  
 4105 et al., *Long-baseline neutrino facility (lbnf) and deep underground neutrino*  
 4106 *experiment (dune) conceptual design report volume 3: Long-baseline neutrino*  
 4107 *facility for dune june 24, 2015*, 1601.05823. 65
- 4108 [91] DUNE collaboration, *Deep Underground Neutrino Experiment (DUNE) Near*  
 4109 *Detector Conceptual Design Report, Instruments* **5** (2021) 31 [2103.13910]. 67,  
 4110 68, 71, 72, 74, 75, 155

## BIBLIOGRAPHY

- 4111 [92] DUNE collaboration, *DUNE Phase II: Scientific Opportunities, Detector*  
4112 *Concepts, Technological Solutions*, 2408.12725. 70, 76
- 4113 [93] DUNE collaboration, *A Gaseous Argon-Based Near Detector to Enhance the*  
4114 *Physics Capabilities of DUNE*, 2203.06281. 72
- 4115 [94] F. Sauli, *Gem: A new concept for electron amplification in gas detectors*, *Nuclear*  
4116 *Instruments and Methods in Physics Research Section A: Accelerators,*  
4117 *Spectrometers, Detectors and Associated Equipment* **386** 531. 74, 78
- 4118 [95] A. Ritchie-Yates et al., *First operation of an ALICE OROC operated in high*  
4119 *pressure Ar-CO<sub>2</sub> and Ar-CH<sub>4</sub>*, *Eur. Phys. J. C* **83** (2023) 1139 [2305.08822]. 77
- 4120 [96] ALICE TPC collaboration, *The upgrade of the ALICE TPC with GEMs and*  
4121 *continuous readout*, *JINST* **16** (2021) P03022 [2012.09518]. 77
- 4122 [97] F. Sauli, *The gas electron multiplier (gem): Operating principles and applications*,  
4123 *Nuclear Instruments and Methods in Physics Research Section A: Accelerators,*  
4124 *Spectrometers, Detectors and Associated Equipment* **805** 2. 78
- 4125 [98] C. Lippmann, *A continuous read-out tpc for the alice upgrade*, *Nuclear*  
4126 *Instruments and Methods in Physics Research Section A: Accelerators,*  
4127 *Spectrometers, Detectors and Associated Equipment* **824** 543. 78
- 4128 [99] C. Calabria, *Large-size triple gem detectors for the cms forward muon upgrade*,  
4129 *Nuclear and Particle Physics Proceedings* **273–275** 1042. 78
- 4130 [100] DUNE collaboration, *The DUNE Far Detector Vertical Drift Technology*,  
4131 *Technical Design Report*, 2312.03130. 83, 84
- 4132 [101] DUNE collaboration, *Deep Underground Neutrino Experiment (DUNE), Far*  
4133 *Detector Technical Design Report, Volume IV: Far Detector Single-phase*  
4134 *Technology*, *JINST* **15** (2020) T08010 [2002.03010]. 85

## BIBLIOGRAPHY

- 4135 [102] DUNE DAQ, “dtp-firmware.”  
4136 <https://gitlab.cern.ch/dune-daq/readout/dtp-firmware>, 2020. 87
- 4137 [103] DUNE DAQ, “dtp-simulation.”  
4138 <https://gitlab.cern.ch/dune-daq/readout/dtp-simulation>, 2020. 90
- 4139 [104] DUNE DAQ, “dtpe emulator.”  
4140 [https://github.com/DUNE-DAQ/dtpe emulator/tree/fmlopez/filter\\_ana](https://github.com/DUNE-DAQ/dtpe emulator/tree/fmlopez/filter_ana),  
4141 2022. 90
- 4142 [105] J. McClellan and T. Parks, *A personal history of the Parks-McClellan algorithm*,  
4143 *IEEE Signal Processing Magazine* **22** (2005) 82. 91
- 4144 [106] G. Turin, *An introduction to matched filters*, *IEEE Transactions on Information*  
4145 *Theory* **6** (1960) 311. 94
- 4146 [107] J.W. Goodman, *Statistical Optics*, Wiley (1985). 96
- 4147 [108] B. Dwork, *Detection of a pulse superimposed on fluctuation noise*, *Proceedings of*  
4148 *the IRE* **38** (1950) 771. 97
- 4149 [109] L. Wainstein and V. Zubakov, *Extraction of Signals from Noise*, Prentice-Hall  
4150 (1962). 97
- 4151 [110] E.D. Church, *Larsoft: A software package for liquid argon time projection drift*  
4152 *chambers*, **1311.6774**. 100, 101
- 4153 [111] S.V. Stehman, *Selecting and interpreting measures of thematic classification*  
4154 *accuracy*, *Remote Sensing of Environment* **62** (1997) 77. 114
- 4155 [112] A.A. Taha and A. Hanbury, *Metrics for evaluating 3d medical image*  
4156 *segmentation: analysis, selection, and tool*, *BMC Medical Imaging* **15** (2015) . 115
- 4157 [113] J. Silk, K.A. Olive and M. Srednicki, *The Photino, the Sun and High-Energy*  
4158 *Neutrinos*, *Phys. Rev. Lett.* **55** (1985) 257. 121

## BIBLIOGRAPHY

- 4159 [114] M. Srednicki, K.A. Olive and J. Silk, *High-Energy Neutrinos from the Sun and*  
4160 *Cold Dark Matter*, *Nucl. Phys. B* **279** (1987) 804. 121
- 4161 [115] J.S. Hagelin, K.W. Ng and K.A. Olive, *A High-energy Neutrino Signature From*  
4162 *Supersymmetric Relics*, *Phys. Lett. B* **180** (1986) 375. 121
- 4163 [116] T.K. Gaisser, G. Steigman and S. Tilav, *Limits on Cold Dark Matter Candidates*  
4164 *from Deep Underground Detectors*, *Phys. Rev. D* **34** (1986) 2206. 121
- 4165 [117] N. Bernal, J. Martín-Albo and S. Palomares-Ruiz, *A novel way of constraining*  
4166 *WIMPs annihilations in the Sun: MeV neutrinos*, *JCAP* **08** (2013) 011  
4167 [1208.0834]. 121, 122, 128
- 4168 [118] C. Rott, J. Siegal-Gaskins and J.F. Beacom, *New Sensitivity to Solar WIMP*  
4169 *Annihilation using Low-Energy Neutrinos*, *Phys. Rev. D* **88** (2013) 055005  
4170 [1208.0827]. 121, 128
- 4171 [119] C. Rott, S. In, J. Kumar and D. Yaylali, *Dark Matter Searches for Monoenergetic*  
4172 *Neutrinos Arising from Stopped Meson Decay in the Sun*, *JCAP* **11** (2015) 039  
4173 [1510.00170]. 121
- 4174 [120] DUNE collaboration, *Searching for solar KDAR with DUNE*, *JCAP* **10** (2021)  
4175 065 [2107.09109]. 121
- 4176 [121] G. Busoni, A. De Simone and W.-C. Huang, *On the Minimum Dark Matter Mass*  
4177 *Testable by Neutrinos from the Sun*, *JCAP* **07** (2013) 010 [1305.1817]. 122
- 4178 [122] V.A. Bednyakov and F. Simkovic, *Nuclear spin structure in dark matter search:*  
4179 *The Zero momentum transfer limit*, *Phys. Part. Nucl.* **36** (2005) 131  
4180 [hep-ph/0406218]. 123
- 4181 [123] A. Gould, *WIMP Distribution in and Evaporation From the Sun*, *Astrophys. J.*  
4182 **321** (1987) 560. 123

## BIBLIOGRAPHY

- 4183 [124] J.N. Bahcall, M.H. Pinsonneault and S. Basu, *Solar models: Current epoch and*  
 4184 *time dependences, neutrinos, and helioseismological properties*, *Astrophys. J.* **555**  
 4185 (2001) 990 [[astro-ph/0010346](#)]. 126
- 4186 [125] T. Golan, J.T. Sobczyk and J. Zmuda, *NuWro: the Wroclaw Monte Carlo*  
 4187 *Generator of Neutrino Interactions*, *Nucl. Phys. B Proc. Suppl.* **229-232** (2012)  
 4188 499. 130
- 4189 [126] G. Cowan, K. Cranmer, E. Gross and O. Vitells, *Asymptotic formulae for*  
 4190 *likelihood-based tests of new physics*, *Eur. Phys. J. C* **71** (2011) 1554 [[1007.1727](#)].  
 4191 131
- 4192 [127] T. Kaluza, *Zum Unitätsproblem der Physik, Sitzungsber. Preuss. Akad. Wiss.*  
 4193 *Berlin (Math. Phys.)* **1921** (1921) 966 [[1803.08616](#)]. 133
- 4194 [128] O. Klein, *Quantum Theory and Five-Dimensional Theory of Relativity. (In*  
 4195 *German and English)*, *Z. Phys.* **37** (1926) 895. 133
- 4196 [129] T. Appelquist, H.-C. Cheng and B.A. Dobrescu, *Bounds on universal extra*  
 4197 *dimensions*, *Phys. Rev. D* **64** (2001) 035002 [[hep-ph/0012100](#)]. 133
- 4198 [130] N. Arkani-Hamed, S. Dimopoulos and G.R. Dvali, *The Hierarchy problem and new*  
 4199 *dimensions at a millimeter*, *Phys. Lett. B* **429** (1998) 263 [[hep-ph/9803315](#)]. 133
- 4200 [131] L. Randall and R. Sundrum, *A Large mass hierarchy from a small extra*  
 4201 *dimension*, *Phys. Rev. Lett.* **83** (1999) 3370 [[hep-ph/9905221](#)]. 133
- 4202 [132] G. Servant and T.M.P. Tait, *Is the lightest Kaluza-Klein particle a viable dark*  
 4203 *matter candidate?*, *Nucl. Phys. B* **650** (2003) 391 [[hep-ph/0206071](#)]. 134
- 4204 [133] H.-C. Cheng, K.T. Matchev and M. Schmaltz, *Radiative corrections to*  
 4205 *Kaluza-Klein masses*, *Phys. Rev. D* **66** (2002) 036005 [[hep-ph/0204342](#)]. 134
- 4206 [134] M. Blennow, J. Edsjö and T. Ohlsson, *Neutrinos from WIMP annihilations using*  
 4207 *a full three-flavor Monte Carlo*, *JCAP* **01** (2008) 021 [[0709.3898](#)]. 134, 137

## BIBLIOGRAPHY

- 4208 [135] J. Edsjö, J. Elevant and C. Niblaeus, *WimpSim Neutrino Monte Carlo*. 134, 137
- 4209 [136] U. Haisch and A. Weiler, *Bound on minimal universal extra dimensions from*  
4210 *anti-B —> X(s)gamma*, *Phys. Rev. D* **76** (2007) 034014 [[hep-ph/0703064](#)]. 136
- 4211 [137] A. Freitas and U. Haisch, *Anti-B —> X(s) gamma in two universal extra*  
4212 *dimensions*, *Phys. Rev. D* **77** (2008) 093008 [[0801.4346](#)]. 136
- 4213 [138] C. Rott, D. Jeong, J. Kumar and D. Yaylali, *Neutrino Topology Reconstruction at*  
4214 *DUNE and Applications to Searches for Dark Matter Annihilation in the Sun*,  
4215 *JCAP* **07** (2019) 006 [[1903.04175](#)]. 139
- 4216 [139] F. Pedregosa, G. Varoquaux, A. Gramfort, V. Michel, B. Thirion, O. Grisel et al.,  
4217 *Scikit-learn: Machine learning in Python*, *Journal of Machine Learning Research*  
4218 **12** (2011) 2825. 145
- 4219 [140] J. Kopp, V. Niro, T. Schwetz and J. Zupan, *DAMA/LIBRA and leptonically*  
4220 *interacting Dark Matter*, *Phys. Rev. D* **80** (2009) 083502 [[0907.3159](#)]. 149
- 4221 [141] PARTICLE DATA GROUP collaboration, *Review of Particle Physics*, *PTEP* **2020**  
4222 (2020) 083C01. 150
- 4223 [142] M. Beltran, D. Hooper, E.W. Kolb and Z.C. Krusberg, *Deducing the nature of*  
4224 *dark matter from direct and indirect detection experiments in the absence of*  
4225 *collider signatures of new physics*, *Phys. Rev. D* **80** (2009) 043509 [[0808.3384](#)].  
4226 151
- 4227 [143] PLANCK collaboration, *Planck 2018 results. VI. Cosmological parameters*, *Astron.*  
4228 *Astrophys.* **641** (2020) A6 [[1807.06209](#)]. 151
- 4229 [144] C. Green, J. Kowalkowski, M. Paterno, M. Fischler, L. Garren and Q. Lu, *The*  
4230 *Art Framework*, *J. Phys. Conf. Ser.* **396** (2012) 022020. 156
- 4231 [145] H. Bethe, *Zur theorie des durchgangs schneller korpuskularstrahlen durch materie*,  
4232 *Annalen der Physik* **397** (1930) 325. 161

## BIBLIOGRAPHY

- 4233 [146] E. Fermi, *The ionization loss of energy in gases and in condensed materials*,  
 4234 *Physical Review* **57** (1940) 485. 162
- 4235 [147] R. Sternheimer, M. Berger and S. Seltzer, *Density effect for the ionization loss of*  
 4236 *charged particles in various substances*, *Atomic Data and Nuclear Data Tables* **30**  
 4237 (1984) 261. 162
- 4238 [148] W.W.M. Allison and J.H. Cobb, *Relativistic Charged Particle Identification by*  
 4239 *Energy Loss*, *Ann. Rev. Nucl. Part. Sci.* **30** (1980) 253. 162
- 4240 [149] W. Blum, L. Rolandi and W. Riegler, *Particle detection with drift chambers*,  
 4241 *Particle Acceleration and Detection* (2008), 10.1007/978-3-540-76684-1. 162
- 4242 [150] ALICE TPC collaboration, *Particle identification of the ALICE TPC via dE/dx*,  
 4243 *Nucl. Instrum. Meth. A* **706** (2013) 55. 162
- 4244 [151] L. Landau, *On the energy loss of fast particles by ionization*, *J. Phys. (USSR)* **8**  
 4245 (1944) 201. 165
- 4246 [152] W. Ulmer and E. Matsinos, *Theoretical methods for the calculation of Bragg*  
 4247 *curves and 3D distributions of proton beams*, *The European Physical Journal*  
 4248 *Special Topics* **190** (2010) 1. 166
- 4249 [153] E. Aprile, A.E. Bolotnikov, A.L. Bolozdynya and T. Doke, *Noble Gas Detectors*,  
 4250 Wiley (Oct., 2008), 10.1002/9783527610020. 169
- 4251 [154] D.S. Wilks, *Statistical Methods in the Atmospheric Sciences*, Academic Press. 206
- 4252 [155] ALICE collaboration, *Production of pions, kaons and protons in pp collisions at*  
 4253  $\sqrt{s} = 900 \text{ gev with alice at the lhc}$ , **1101.4110**. 208
- 4254 [156] U. Einhaus, *Charged hadron identification with de/dx and time-of-flight at future*  
 4255 *higgs factories*, **2110.15115**. 208

## BIBLIOGRAPHY

- 4256 [157] R. Frühwirth, *Application of filter methods to the reconstruction of tracks and*  
4257 *vertices in events of experimental high energy physics*, Ph.D. thesis, Technischen  
4258 Universität Wien, 1988. 213
- 4259 [158] P. Astier, A. Cardini, R.D. Cousins, A. Letessier-Selvon, B.A. Popov and  
4260 T. Vinogradova, *Kalman filter track fits and track breakpoint analysis*, *Nuclear*  
4261 *Instruments and Methods in Physics Research Section A: Accelerators,*  
4262 *Spectrometers, Detectors and Associated Equipment* **450** (2000) 138. 213
- 4263 [159] T2K UK collaboration, *The Electromagnetic Calorimeter for the T2K Near*  
4264 *Detector ND280*, *JINST* **8** (2013) P10019 [1308.3445]. 222
- 4265 [160] J.E. Gaiser, *Charmonium Spectroscopy From Radiative Decays of the  $J/\psi$  and  $\psi'$* ,  
4266 Ph.D. thesis, Stanford University, 1982. 227